UNIVERSIDADE FEDERAL DE SANTA CATARINA
CAMPUS TRINDADE
PROGRAMA DE PÓS-GRADUAÇÃO EM ENGENHARIA MECÂNICA

Arthur Kleyton Azevedo de Araújo

Effect of non-uniform heating on horizontal flow boiling of R141b

Florianópolis
2024

Arthur Kleyton Azevedo de Araújo

Effect of non-uniform heating on horizontal flow boiling of R141b

Tese submetida ao Programa de Pós-Graduação em Engenharia Mecânica da Universidade Federal de Santa Catarina como requisito parcial para a obtenção do título de Doutor em Engenharia Mecânica.

Orientador: Prof. Júlio César Passos, Dr.

Florianópolis

2024

Ficha catalográfica gerada por meio de sistema automatizado gerenciado pela BU/UFSC.
Dados inseridos pelo próprio autor.

de Araújo, Arthur Kleyton Azevedo
Effect of non-uniform heating on horizontal flow boiling of R141b / Arthur Kleyton Azevedo de Araújo ; orientador, Júlio César Passos, 2024.
159 p.

Tese (doutorado) - Universidade Federal de Santa Catarina, Centro Tecnológico, Programa de Pós-Graduação em Engenharia Mecânica, Florianópolis, 2024.

Inclui referências.

1. Engenharia Mecânica. 2. Flow boiling. 3. Non-uniform heating. 4. Two-phase flow. I. Passos, Júlio César. II. Universidade Federal de Santa Catarina. Programa de Pós Graduação em Engenharia Mecânica. III. Título.

Arthur Kleyton Azevedo de Araújo

Effect of non-uniform heating on horizontal flow boiling of R141b

O presente trabalho em nível de Doutorado foi avaliado e aprovado, em 18 de dezembro de 2023, pela banca examinadora composta pelos seguintes membros:

Prof. Gherhardt Ribatski, Dr.
Universidade de São Paulo - USP

Prof. Jader Riso Barbosa Júnior, Dr.
Universidade Federal de Santa Catarina - UFSC

Profa. Catherine Colin, Dra.
Université de Toulouse - France

Prof. Jaco Dirker, Dr.
University of Pretoria – South Africa

Certificamos que esta é a versão original e final do trabalho de conclusão que foi julgado adequado para obtenção do título de Doutor em Engenharia Mecânica.

ICP-Edu
Documento assinado digitalmente
Henrique Simas
Data: 15/03/2024 18:28:33-0300
CPF: ***.194.639-**
Verifique as assinaturas em https://v.ufsc.br

Coordenação do Programa de Pós-Graduação

ICP-Edu
Documento assinado digitalmente
Julio Cesar Passos
Data: 15/03/2024 17:48:48-0300
CPF: ***.357.447-**
Verifique as assinaturas em https://v.ufsc.br

Prof. Júlio César Passos, Dr.
Orientador

This work is dedicated to my parents,
for instilling in me an interest and admiration for knowledge,
and to my wife, Paula Nascimento, whose unconditional support
allowed me to remain healthy.

Acknowledgements

I would like to express my sincere gratitude to all of the people and institutions that somehow contributed to this work. I would like to thank...

...my wife, Paula, without whose support over those years I would never have finished this doctorate.

...my parents, Ana Célia and Francisco das Chagas, who believed in my competence and whose financial support allowed me to get through the hard times. ...my supervisor, Professor Júlio César Passos, for sharing his knowledge and guidance during this time, as well as his dedication to making this work the best possible.

...POSMEC, which was always available to provide precise information and for the financial support that allowed the experimental work to be done.

...FAPESC for the scholarship that enabled me to perform the work.

...my lab colleagues: Alexander Leyton, Rafael Passarella, Victor Pigozzo, Bruna Oliveira, and Felipe Emer, especially Gabriel Pereira and Carlos Eduardo Perin, who have worked directly with me and given their best to ensure the best results.

...the LEPTEN technicians, Leandro da Silva and Uallas de Brito, for their support whenever needed to make things happen.

...the Federal University of Santa Catarina – UFSC, which became my second home during the time of this doctoral research.

...my colleagues from the Netherlands, especially Professor Cees van der Geld, for sharing his knowledge and guidance during my time there; Leander Boer, my office mate, who shared his knowledge and dedicated his time so I could conduct experimental work within six months at the Eindhoven University of Technology – TUe; and Rodrigo Lira, my Brazilian fellow who was always there whenever needed.

...my friends from Rio Grande do Norte, Aidée Torres, Felipe Freitas, and João Gutemberg, who lived together with me here in Florianópolis and helped me adapt to a new place during the early stages of this doctoral research.

...and all others who somehow contributed to this work.

‘The same boiling water that softens the potato hardens the egg. It’s what you’re made of. Not the circumstances.”

Unknown

Resumo

A Energia Solar Concentrada (CSP, do inglês *Concentrating Solar Power*) com Refletores Lineares de Fresnel (LFR, do inglês *Linear Fresnel Reflectors*) com Geração Direta de Vapor (DSG, do inglês *Direct Steam Generation*) tem potencial como fonte de energia limpa e renovável. Esta pesquisa aborda a complexidade introduzida por essas tecnologias, focando na distribuição não uniforme de radiação em absorvedores trapezoidais sem refletores secundários dos LFRs. Especificamente, avalia o impacto do fluxo de calor não uniforme no escoamento horizontal em ebulição de R141b em um tubo de aço inoxidável com diâmetro interno de 10,92 mm. O experimento considera duas velocidades mássicas (50 e 150 kg $\mathrm{m}^{-2}\mathrm{s}^{-1}$) e dois fluxos de calor (3,4 e 10,5 kW m^{-2}), juntamente com três diferentes condições de aquecimento (uniforme, por baixo e por cima). Os resultados revelam influências significativas no coeficiente de transferência de calor, especialmente para padrões de escoamento não anulares, embora nenhuma influencia tenha sido observada no gradiente de pressão. Os dados experimentais foram testados com dez correlações para queda de pressão e doze para o coeficiente de transferência de calor. O estudo mostra os modelos mais precisos para prever essas variáveis e destaca os melhores. A análise de informação mútua identifica os grupos adimensionais mais influentes na previsão do número de Nusselt bifásico, onde os dois números de Reynolds bifásicos derivados deste trabalho demonstram as menores incertezas na estimativa desse número. Além disso, o trabalho fornece uma avaliação abrangente das condições assimétricas de aquecimento no escoamento em ebulição, avançando tanto a compreensão acadêmica quanto as aplicações industriais no contexto da geração de energia limpa e renovável.

Palavras-chaves: escoamento horizontal em ebulição; escoamento bifásico; fluxo de calor não uniforme; transferência de calor; números adimensionais

Abstract

Concentrated Solar Power (CSP) and Linear Fresnel Reflectors (LFR) with Direct Steam Generation (DSG) hold promise as clean and renewable energy sources. This research addresses the complexity introduced by these technologies, focusing on the non-uniform radiation distribution in trapezoidal absorbers without secondary reflectors from LFRs. Specifically, it evaluates the impact of non-uniform heat flux on horizontal flow boiling of R141b in a stainless steel tube of 10.92 mm inner diameter. The experiment considers two mass velocities (50 and 150 kg $m^{-2}s^{-1}$) and two heat fluxes (3.4 and 10.5 kW m^{-2}), along with three different heating conditions (uniform, bottom, and top). The findings reveal significant influences on the heat transfer coefficient, especially for non-annular flow patterns, though none was seen for the pressure drop gradient. The experimental data was put against ten correlations for pressure drop and twelve for heat transfer coefficient. The study shows the most accurate models for predicting them and highlights the best ones. Mutual information analysis identifies the most influential dimensionless groups in predicting the two-phase Nusselt number, where the two derived two-phase Reynolds numbers demonstrate the lowest uncertainties in estimating it. Moreover, the work provides a comprehensive evaluation of asymmetric heating conditions in flow boiling, advancing both academic understanding and industrial applications in the context of clean and renewable energy generation.

Keywords: horizontal flow boiling; two-phase flow; non-uniform heat flux; heat transfer; dimensionless numbers

Resumo expandido

Introdução

A energia solar concentrada é uma fonte alternativa para conversão de energia. A utilização de refletores lineares de Fresnel combinada com a geração direta de vapor têm potencial para redução dos custos de geração. No entanto essa combinação traz complexidades aos sistemas de controle e operação de tais usinas. Uma das principais características dos absorvedores montados em cavidades trapezoidais utilizados para coleta da radiação solar é a distribuição da irradiação solar não uniforme nas superfícies dos tubos. Os sistemas de geração direta de vapor trabalham usualmente em pressões e temperaturas mais elevadas e consequentemente necessitam de materiais mais robustos, como aço inoxidável, e portanto sofrem maiores estresses térmicos. Esses estresses térmicos podem ser ampliados tendo em vista a distribuição de fluxo de calor não uniforme nas paredes dos tubos.

Tendo em vista este cenário, o presente estudo busca investigar os efeitos do aquecimento circunferencial não uniforme sobre o escoamento horizontal em ebulição. Para tal, os seguintes objetivos específicos serão avaliados:

- Analisar os efeitos do aquecimento circunferencial não uniforme sobre o desenvolvimento de padrões;
- Avaliar como a distribuição do fluxo de calor influencia no início da ebulição nucleada;
- Investigar como a ebulição nucleada molda a distribuição do fluxo de calor não uniforme;
- calcular experimentalmente o Coeficiente de Transferência de Calor (CTC) e a Queda de Pressão (QP) na seção de teste;
- Avaliar a influência da condição de aquecimento no CTC e QP;
- Comparar os CTC e QD com correlações da literatura;
- Analisar os números adimensionais para melhor ajuste de futuros modelos.

Materiais e métodos

Uma bancada experimental *indoor* foi desenvolvida para simular condições de aquecimento não uniforme, permitindo o estudo das condições termo hidráulicas com aquecimento da porção circunferencial inferior, superior e uniforme do tubo. Foi utilizado o fluido refrigerante R141b, que apesar de ser um fluido de limpeza de sistemas de refrigeração e estar em fase de substituição, apresenta uma baixa entalpia de vaporização e de saturação de 36 °C. Isto permite com que a bancada seja menos robusta em termos de isolamento e comprimento, além disso, por estar em fase de substituição é mais barato. Com a utilização de um medidor de vazão e sensores de pressão e temperatura distribuídos na entrada e saída da seção de teste, bem como termopares embutidos na parede do tubo nas posições superior, lateral e inferior do tubo, foi possível avaliar a queda de pressão e calcular o CTC experimental. Tendo em vista que a condição de fluxo de calor não uniforme distorce a distribuição interna deste fluxo, um modelo numérico de difusão de calor foi desenvolvido para calcular o CTC experimental. Os testes de perda de calor mostraram que tanto o preaquecedor quanto a seção de teste perdem no máximo 5% e 6% de calor para o ambiente, respectivamente, o que pode ser considerado satisfatório. Os resultados de número de Nusselt experimental foram comparados com os calculados pela correlação de Gnielinski e apresentaram resultados satisfatórios. A correlação previu 91,7% dos pontos dentro do intervalo de $\pm 30\%$.

Resultados e discussões

Os resultados de CTC monofásicos com aquecimento uniforme e não uniforme não apresentaram dependência do modo de aquecimento. Os valores de número de Richardson indicam que a convecção forçada é dominante sobre os efeitos de escoamento secundário devido aos efeitos de empuxo. A totalidade dos dados ficaram entre o intervalo de $\pm 30\%$ de erro, e a correlação de Gnielinski apresentou um Erro Percentual Médio Absoluto de 7,29%.

Foram realizados testes bifásicos para duas velocidades mássicas 50 e 150 kg $\mathrm{m}^{-2}\mathrm{s}^{-1}$, e um fluxo de calor para cada uma, 3,4 e 11,0 kW m^{-2}, respectivamente. O título de vapor variou de zero a aproximadamente 0,95. O aquecimento por baixo provocou distorção na distribuição de fluxo de calor interno na parede do tubo quando se iniciou a ebulição. O aquecimento uniforme provocou uma maior perturbação na pressão quando o escoamento passou de monofásico para bifásico, quando comparado ao aquecimento por baixo. Foram observados os padrões de escoamento *slug*, *slug*+estratificado ondulado, estratificado ondulado, intermitente e anular. Ao contrário do apresentado por Wang *et al.* (2019), não foram verificadas nenhuma influência do tipo de aquecimento em relação ao desenvolvimento dos padrões. No entanto, essa diferença pode ter ocorrido devido à abordagem diferente dos trabalhos, enquanto Wang *et al.* (2019) mantiveram a mesma potência dissipada em ambos os modos de aquecimento (uniforme e por baixo), nesta tese foi mantido o mesmo fluxo de calor (metade da potência para os casos não uniformes) para todos os modos de aquecimento. O mapa de padrões de Wojtan, Ursenbacher and Thome (2005b) teve uma precisão de 75,3% dos pontos experimentais, porém, alguns pontos em que o mapa falhou em prever estavam próximos a linha de transição de padrões. Apesar de serem mostradas linhas definidas, essa transição é na verdade mais abrangente. Seria injusto julgar a precisão do mapa em torno desses pontos.

Assim como observado por Dirker, Scheepers and Meyer (2022) o modo de aquecimento não influenciou a queda de pressão no escoamento em ebulição. O modelo de Cioncolini, Thome and Lombardi (2009) apresentou o melhor desempenho ao prever os gradientes de queda de pressão experimentais, com Erro Percentual Médio Absoluto (EPMA) de 20,41% e prevendo 86,9% dos dados no intervalo de $\pm 30\%$. Tendo em vista que a maioria dos pontos utilizados para análise da queda de pressão foram de escoamento anular, era esperado que este modelo apresentasse o melhor desempenho, pois foi construído especificamente para o escoamento anular.

A análise ANOVA demonstrou que o CTC bifásico sofre influência do modo de aquecimento desde que o padrão de escoamento não seja anular. No geral o aquecimento por baixo apresentou maiores CTC quando comparado ao aquecimento uniforme e superior. Os modelos de Wattelet *et al.* (1993) e Wojtan, Ursenbacher and Thome (2005b) apresentaram os melhores desempenhos ao prever o CTC para a velocidade mássica mais baixa (50 kg $\mathrm{m^{-2}s^{-1}}$), com EPMA de 27,7% e 27.1%, respectivamente. Para a velocidade mássica de 150 kg $\mathrm{m^{-2}s^{-1}}$, o modelo de Wattelet *et al.* (1993) apresentou o melhor EPMA (12,3%) com 92,5% dos dados no intervalo de $\pm 30\%$ de erro. Apesar do modelo de Fang, Wu and Yuan (2017) de modo geral ter apresentado valores de EPMA menores que 6% considerando apenas os dados de aquecimento uniforme, ele se provou um modelo superdimensionado e deve ser utilizado com cautela.

A análise de informação mútua sobre os grupos adimensionais mostrou que os números de Reynolds bifásicos desenvolvidos nesta tese causam a menor incerteza sobre o número de Nusselt bifásico. Apesar da falta de dados para uma maior verificação, estes números adimensionais se mostram como importantes na previsão da transferência de calor do escoamento em ebulição.

Conclusões

Os resultados desta tese mostraram que o aquecimento circunferencial não uniforme distorce a distribuição do fluxo de calor na parede do tubo quando o escoamento passa de monofásico para o bifásico. Nenhuma influência foi observada quanto ao modo de aquecimento e o desenvolvimento dos padrões de escoamento. Assim como Dirker, Scheepers and Meyer (2022), não houve influência do modo de aquecimento sobre a queda de pressão. No geral, o aquecimento por baixo apresentou maiores CTC quando comparado aos modos de aquecimento uniforme e de topo, porém apenas quando o tipo de escoamento não é anular. Os números de Reynolds bifásicos que consideram o transporte de quantidade de movimento por difusão e advecção do vapor e do líquido apresentaram as menores incertezas para prever o número de Nusselt bifásico.

Palavras-chaves: Escoamento horizontal em ebulição; Escoamento bifásico; Fluxo de calor não uniforme;

List of Figures

Figure 1 – Schematic drawing of a FLR trapezoidal cavity absorber. 28

Figure 2 – Wang *et al.* (2019) and Dirker, Scheepers and Meyer (2022) temperature measurement cross-section and heating schematics. 32

Figure 3 – Transient behavior of heat flux, pressure drop, mass velocity, and wall temperature from Qi *et al.*'s work. 35

Figure 4 – Transient behavior of heat flux, inlet pressure, mass velocity, pressure drop, and wall temperature from Dário's work. 36

Figure 5 – Kattan, Thome and Favrat's flow pattern map for adiabatic flow of R134a at 10.3 °C in a 12 mm diameter tube (S - Stratified; SW - Stratified-wavy; I - Intermittent; A - Annular; MF - Mist flow). 38

Figure 6 – Wojtan, Ursenbacher and Thome's flow pattern map for diabatic flow of R22 at 5 °C in a 13.84 mm diameter tube (S - Stratified; Slug; SW - Stratified-wavy; I - Intermittent; A - Annular; D - Dryout; MF - Mist flow). 40

Figure 7 – Barbieri, Jabardo and Bandarra Filho's inttermitent to annular transition line on the Kattan, Thome and Favrat's map. 41

Figure 8 – Experimental facility schematic for flow boiling with non-uniform circumferential heating tests. 68

Figure 9 – Second preheater with insulation layer. 71

Figure 10 – Test section with thermocouple wires and insulation layer. 71

Figure 11 – Thermocouple measurement sections along the tube (a) and distribution along tube cross-section (b). 72

Figure 12 – Viewing section. 73

Figure 13 – Camera set-up. 73

Figure 14 – Thermocouple measurement schematics. 75

Figure 15 – Eletrical circuit to measure the current and voltage drop in the preheater and in test section. 75

Figure 16 – Three cross section samples for the thermocouple placement into the tube wall. 77

Figure 17 – Outer (solid line) and inner (dashed line) radial heat flux for uniform heating under (a) low HTC and (b) high HTC, and bottom only heating under (c) low HTC and (d) high HTC. 80

Figure 18 – Pictures of (a) tube samples and (b) surface characterization testing. 82

Figure 19 – Heat loss rate versus temperature difference between the ambient and the mean fluid temperature. 85

Figure 20 – Heat rate imposed versus ambsorbed by the preheater and test section. . . . 86

Figure 21 – Predicted versus experimental HTC for single-phase flow validation. 87

Figure 22 – Histogram of the single-phase data points for the inlet temperature, mass flow rate, heat flux, and heating condition. 89
Figure 23 – Single-phase heat transfer coefficient along the tube length for three heating conditions (uniform, bottom, and top). 90
Figure 24 – Single-phase Nusselt Number versus Reynolds Number for three heating conditions (uniform, bottom, and top). 91
Figure 25 – Comparison between the theoretical Nusselt number predicted by Gnielinski correlation and experimental Nusselt number for single-phase flow under three heating conditions (uniform, bottom, and top). 92
Figure 26 – Two-phase flow dataset histogram of the following features: mass velocity, saturation temperature, heat flux, quality, flow pattern, and heating condition. 93
Figure 27 – Transient behavior of mean wall temperature of each measurement section and superheat temperature for uniform and bottom heating with $G \approx 50$ kg m^{-2}s^{-1}. 95
Figure 28 – Transient behavior of mean wall temperature of each measurement section and superheat temperature for uniform and bottom heating with $G \approx$ 150 kg m^{-2}s^{-1}. 96
Figure 29 – Transient behavior of top (T_t), side (T_s), and bottom (T_b) wall temperature for the fourth cross-section (middle of the tube), heat flux, mass velocity, and saturation pressure for uniform (black lines) and bottom (gray lines) heating for $G \approx 50$ kg m^{-2}s^{-1}. 97
Figure 30 – Transient behavior of top (T_t), side (T_s), and bottom (T_b) wall temperature for the fourth cross-section (middle of the tube), heat flux, mass velocity, and saturation pressure for uniform (black lines) and bottom (gray lines) heating for $G \approx 150$ kg m^{-2}s^{-1}. 98
Figure 31 – Flow pattern pictures from the experimental work and how they were labeled. 99
Figure 32 – Bar plot with the frequency of flow pattern for the two-phase flow experiments. 99
Figure 33 – Experimental flow pattern on the Wojtan flow pattern map for $p_{sat} = 140$ kPa, $d_{in} = 10.96$ mm, and $q'' = 11.0$ kW m^{-2}. 100
Figure 34 – Frame sequence of a droplet rewetting the upper surface of the tube for $G = 50$ kg m^{-2}s^{-1} and quality over 90% with bottom heating. 101
Figure 35 – Experimental pressure drop gradient versus quality for the three heating conditions (uniform, bottom, and top) and $G = 150$ kg m^{-2}s^{-1}, $T_{sat} = 39$ °C, $q'' = 10.5$ kW m^{-2}. 102
Figure 36 – Experimental pressure drop gradient versus the value predicted for each correlation with the lines of ±15% and ±30% error for $G = 150$ kg m^{-2}s^{-1}. 104
Figure 37 – Experimental heat transfer coefficient versus quality for the three heating conditions (uniform, bottom, and top): (a) $G = 50$ kg m^{-2}s^{-1}, $T_{sat} = 34$ °C, $q'' = 3.4$ kW m^{-2}; (b) $G = 150$ kg m^{-2}s^{-1}, $T_{sat} = 39$ °C, $q'' = 10.5$ kW m^{-2}. 105

Figure 38 – Average experimental heat transfer coefficient versus quality for the three heating conditions (uniform, bottom, and top): (a) $G = 50$ kg m^{-2}s^{-1}, $T_{sat} = 34$ °C, $q'' = 3.4$ kW m^{-2}; (b) $G = 150$ kg m^{-2}s^{-1}, $T_{sat} = 39$ °C, $q'' = 10.5$ kW m^{-2}. 106
Figure 39 – Inner heat flux distribution in $\hat{r}$ direction for the three heating conditions (— uniform, — bottom, and — top) for $x \approx 0.55$ and mass velocities of (a) 50 kg m^{-2}s^{-1} and (b) 150 kg m^{-2}s^{-1}. 108
Figure 40 – Experimental heat transfer coefficient versus the value predicted for each correlation with the lines of $\pm 15\%$ and $\pm 30\%$ error for $G = 50$ kg m^{-2}s^{-1}. . 111
Figure 41 – Experimental heat transfer coefficient versus the value predicted for each correlation with the lines of $\pm 15\%$ and $\pm 30\%$ error for $G = 150$ kg m^{-2}s^{-1}. 114
Figure 42 – Wall temperature standard deviation for the cross-section of the tube against quality and two mass velocities. 117
Figure 43 – Top and bottom wall temperature against quality and two mass velocities. . . 118
Figure 44 – Mutual information scores for the forced convection set of dimensionless parameters. 122
Figure 45 – Mutual information scores for the nucleate boiling set of dimensionless parameters. 122
Figure 46 – Mutual information scores for the surface tension effect set of dimensionless parameters. 123
Figure 47 – Mutual information scores for the property ratio and categorical features set. 123
Figure 48 – Omega 30AWG ($\approx \phi 0.26$ mm) thermocouple. 138
Figure 49 – Schematics of the calibration procedure. 139
Figure 50 – Thermocouple signal from channel 109 versus reference temperature from PT100. 140
Figure 51 – Pressure transmitter calibration experimental apparatus. 144
Figure 52 – Reference value and absolute pressure transmitter measurements for calibration. 145

List of Tables

Table 1 – List of works and their equation for calculating the wall superheat temperature. 34
Table 2 – List of the main works, their heating conditions, tested fluids, and diameters. 43
Table 3 – List of best-fitting friction pressure drop models from each work. 44
Table 4 – List of the homogeneous models and the equation for calculating the two-phase flow viscosity. 45
Table 5 – Table for values of C according to the flow conditions. 46
Table 6 – Values of B for smooth tubes recommended by Chisholm (1973). 47
Table 7 – Table for values of A, p, q, r. 51
Table 8 – List of best-fitting heat transfer coefficient models from each work. 54
Table 9 – Klimenko C coefficients for nucleate boiling HTC. 57
Table 10 – Kandlikar C coefficients for convective and nucleate boiling HTC. 58
Table 11 – Fluid-dependent parameter for Kandlikar's model. 58
Table 12 – Jabardo, Bandarra Filho and Lima's model coefficients for two-phase flow HTC calculation. 60
Table 13 – List of the homogeneous models and the equation for calculating the two-phase flow viscosity. 65
Table 14 – List of the homogeneous models and the equation for calculating the two-phase flow viscosity. 66
Table 15 – Equipment and instrumentation for the convective boiling experimental test rig. 70
Table 16 – Measuring devices and their output signal and range. 74
Table 17 – Results from surface characterization. 82
Table 18 – Experiments setup for test rig validation. 87
Table 19 – Relative uncertainties for the inlet temperature, mass flow rate, heat flux, and heat transfer coefficient for the single-phase flow experiments. 90
Table 20 – Two-way ANOVA test table for all single-phase data points. 92
Table 21 – Relative uncertainties for the saturation pressure, mass velocity, and heat flux, and quality uncertainty for the two-phase flow experiments. 94
Table 22 – One-way ANOVA test table for all data points from two-phase flow pressure drop gradient. 102
Table 23 – Summary of statistic metrics for correlations comparison with $G = 150\,\mathrm{kg\,m^{-2}s^{-1}}$ of all data points, with the best values highlighted in bold. 103
Table 24 – Two-way ANOVA test table for all data points from two-phase flow experiments. 107
Table 25 – Two-way ANOVA test tables with and without annular data points from two-phase flow experiments. 107

Table 26 – Summary of statistic metrics for correlations comparison with $G = 50\,\mathrm{kg\,m^{-2}s^{-1}}$ of only the uniform heating condition data points, with the best values highlighted in bold. 112
Table 27 – Summary of statistic metrics for correlations comparison with $G = 50\,\mathrm{kg\,m^{-2}s^{-1}}$ of all data points, with the best values highlighted in bold. 113
Table 28 – Summary of statistic metrics for correlations comparison with $G = 150\,\mathrm{kg\,m^{-2}s^{-1}}$ of only the uniform heating condition data points, with the best values highlighted in bold. 115
Table 29 – Summary of statistic metrics for correlations comparison with $G = 150\,\mathrm{kg\,m^{-2}s^{-1}}$ of all data points, with the best values highlighted in bold. 116
Table 30 – Cubic function coefficients for each thermocouple (type E: from CH102 to CH210, type T: from CH211 to CH213. 141
Table 31 – Calibration standard uncertainties for the thermocouples (type E: from CH102 to CH210, type T: from CH211 to CH213. 142
Table 32 – Type B uncertainty from sensors calibration and errors. 147
Table 33 – Accuracy of readings and range for the 34972A data logger. 147
Table 34 – Maximum, minimum, and 90% percentile of uncertainties for all direct experimental points. 157
Table 35 – Maximum, minimum, and 90% percentile of relative uncertainties for all indirect experimental points. 158

List of abbreviations and acronyms

A	Annular flow
CHF	Critical Heat Flux
CSP	Concentrating Solar Power
D	Dryout
DSG	Direct Steam Generation
FLR	Linear Fresnel Reflector
HTC	Heat Transfer Coefficient
I	Intermittent
MAE	Mean Absolute Error
MAPE	Mean Absolute Percentage Error
MF	Mist Flow
MI	Mutual Information
MPE	Mean Percentage Error
MRE	Mean Relative Error
ONB	Onset of Nucleate Boiling
PD	Pressure Drop
PDG	Pressure Drop Gradient
S	Stratified flow
SW	Stratified-wavy flow

List of symbols

A_1	Constant from Friedel's correlation [-]
A_2	Constant from Friedel's correlation [-]
A_3	Constant from Friedel's correlation [-]
A_{cs}	Cross-section area [m^2]
A_l	Liquid area [m^2]
A_h	Heated area [m^2]
B	Constant from Chisholm's correlation [-]
Bd	Bond Number [-]
Bo	Boiling Number [-]
c_p	Specific heat at constant pressure [J kg^{-1} K^{-1}]
C	Constant from Lockhart and Martinelli's or Müller-Steinhagen and Heck's correlation [-]
Co	Convection Number [-]
d_{in}	Tube inner diameter [m]
e	Entrainement fraction [-]
e_i	Inlet entrainement fraction [-]
e_o	Outlet entrainement fraction [-]
E	Enhancement factor [-]
f_l	Liquid friction factor [-]
f_{lo}	Liquid only friction factor [-]
f_{tp}	Two-phase friction factor [-]
f_v	Vapor friction factor [-]
f_{vo}	Vapor only friction factor [-]
F_{fl}	Fluid-dependent factor from Kandlikar's correlation [-]

Fr	Froude Number [-]
Fr_l	Liquid Froude Number [-]
Fr_{lo}	Liquid only Froude Number [-]
Fr_m	Momentum Froude Number [-]
Fr_{tp}	Two-phase Froude Number [-]
Fr_v	Vapor Froude Number [-]
Fr_{vo}	Vapor only Froude Number [-]
g	Gravitational acceleration [m s^{-2}]
G	Mass velocity [kg $\mathrm{m}^{-2}\mathrm{s}^{-1}$]
G_w	Stratified-wavy threshold mass velocity [kg $\mathrm{m}^{-2}\mathrm{s}^{-1}$]
G_s	Stratified threshold mass velocity [kg $\mathrm{m}^{-2}\mathrm{s}^{-1}$]
Gz	Graetz Number [-]
h_b	bottom wall heat transfer coefficient [W m^{-2} K^{-1}]
h_{dryout}	Dryout heat transfer coefficient [W m^{-2} K^{-1}]
h_{cb}	Convective boiling heat transfer coefficient [W m^{-2} K^{-1}]
h_{in}	Inlet enthalpy [J kg^{-1}]
h_l	Single-phase liquid heat transfer coefficient [W m^{-2} K^{-1}]
h_l	Liquid enthalpy [J kg^{-1}]
h_{lv}	Vaporization enthalpy [J kg^{-1}]
h_{mist}	Mist flow heat transfer coefficient [W m^{-2} K^{-1}]
h_{nb}	Nucleate boiling heat transfer coefficient [W m^{-2} K^{-1}]
h_{ph}	Pre-heater inlet enthalpy [J kg^{-1}]
h_s	Side wall heat transfer coefficient [W m^{-2} K^{-1}]
h_{sp}	Single-phase heat transfer coefficient [W m^{-2} K^{-1}]
h_t	Top wall heat transfer coefficient [W m^{-2} K^{-1}]
h_{tp}	Two-phase heat transfer coefficient [W m^{-2} K^{-1}]

h_v	Single-phase vapor heat transfer coefficient [W m^{-2} K^{-1}]
h_v	Vapor enthalpy [J kg^{-1}]
h_{wet}	Wet surface heat transfer coefficient [W m^{-2} K^{-1}]
J_v	Dimensionless vapor velocity [-]
K_p	Pressure dimensionless parameter from Klimenko's correlation [-]
K_λ	Thermal conductivity ratio from Klimenko's correlation [-]
La	Laplace constant from Klimenko's correlation [-]
L_{ts}	Test section length [m]
$\dot{m}$	Mass flow rate [kg s^{-1}]
M	Molecular weight [kg kmol^{-1}]
Nu	Nusselt number [-]
Nu_{cb}	Convective boiling Nusselt number [-]
Nu_{nb}	Nucleate boiling Nusselt number [-]
Nu_{tp}	Two-phase Nusselt number [-]
p	Pressure [Pa]
p_{ph}	Pre-heater inlet pressure [Pa]
p_r	Reduced pressure [-]
p_{sat}	Saturation pressure [Pa]
p_{ts}	Test section inlet pressure [Pa]
Pe_*	Modified Peclet number [-]
Pr	Prandtl Number [-]
Pr_l	Liquid Prandtl Number [-]
Pr_v	Vapor Prandtl Number [-]
Pr_{tp}	Two-phase Prandtl Number [-]
q''	Heat flux [W m^{-2}]
$\dot{q}$	Heat rate [W]

$\dot{q}_{loss}$	Pre-heater heat rate [W]
$\dot{q}_{ph}$	Pre-heater heat rate [W]
$\dot{q}_{ts}$	Test section heat rate [W]
R^{+}	Dimensionless tube radius [-]
R_s	Shunt resistance [Ω]
Re	Reynolds Number [-]
Re_H	Homogeneous Reynolds Number [-]
Re_l	Liquid Reynolds Number [-]
Re_{lo}	Liquid only Reynolds Number [-]
Re_m	Mixture Reynolds Number [-]
Re_v	Vapor Reynolds Number [-]
Re_{vo}	Vapor only Reynolds Number [-]
$\mathrm{Re}_{2\phi}$	Two-phase Reynolds Number [-]
$\mathrm{Re}_{2\phi;1}$	Two-phase Reynolds Number only liquid momentum diffusion [-]
$\mathrm{Re}_{2\phi;2}$	Two-phase Reynolds Number liquid and vapor momentum diffusion[-]
Re_{δ}	Liquid film Reynolds Number [-]
S	Suppression factor [-]
t	Liquid film thickness [m]
t^{+}	Dimensionless liquid film thickness or film thickness Reynolds number from Cioncolini and Thome's correlation [-]
T_B	Bulk temperature [K or °C]
T_{in}	Inlet temperature [K or °C]
T_{sat}	Saturation temperature [K or °C]
T_w	Wall temperature [K or °C]
V_r	Resistance voltage drop [V]
V_s	Shunt voltage drop [V]

w	Heat flux weight [-]
w_m	mixture velocity [m s^{-1}]
We	Weber Number [-]
We$_c$	Core flow Weber Number [-]
We$_l$	Liquid Weber Number [-]
We$_{lo}$	Liquid only Weber Number [-]
We$_m$	Momentum Weber Number [-]
We$_v$	Vapor Weber Number [-]
We$_{vo}$	Vapor only Weber Number [-]
x	Vapor quality [-]
x_{di}	Dryout inception vapor quality [-]
x_{de}	Dryout completion vapor quality [-]
x_i	Inlet vapor quality [-]
x_{ia}	Intermittent to annular vapor quality [-]
x_o	Outlet vapor quality [-]
x_{ph}	Pre-heater inlet vapor quality [-]
X	Lockhart-Martinelli parameter [-]
Y	Groenenveld parameter [-]
z	Axial direction [m]
Zu	Zuber Number [-]

Greek letters

α	Void fraction [-]
α_i	Inlet void fraction [-]
α_o	Outlet void fraction [-]
Γ	Property parameter from Baroczy's work [-]

Γ	Tube perimeter [m]
Γ_{lf}^{+}	Dimensionless lquid film mass flow rate [-]
δ	Liquid film thickness [m]
ΔP_{int}	Pressure drop [Pa]
ΔP_{ext}	Pump differential pressure [Pa]
ΔT_{sup}	Wall superheat [K or °C]
ΔT_{sub}	Subcooled level [K or °C]
θ	Inclination angle [degree]
θ_{dry}	Dry angle [rad]
θ_{strat}	Stratification angle [rad]
κ_l	Liquid thermal conductivity [W m^{-1} K^{-1}]
κ_v	Vapor thermal conductivity [W m^{-1} K^{-1}]
μ	Viscosity [Pa s]
μ_l	Liquid viscosity [Pa s]
μ_{lw}	Liquid viscosity at wall temperature [Pa s]
μ_{tp}	Two-phase viscosity [Pa s]
μ_v	Vapor viscosity [Pa s]
ν_l	Liquid dynamic viscosity [m^{2}s^{-1}]
ρ	Density [kg m^{-3}]
ρ_c	Core flow density [kg m^{-3}]
ρ_H	Homogeneous model density [kg m^{-3}]
ρ_l	Liquid density [kg m^{-3}]
ρ_m	Momentum density [kg m^{-3}]
ρ_v	Vapor density [kg m^{-3}]
σ	Surface tension [N m^{-1}]
ϕ_l^2	Liquid two-phase multiplier [-]

ϕ^2_{lo}	Liquid-only two-phase multiplier [-]
ψ	Enhancement factor from Shah's correlation [-]

Subscripts

$mist$	Relative to mist flow
$strat$	Relative to stratified flow
$wavy$	Relative to stratified-wavy flow

Contents

1 INTRODUCTION . . . 27
1.1 Objective . . . 28
1.2 Thesis structure . . . 29

2 LITERATURE REVIEW . . . 30
2.1 Circumferential non-uniform heating on horizontal flow boiling . . . 30
2.2 Onset of nucleate boiling on flow boiling . . . 32
2.3 Horizontal flow pattern maps and transition lines . . . 37
2.4 Horizontal flow boiling pressure drop . . . 42
2.4.1 Friction pressure drop gradient . . . 43
2.4.2 Acceleration pressure drop gradient . . . 50
2.5 Horizontal flow boiling heat transfer . . . 52
2.5.1 Dimensionless groups for two-phase HTC analysis . . . 63
2.6 Summary . . . 67

3 MATERIALS AND METHODS . . . 68
3.1 Experimental apparatus . . . 68
3.1.1 Working fluid . . . 69
3.1.2 Equipment . . . 69
3.1.3 Measuring techniques . . . 74
3.1.4 Experimental features . . . 75
3.2 Tube surface characterization . . . 81
3.3 Experimental procedure . . . 82
3.4 Heat loss test . . . 83
3.5 Single-phase validation . . . 85
3.6 Summary . . . 88

4 RESULTS AND DISCUSSION . . . 89
4.1 Single-phase flow . . . 89
4.2 Two-phase flow . . . 92
4.2.1 Onset of nucleate boiling under non-uniform heat flux . . . 93
4.2.2 Flow pattern identification . . . 98
4.2.3 Pressure drop gradient . . . 101
4.2.4 Heat transfer coefficient . . . 104
4.2.5 Temperature distribution on tube wall . . . 116
4.2.6 Dimensionless group analysis . . . 119

5 CONCLUSIONS 125
5.1 Recomendations for future works 127

BIBLIOGRAPHY 128

APPENDIX A – THERMOCOUPLE CALIBRATION 138

APPENDIX B – PRESSURE TRANSMITTER CALIBRATION . . . 143

APPENDIX C – STATISTICAL ANALYSIS 146
C.1 Sensors calibration and type B uncertainties 146
C.2 Type A uncertainties 148
C.3 Combined standard uncertainties 148
C.4 Expanded uncertainties 148
C.5 Statistic metrics for evaluating models 149
C.6 ANOVA test 149
C.7 Mutual information 150

APPENDIX D – UNCERTAINTIES 151
D.1 Direct measurement sparameters 151
D.1.1 Temperatures 151
D.1.2 Pressure 151
D.1.3 Mass flow rate 151
D.1.4 Voltage and current 152
D.2 Experimental features uncertainty 152
D.2.1 Heat rates 152
D.2.2 Heat fluxes 153
D.2.3 Single phase bulk temperature 153
D.2.4 Two phase bulk temperature 153
D.2.5 Mass velocity 154
D.2.6 Test section inlet quality 154
D.2.7 Test section outlet quality 155
D.2.8 Local heat transfer coefficient 155
D.2.9 Test section mean heat transfer coefficient 156
D.2.10 Pressure drop gradient 156
D.3 Uncertainty values table for all data 156

1 Introduction

Concentrated Solar Power (CSP) is an alternative and renewable energy source with great potential for electric and thermal energy generation. Besides that, its application in remote locations, far from power grids and challenging access to highways and fuel distribution centers, has motivated the R&D industry's investment towards this. Linear Fresnel Reflectors (FLR) for CSP have the potential to reduce energy production costs compared to parabolic troughs technology. This possibility is even better by combining Direct Steam Generation (DSG). This technology (CSP + DSG) evolved in recent years, with much research being done and some power plants already operating commercially, either for electricity generation, such as TSE-1 in Thailand, or heat generation for industrial processes, such as Jordan Pharmaceutical Company's solar power plant (RAM Pharma) (ZARZA *et al.*, 2002; ZARZA *et al.*, 2004; KRÜGER *et al.*, 2012; ALGUACIL *et al.*, 2014; MUÑOZ-ANTÓN *et al.*, 2014; ABBAS *et al.*, 2016; BERGER *et al.*, 2016; SÁ *et al.*, 2018).

DSG's main characteristic is the two-phase flow with phase change. In this context, the liquid turns into vapor as heat is applied, which can be utilized for electric power generation or industrial processes. The thermo-hydraulic behavior of two-phase flow has three main points: the flow pattern, the pressure drop, and the heat transfer. They are interconnected and have a direct influence on energy conversion efficiency. These inherent complexities of DSG technology should be rigorously evaluated.

As Serrano-Aguilera, Valenzuela and Parras (2014) stated, CSP with DSG works on higher pressure than usual, which requires thicker tube walls. That also induces higher thermal gradients and, consequently, higher thermal stresses. Sá *et al.* (2018), in their extensive review of the combination of CSP and DSG, highlighted the advantages and drawbacks of it. Those solar power plants allow working with higher temperatures than the ones with thermal oil as heat transfer fluid. In addition, the two-phase flow instabilities increase the thermal stresses on the absorber tubes, not to mention the changes in heat transfer along the circuit due to the flow pattern changes. All of this can cause tube bending and eventually may lead to failure.

Sá *et al.* (2018) also pointed out that the combination of these technologies brings complexity to generation systems. Some FLR absorbers, such as trapezoidal (Figure 1), feature the circumferential distribution of non-uniform solar radiation. This particularity, combined with two-phase flow, changes the thermohydraulic behavior of solar power plants. The circumferential non-uniformity in heat flux distribution on the absorber tubes is a challenge to the physical analysis and induces changes to the two-phase flow behavior, either in flow patterns or the thermal hydraulics (ZHU *et al.*, 2014; OKAFOR; DIRKER; MEYER, 2017; KHARANGATE *et al.*, 2015; KHARANGATE; O'NEILL; MUDAWAR, 2016a; KHARANGATE; O'NEILL;

MUDAWAR, 2016b; WANG *et al.*, 2019; DIRKER; SCHEEPERS; MEYER, 2022).

Figure 1 – Schematic drawing of a FLR trapezoidal cavity absorber.

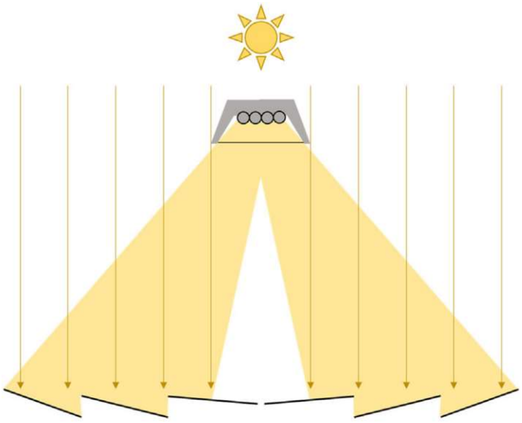

Source: Sá *et al.* (2018).

New applications bring new boundary conditions to the problem. Evaluating how circumferential non-uniform heating influences flow boiling is a hypothesis still under development. This feature is relevant for LFR absorbers and the context of technology development, either in cost reduction or efficiency increase. Then, investigating these flow condition peculiarities and developing tools and techniques which help understand the phenomena are fundamental for academic research and engineering advancement.

1.1 Objective

This study is motivated by DSG application on CSP technology, regarding the aspects and boundary conditions of LFR. The research is inserted in the same conditions found in solar power plants with LFR, i.e., macroscale context, a vastly explored area with solid knowledge. Flow boiling is an extensive topic with many particularities, and addressing everything about it is unlikely. With this in mind, the work limits itself to the analysis of flow patterns, heat transfer coefficient, and pressure drop. In this sense, the research's general objective is to evaluate the non-uniform heating effects on horizontal flow boiling. This requires the following specific objectives.

- Analyse the effect of the circumferential non-uniform heat flux on the flow patterns development;
- Evaluate how the heat flux distribution influences the Onset of Nucleate Boiling;
- Investigate how the flow boiling heat transfer shapes the non-uniform heat flux distribution;
- Assess the Heat Transfer Coefficient (HTC) and Pressure Drop (PD) on the test section;
- Evaluate the influence of the heating conditions on the HTC and PD;

- Compare the HTC and PD with correlations from the literature;
- Analyze the dimensionless groups for better fitting future models.

1.2 Thesis structure

This work is divided into five chapters, introduction, literature review, materials and methods, results and discussion, and conclusions. The chapter 1 presents a brief contextualization showing the motivation and the aspects of CSP with DSG solar power plants, in addition to the scope of the research and its objectives. The chapter 2 presents the literature review regarding the circumferential non-uniform heating, pressure drop, heat transfer coefficient, and two-phase flow instabilities. There, the features, which allowed this thesis to be done, are highlighted. The chapter 3 presents the experimental apparatus and its equipment, not to mention the methods used to evaluate the data to accomplish the objectives of this work. The chapter 4 presents the results from the experimental work for both single-phase and two-phase flow, as well as the comparison with the prediction methods. The results are also discussed, and the main achievements are stressed. The chapter 5 wraps up every specific objective and presents the main findings, along with suggestions for future works.

2 Literature review

This chapter covers the main published works regarding horizontal flow boiling, the Onset of Nucleate Boiling (ONB), non-uniform heating, horizontal flow pattern maps, pressure drop, heat transfer, and two-phase flow instabilities. First, it presents the main works on circumferential non-uniform heating, with focused attention to how the researchers assessed the HTC and the internal heat flux, highlighting their main findings. Then, it presents the criteria and features of ONB, focusing on its identification and impacts on flow boiling. The development of flow pattern maps and the contribution of each work to flow pattern prediction is added to the discussion. The techniques for assessing the friction and acceleration pressure drop are also described. After, an extensive analysis of the pressure drop and HTC models is shown, highlighting the best-fitting ones from the literature and their characteristics. Last, the instabilities inherent in two-phase flow are discussed, as well as their impact on the design and operation of these systems. Finally, a chapter summary resumes the main points.

2.1 Circumferential non-uniform heating on horizontal flow boiling

Non-uniform heating conditions have been poorly studied in the development of flow boiling research. Few studies relate this feature and its effects on the two-phase flow. Yet, some researchers show relevant results by assessing the influence of the heating condition on it, most of them with the motivation of combining DSG with CSP.

Wang *et al.* (2019), motivated by the DSG with PT solar collectors, conducted experiments of horizontal flow boiling of R-245fa under non-uniform heating (bottom half heating) in a tube of 10.00 mm of diameter for mass velocities from 192.9 to 385.8 kg $m^{-2}s^{-1}$, heat fluxes from 9.95 to 35.9 kW m^{-2} and saturation temperatures from 40 to 60 °C. The authors used a high-speed camera for flow pattern identification. They concluded that the transition between intermittent and annular flow was anticipated when heating the bottom half of the tube. The researchers also stated that the bottom heating favors the activation of nucleation sites, enhancing the nucleate boiling heat transfer and, consequently, the HTC overall. However, they did not provide a comparison of the HTC with the uniform heating. Their experimental data was underestimated by four classic correlations, which they attributed to the enhancement of activated nucleation sites due to the higher deposition of liquid on the lower part of the tube. The correlation of Gungor and Winterton (1986) presented the lowest MAE and MRE. Since the classic correlations failed to predict their experimental data, they proposed a new one based on the work of Gungor and Winterton (1986). Their new correlation predicted 94% of the data within 20% of error.

Dirker, Scheepers and Meyer (2022), on the same motivation, performed experiments of horizontal flow boiling of R-245fa under eight non-uniform conditions of heat flux in a tube of 8.5 mm diameter. They run experiments with mass velocities of 200 and 300 kg $m^{-2}s^{-1}$, saturation temperatures of 35 and 40 °C, qualities ranging from 0.2 to 0.7, and 6.8 kW m^{-2} of heat flux. The tube perimeter was divided into six heating sections which covered the entire tube length. To keep the heat transfer rate the same for every heating condition, the researchers calculated the outer heat flux so the inner heat flux was approximately equivalent for all circumferential distributions. The authors concluded that the heating condition affected the heat transfer coefficient significantly. The HTC for the side heating conditions were 40% lower than the uniformly heated, while for the top and bottom heating, they were 25% lower. They also stated the reduction of HTC was accentuated by the increase in vapor quality and that the heating condition did not affect the pressure drop.

One of the main concerns about circumferential non-uniform heating is the wall temperature measurement and the HTC calculations. Wang *et al.* (2019) and Dirker, Scheepers and Meyer (2022) took different approaches on measuring the inner wall temperature. Figure 2 illustrates the thermocouple placement for Wang *et al.* (2019) and Dirker, Scheepers and Meyer (2022). Wang *et al.* (2019) assumed that the semi-circumferential or parabolic heat distribution outside the tube does not significantly influence the temperature distribution, simplifying the boundary condition. Therefore, they calculate the inner wall temperature with an analytical solution with the outer wall temperature measurement and heat flux as boundary conditions. Their test section had seven measurement sections on the tube length, each with four thermocouples attached to the outer wall, one on each side, one on top, and one on the bottom. Dirker, Scheepers and Meyer (2022) embedded the thermocouple tips into the tube wall. Nine temperature measurement sections were used to assess the HTC along the tube. Each section had six thermocouples placed in the middle of each heating section. The HTC was calculated through an inverse heat transfer model given the temperature measurements, thermocouple position, and heat flux. These approaches gave insights and will be discussed further on the chapter 3.

These studies evaluated the thermal-hydraulics of horizontal flow boiling in a circular smooth tube under circumferential non-uniform heating. Although they added valuable information on how the heating condition affects the HTC, flow patterns, and pressure drop, a phenomenological understanding is missing. An evaluation of recent correlations for HTC prediction and dimensionless groups could be done to understand these effects. None of the works evaluated the influence of the heating condition on the partial dryout. However, some researchers have studied the Critical Heat Flux (CHF) on a rectangular channel with bottom and top heating conditions, which goes beyond the scope of this work (KHARANGATE *et al.*, 2015; KHARANGATE; O'NEILL; MUDAWAR, 2016a; KHARANGATE; O'NEILL; MUDAWAR, 2016b).

Figure 2 – Wang *et al.* (2019) and Dirker, Scheepers and Meyer (2022) temperature measurement cross-section and heating schematics.

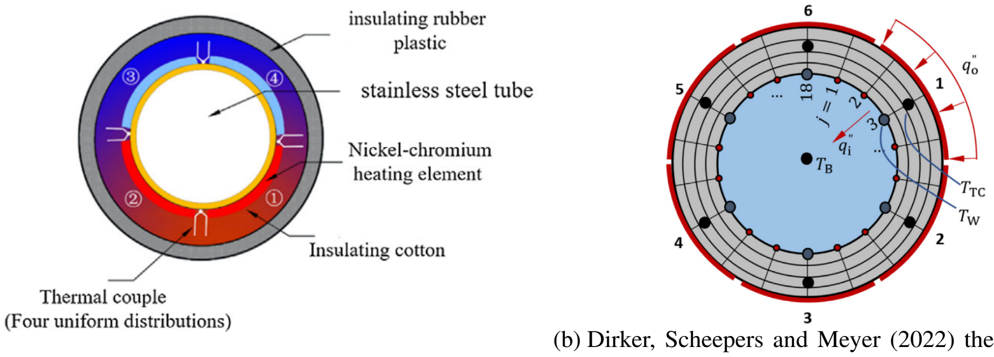

(a) Wang *et al.* (2019) thermocouple distribution

(b) Dirker, Scheepers and Meyer (2022) thermocouple distribution

Source: Adapted from Wang *et al.* (2019) and Dirker, Scheepers and Meyer (2022).

2.2 Onset of nucleate boiling on flow boiling

The Onset of Nucleate Boiling (ONB) marks the transition between single-phase flow heat transfer and forced convective heat transfer with nucleate boiling. The heat transfer coefficient is constant for a steady-state single-phase flow with constant heat flux applied to the tube surface, therefore, the wall temperature increases linearly along the tube. The energy balance for the fluid under these conditions is given by:

$$q'' = \frac{Gd_{in}}{4z} c_p \left[T_b\left(z\right) - T_{in}\right], \tag{1}$$

where q'' is the heat flux applied to the tube wall, G is the mass velocity, c_p is the specific heat at constant pressure, $T_b\left(z\right)$ is the bulk temperature at the position z, and T_{in} is the inlet temperature. The convective heat transfer boundary condition is given by:

$$q'' = h_{sp}\left[T_w\left(z\right) - T_b\left(z\right)\right], \tag{2}$$

where h_{sp} is the single-phase heat transfer coefficient, and $T_w\left(z\right)$ is the wall temperature at the position z. Combining $T_b\left(z\right)$ from Equation 1 and Equation 2, then:

$$T_w\left(z\right) = \frac{q''}{h_{sp}}\left[1 + 4\left(\frac{h_{sp}}{Gc_p}\right)\left(\frac{z}{d_{in}}\right)\right] + T_{in}. \tag{3}$$

The wall superheat is given by the difference between the wall and the saturation temperature. Subtracting the saturation temperature at both sides of Equation 3 gives:

$$T_w\left(z\right) - T_{sat} = \frac{q''}{h_{sp}}\left[1 + 4\left(\frac{h_{sp}}{Gc_p}\right)\left(\frac{z}{d_{in}}\right)\right] - \left(T_{sat} - T_{in}\right), \tag{4}$$

where $T_w\left(z\right) - T_{sat}$ is the wall superheat $\Delta T_{sup}\left(z\right)$ and $T_{sat} - T_{in}$ is the subcooled level ΔT_{sub}, then:

$$\Delta T_{sup}\left(z\right) = \frac{q''}{h_{sp}}\left[1 + 4\left(\frac{h_{sp}}{Gc_p}\right)\left(\frac{z}{d_{in}}\right)\right] - \Delta T_{sub}. \tag{5}$$

As the wall temperature, the wall superheat increases linearly along the tube surface. Equation 5 gives some insights for ONB identification for experimental work. As soon as the nucleate boiling flow starts, the heat transfer coefficient increases, changing the linear growth behavior of the wall superheat. This intersection is usually used for identifying the ONB inception (BERGLES; ROHSENOW, 1964; SONG *et al.*, 2017).

Finding the minimum wall superheat, given the heat flux, which triggers nucleate boiling, has been a topic of study for a long time. As stated by several authors, the ONB indicates the start of the nucleate boiling regime. Many parameters influence it, such as the wall roughness or cavity radii that can have more probability of nucleating, wall temperature, heat flux, and system pressure, to name a few. It is well known that the minimum wall superheat must be attended, and a range of cavity sizes must be available at the surface to be active. Most models follow the principles of the bubble dynamics theory, liquid-vapor equilibrium, and Clausius-Clapeyron equation from the pool boiling modeling. Next, these models are discussed and followed by the presentation of the associated equations.

Hsu (1962), Bergles and Rohsenow (1964), Sato and Matsumura (1964), each conducting independent works, performed analytical solutions for the ONB inception based on those premises. Hsu (1962), Bergles and Rohsenow (1964) considered that the bubbles would grow as long as the temperature at the bubble height is higher than the temperature of the vapor, which breaks the liquid-vapor equilibrium, and the bubble would grow. Both considered a hemispherical bubble in their analysis. Despite providing a mathematical solution, the procedure does not show an explicit dependence on the incipient heat flux; therefore, Bergles and Rohsenow (1964) found it more convenient to propose an empirical model for predicting the heat flux for ONB incipience. Sato and Matsumura (1964) considered that the bubble would grow if the temperature of the superheated liquid layer around it is higher than the temperature inside the bubble. They assumed a spherical bubble to build their model. Davis and Anderson (1966) solved the analytical model of Hsu (1962) considering the contact angle of fluid with the solid surface and incorporated it into their model.

Hino and Ueda (1985) identified the boiling incipience by looking at the wall temperature distribution along the tube. The authors stated that the first bubbles were seen when there was a sharp drop in wall temperature for heating with imposed heat flux. By increasing the heat flux, they also noted that the ONB location shifted upstream. When comparing their data with the correlations from Sato and Matsumura (1964) and Bergles and Rohsenow (1964), they found that the wall superheat was underpredicted for both. Those correlations consider that there is a wide range of cavity sizes on the surface that can be activated. Though, for their experiment, they found a maximum cavity size (r^*_{max}) ranging from 0.22 to 0.34 µm, in which cavities larger than that r^*_{max} would not be activated.

Marsh and Mudawar (1989) showed that well-wetting fluids tend to flood larger wall cavities, and the boiling incipience depends more on the size of the vapor embryos than the cavities sizes themselves. Celata, Cumo and Setaro (1992) on their studies over the hysteresis of well-wetting fluids, observed the same behavior as Marsh and Mudawar (1989). Since the embryo is inside the cavity, the temperature of the bubble is similar to the surface temperature. The previous models account for the heat transfer between the superheated liquid layer around the bubble, though, for well-wetting fluid, the contact of the embryo with the liquid is lower. Thus, the wall superheat required to initiate nucleate boiling would be higher than the values predicted by the incipient theories. Basu, Warrier and Dhir (2002) revisiting the classical models on the superheat equation incorporated the number of active nucleation sites and contact angle to the incipient boiling prediction methods. Their model's application range is wide, and accounts for various liquid-surface pairs, even refrigerants.

The classical theories of ONB rely on the heat diffusion through the liquid layer to the bubbles, though for flow boiling, Steiner and Taborek (1992) considered the thermal resistance of the superheated liquid film as the liquid convective heat transfer coefficient. Zürcher, Thome and Favrat (2000) on the same idea proposed a critical heat transfer coefficient that would trigger the ONB. Their model considered the influence of the heat flux and even the flow pattern into the HTC for the ONB calculation.

Table 1 lists the work and their equations for predicting the wall superheat temperature.

Table 1 – List of works and their equation for calculating the wall superheat temperature.

Authors	Equation	
Hsu (1962)	$\Delta T_{sup} = \sqrt{\dfrac{12.8\ \sigma T_{sat} q''_{onb}}{\kappa_l h_{lv} \rho_v}}$	(6)
Sato and Matsumura (1964)	$\Delta T_{sup} = \sqrt{\dfrac{8\ \sigma T_{sat} q''_{onb}}{\kappa_l h_{lv} \rho_v}}$	(7)
Bergles and Rohsenow (1964)	$q''_{onb} = 5.30\ p^{1.156} \left(1.80\ \Delta T_{sup}\right)^{2.41/p^{0.0234}}$	(8)
Davis and Anderson (1966)	$\Delta T_{sup} = \sqrt{\dfrac{8\left(1+\cos\theta\right) \sigma T_{sat} q''_{onb}}{\kappa_l h_{lv} \rho_v}}$	(9)
Frost and Dzakowic (1967 apud CELATA; CUMO; SETARO, 1992)	$\Delta T_{sup} = \mathrm{Pr}_l \sqrt{\dfrac{8 \sigma T_{sat} q''_{onb}}{\kappa_l h_{lv} \rho_v}}$	(10)
Hino and Ueda (1985)	$q''_{onb} = \dfrac{\kappa_l}{r^*_{max}} \left(T_w - T_{sat}\right)_{onb} - \dfrac{2\ \sigma \kappa_l T_{sat}}{h_{lv} \rho_v \left(r^*_{max}\right)^2}$	(11)
Marsh and Mudawar (1989)	$\sqrt{\dfrac{28\ \sigma T_{sat} \upsilon_{lv} q''_{onb}}{\kappa_l h_{lv}}}$	(12)
Celata, Cumo and Setaro (1992)	$\Delta T_{sup} = \dfrac{p_l T_{sat} \left(\upsilon_v - \upsilon_l\right)}{h_{lv} \mathrm{Re}_{sat}{}^{0.2} \mathrm{Pr}_{sat}{}^{0.5} \pi}$	(13)

Source: Author.

Qi *et al.* (2007) on their studies of liquid nitrogen in micro-channels published the time series of their data. They showed the transient behavior of the pressure drop, mass velocity, and wall temperature when the ONB is achieved. Figure 3 depicts the transient behavior of heat flux, pressure drop, mass velocity, and wall temperature from their work. They state that when ONB starts, the pressure drop increases and the mass velocity decreases drastically. The wall temperatures also decreased when flow boiling started. Through their seven wall temperature measurements, they could identify where ONB happened by the temperature drop. The temperature drop ranged from 1 to 5 °C.

Figure 3 – Transient behavior of heat flux, pressure drop, mass velocity, and wall temperature from Qi *et al.*'s work.

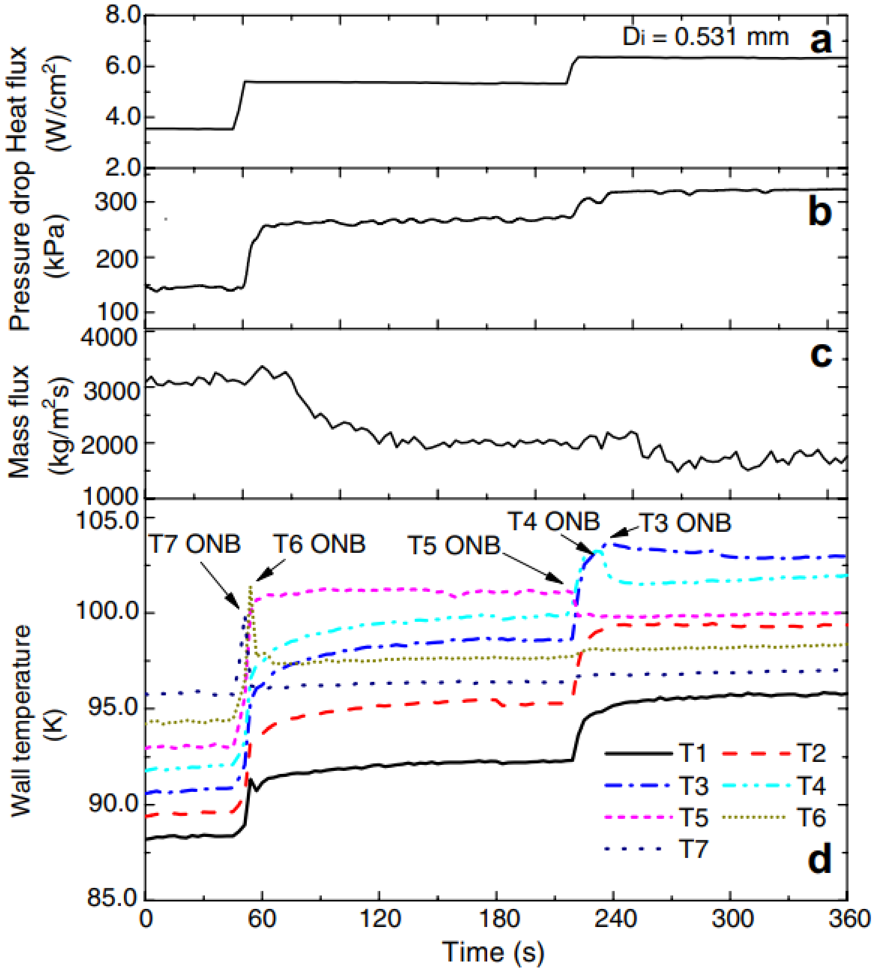

Source: Qi *et al.* (2007).

Dário (2013), in his doctoral thesis, also published the transient behavior of heat flux, saturation pressure, mass velocity, pressure drop, and wall temperature. Figure 4 shows the transient behavior of Dário's work. The author observed the same behavior as Qi *et al.* (2007), while reaching ONB, the pressure drop increased, and the wall temperature dropped substantially. The inlet pressure also increased when flow boiling started and stabilized at a new steady position. In contrast, the mass velocity decreased when ONB started and reached another steady point as the pressure stabilized.

Song *et al.* (2017) identified ONB by the change in the wall temperature gradient, i.e.,

Figure 4 – Transient behavior of heat flux, inlet pressure, mass velocity, pressure drop, and wall temperature from Dário's work.

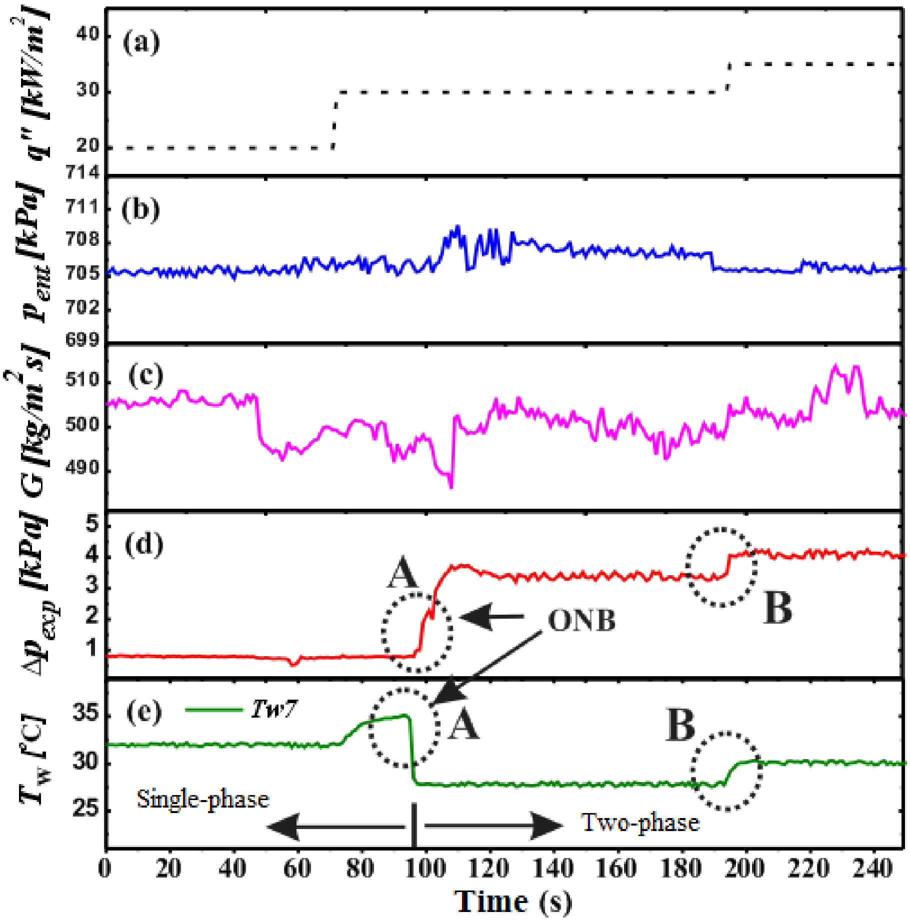

Source: Dário (2013).

the transition of heat transfer mechanism (from single-phase to forced convection with nucleate boiling). Due to the higher heat transfer coefficients, the wall superheat needed for ONB is higher for higher mass velocities. Yuan *et al.* (2018) revisited the classical models for predicting the ONB. They formulated a neat correlation based on a Gibbs free energy analysis. As was observed by Song *et al.* (2017), they stated that the wall superheat increases with the heat transfer coefficient, though this happens because of the change in the bubble nucleation mechanism. As the heat transfer coefficient increases, the bubble nucleation type I (with preference of nucleation sites) transitions to type II (without preference of nucleation sites). Their model also captured the effect of contact angle. For well-wetting fluids, the wall superheat for ONB is higher for the same heat flux, which corroborates with the observations of Marsh and Mudawar (1989) and Celata, Cumo and Setaro (1992).

Overall, the criteria for ONB have been discussed for a long time. The transition of heat transfer mechanisms, i.e., from single-phase to forced convection with nucleate boiling, is a criterion well used to identify the ONB position. The mechanisms for bubble growth and boiling incipience are well understood and give the reason for it to happen. The fluid characteristics, such as contact angle, can influence the ONB inception and differs from the classical predicting methods. The transient behavior of system parameters also reveals insightful patterns for ONB and must be accounted for its identification. Regarding the circumferential non-uniform heating condition, the ONB can be misleading for the indirectly heated part of the tube wall. Checking for the wall superheat and the transient behavior of the data is pivotal for boiling inception.

2.3 Horizontal flow pattern maps and transition lines

Flow patterns or flow regimes are features of the two-phase flow and can be influenced by several parameters such as fluid property, channel geometry, heat flux, pressure, temperature, etc. Several researchers state that flow patterns influence heat transfer and pressure drop directly. Therefore, understanding how they develop along the channel is critical to a reliable thermal hydraulic analysis. Studies related to predicting flow patterns have been relevant over time. The main flow pattern maps used are Hewitt and Roberts (1969) for vertical flow and Baker (1953), Taitel and Dukler (1976), Steiner and Kind (2010) and Kattan, Thome and Favrat (1998a) for horizontal flow.

Using data from several researchers, Baker (1953) published a generalized map for oil and gas adiabatic flow patterns. However, Rouhani and Sohal (1983) found that this map failed to identify some flow patterns in certain situations. Several researchers have published flow pattern maps, such as White and Huntington (1955), Hoogendoorn (1959), Govier and Omer (1962), Eaton *et al.* (1967), and many others. Mandhane, Gregory and Aziz (1974), based on a database with approximately 6,000 points for air/water horizontal flow, proposed a unified flow pattern map and compared it with the Baker (1953), Hoogendoorn (1959) and Govier and Omer (1962) maps. In general, this map obtained better results when compared to the data available for two-phase flow.

Despite attempts, it was Taitel and Dukler (1976) that got the best results. The researchers proposed a theoretical map based on analytical mechanistic models to determine the transition curves between flow regimes. The theoretical model considers the transitions between the five basic patterns for horizontal two-phase flow (stratified, stratified-wavy, intermittent, annular, and bubbly). The map correlates the Lockhart-Martinelli parameter (X) with the dimensionless parameters (K, T, and F) proposed by the authors. This map's reliability is validated by its application to the present day and is the baseline for many other maps. Later, Steiner (1993 apud STEINER; KIND, 2010), based on their experiments with R-12 and R-22, proposed modifications to the Taitel and Dukler (1976) map.

Many studies came up with modifications to these maps to include the diabatic effects in the transition lines. Kattan, Thome and Favrat (1998a) published modifications on Steiner's map, making its implementation easier by changing its coordinates to vapor quality and mass velocity and adding heat flux's influence. This intuitive approach allows pattern development visualization along the flow. The researchers restricted the analysis to transition lines from stratified-wavy to annular and from annular to mist flow. Although they also identified the beginning of partial dryout, they incorporated these effects into the stratified wavy/annular transition line. Visually, it is hard to differentiate between these two regimes. This difference is in the definition of each one, dryout represents the liquid film evaporation at the top of the tube, as for the stratified-wavy flow, the liquid film does not come into contact with the tube top.

Kattan, Thome and Favrat (1998a) have tested five refrigerants (R123, R134a, R402a, R404a, and R502) under evaporation conditions ($0.44 \leq q''$ [kW m^{-2}]≤ 36.54) in a 12 mm diameter pipe and predicted accurately 96% of the 702 points analyzed. In addition, the authors corrected the miscomprehension in Steiner's map, which predicted that mist flow becomes annular with vapor quality increasing. Just as the work of Taitel and Dukler (1976), the map proposed by Kattan, Thome and Favrat (1998a) is the baseline for several other maps. Figure 5 illustrates this map with the transition lines between patterns (x_{IA}, G_{wavy}, G_{strat} and G_{mist}).

Figure 5 – Kattan, Thome and Favrat's flow pattern map for adiabatic flow of R134a at 10.3 °C in a 12 mm diameter tube (S - Stratified; SW - Stratified-wavy; I - Intermittent; A - Annular; MF - Mist flow).

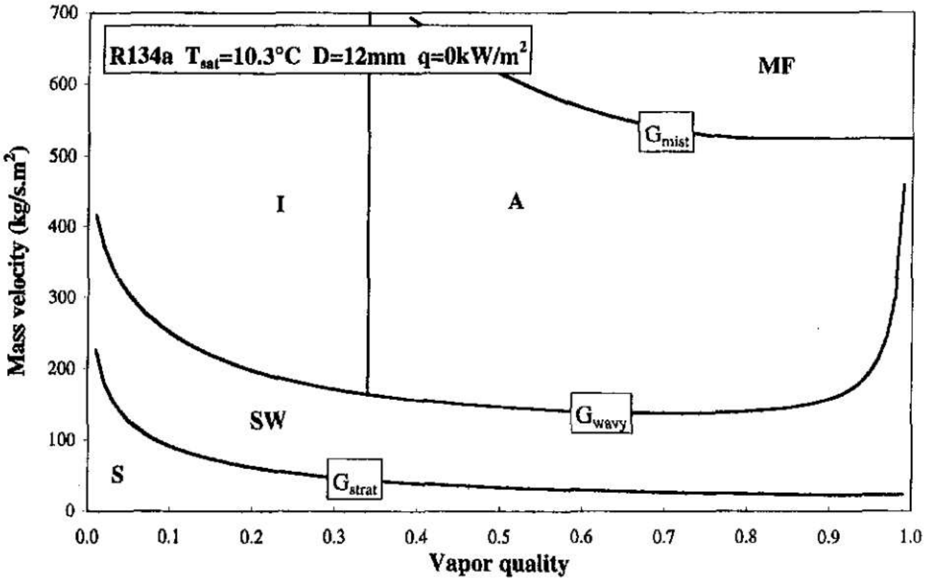

Source: Kattan, Thome and Favrat (1998a).

Thome and his co-workers have dedicated enough to this issue over the following years. Zürcher, Favrat and Thome (2002) proposed changes to the map published by Kattan, Thome and Favrat (1998a) for better prediction of HFC-134a, HFC-407C, and ammonia (R717) flow patterns. They tested HFC refrigerants in a 10.92 mm diameter tube and heat flux ranging from 2 to 5 kW m^{-2}, while for ammonia, they used a 14 mm diameter tube and heat flux varying from 5 to 7 kW m^{-2}. The aim was to evaluate the transition from stratified to stratified-wavy flow since Kattan, Thome and Favrat (1998a) did not reach mass velocities for this transition. They concluded that Kattan, Thome and Favrat (1998a) map predicted well the HFC-134a and HFC-407C flow patterns. Though, for ammonia, they proposed modifications to Steiner and Kind's map and Kattan, Thome and Favrat's assumptions to include fluids with distinct properties. The new map predicted well the flow patterns for HFC-134a, HFC-407C, and ammonia, increasing its range of applications.

Interestingly, the authors did not find heat flux influence in the transition between stratified and stratified-wavy flow, nor between intermittent and annular flow, and therefore did not propose any changes to those lines. However, they found that the equation described by Taitel and Dukler (1976) better predicted the transition between stratified and stratified-wavy flow. They thought that instead of expressing transition lines as a function of the dimensionless cross-sectional area, they could do it as a function of the void fraction. This approach gives a direct physical sense to the problem, evaluating the relation of areas between liquid and vapor in the tube.

Thome and El Hajal (2003), from the work done by Zürcher, Favrat and Thome (2002), published a simplified version of the flow pattern map. In this version, the transition equations are only a function of void fraction and mass velocity, making its implementation easier but keeping its accuracy. This map accurately predicted seven refrigerant flow patterns and is valid for adiabatic and diabatic conditions. Although the Zürcher, Favrat and Thome (2002) experiments have been performed only for 10.96 and 14 mm diameter, the authors state that the map can be extrapolated to diameters from 3 to 22 mm since it is built from the Taitel and Dukler's and Steiner and Kind's maps.

Wojtan, Ursenbacher and Thome (2005b) reevaluated the transition lines using dynamic void fraction measurements and local heat transfer coefficient variations. The researchers tested two refrigerants (R22 and R410A) in a 13.84 mm diameter tube under heat fluxes ranging from 2 to 57.5 kW m^{-2}. They used the same idea from Kattan, Thome and Favrat (1998a) to identify the dryout inception. This technique allowed for identifying and equating the transition lines between annular and dryout and between dryout and mist flow. The authors introduced these transition lines to Thome and El Hajal's map. These modifications allowed for identifying and differentiating stratified wavy from partial dryout. In addition, they also subdivided the stratified-wavy region into three zones: slug, slug/stratified-wavy, and stratified-wavy. The transition lines were also adjusted to vapor quality below the intermittent-annular transition. In general, the map keeps its accuracy and is easily integrated with pattern-based heat transfer and pressure drop models. Figure 6 shows Wojtan, Ursenbacher and Thome's map.

Cheng *et al.* (2006) explored the Wojtan, Ursenbacher and Thome (2005b) map by modifying their transition lines to predict CO_2 flow patterns. The authors investigated the heat transfer mechanisms and proposed a flow pattern-based model from their experimental data. They also evaluated the heat transfer coefficient of nucleate boiling and suppression factor, incorporating these effects into the model. Their model predicted 75.5% of the collected data within ±30% for several conditions of pipe diameters, mass velocities, heat fluxes, and saturation temperatures. Further experiments allowed the researchers to improve this map, Cheng *et al.* (2008) published updates to it, as well as a flow pattern-based pressure drop model.

Figure 6 – Wojtan, Ursenbacher and Thome's flow pattern map for diabatic flow of R22 at 5 °C in a 13.84 mm diameter tube (S - Stratified; Slug; SW - Stratified-wavy; I - Intermittent; A - Annular; D - Dryout; MF - Mist flow).

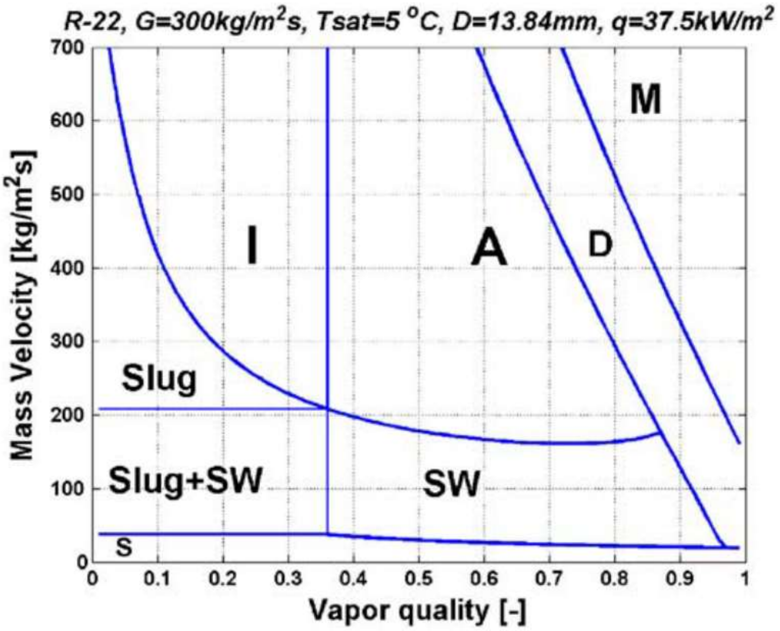

Source: Wojtan, Ursenbacher and Thome (2005b).

Cheng, Ribatski and Thome (2008) did an extensive literature review on flow pattern maps and realized that many papers used visual methods to identify the flow regime. They claim that this approach induces errors, leading to disagreement among researchers about flow pattern maps. Finally, the authors state that flow pattern-based models of pressure drop and heat transfer coefficients should be improved from more collected experimental data. Some authors suggest dynamic void fractions measurements to identify the flow patterns, as done by Wojtan, Ursenbacher and Thome (2005b), to reduce the visual method subjectivity in identifying flow patterns.

Barbieri, Jabardo and Bandarra Filho (2008) performed adiabatic and diabatic convective boiling experiments with R134a and compared their results with various pattern maps. They tested several tube diameters (6.2 to 12.6 mm) with heat flux varying from 5 to 10 kW m^{-2}. Even though Kattan, Thome and Favrat (1998a) had the best prediction results, the authors proposed changes to the transition line criterion between the intermittent and annular regimes. The researchers realized that this transition changes accordingly to tube diameter, mass velocity, and vapor quality. Based on their experimental results, they proposed a new transition line to the Kattan, Thome and Favrat's map using the dimensionless liquid Froude Number (Fr_l) and the Lockhart-Martinelli parameter (X_{tt}). The highlight is that this line was one of the last to be modified remaining from Taitel and Dukler's map until Barbieri, Jabardo and Bandarra Filho (2008) proposed this approach. Before that, the transition line was defined by a Lockhart-Martinelli parameter fixed value. Figure 7 shows the Barbieri, Jabardo and Bandarra Filho's transition line on the Kattan, Thome and Favrat's map

Figure 7 – Barbieri, Jabardo and Bandarra Filho’s inttermitent to annular transition line on the Kattan, Thome and Favrat’s map.

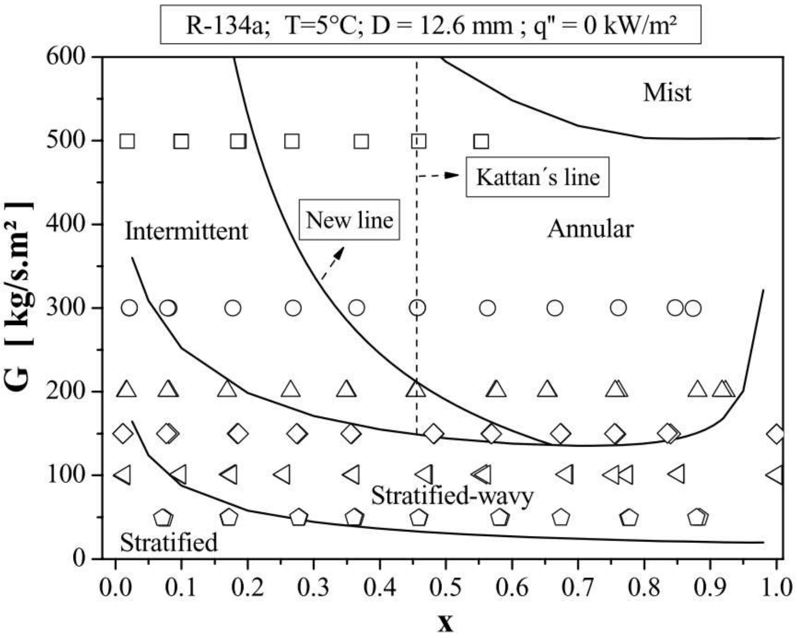

Source: Barbieri, Jabardo and Bandarra Filho (2008).

Canière *et al.* (2010) used a capacitive void fraction measurement technique to improve the objectivity of pattern maps. However, the mass velocities studied allowed only slug, intermittent, and annular pattern observations. The authors compared their measurements with the correlation proposed by Barbieri, Jabardo and Bandarra Filho (2008) and found good agreement between the results. Transition lines would be better defined as a range of values for which the transition occurs. Therefore, they proposed a probabilistic correlation for the transition between the intermittent and annular flow based on the correlation published by Barbieri, Jabardo and Bandarra Filho (2008).

Over the years, the necessity for compact, minimalist heat exchangers has guided studies about flow pattern maps. Consequently, the maps have been modified to predict the flow patterns for those systems. One particular feature of microchannels is that the surface tension effects are dominant over the gravity effects, suppressing the stratified flow. Although this work focuses on macro scale tubes, some researches deserve attention, as the paper published by Ong and Thome (2011). This work differs from others by proposing a pattern map that includes the channel confinement effect, thus identifying a threshold between the micro and macro scales. They inserted some dimensionless numbers into the transition lines, such as Boiling (BO), Bond (Bo), Confinement (Co), Eötvös (Eo), Reynolds (Re), and Weber (We) numbers. This approach allows for verifying the dominant phenomenological effects on the flow.

This premise has continued to influence several other researchers and many papers have reemerged supporting dimensionless numbers to describe transition lines. Zhuang *et al.* (2016) performed experiments with R170 and a high-speed camera to identify the flow patterns. The researchers compared their results with several maps, though none could accurately predict their collected data. Therefore, they proposed new transition lines based on the Lockhart-Martinelli parameter and the modified Weber number.

This same research group developed a diabatic convective boiling study with R1234ze(E). As Zhuang *et al.* (2016), Yang *et al.* (2018) concluded, none of the classical maps accurately predicted their experimental flow patterns. The authors also introduced three dimensionless numbers to build their R1234ze(E) flow pattern map. Lately, they also published a new model for predicting the R600a flow patterns. Yang *et al.* (2019) also argued that none of the proposed models predicted the flow patterns found in their experiments.

Wang *et al.* (2019) on their studies on the circumferential non-uniform heating effects on the horizontal flow boiling recorded the flow patterns and compared them with existing correlations for transition lines. Besides the images, they used the times series of the mean grayscale value to evaluate the flow pattern, avoiding any mistakes from a single-frame analysis. They concluded that for the same heat flux, the transition from intermittent to annular flow happens for lower quality when heating from the bottom than heating uniformly. Ong and Thome's transition line best agreed with their experimental data. They attribute the sooner transition to the flow instabilities caused by the non-uniform heating.

Table 2 lists the main works, their heating conditions, tested fluids, and diameters. The divergence among researchers about two-phase flow pattern predictions is still relevant. The fact is that each researcher proposes a transition line that best describes their experiment, thus generating a considerable amount of transition models. Moreover, the idea that the transition occurs singularly is unlikely proven, and further studies on that subject are needed.

2.4 Horizontal flow boiling pressure drop

Flow boiling pressure drop predictions are based on two main models, the homogeneous and the separated flow. Both come from the conservation of momentum equation. For simplicity, only the liquid-only form will be presented. In general, the momentum equation reduces in terms of pressure drop gradient as follows:

$$-\underbrace{\left(\frac{\mathrm{d}p}{\mathrm{d}z}\right)}_{\substack{\text{Total}\\\text{pressure}\\\text{drop}}} = -\underbrace{\phi_{lo}^2\left(\frac{\mathrm{d}p}{\mathrm{d}z}\right)_{lo}}_{\substack{\text{Friction}\\\text{pressure}\\\text{drop}}} + \underbrace{\frac{\mathrm{d}}{\mathrm{d}z}\left[\frac{G^2x^2}{\rho_v\alpha} + \frac{G^2\left(1-x\right)^2}{\rho_l\left(1-\alpha\right)}\right]}_{\substack{\text{Acceleration}\\\text{pressure}\\\text{drop}}} - \underbrace{\left[\left(1-\alpha\right)\rho_l + \alpha\rho_v\right]g\sin\theta}_{\substack{\text{Gravitational}\\\text{pressure}\\\text{drop}}}, \quad (14)$$

where ${\phi_{lo}}^2$ is the two-phase flow multiplier, $\left(\mathrm{d}P/\mathrm{d}z\right)_{lo}$ is the single-phase liquid only pressure drop gradient, α is the void fraction, and θ is the tube inclination angle. For horizontal flow boiling θ is zero, and the gravitational pressure drop gradient term reduces to zero, then, Equation 14

Table 2 – List of the main works, their heating conditions, tested fluids, and diameters.

Authors	Heating conditions	Fluids	Diameters
Taitel and Dukler (1976)	Adiabatic	—	3 to 22 mm
Steiner and Kind (2010)	Adiabatic	R12 and R22	3 to 22 mm
Kattan, Thome and Favrat (1998a)	Diabatic	R134a, R123, R402A, R404A and R502	12 mm
Zürcher, Favrat and Thome (2002)	Diabatic	HFC-134a, HFC-407C and Ammonia	10.92 and 14 mm
Thome and El Hajal (2003)	Diabatic	—	10.92 and 14 mm
Wojtan, Ursenbacher and Thome (2005b)	Diabatic	R222 and R410A	13.84 mm
Cheng *et al.* (2008)	Diabatic	CO_2	0.6 to 10 mm
Barbieri, Jabardo and Bandarra Filho (2008)	Diabatic	R134a	6.2 to 12.6 mm
Zhuang *et al.* (2016)	Diabatic	R170	4 mm
Yang *et al.* (2019)	Diabatic	R600a	6 mm

Source: Author.

becomes:

$$\underbrace{-\left(\frac{\mathrm{d}p}{\mathrm{d}z}\right)}_{\substack{\text{Total}\\\text{pressure}\\\text{drop}}} = \underbrace{-\,\phi_{lo}^{2}\left(\frac{\mathrm{d}p}{\mathrm{d}z}\right)_{lo}}_{\substack{\text{Friction}\\\text{pressure}\\\text{drop}}} + \underbrace{\frac{\mathrm{d}}{\mathrm{d}z}\left[\frac{G^{2}x^{2}}{\rho_{v}\alpha}+\frac{G^{2}\left(1-x\right)^{2}}{\rho_{l}\left(1-\alpha\right)}\right]}_{\substack{\text{Acceleration}\\\text{pressure}\\\text{drop}}}. \tag{15}$$

Thus, the total pressure drop is the sum of the friction and the acceleration pressure drop. The acceleration term depends on measurable parameters such as fluid properties, mass velocity, quality, and void fraction. The experimental pressure drop measured by differential pressure transmitters gives the total pressure drop, which accounts for both frictional and acceleration terms. Therefore, it is common practice to calculate the acceleration term and subtract it from the total pressure drop to obtain the frictional pressure drop (WOJTAN; URSENBACHER; THOME, 2005b; CHEN; SHI, 2014; HARDIK; PRABHU, 2016; de Oliveira; COPETTI; PASSOS, 2017).

2.4.1 Friction pressure drop gradient

Models for frictional pressure drop predictions have been developed throughout the years. Many researchers have compared independent data with the existing correlations from the literature to validate them and/or propose new ones. An analysis of the best-fitting models from 12 papers (from 1964 to 2023, totaling 73 correlations) was used as a filter for the correlation evaluation for this work. Table 3 lists the best-fitting models from each work. Ten models were selected for further analysis and comparison with the experimental data. The models are as follows: Lockhart and Martinelli (1949), Cicchitti *et al.* (1959), Dukler, Wicks III and Cleveland (1964b), Chisholm (1973), Friedel (1979), Beattie and Whalley (1982), Müller-Steinhagen and Heck (1986), Hardik and Prabhu (2016), Cioncolini and Thome (2017), and Nie *et al.* (2023).

Table 3 – List of best-fitting friction pressure drop models from each work.

Authors	Best-fitting models
Dukler, Wicks III and Cleveland (1964a)	Lockhart and Martinelli (1949)
Beattie and Whalley (1982)	Dukler, Wicks III and Cleveland (1964b) Beattie and Whalley (1982)
Müller-Steinhagen and Heck (1986)	Dukler, Wicks III and Cleveland (1964b) Beattie and Whalley (1982) Müller-Steinhagen and Heck (1986)
García *et al.* (2007)	Dukler, Wicks III and Cleveland (1964b) Beattie and Whalley (1982)
Chen and Shi (2014)	Friedel (1979) Müller-Steinhagen and Heck (1986)
Hardik and Prabhu (2016)	Chisholm (1973) Müller-Steinhagen and Heck (1986)
de Oliveira, Copetti and Passos (2017)	Dukler, Wicks III and Cleveland (1964b) Cicchitti *et al.* (1959) Beattie and Whalley (1982)
Cioncolini and Thome (2017)	Cicchitti *et al.* (1959) Dukler, Wicks III and Cleveland (1964b) Beattie and Whalley (1982) Cioncolini and Thome (2017)
Mastrullo *et al.* (2018)	Lockhart and Martinelli (1949) Friedel (1979) Cioncolini and Thome (2017)
Tank *et al.* (2021)	Lockhart and Martinelli (1949) Friedel (1979) Hardik and Prabhu (2016)
Nie *et al.* (2023)	Cicchitti *et al.* (1959) Müller-Steinhagen and Heck (1986) Nie *et al.* (2023)

Source: Author.

The assumptions for the homogeneous flow are that the liquid and vapor flow at the same velocity and that two-phase flow can be considered a single-phase flow of a pseudo-fluid with pseudo-properties. The equal velocities assumption is valid for the bubbly and mist flow, in which the liquid carries the dispersed bubbles and the vapor core the entrained droplets, respectively. The liquid-only two-phase multiplier for the homogeneous flow is given by:

$$\phi_{lo}^2 = \frac{f_{tp}}{f_{lo}}\frac{\rho_l}{\rho_H}, \tag{16}$$

where the homogeneous density ρ_H is calculated as:

$$\frac{1}{\rho_H} = \frac{x}{\rho_v} + \frac{1-x}{\rho_l}. \tag{17}$$

The two-phase f_{tp} and liquid-only f_{lo} friction factors are calculated from the Blasius equation, which yield:

$$\frac{f_{tp}}{f_{lo}} = \left(\frac{\mu_l}{\mu_{tp}}\right)^{-1/4}, \tag{18}$$

where μ_l and μ_{tp} are the saturated liquid viscosity and two-phase viscosity, respectively. Therefore, the friction pressure drop gradient term can be written as:

$$\left(\frac{\mathrm{d}p}{\mathrm{d}z}\right)_f = 2\frac{f_{lo}G^2}{\cancel{\rho_l} d_{in}}\left(\frac{\cancel{\rho_l}}{\rho_H}\right)\left(\frac{\mu_l}{\mu_{tp}}\right)^{-1/4}, \tag{19}$$

than,

$$\left(\frac{\mathrm{d}p}{\mathrm{d}z}\right)_f = 2\frac{f_{lo}G^2}{\rho_H d_{in}}\left(\frac{\mu_l}{\mu_{tp}}\right)^{-1/4}. \tag{20}$$

The challenge of the homogeneous model is to determine the two-phase viscosity.

Cicchitti *et al.* (1959) proposed that the two-phase viscosity should be calculated similarly to the two-phase specific volume, i.e., a weighted sum of the liquid and vapor viscosity with the quality. Dukler, Wicks III and Cleveland (1964b) argues that the correct weighting factor for mixtures considering the homogeneous model assumption of no slip between the phases should be the volume fraction of the liquid. Beattie and Whalley (1982), from mixing-length theory, adapted the viscosity of the bubble and annular flow into one combined correlation for calculating the two-phase one. The model depends only on the liquid and vapor viscosities and the void fraction. The authors discuss that this method allows accounting for the flow patterns since it captures the interaction of the gas-liquid interfaces with the flow. Despite being built for adiabatic and round tubes, the model has been proven to be accurate for diabatic flow, as shown by Müller-Steinhagen and Heck (1986), García *et al.* (2007), de Oliveira, Copetti and Passos (2017), and Cioncolini and Thome (2017). All these approaches keep the continuity of the pressure drop from the single-phase flow of liquid to vapor. Table 4 lists the homogeneous models and the equation for calculating the two-phase flow viscosity.

Table 4 – List of the homogeneous models and the equation for calculating the two-phase flow viscosity.

Authors	Equation	
Cicchitti *et al.* (1959)	$\mu_{tp} = x\mu_v + (1-x)\,\mu_l$	(21)
Dukler, Wicks III and Cleveland (1964b)	$\mu_{tp} = \rho_H\left[x\frac{\mu_v}{\rho_v} + (1-x)\,\frac{\mu_l}{\rho_l}\right]$	(22)
Beattie and Whalley (1982)	$\mu_{tp} = \mu_v\alpha + \mu_l\,(1-\alpha)\,(1+2.5\alpha)$	(23)

Source: Author.

For the separated flow model the assumptions are that the vapor and liquid velocities are constant but not necessarily equal and the phases are in thermodynamic equilibrium. From Equation 15, the friction pressure drop for the separated flow models rely on empirical correlations for the two-phase flow multiplier. The two-phase multiplier is defined as the ratio between the two-phase and the single-phase friction pressure drop gradient, where the single-phase can be written as a function of the liquid, liquid-only, vapor, and vapor-only.

Lockhart and Martinelli (1949), a classic from two-phase flow pressure drop, evaluated the pressure drop for an isothermal two-phase flow of air and several liquids. They evaluated four combinations of liquid and gas flow, viscous-turbulent (vt), viscous-viscous (vv), turbulent-turbulent (tt), and turbulent-viscous (tv). Their work introduced one of the main parameters for two-phase flow, which would become the Lockhart-Martinelli parameter (X). This parameter is given as the ratio between the frictional pressure drop of the liquid and vapor phases flowing separately, as follows:

$$X^2 = \left(\frac{\mathrm{d}p}{\mathrm{d}z}\right)_l \Big/ \left(\frac{\mathrm{d}p}{\mathrm{d}z}\right)_v . \tag{24}$$

The Lockhart-Martinelli parameter for both liquid and vapor turbulent is given by:

$$X_{tt} = \left(\frac{1-x}{x}\right)^{0.9} \left(\frac{\rho_v}{\rho_l}\right)^{0.5} \left(\frac{\mu_l}{\mu_v}\right)^{0.1} . \tag{25}$$

They verified that the two-phase multiplier correlated with the Lockhart-Martinelli parameter for any flow type. The authors proposed a graphical correlation for the two-phase multiplier, which latter would be written as a function of the Lockhart-Martinelli parameter as follows:

$$\phi_l^2 = 1 + \frac{C}{X} + \frac{1}{X^2}, \tag{26}$$

where ϕ_l^2 is the liquid two-phase multiplier, and C is a constant which depends on the flow condition. The liquid-only two-phase multiplier is calculated from ϕ_l^2 as follows:

$$\phi_{lo}^2 = \phi_l^2 \left(1-x\right)^{1.75} . \tag{27}$$

Table 5 gives the value for C depending on the four flow conditions. As the model of Beattie and Whalley (1982), the authors suggested that this model could be used for the prediction of pressure drop of evaporation or condensation, which has been proved by several independent works such as Mastrullo *et al.* (2018) and Tank *et al.* (2021).

Table 5 – Table for values of C according to the flow conditions.

Liquid	Gas	C
Viscous	Turbulent	12
Viscous	Viscous	5
Turbulent	Turbulent	20
Turbulent	Viscous	10

Source: Author.

Chisholm (1973) argued that the models for evaporating flow were complicated and needed to be more convenient and accurate for industry applications. Then, they proposed a new correlation by changing the two-phase multiplier equation, incorporating the physical property index from Baroczy (1963) to the Lockhart-Martineli parameter and the C constant from Lockhart and Martinelli (1949). Thus, the two-phase multiplier can be written as:

$$\phi_{lo}^2 = 1 + \left(\Gamma^2 - 1\right)\left[Bx^{0.875}\left(1-x\right)^{0.875} + x^{1.75}\right], \tag{28}$$

where Γ is the physical property index given by:

$$\Gamma = \left(\frac{\rho_l}{\rho_v}\right)^{0.5}\left(\frac{\mu_v}{\mu_l}\right)^{0.125}. \tag{29}$$

The author recommends that values of B for smooth tubes should be calculated as shown in Table 6.

Table 6 – Values of B for smooth tubes recommended by Chisholm (1973).

Γ	G [kg m^{-2}s^{-1}]	B	
≤ 9.5	≤ 500	4.8	(30)
	$500 < G < 1,900$	$2,400/G$	(31)
	$\geq 1,900$	$55/G^{0.5}$	(32)
$9.5 < \Gamma < 28$	≤ 600	$520/\left(\Gamma G^{0.5}\right)$	(33)
	> 600	$21/\Gamma$	(34)
≥ 28		$\dfrac{15,000}{\Gamma^2 G^{0.5}}$	(35)

Source: Chisholm (1973).

Friedel (1979 apud COLLIER; THOME, 1994) based on a larger database optimized an equation for the two-phase multiplier. Unfortunately, it was not possible to find the original work of Friedel (1979) and works citing him do not provide sufficient information. The liquid-only two-phase flow multiplier can be calculated as follows:

$$\phi_{lo}^2 = A_1 + \frac{3.24 A_2 A_3}{\mathrm{Fr}^{0.045}\mathrm{We}^{0.035}}, \tag{36}$$

where A_1, A_2, and A_3 are given by:

$$A_1 = \left(1-x\right)^2 + x^2\left(\frac{\rho_l f_{vo}}{\rho_v f_{lo}}\right), \tag{37}$$

$$A_2 = x^{0.78}\left(1-x\right)^{0.224}, \tag{38}$$

$$A_3 = \left(\frac{\rho_l}{\rho_v}\right)^{0.91}\left(\frac{\mu_v}{\mu_l}\right)^{0.19}\left(1 - \frac{\mu_v}{\mu_l}\right)^{0.7}, \tag{39}$$

where f_{vo} and f_{lo} are calculated from Blausius equation. The Froude and Weber numbers are calculated as follows:

$$\mathrm{Fr} = \frac{G^2}{g d_{in} {\rho_H}^2}, \tag{40}$$

and

$$\mathrm{We} = \frac{G^2 d_{in}}{\rho_H \sigma}. \tag{41}$$

Despite little information, many works point Friedel (1979) as one of the best models for predicting frictional pressure drop gradient (CHEN; SHI, 2014; MASTRULLO *et al.*, 2018; TANK *et al.*, 2021).

Müller-Steinhagen and Heck (1986) argued that the correlations based on databanks contained various constants and presented deviation higher than 100% for conditions outside their application range. Thus, they proposed a more elementary approach by considering only the liquid and gas friction pressure drop as follows:

$$\left(\frac{\mathrm{d}p}{\mathrm{d}z}\right)_{f,tp}=\left\{\left(\frac{\mathrm{d}p}{\mathrm{d}z}\right)_{f,l}+2\left[\left(\frac{\mathrm{d}p}{\mathrm{d}z}\right)_{f,v}-\left(\frac{\mathrm{d}p}{\mathrm{d}z}\right)_{f,l}\right]x\right\}(1-x)^{1/C}+\left(\frac{\mathrm{d}p}{\mathrm{d}z}\right)_{f,v}x^{C}, \quad (42)$$

where they fitted the value of C from a curve-fitting model based on 9,300 data points, which yielded $C = 3$. The friction pressure drop gradients of liquid and gas are given as:

$$\left(\frac{\mathrm{d}p}{\mathrm{d}z}\right)_{f,l}=f_l\frac{G^2}{2\rho_l d_{in}}, \quad (43)$$

and

$$\left(\frac{\mathrm{d}p}{\mathrm{d}z}\right)_{f,v}=f_v\frac{G^2}{2\rho_v d_{in}}. \quad (44)$$

The friction factors for the liquid and gas are given by:

$$f_l=\frac{64}{\mathrm{Re}_l},\ f_v=\frac{64}{\mathrm{Re}_v}\ \text{for}\ \mathrm{Re}_l,\ \mathrm{Re}_v\leq 1,187, \quad (45)$$

$$f_l=\frac{0.3164}{\mathrm{Re}_l{}^{1/4}},\ f_v=\frac{0.3164}{\mathrm{Re}_v{}^{1/4}}\ \text{for}\ \mathrm{Re}_l,\ \mathrm{Re}_v>1,187 \quad (46)$$

where

$$\mathrm{Re}_l=\frac{Gd_{in}}{\mu_l}\ \text{and}\ \mathrm{Re}_v=\frac{Gd_{in}}{\mu_v}. \quad (47)$$

Although simple, their model proved to be accurate for independent data such as Chen and Shi (2014), Hardik and Prabhu (2016), and Nie *et al.* (2023).

Hardik and Prabhu (2016) argued that the correlations for high-pressure deviate from the experimental data of low-pressure systems and proposed a correlation based on the liquid two-phase multiplier from Equation 26. Although they stated that they derived from Chisholm's work, they modified the Lockhart and Martinelli (1949) form of the liquid two-phase multiplier. From a parametric study, the authors found that for low-pressure flow boiling systems, the friction pressure drop gradient is highly dependent on the tube diameter and correlated the C value from Equation 26 as follows:

$$C=18\,e^{0.14\,d_{in}}. \quad (48)$$

This approach seems to improve the prediction of Lockhart and Martinelli's model since it shows lower MAE for Tank *et al.*'s studies on flow boiling in horizontal straight tubes.

Cioncolini, Thome and Lombardi (2009) proposed a unified model to predict the pressure drop for adiabatic annular flow. Their models are based on dimensional analysis and therefore incorporate physical effects that empirical parametric models neglect, such as the vapor core velocity, liquid entrainment, and liquid film thickness. Also, the models are for both macro and micro scales, whether turbulent or laminar flow. Later, with a larger database and the research development, Cioncolini and Thome (2017) have improved the Cioncolini, Thome and Lombardi (2009) model to macroscale applications. They extended the applicability to diabatic flow, non-circular sections (annular), and horizontal flow with low mass velocities. By extending the model for lower mass velocities, they incorporated the liquid film asymmetry effects inherent in horizontal flow in which gravity plays a relevant role. The friction pressure drop gradient is given by:

$$\left(\frac{\mathrm{d}p}{\mathrm{d}z}\right)_{f,tp} = 2f_{tp}\frac{G^2}{\rho_m d_{in}}, \tag{49}$$

where ρ_m is the momentum density, given by:

$$\rho_m = \left[\frac{(1-e)^2(1-x)^2 x}{(1-e)\,x\,\rho_l - e\,\alpha\,(1-x)\,\rho_v} + \frac{e\,x\,(1-x)+x^2}{\alpha\,\rho_v}\right]^{-1}, \tag{50}$$

where e is the entrainment liquid fraction and is calculated by:

$$e = \left(1 + 279.6\ \mathrm{We}_c{}^{-0.8395}\right)^{-2.209}. \tag{51}$$

The core flow Weber number, We_c, and the droplet laden gas core density, ρ_c, are given by:

$$\mathrm{We}_c = \frac{\rho_c x^2 G^2 d_{in}}{\rho_v{}^2\sigma},\ \text{and}\ \rho_c = \frac{x + e\,(1+x)}{\frac{x}{\rho_v} + \frac{e(1-x)}{\rho_l}}. \tag{52}$$

The We_c, e, and ρ_c are solved iteratively.

The f_{tp} is the two-phase Fanning friction factor calculated from:

$$f_{tp} = 0.2140\ \mathrm{We}_m{}^{-0.3884}\ \text{for}\ 10^2 \leq \mathrm{We}_m \leq 10^5, \tag{53}$$

$$f_{tp} = 0.2140\ \mathrm{We}_m{}^{-0.3884}\frac{0.1009\ \mathrm{Fr}_m{}^{0.6425}}{1 + 0.1009\ \mathrm{Fr}_m{}^{0.6425}}\ \text{for}\ \mathrm{Fr}_m \geq 3 \tag{54}$$

where We_m and Fr_m are the momenta Weber and Froude numbers, respectively, and are calculated as follows:

$$\mathrm{We}_m = \frac{G^2 d_{in}}{\rho_m \sigma},\ \text{and}\ \mathrm{Fr}_m = \frac{G^2}{g\rho_m d_{in}}. \tag{55}$$

Nie *et al.* (2023), by combining machine learning methods, proposed a universal correlation for predicting the friction pressure drop gradient. To keep the physical insights usually lost with machine learning, they explored 40 flow parameters and their impact on the pressure drop gradient from a database with 8,663 experimental points. Their parametric analysis showed that the main parameters are the dimensionless vapor velocity (J_v), quality (x), two-phase Froude number (Fr_{tp}), vapor friction pressure drop gradient [$(\mathrm{d}p/\mathrm{d}z)_v$], and Bond number (Bd). Since the impact of the vapor friction pressure drop gradient is higher than the liquid's, the author built their correlation based on the vapor two-phase multiplier as follows:

$$\phi_v^2 = 1 + CX^n + X^2. \tag{56}$$

By combining the definition of the two-phase multiplier and the Lockhart-Martinelli parameter from Equation 24, then:

$$-\left(\frac{\mathrm{d}p}{\mathrm{d}z}\right)_{f,tp} = -\left(\frac{\mathrm{d}p}{\mathrm{d}z}\right)_{f,v} + C\left(\frac{\mathrm{d}p}{\mathrm{d}z}\right)_{f,v}^{1-n/2}\left(\frac{\mathrm{d}p}{\mathrm{d}z}\right)_{f,l}^{n/2} - \left(\frac{\mathrm{d}p}{\mathrm{d}z}\right)_{f,l}. \tag{57}$$

The values of C are calculated for annular flow and non-annular flow as follows:

$$C = \begin{cases} 0.94\,\mathrm{Fr}_{tp}{}^{0.26}x^{-0.4}\mathrm{Bd}^{0.05}J_v{}^{-0.35}, \text{ and } n = 0.55 & \text{for annular flow,} \\ \mathrm{Co}^{0.47} + 0.291\,\mathrm{Fr}_{tp}{}^{0.55}\mathrm{Bd}^{0.13}J_v{}^{-0.72} \text{ and } n = 0.73 & \text{for non-annular flow.} \end{cases} \tag{58}$$

The dimensionless parameters are calculated as follows:

$$\mathrm{Fr}_{tp} = \frac{G^2}{g\rho_H{}^2 d_{in}}, \tag{59}$$

$$\mathrm{Bd} = \frac{(\rho_l - \rho_v)\,g\,d_{in}}{\sigma}, \tag{60}$$

$$J_v = \frac{G\,x}{\left[g\,d_{in}\rho_v\,(\rho_l - \rho_v)\right]^{0.5}}, \tag{61}$$

$$\mathrm{Co} = \left(\frac{1-x}{x}\right)^{0.8}\left(\frac{\rho_v}{\rho_l}\right)^{0.5}. \tag{62}$$

Although more robust, this approach is similar to the Hardik and Prabhu's, except that they correlate the C value for several dimensionless numbers while Hardik and Prabhu (2016) made it only with the tube diameter.

2.4.2 Acceleration pressure drop gradient

As mentioned, the friction pressure drop is measured by predicting the acceleration term and removing it from the total pressure drop. Therefore, each friction pressure drop model proposes an approach for calculating the acceleration term. A void-fraction model must be chosen for those models built on databases for friction pressure drop.

For the homogeneous models, the equal velocities of liquid and vapor assumption yield the void fraction to be calculated by:

$$\alpha = \frac{x/\rho_v}{(1-x)/\rho_l + (x/\rho_v)}. \tag{63}$$

Combining Equation 63 with the acceleration term of Equation 15 gives:

$$\left(\frac{\mathrm{d}p}{\mathrm{d}z}\right)_a = G^2 \frac{\mathrm{d}}{\mathrm{d}z}\left[\frac{(1-x)}{\rho_l} + \frac{x}{\rho_v}\right]. \tag{64}$$

The term between brackets is the homogeneous specific volume, and Equation 64 reduces to:

$$\left(\frac{\mathrm{d}p}{\mathrm{d}z}\right)_a = G^2 \frac{\mathrm{d}}{\mathrm{d}z}\left(\frac{1}{\rho_H}\right), \tag{65}$$

where ρ_H is the homogeneous density. From the experimental work, the acceleration term can be calculated from the definition of the derivative as follows:

$$\left(\frac{\mathrm{d}p}{\mathrm{d}z}\right)_a = G^2 \left\{\left[\frac{1-x_o}{\rho_l} + \frac{x_o}{\rho_v}\right] - \left[\frac{1-x_i}{\rho_l} + \frac{x_i}{\rho_v}\right]\right\} \Big/ L_{ts}, \tag{66}$$

where x_o and x_i are the quality at the outlet and inlet, respectively, and L_{ts} is the length of the test tube.

Butterworth (1975) noted that the majority of void fraction correlations could be written as:

$$\alpha = \left[1 + A\left(\frac{1-x}{x}\right)^p \left(\frac{\rho_v}{\rho_l}\right)^q \left(\frac{\mu_l}{\mu_v}\right)^r\right]^{-1}, \tag{67}$$

where p, q, and r, are given by Table 7. For the models evaluated in this work, only the values for the homogeneous model and the separated flow models of Lockhart and Martinelli (1949) and Baroczy (1963) are shown. No information was found about which void fraction model should be used for Friedel's, Müller-Steinhagen and Heck's, and Nie *et al.*'s models.

Table 7 – Table for values of A, p, q, r.

Model	A	p	q	r
Homogeneous	1	1	1	0
Lockhart and Martinelli	0.28	0.64	0.36	0.07
Baroczy	1	0.74	0.65	0.13

Source: Author.

Hardik and Prabhu (2016) proposed the void fraction calculation using the Steiner and Kind's version of Rouhani and Axelsson's model as follows:

$$\alpha = \frac{x}{\rho_v}\left\{[1 + 0.12(1-x)]\left(\frac{x}{\rho_v} + \frac{1-x}{\rho_l}\right) + \frac{1.18(1-x)[g\sigma(\rho_l - \rho_g)]^{0.25}}{G^2 {\rho_l}^{0.5}}\right\}^{-1}. \tag{68}$$

The acceleration pressure drop gradient is calculated from Equation 15, as follows:

$$\left(\frac{\mathrm{d}p}{\mathrm{d}z}\right)_a = G^2 \left\{\left[\frac{{x_o}^2}{\rho_v \alpha_o} + \frac{(1-x_o)^2}{\rho_l(1-\alpha_o)}\right] - \left[\frac{{x_i}^2}{\rho_v \alpha_i} + \frac{(1-x_i)^2}{\rho_l(1-\alpha_i)}\right]\right\} \Big/ L_{ts}, \tag{69}$$

where α_o, and α_i are the void fraction at the outlet and inlet of the test tube.

Cioncolini and Thome (2017) used the Cioncolini and Thome's method for calculating the void fraction as follows:

$$\alpha = \frac{h\,x^n}{1+(h-1)\,x^n}, \tag{70}$$

where h and n are given by:

$$h = -2.129 + 3.129 \left(\frac{\rho_v}{\rho_l}\right)^{-0.2186}, \tag{71}$$

and

$$n = 0.3487 + 0.6513 \left(\frac{\rho_v}{\rho_l}\right)^{0.5150}. \tag{72}$$

Cioncolini and Thome (2017) acceleration pressure drop gradient is calculated as follows:

$$\left(\frac{\mathrm{d}p}{\mathrm{d}z}\right)_a = G^2 \frac{\mathrm{d}}{\mathrm{d}z}\left[\frac{1}{\rho_m}\right], \tag{73}$$

combining Equation 50 with Equation 73 yields in:

$$\left(\frac{\mathrm{d}p}{\mathrm{d}z}\right)_a = G^2 \frac{\mathrm{d}}{\mathrm{d}z}\left[\frac{(1-e)^2\,(1-x)^2\,x}{(1-e)\,x\,\rho_l - e\,\alpha\,(1-x)\,\rho_v} + \frac{e\,x\,(1-x)+x^2}{\alpha\,\rho_v}\right], \tag{74}$$

from the definition of derivative, then:

$$\begin{aligned}\left(\frac{\mathrm{d}p}{\mathrm{d}z}\right)_a = G^2 \Bigg\{ &\left[\frac{(1-e_o)^2\,(1-x_o)^2\,x_o}{(1-e_o)\,x_o\,\rho_l - e_o\,\alpha_o\,(1-x_o)\,\rho_v} + \frac{e_o\,x_o\,(1-x_o)+{x_o}^2}{\alpha_o\,\rho_v}\right] + \\ &- \left[\frac{(1-e_i)^2\,(1-x_i)^2\,x_i}{(1-e_i)\,x_i\,\rho_l - e_i\,\alpha_i\,(1-x_i)\,\rho_v} + \frac{e_i\,x_i\,(1-x_i)+{x_i}^2}{\alpha_i\,\rho_v}\right]\Bigg\} \Big/ L_{ts},\end{aligned} \tag{75}$$

where e_o, and e_i are the entrainment of liquid droplets to the vapor core at the inlet and outlet of the test tube, respectively.

2.5 Horizontal flow boiling heat transfer

Several researchers compared data banks and performed experiments to assess the heat transfer coefficient for two-phase flow. Many of them compared these data with existing correlations and proposed new ones. As done for the pressure drop gradient, the best-fitting models, extracted from over 20 papers (1966-2022), were chosen for evaluation. Table 8 lists the best-fitting for each analyzed paper. Out of the nineteen best-fitting models, only those accounting for horizontal flow were evaluated. Wojtan, Ursenbacher and Thome (2005a)'s model was preferable since it is an update to the Kattan, Thome and Favrat's work. Despite Zou *et al.*'s model showing good performance, their correlation is identical to Gungor and Winterton's for pure refrigerants. Then the list reduces to 13 models, which are: Shah (1982), Gungor and Winterton (1986), Klimenko (1990), Kandlikar (1990), Liu and Winterton (1991), Wattelet *et al.*

(1993), Jabardo, Bandarra Filho and Lima (1999), Wojtan, Ursenbacher and Thome (2005a), Del Col (2010), Cioncolini and Thome (2011), Fang, Wu and Yuan (2017), Wang *et al.* (2019), and Paul, Fernandino and Dorao (2021).

Table 8 – List of best-fitting heat transfer coefficient models from each work.

Authors	Best-fitting models
Chen (1966)	Chen (1966)
Gungor and Winterton (1986)	Shah (1982) Gungor and Winterton (1986)
Klimenko (1988)	Klimenko (1988)
Kandlikar (1990)	Kandlikar (1990) Shah (1982) Bjorg, Hall and Rohsenow (1982)
Liu and Winterton (1991)	Gungor and Winterton (1987) Liu and Winterton (1991)
Wattelet *et al.* (1993)	Kandlikar (1990) Wattelet *et al.* (1993)
Kattan, Thome and Favrat (1998b)	Kattan, Thome and Favrat (1998b)
Jabardo, Bandarra Filho and Lima (1999)	Shah (1982) Kandlikar (1990) Wattelet *et al.* (1993)
Wojtan, Ursenbacher and Thome (2005a)	Wojtan, Ursenbacher and Thome (2005a)
Zou *et al.* (2010)	Liu and Winterton (1991) Zou *et al.* (2010)
Del Col (2010)	Liu and Winterton (1991) Wojtan, Ursenbacher and Thome (2005a) Del Col (2010)
Cioncolini and Thome (2011)	Bjorg, Hall and Rohsenow (1982) Cioncolini and Thome (2011)
Grauso *et al.* (2013)	Shah (1976) Kandlikar (1990) Wattelet *et al.* (1993)
Chen and Shi (2013)	Zou *et al.* (2010)
Zou *et al.* (2015)	Zou *et al.* (2010)
Hardik and Prabhu (2016)	Kandlikar (1990) Shah (1982)
Yuan *et al.* (2017)	Fang, Wu and Yuan (2017)
Fang, Wu and Yuan (2017)	Wattelet *et al.* (1993) Yuan *et al.* (2017)
Mastrullo *et al.* (2018)	Liu and Winterton (1991) Cioncolini and Thome (2011)
Lillo *et al.* (2019)	Wojtan, Ursenbacher and Thome (2005b) Del Col (2010)
Fang *et al.* (2019)	Fang, Wu and Yuan (2017)
Wang *et al.* (2019)	Gungor and Winterton (1986) Wang *et al.* (2019)
Paul, Fernandino and Dorao (2021)	Chen (1966) Paul, Fernandino and Dorao (2021)
Bediako, Dančová and Vít (2022)	Wattelet *et al.* (1993)

Source: Author.

The heat transfer coefficient models can be categorized into four approaches: the enhancement, the superposition, the greater of two, and the asymptotic models (WATTELET *et al.*, 1993; de Oliveira; COPETTI; PASSOS, 2017). There are many variations disposable in the literature, either combining approaches or proposing different ways of calculating the features of each model. The selected models are a compilation of all types of correlation, with many combining different approaches.

Shah (1982) published the equations for his generalyzed graphical model (SHAH, 1976) for heat transfer coefficient calculation. His strictly empirical model was built from 3,000 data points of 12 different fluids, pipe materials, and orientations. The author proposed an enhancement factor as follows:

$$\psi = \frac{h_{tp}}{h_l}, \tag{76}$$

where h_{tp} is the two-phase flow heat transfer coefficient, h_l is the superficial heat transfer coefficient of the liquid phase, and ψ is the enhancement factor. The superficial heat transfer coefficient of the liquid phase is calculated by the Dittus-Boelter equation:

$$h_l = 0.023\,\mathrm{Re}_l{}^{0.8}\mathrm{Pr}_l{}^{0.4}\frac{\kappa_l}{d_{in}}, \tag{77}$$

where Re_l is the liquid Reynolds number, Pr_l is the liquid Prandtl number, κ_l is the liquid thermal conductivity, and d_{in} is the tube inner diameter. The enhancement factor ψ depends on the convection number (Co), Boiling number (Bo), and liquid Froude number (Fr_l) as follows:

- For $N > 1.0$:

$$\psi_{nb} = \begin{cases} 230\,\mathrm{Bo}^{0.5} & \text{for Bo} > 0.3 \times 10^{-4} \\ 1 + 46\,\mathrm{Bo}^{0.5} & \text{for Bo} < 0.3 \times 10^{-4} \end{cases}, \tag{78}$$

$$\psi_{cb} = 1.8/N^{0.8}, \tag{79}$$

$$\psi = \max\left[\psi_{nb}; \psi_{cb}\right], \tag{80}$$

where the subscripts nb and cb mean nucleate boiling and convective boiling, respectively.

- For $0.1 < N \leq 1.0$:

$$\psi_{bs} = F\,\mathrm{Bo}^{0.5} e^{2.74\,N^{-0.1}}, \tag{81}$$

$$\psi = \max\left[\psi_{bs}; \psi_{cb}\right], \tag{82}$$

where the subscript bs means boiling suppression, and ψ_{cb} is calculated by Equation 79.

- For $N \leq 0.1$:

$$\psi_{bs} = F\,\mathrm{Bo}^{0.5} e^{2.47\,N^{-0.15}}, \tag{83}$$

$$\psi = \max\left[\psi_{bs}; \psi_{cb}\right], \tag{84}$$

where ψ_{cb} is calculated by Equation 79.

The constant F can be calculated as follows:

$$F = \begin{cases} 14.7 & \text{for Bo} \geq 11 \times 10^{-4} \\ 15.43 & \text{for Bo} < 11 \times 10^{-4} \end{cases} . \tag{85}$$

For vertical tubes $N = \text{Co}$ and for horizontal tube with $\text{Fr}_{lo} \leq 0.04$:

$$N = 0.38\,{\text{Fr}_{lo}}^{-0.3}\text{Co}. \tag{86}$$

This model is very robust and has been tested against many independent data. Several researchers, such as Gungor and Winterton (1986), Kandlikar (1990), Jabardo, Bandarra Filho and Lima (1999), Grauso *et al.* (2013), and Hardik and Prabhu (2016), have shown good agreement with Shah's correlation. Above that, the model is simple and easy to apply.

Gungor and Winterton (1986), from a data bank with 3,693 saturated boiling data points, built a superposition correlation. They used the database to correlate the enhancement and suppression factors. The superposition model is given by:

$$h_{tp} = E\,h_l + S\,h_{nb}, \tag{87}$$

where h_l is given by Equation 77, and h_{nb} is the Cooper's correlation as follows:

$$h_{nb} = 55\,{p_r}^{0.12}\left(-\log_{10} p_r\right)^{-0.55} M^{-0.5} q''^{0.67}, \tag{88}$$

where p_r is the reduced pressure, M is the molar mass, and q'' is the heat flux. They correlated the enhancement factor E as a function of the Boiling number and the Lockhart-Martinelli parameter, as follows:

$$E = 1 + 24{,}000\ \text{Bo}^{1.16} + 1.37\left(1/X_{tt}\right)^{0.86}. \tag{89}$$

The suppression factor S is a function of the enhancement factor and the liquid Reynolds number, such as:

$$S = \left(1 + 1.15 \times 10^{-6} E^2 {\text{Re}_l}^{1.17}\right)^{-1}. \tag{90}$$

For horizontal flow with $\text{Fr}_{lo} < 0.05$, the author suggested that the enhancement and suppression factor should be multiplied by ${\text{Fr}_{lo}}^{(0.1-2\ \text{Fr}_{lo})}$, and ${\text{Fr}_{lo}}^{0.5}$, respectively.

Their model can be applied to both saturated and subcooled boiling. As Shah's, Gungor and Winterton's model has been put to the test by various works (LIU; WINTERTON, 1991; Del Col, 2010; WANG *et al.*, 2019), and provided accurate predictions for the two-phase flow HTC. Their model is also the basis for other models, such as Del Col (2010) and Wang *et al.* (2019).

Klimenko (1990) updated his first correlation (KLIMENKO, 1988) from a database with 3,000 data points for 21 different fluids on saturated and nucleate boiling. The model is based on the approach of the greater of the two, which consists of calculating both convective and nucleate boiling HTC, and the higher value is taken as the two-phase HTC. The author was the first to incorporate the surface material into the correlation. Their correlation is expressed in terms of Nusselt numbers and is given by:

$$\mathrm{Nu}_{tp} = \max\left[\mathrm{Nu}_{nb}; \mathrm{Nu}_{cb}\right], \tag{91}$$

where Nu_{nb} and Nu_{cb} are the nucleate and convective boiling Nussel numbers, respectively.

The nucleate boiling Nusselt number is calculated by:

$$\mathrm{Nu}_{nb} = C\, \mathrm{Pe}_*{}^{0.6} K_p{}^{0.54} \mathrm{Pr}_l{}^{-0.33} K_\lambda{}^{0.12}, \tag{92}$$

where Pe_* is the modified Peclet number, K_p is the dimensionless parameter related to pressure and Laplace constant, and K_λ is the ratio between the wall and fluid thermal conductivity. The Pe_* is given by:

$$\mathrm{Pe}_* = \frac{q''\mathrm{La}}{h_{lv}\rho_v\alpha_l}, \tag{93}$$

where La is the Laplace constant or capillary length, given by:

$$\mathrm{La} = \left[\frac{\sigma}{g\left(\rho_l - \rho_v\right)}\right]^{0.5}. \tag{94}$$

The dimenssionless parameter K_p is given by:

$$K_p = \frac{p\,\mathrm{La}}{\sigma}, \tag{95}$$

where p is the saturation pressure in Pa. The constant C depends on the fluid and is given by Table 9.

Table 9 – Klimenko C coefficients for nucleate boiling HTC.

Fluids	C
Freons	7.6×10^{-3}
Organic fluids	6.8×10^{-3}
Cryogenic fluids	6.1×10^{-3}
Water	4.9×10^{-3}

Source: Klimenko (1990).

The convective boiling Nusselt number is calculated by:

$$\mathrm{Nu}_{nb} = 0.087\, \mathrm{Re}_m{}^{0.6} \mathrm{Pr}_l{}^{1/6} \left(\rho_v/\rho_l\right)^{0.2} K_\lambda{}^{0.09}, \tag{96}$$

where Re_m is the Reynolds number of the mixture, given by:

$$\mathrm{Re}_m = \frac{w_m\mathrm{La}}{\nu_l}, \tag{97}$$

where w_m is the two-phase mixture velocity, given by:

$$w_m = \frac{G}{\rho_l}\left[1 + x\left(\frac{\rho_l}{\rho_v} - 1\right)\right]. \tag{98}$$

Kandlikar (1990) also used a database with 5,246 data points to extend his correlation for two-phase flow HTC. According to him, the correlation captures the correct trend of HTC related to quality. His model is strictly empirical, and the ratio of the two-phase and the liquid HTC, given by the Dittus-Boelter correlation, is a function of the Boiling number, liquid-only Froude Number, Convection number, and a fluid-dependent factor. The following relation gives the two-phase flow HTC:

$$\frac{h_{tp}}{h_l} = C_1 \mathrm{Co}^{C_2} \left(25\,\mathrm{Fr}_{lo}\right)^{C_5} + C_3 \mathrm{Bo}^{C4} F_{fl}, \tag{99}$$

where the constants C_1, C_2, C_3, C_4, and C_5 are given by the Table 10. For vertical and horizontal flow with $\mathrm{Fr}_{lo} > 0.04$, C_5 is equal to zero. Then, the two-phase flow HTC is given by the higher value of the convective and nucleate boiling HTC.

Table 10 – Kandlikar C coefficients for convective and nucleate boiling HTC.

Constant	Convective	Nucleate boiling
C_1	1.1360	0.6683
C_2	-0.9	-0.2
C_3	667.2	1058.0
C_4	0.7	0.7
C_5	0.3	0.3

Source: Kandlikar (1990).

The fluid-dependent parameter is given by Table 11. The author suggests another paper for calculating the F_{fl}, though it was not possible to access the document.

Table 11 – Fluid-dependent parameter for Kandlikar's model.

Fluid	F_{fl}
Water	1.00
R11	1.30
R12	1.50
R13B1	1.31
R22	2.2
R113	1.30
R114	1.24
R152a	1.10
Nitrogen	4.70
Neon	3.50

Source: Kandlikar (1990).

By inputting a fluid-dependent variable into the HTC model, Kandlikar (1990) makes his model more flexible and adjustable fluid-wise. He also highlights that the model captures the trend of the HTC with quality. Over time, his model has been tested and proved accurate for Wattelet *et al.* (1993), Jabardo, Bandarra Filho and Lima (1999), Grauso *et al.* (2013), and Hardik and Prabhu (2016), though some recent works seem to forget about it.

Liu and Winterton (1991) to extend the models to subcooled boiling, used the same databank as Gungor and Winterton (1987). The author proposed a superposition model from 4,202 data points for saturated boiling and 991 data points for subcooled boiling. Their model is similar to the Gungor and Winterton's, changing the correlation for enhancement and suppression factors calculation. The enhancement factor is calculated by:

$$F = \left[1 + x\,\mathrm{Pr}_l\left(\frac{\rho_l}{\rho_v} - 1\right)\right]^{0.35}, \tag{100}$$

and the suppression factor by:

$$S = \left(1 + 0.055\,F^{0.1}\mathrm{Re}_{lo}{}^{0.16}\right)^{-1}. \tag{101}$$

The authors kept the same approach for horizontal flow as Gungor and Winterton (1986), for Fr lower than 0.05, the enhancement and suppression factors should be multiplied by $\mathrm{Fr}_{lo}{}^{(0.1-2\ \mathrm{Fr}_{lo})}$, and $\mathrm{Fr}_{lo}{}^{0.5}$, respectively. They state that despite being built on saturated cryogenic fluids and subcooled boiling, the model was accurate nonetheless. As many models presented here, Liu and Winterton (1991) proved accurate for many other works (ZOU *et al.*, 2010; Del Col, 2010; MASTRULLO *et al.*, 2018).

Wattelet *et al.* (1993) from his experiments with R134a, MP39, and R12 proposed a new correlation for stratified-wavy and annular flow with low mass velocity. They argue that the correlations did not capture the effect of zeotropic mixtures and the concentration effect of their concentration gradients on nucleate and convective boiling, mainly due to the lower turbulent mixing of stratified wavy flow. They represented the two-phase flow HTC using the asymptotic model as follows:

$$h_{tp} = \left[h_{nb}{}^{n} + h_{cb}{}^{n}\right]^{1/n}, \tag{102}$$

where $n = 2$, h_{nb} is given by Cooper (1984) (Equation 88), and h_{cb} is:

$$h_{cb} = F\,h_l\,R, \tag{103}$$

where h_l is the liquid heat transfer coefficient calculated by the Dittus-Boelter correlation, values F and R are calculated by:

$$F = 1 + 1.925\,X_{tt}'^{\,-0.83}, \tag{104}$$

$$R = \begin{cases} 1.32\,\mathrm{Fr}_{lo}{}^{0.2} & \text{for } \mathrm{Fr}_{lo} < 0.25 \\ 1 & \text{for } \mathrm{Fr}_{lo} \geq 0.25 \end{cases}, \tag{105}$$

where the modified Lockhart-Martinelli parameter is:

$$X_{tt}' = 0.551\,p_r{}^{0.492}\left(\frac{1-x}{x}\right)^{0.9}, \tag{106}$$

The researchers try to differentiate the annular from the stratified-wavy correlation, by adding R as a function of the liquid Froude number, i.e., for $\mathrm{Fr}_{lo} \leq 0.25$ the flow is supposed to be stratified-wavy and for $\mathrm{Fr}_{lo} > 0.25$ annular. Their model showed accurate prediction for various works on horizontal flow, such as Jabardo, Bandarra Filho and Lima (1999), Grauso *et al.* (2013), Fang, Wu and Yuan (2017), and Bediako, Dančová and Vít (2022).

Jabardo, Bandarra Filho and Lima (1999), from his experimental work, proposed a correlation for the HTC based on the Lockhart-Martinelli parameter, Boiling number, and Froude number. Their database was mainly composed of halocarbon refrigerants and few operating conditions. To capture all heat transfer mechanisms for horizontal flow, they correlated the HTC with the Lockhart-Martinelli parameter, Boiling number, and Froude number. They based their correlation on the enhancement model as follows:

$$\frac{h_{tp}}{h_l} = 1 + C\ {X_{tt}}^{m}\mathrm{Bo}^{n}{\mathrm{Fr}_{lo}}^{p}, \tag{107}$$

where the coefficients C, m, n, and p, are given in Table 12. This way, they argued that both convective and nucleate boiling effects are evaluated together. They checked for the accuracy of their model with independent databases, which proved to be more accurate than classical models such as Kandlikar (1990) and Wattelet *et al.* (1993).

Table 12 – Jabardo, Bandarra Filho and Lima's model coefficients for two-phase flow HTC calculation.

	C	m	n	p
$\mathrm{Fr}_{lo} < 1.0$	125	-0.65	0.3	0.5
$\mathrm{Fr}_{lo} \geq 1.0$	40	-0.65	0.3	0.0

Source: Author.

In addition to the new map, Wojtan, Ursenbacher and Thome (2005a) also presented their model for calculating the heat transfer coefficient. They proposed several changes to Kattan, Thome and Favrat's model, extending the application of it to qualities below 0.15 and covering the whole range of vapor quality ($0.0 < x < 1.0$). To do so, they extend their database with 368 datapoints for post dryout regime, and 1,250 for R22 and R410a at mass velocities from 70 to 700 kg $\mathrm{m}^{-2}\mathrm{s}^{-1}$ and heat fluxes from 2.0 to 57.5 kW m^{-2}. Their model is pattern-based, i.e., the HTC calculation depends on the flow regime. The main parameter to differentiate the flow pattern is the dry angle (θ_{dry}), defined as the angle created by the arc of the dry perimeter. The authors proposed that the two-phase HTC should be calculated as:

$$h_{tp} = \frac{\theta_{dry}h_v + (2\pi - \theta_{dry})\,h_{wet}}{2\pi}, \tag{108}$$

where h_v is the vapor HTC, and h_{wet} is the wetted HTC. The vapor HTC is calculated by the Dittus-Boelter equation for the vapor as:

$$h_v = 0.023\ {\mathrm{Re}_v}^{0.8}{\mathrm{Pr}_v}^{0.4}\frac{\kappa_v}{d_{in}}, \tag{109}$$

and the wetted HTC is given by the asymptotical model as follows:

$$h_{wet} = \left[{h_{cb}}^{3} + {h_{nb}}^{3}\right]^{1/3}, \tag{110}$$

where h_{nb} is calculated by the equation of Cooper (Equation 88), and h_{cb} is:

$$h_{cb} = 0.0133\,\mathrm{Re}_{\delta}{}^{0.69}\mathrm{Pr}_l{}^{0.4}\frac{\kappa_v}{\delta}, \tag{111}$$

where δ is the liquid film thickness. The authors used the expression suggested by Thome, Hajal and Cavallini (2003) to calculate the liquid film thickness, which is given by:

$$\delta = \frac{d_{in}}{2} - \left[\left(\frac{d_{in}}{2}\right)^2 - \frac{2\,A_l}{(2\pi - \theta_{dry})}\right]^{0.5}, \tag{112}$$

if $\delta > d_{in}/2$, than $\delta = d_{in}/2$.

As mentioned, the θ_{dry} is pattern dependent and is given by:

$$\theta_{dry} = \begin{cases} 0 & \text{for slug, intermittent, and annular flow} \\ \left[\dfrac{G_w - G}{G_w - G_s}\right]^{0.61}\theta_{strat} & \text{for stratified-wavy flow} \\ \dfrac{x}{x_{ia}}\left[\dfrac{G_w - G}{G_w - G_s}\right]^{0.61}\theta_{strat} & \text{for slug + stratified-wavy flow} \end{cases}. \tag{113}$$

where θ_{strat} is the stratification angle and is a function of the void fraction as follows:

$$\theta_{strat} = 2\pi - 2\left\{\begin{array}{c} \pi\,(1-\alpha) + \left(\dfrac{3\pi}{2}\right)^{1/3}\left[1 - 2\,(1-\alpha) + (1-\alpha)^{1/3} - \alpha^{1/3}\right] + \\ -\frac{1}{200}\,(1-\alpha)\,\alpha\,[1 - 2\,(1-\alpha)]\,[1 + 4\,((1-\alpha)^2 + \alpha^2)] \end{array}\right\}. \tag{114}$$

For mist flow, the authors suggested the HTC should be calculated by:

$$h_{mist} = 0.0117\,\mathrm{Re}_H{}^{0.79}\mathrm{Pr}_v{}^{1.06}Y^{-1.83}\frac{\kappa_v}{d_{in}}, \tag{115}$$

where Re_H is the homogeneous Reynolds number, and Y is the multiplying factor from Groeneveld (1973) and is given by:

$$Y = 1 - 0.1\left[\left(\frac{\rho_l}{\rho_v}\right)(1-x)\right]^{0.4}. \tag{116}$$

Their main contribution was a correlation for partial dryout heat transfer coefficient. As the HTC sharply decreases when reaching partial dryout, their proposal based on an interpolation between the annular regime and mist flow HTC is pertinent. They wrote the correlation as follows:

$$h_{dryout} = h_{tp}\,(x_{di}) - \frac{x - x_{di}}{x_{de} - x_{di}}\,[h_{tp}\,(x_{di}) - h_{mist}\,(x_{de})], \tag{117}$$

where $h_{tp}\,(x_{di})$ is the two-phase HTC evaluated at the quality of dryout inception (x_{di}) with the respective flow pattern, and $h_{mist}\,(x_{de})$ is the mist flow HTC evaluated at the dryout completion quality (x_{de}).

Wojtan, Ursenbacher and Thome's model relays on identifying the flow pattern to apply the best correlation. Therefore, it depends on the accuracy of the flow pattern map and/or flow visualization, which on numerous occasions, is not feasible. The model is more complex than most of the correlations available in the literature and sometimes can be overlooked by simple ones that give similar errors. Nevertheless, other researchers tested their model, which proved accurate for the works of Del Col (2010) and Lillo *et al.* (2019).

Del Col (2010) performed experiments on the flow boiling of halogenated refrigerants in a horizontal smooth tube. Comparing their data with the correlations from Gungor and Winterton's, Kandlikar's, and Liu and Winterton's works, he found the best agreement with Gungor and Winterton's model. To better fit his experimental data, he proposed multiplying the Gungor and Winterton's correlation by 1.2. He also states that the modified correlation is not intended to be a general tool for flow boiling but to be used within the operating conditions of his data.

Cioncolini and Thome (2011), on his algebraic turbulence modeling of annular flow, proposed a correlation for annular flow HTC. Their model can predict the average liquid film thickness, void fraction, and convective heat transfer coefficient. The model accounts for the heat transfer through the liquid film, deviating from the classical approaches, which consider the single-phase HTC. Thus the HTC can be calculated as follows:

$$h_{tp} = 77 \times 10^{-3}\, t^{+0.90} \mathrm{Pr}_l^{\,0.52} \frac{\kappa_l}{t} \text{ for } \begin{cases} 10 \leq t^+ \leq 800 \\ 0.86 \leq \mathrm{Pr}_l \leq 6.1 \end{cases}, \tag{118}$$

where t and t^+ are the average liquid film thickness and the dimensionless average liquid film thickness, respectively. The average liquid film thickness is given by:

$$t = \frac{d_{in}}{2}\left(1 - \alpha^{0.5}\right). \tag{119}$$

while the dimensionless average liquid film thickness is given by:

$$t^+ = \max\left[\left(\frac{2\Gamma^+_{lf}}{R^+}\right);\ 0.066\frac{\Gamma^+_{lf}}{R^+}\right], \tag{120}$$

where Γ^+_{lf}/R^+ is the ratio between the dimensionless liquid film mass flow rate and the dimensionless tube radius, which is given by:

$$\frac{\Gamma^+_{lf}}{R^+} = (1-e)(1-x)\frac{Gd_{in}}{4\mu_l}. \tag{121}$$

Their model was tested for independent data from 8 works and proved accurate for the work of Mastrullo *et al.* (2018) too.

Fang, Wu and Yuan (2017) from a database of 17,778 data points for saturated flow boiling with 13 fluids developed a generalized correlation for the heat transfer coefficient. Their model was then validated with 6,664 data points independent from the first database. They investigated the dimensionless groups from 45 existing correlations and found that 13 dimensionless numbers appeared frequently. From that, they proposed their correlation as follows:

$$\mathrm{Nu}_{tp} = h_{tp}\frac{d_{in}}{\kappa_l} = F_f\, M^{-0.18}\mathrm{Bo}^{0.98}\mathrm{Fr}_{lo}^{\,0.48}\mathrm{Bd}^{0.72}\left(\frac{\rho_l}{\rho_v}\right)^{0.29}\left[\ln\left(\frac{\mu_{lf}}{\mu_{lw}}\right)\right]^{-1} Y, \tag{122}$$

where F_f is a fluid-dependent parameter, μ_{lf} is the viscosity of the liquid at the fluid temperature, μ_{lw} is the viscosity of the liquid at the wall temperature, and Y is a parameter dependent on the reduced pressure as follows:

$$Y = \begin{cases} 1 & \text{for } p_r \leq 0.43 \\ 1.38 - {p_r}^{1.15} & \text{for } p_r > 0.43 \end{cases} . \tag{123}$$

The authors even suggest that the model can be applied to rectangular channels with three-sided wall heating, correcting for the effective heat transfer area. They highlight that the model depends on the wall temperature, and its accuracy can deteriorate because of its uncertainty. Due to the fluid-dependent parameter, the model accuracy can also deviate if a non-appropriate value is used.

Wang *et al.* (2019) while comparing their experimental data with correlations, found that all of them underpredicted the HTC. They stated that the non-uniform heating favors the activation of nucleation sites, increasing the nucleate boiling heat transfer, and therefore proposed a new correlation based on the superposition model of Gungor and Winterton (1986). The authors kept the enhancement factor from Gungor and Winterton's model and proposed a new way of calculating the suppression factor as follows:

$$S = \left(1.027 + 5.85 \times 10^{-8}\ F^{1.54}\mathrm{Re}_l{}^{1.382}\right)^{-3.75} . \tag{124}$$

Their model has been tested for two independent works (KUBO *et al.*, 2022; AGUSTIARINI *et al.*, 2023) and did not show good accuracy for both, though it is the only one built on non-uniform heating data.

As can be seen, there are numerous models available in the literature to do the same job. Many researchers tried to propose generalized correlations, though it seems impossible to wrap every flow condition into one universal representation. Recently, there was a trend to build models from machine learning based on huge databases. However, most of them are complex to implement and physically weak, which, as Cooper would say, "It is not attractive to the practical man".

2.5.1 Dimensionless groups for two-phase HTC analysis

As could be noted, the pursuit of a generalized model that can predict the HTC or the pressure drop gradient has been the object of study for many years. Unlike the single-phase flow, which has several well-established correlations and prediction methods, the two-phase flow physics is complex, and research is still under development. Scaling is one of the techniques to understand which mechanisms are dominant over the two-phase flow.

On scaling, the Pi of Buckingham approach is most used to account for the dimensionless groups that describe certain phenomena. Delil (2003), from similarity considerations, identify

18 π-numbers which are relevant for the thermal gravitational pumped two-phase systems. The author states that the numbers are not always relevant for every part of the system, and identifying the combination of them that better suits the problem at hand is the best approach for scaling.

Picanço, Passos and Bandarra Filho (2009) also used that technique to identify the main dimensionless numbers to build their HTC correlation for convective boiling in smooth and microfin short tubes. The authors found over ten dimensionless groups from 22 parameter combinations. However, many of them do not give an explicit interpretation, and the authors kept with the classical ones, such as the Reynolds number, Prandtl number, and slip ratio.

From the approach on two-phase flow scaling by Dorao, Drewes and Fernandino (2018), Paul, Fernandino and Dorao (2021) in their search to simplify HTC prediction for two-phase flow, found that the enhancement factors can somehow be correlated with the vapor Reynolds number. They showed that many correlations, like Chen (1966), Gungor and Winterton (1986), and Kandlikar (1990), enhancement factors are actually dependent on the vapor Reynolds number. The authors stated that, instead of looking for new dimensionless numbers, identifying the dominant ones reduces the complexity of the correlations, making them easier to apply. Then, they propose the HTC to be dependent only on the two-phase Reynolds number $\mathrm{Re}_{2\phi} = \mathrm{Re}_l + \mathrm{Re}_v$, and the two-phase Prandtl number $\mathrm{Pr}_{2\phi} = (1 - x)\,\mathrm{Pr}_l + x\,\mathrm{Pr}_{2\phi}$.

Lin *et al.* (2022), while building their general correlation for HTC correlation of flow boiling in microfin tubes, split the heat transfer mechanisms into three groups: nucleate boiling, forced convection, and surface tension effects. They evaluated several HTC correlations related to those groups and devised a set of dimensionless numbers that better represented each of them. For nucleate boiling, the authors selected the Boiling number, reduced pressure, and molecular weight. The liquid Reynolds number, liquid Prandtl number, Lockhart-Martinelli parameter, Convection number, and the ratios of the liquid-vapor density, viscosity, and quality were selected for the forced convection mechanism. The liquid Weber number and Bond number represented the surface tension effects. The authors went through several machine learning simulations to determine the best dimensionless groups between the selected ones to build their power law correlation. They found that the Boiling number, reduced pressure, molecular weight, liquid Reynolds number, liquid Prandtl number, Convection number, and Bond number were the optimal dimensionless group to derive the HTC.

Table 13 lists the compilation of the dimensionless numbers from the correlations. The Froude, Reynolds, and Weber numbers are presented in two ways: liquid/vapor and liquid/vapor only. Some authors do not distinguish the nomenclature, thus generating confusion about which form of calculating the specific number they proposed for their correlation. Therefore, for this work, the notation with $_l$ or $_v$ subscript considers the superficial velocity of liquid and vapor, respectively, and the $_{lo}$ or $_{vo}$ represents the velocity as if only liquid or vapor was flowing, respectively.

Table 13 – List of the homogeneous models and the equation for calculating the two-phase flow viscosity.

Dimensionless numbers	Equation	
Bond number	$\mathrm{Bd} = \frac{g\left(\rho_l - \rho_v\right)\,{d_{in}}^2}{\sigma}$	(125)
Boiling number	$\mathrm{Bo} = \frac{q''}{G\,h_{lv}}$	(126)
Convection number	$\mathrm{Co} = \left(\frac{1-x}{x}\right)^{0.8}\left(\frac{\rho_v}{\rho_l}\right)^{0.5}$	(127)
Liquid Froude number	$\mathrm{Fr}_l = \frac{G^2\left(1-x\right)^2}{{\rho_l}^2 g\,d_{in}}$	(128)
Vapor Froude number	$\mathrm{Fr}_v = \frac{G^2 x^2}{{\rho_v}^2 g\,d_{in}}$	(129)
Liquid only Froude number	$\mathrm{Fr}_{lo} = \frac{G^2}{{\rho_l}^2 g\,d_{in}}$	(130)
Vapor only Froude number	$\mathrm{Fr}_{vo} = \frac{G^2}{{\rho_v}^2 g\,d_{in}}$	(131)
Reduced pressure	$p_r = p/p_{crit}$	(132)
Liquid Prandtl number	$\mathrm{Pr}_l = \nu_l/\alpha_l$	(133)
Vapor Prandtl number	$\mathrm{Pr}_v = \nu_v/\alpha_v$	(134)
Liquid Reynolds number	$\mathrm{Re}_l = \frac{G\left(1-x\right)d_{in}}{\mu_l}$	(135)
Vapor Reynolds number	$\mathrm{Re}_v = \frac{Gxd_{in}}{\mu_v}$	(136)
Liquid only Reynolds number	$\mathrm{Re}_{lo} = \frac{G\,d_{in}}{\mu_l}$	(137)
Vapor only Reynolds number	$\mathrm{Re}_{vo} = \frac{G\,d_{in}}{\mu_v}$	(138)
Liquid Weber number	$\mathrm{We}_l = \frac{G^2\left(1-x\right)^2 d_{in}}{\rho_l\sigma}$	(139)
Vapor Weber number	$\mathrm{We}_v = \frac{G^2x^2d_{in}}{\rho_v\sigma}$	(140)
Liquid only Weber number	$\mathrm{We}_{lo} = \frac{G^2d_{in}}{\rho_l\sigma}$	(141)
Vapor only Weber number	$\mathrm{We}_{vo} = \frac{G^2d_{in}}{\rho_v\sigma}$	(142)
Lockhart-Martinelli Param.	$X_{tt} = \left(\frac{1-x}{x}\right)^{0.9}\left(\frac{\rho_v}{\rho_l}\right)^{0.5}\left(\frac{\mu_l}{\mu_v}\right)^{0.1}$	(143)

Source: Author.

Table 14 lists the compilation of the alternative and unusual ways of writing the dimensionless numbers from the correlations. These dimensionless numbers were taken from the works of Klimenko (1990), Wattelet *et al.* (1993), Wojtan, Ursenbacher and Thome (2005a), Cioncolini and Thome (2011), and Paul, Fernandino and Dorao (2021). Klimenko (1990) built his correlation based on modified Reynolds and Peclet numbers, as well as the Laplace constant and two other dimensionless parameters (K_κ and K_p). Wattelet *et al.* (1993) proposed a modified Lockhart-Martinelli parameter by translating the viscosity and density ratios into the reduced pressure. Wojtan, Ursenbacher and Thome (2005a) used the Groeneveld factor, the liquid film Reynolds number, and the homogeneous Reynolds number to account for the HTC. Cioncolini and Thome (2011) introduced the dimensionless liquid film thickness and stated it can also be interpreted as the liquid film Reynolds number. As mentioned, Paul, Fernandino and Dorao (2021) suggested the two-phase Reynolds number and Prandtl number to correlate with the two-phase Nusselt number. The others cited research had their dimensionless numbers written as shown in Table 13 according to how they are shown in the correlations.

Table 14 – List of the homogeneous models and the equation for calculating the two-phase flow viscosity.

Authors	Equation	
Relative thermal conductivity (KLIMENKO, 1990)	$K_\kappa = \dfrac{\kappa_w}{\kappa_l}$	(144)
Pressure dimensionless param. (KLIMENKO, 1990)	$K_p = \dfrac{p\,\mathrm{La}}{\sigma}$	(145)
Modified Peclet number (KLIMENKO, 1990)	$\mathrm{Pe}_* = \dfrac{q''\mathrm{La}}{h_{lv}\rho_v\alpha_l}$	(146)
Laplace constant (KLIMENKO, 1990)	$\mathrm{La} = \left[\dfrac{\sigma}{g\left(\rho_l - \rho_v\right)}\right]^{0.5}$	(147)
Mixture Reynolds number (KLIMENKO, 1990)	$\mathrm{Re}_m = \dfrac{W_m b}{\nu_l}$	(148)
Modified Lockhart-Martineli param. (WATTELET *et al.*, 1993)	$X'_{tt} = 0.551\, {p_r}^{0.492} \left(\dfrac{1-x}{x}\right)^{0.9}$	(149)
Liquid film Reynolds number (WOJTAN; URSENBACHER; THOME, 2005a)	$\mathrm{Re}_\delta = \dfrac{4G\delta\left(1-x\right)}{\mu_l\left(1-\alpha\right)}$	(150)
Homogeneous Reynolds number (WOJTAN; URSENBACHER; THOME, 2005a)	$\mathrm{Re}_H = \dfrac{Gd_{in}}{\mu_v}\left[x + \dfrac{\rho_v}{\rho_l}\left(1-x\right)\right]$	(151)
Groeneveld factor (WOJTAN; URSENBACHER; THOME, 2005a)	$Y = 1 - 0.1\left[\left(\dfrac{\rho_l}{\rho_v} - 1\right)\left(1-x\right)\right]$	(152)
Liquid film Reynolds number (CIONCOLINI; THOME, 2011)	$t^+ = \max\left\{\begin{matrix}\sqrt{2\left[\left(1-e\right)\left(1-x\right)\dfrac{Gd_{in}}{4\mu_l}\right]}; \\ 0.066\left(1-e\right)\left(1-x\right)\dfrac{Gd_{in}}{4\mu_l}\end{matrix}\right\}$	(153)
Two-phase Reynolds number (PAUL; FERNANDINO; DORAO, 2021)	$\mathrm{Re}_{tp} = \mathrm{Re}_l + \mathrm{Re}_v$	(154)
Two-phase Prandtl number Paul, Fernandino and Dorao (2021)	$\mathrm{Pr}_{tp} = \left(1-x\right)\mathrm{Pr}_l + x\,\mathrm{Pr}_{2\phi}$	(155)

Source: Author.

Apart from the dimensionless numbers, liquid/vapor property ratios such as viscosity and density are usually incorporated into the correlations. Fang, Wu and Yuan (2017) included the ratio between the liquid viscosity at saturation temperature and the liquid viscosity at the wall temperature to their correlation. This is similar to the laminar single-phase flow approach for calculating the HTC when the wall temperature is higher than the bulk temperature of the fluid.

2.6 Summary

The chapter showed the particularities of circumferential non-uniform heating works and how each assessed the HTC. It also discussed the ONB criteria and how it changes for well-wetting fluids, not to mention the transient behavior of flow parameters when nucleate boiling initiates and the techniques for its identification. There are many correlations available in the literature for predicting the pressure drop and heat transfer coefficient, though only one assesses the effects of circumferential non-uniform heating. In terms of pressure drop, Dirker, Scheepers and Meyer (2022) showed that the circumferential non-uniform heating does not influence it. For the heat transfer, on the other hand, Wang *et al.* (2019) and Dirker, Scheepers and Meyer (2022) disagreed, whereas the first showed improvement on the HTC when heating from the bottom, the latter presented lower HTC. This literature review allowed designing and gave insights on the analysis for better comprehending the effects of circumferential non-uniform heating on horizontal flow boiling.

3 Materials and methods

This chapter describes the materials and methods used to achieve the research objectives. First, it presents the experimental apparatus, where the working fluid, equipment, measuring technique, and experiment features are described. Then, it describes the experimental procedure and heat loss analysis. Next, the statistical approach to deal with the uncertainties is highlighted. Finally, the test rig validation method is presented. A chapter summary resumes the main points.

3.1 Experimental apparatus

Figure 8 illustrates a schematic drawing of the experimental facility that emulates flow boiling with uniform or non-uniform circumferential heating. The thicker lines denote the tube with an inner diameter of 10.92 mm, while the thinner ones of 4.57 mm.

Figure 8 – Experimental facility schematic for flow boiling with non-uniform circumferential heating tests.

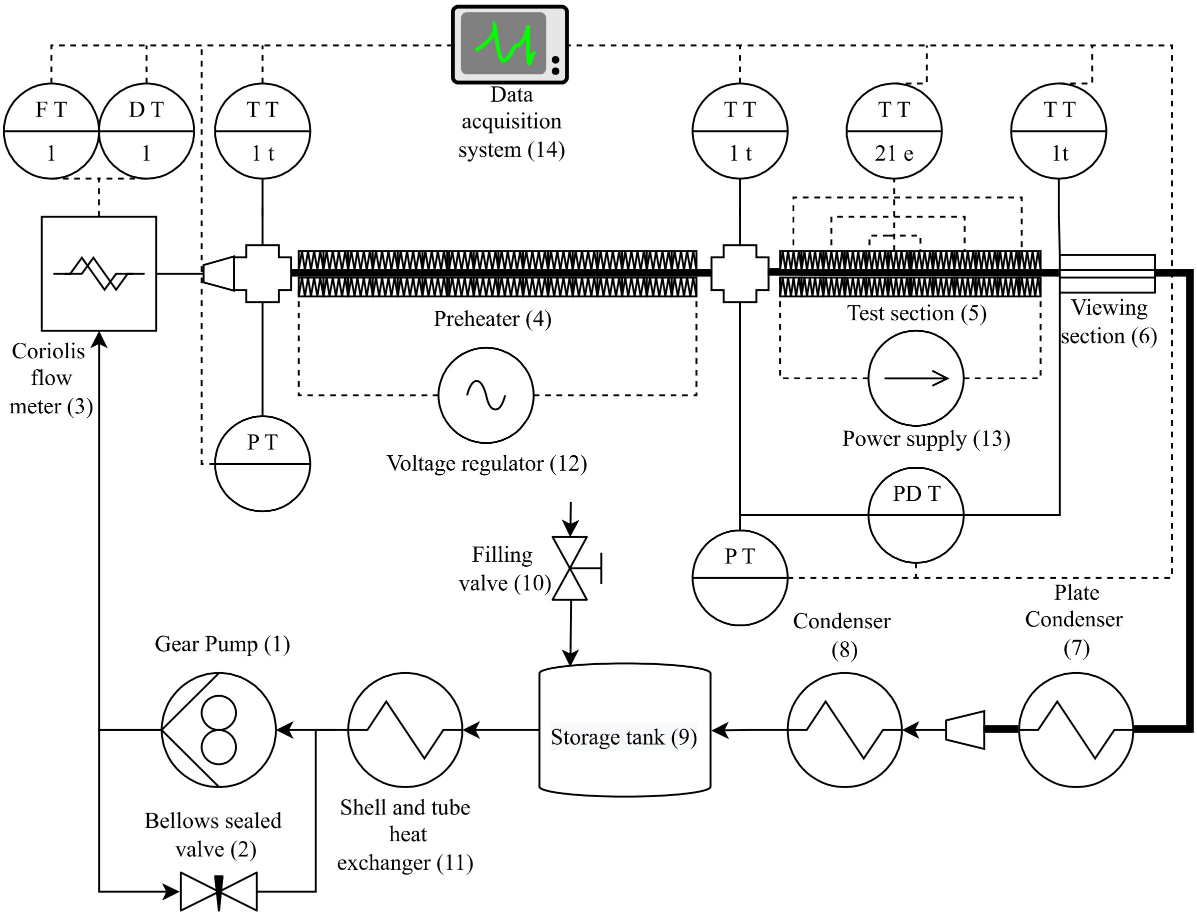

Source: Author.

The hydraulic circuit starts at the pump, which pumps the fluid through the Coriolis flowmeter. Subcooled liquid enters the preheater, where heat is supplied by four nickel-chrome electrical resistance strips, two on the bottom and two on top of the tube length. This setting allows testing both uniform and non-uniform heating. The preheater is approximately 4 m long with an inner diameter of 10.92 mm and mainly controls the vapor quality at the test section inlet.

A T-type thermocouple probe and two pressure transmitters (differential and absolute) are coupled at the test section inlet. The 0.50 m test section is made of stainless steel (SS-AISI 316) and has four nickel-chrome resistance strips arranged the same way as on the preheater. A T-type thermocouple probe and the other differential pressure transmitter socket are at the test section outlet. As for the preheater, both heating conditions can be set in the test section.

A viewing section is attached immediately after the test section. Although adiabatic, this section allows viewing the flow patterns immediately after leaving the test section. It is assumed that the patterns are the same as the ones inside the heating section. From the viewing section, the fluid flows into the condensers.

Due to the high cooling power required, two heat exchangers in series are used to condense the fluid. The first is a plate heat exchanger, and the second is a simple shell and tube. The first condenses most of the fluid, while the second ensures the temperature is below saturation before going to the storage tank. From the storage tank, the fluid passes through a second shell and tube heat exchanger, which sets the temperature in the preheater and guarantees that only liquid goes into the pump. A pump bypass with a bellows sealed valve controls the system mass flow rate, allowing fine control of the mass velocities when boiling starts.

3.1.1 Working fluid

Water as the working fluid for convective boiling experiments requires high power, mainly due to its high latent heat of vaporization. Moreover, because of its high saturation temperature at atmospheric pressure ($\approx$100 °C), the system would require robust insulation and appropriate equipment for this condition. Working with pressures below 1 atm also brings complexities to the experiment. Therefore, using R141b (1,1-dichloro-1-fluoro ethane) is appropriate for the study. Its saturation temperature at 1.8 bar (49.5 °C) is closer to the room temperature, reducing thermal losses. Besides, its latent heat of vaporization (214.6 kJ kg^{-1}) is ten times smaller than water's (2211 kJ kg^{-1}), which requires lower heat rates to evaporate all of the fluid. In addition, its thermophysical properties are accessible by REFPROP, EES, and CoolProp libraries, which allow performing calculations and analysis with the experimental data.

3.1.2 Equipment

Table 15 lists the equipment used on the test rig and their features.

A direct current electric motor drives the positive displacement magnetically driven gear pump. The motor is attached to an adjustable speed DC controller, which allows controlling the

Table 15 – Equipment and instrumentation for the convective boiling experimental test rig.

	Equipment	Brand/Model	Features
1	Magnetically driven gear pump	Tuthill/TXS080	0-3800 RPM 0-568 kg m^{-2}s^{-1}
2	Bellows sealed valve	Swagelok/SS-4BK	
3	Coriolis flowmeter	Siemens/ SITRANS F C MASS 2100 DI 3	0-2900 kg m^{-3} 0-240 kg h^{-1} 0-741 kg m^{-2}s^{-1}
4	Preheater	⌀10.92 mm	AC voltage regulator
5	Test section	⌀10.92 mm	DC power supply
6	Viewing section	Borosilicate glass	
7	Plate condenser	40 plate	Water coolant
8	Condenser	Shell and tube	Water coolant
9	Storage tank	Stainless steel	
10	Globe valve		
11	Heat exchanger	Shell and tube	Water coolant
12	Voltage regulator	JNG/TDGC2-10	0-250 Vac/0-40 Aac
13	Power supply	Keysight/N8733A	0-15 Vdc/0-220 Adc
14	Data aquisition system	Agilent/34972A Multiplexer/34901A	44 channels

Source: Author.

pump rotation, thus, the flow rate. The pump model is the TXS080 and gives mass velocities up to 568 kg/(m^{2}s) with R141b and an inner diameter of 10.92 mm. The maximum differential pressure is 17.2 bar.

The Coriolis flowmeter measures flow rates up to 250 kg/h, which yields mass velocities up to 741 kg/(m^{2}s). In addition to the flow rate, the device measures temperature and fluid density up to 2900 kg/m^3. The transmitter can give two outputs, one analog output (4-20 mA) and one digital output (0-10 kHz). The flow rate is measured by the current signal, while the density by the frequency signal.

Figure 9 shows the preheater with thermal insulation. According to Lima and Thome (2012) and Lima and Thome (2013), the effects of pipe curves on pressure drop and flow patterns are lower than 10% for distances greater than $150d$ from it. Therefore, it would require a 1.6 m long straight section upstream of the test section to mitigate these effects. Thus, the preheater is a 4 m straight section. An absolute pressure transmitter (WARME/WTP-4010), with a 4-20 mA output signal for a 0-3 bar range, and a T-type thermocouple probe allow for determining the thermodynamic state at the preheater inlet. As stated in section 3.1, heat is provided by four nickel chrome resistance electrically isolated with Kapton® tape. The AC voltage regulator can dissipate up to 10 kW (250 V and 40 A) to the preheater, although the maximum power required is 4.7 kW. The preheater ensures the desired experimental conditions in the test section, especially the inlet vapor quality.

Figure 9 – Second preheater with insulation layer.

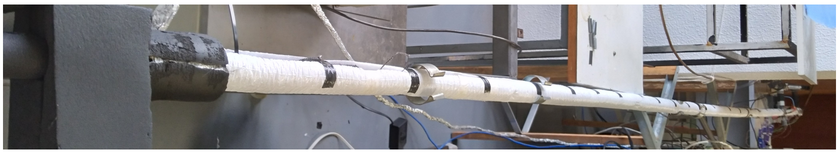

Source: Author.

Figure 10 shows the test section with the thermocouple wires with and without the insulation layer. The test section is a 0.5 m long stainless steel tube with an inner diameter of 10.92 mm and four nickel-chrome resistance along it. The resistances are electrically insulated with Kapton® tape. A layer of fiberglass tape presses the resistance strips against the tube, ensuring their contact with its surface and assuring proper insulation. On top of that, there is also a layer with insulation material. Two DC power suppliers provide power to the test section. They are connected in series to match the current and voltage levels to disperse the highest heat for the given resistance. The power suppliers, model Keysight N8733A, can give up to 3.3 kW each, which gives 6.6 kW when set in series.

Figure 10 – Test section with thermocouple wires and insulation layer.

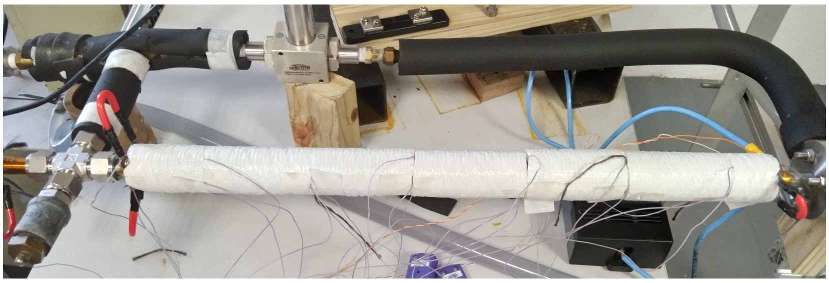

(a) Test section with insulation

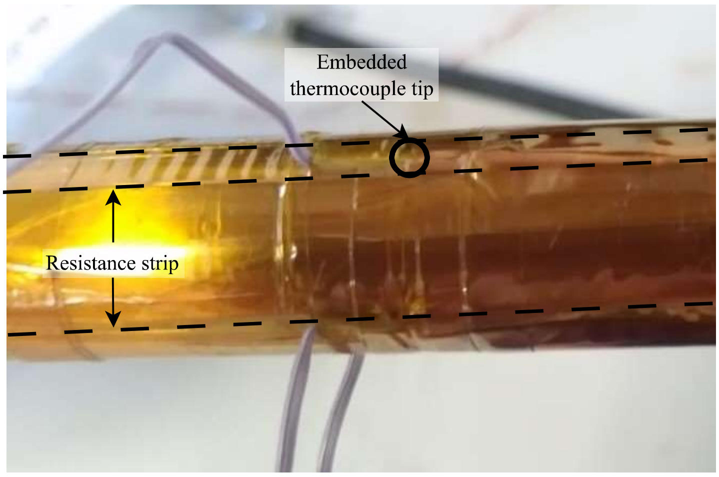

(b) Thermocouple positioning without thermal insulation

Source: Author.

Figure 11 illustrates the seven wall temperature measurement sections and distribution of the thermocouples through the tube cross-section. The first measuring section is 10 mm (δ_l) from where the heating starts. The sections are placed 80 mm (Δ_l) from each other, and the last one is 10 mm from where the heating ends. Each section has three E-type thermocouples installed, one on top, one on the bottom, and one on the right. This thermocouple distribution gives the difference between the top and bottom temperatures, which helps to identify the dry-out inception. Additionally, it allows a more accurate assessment of the local heat transfer coefficient by evaluating the temperatures along the tube perimeter. The thermocouple tips were soldered into the tube wall, ensuring proper measurement right where it is positioned. A deeper discussion is provided at subsection 3.1.4.

Figure 11 – Thermocouple measurement sections along the tube (a) and distribution along tube cross-section (b).

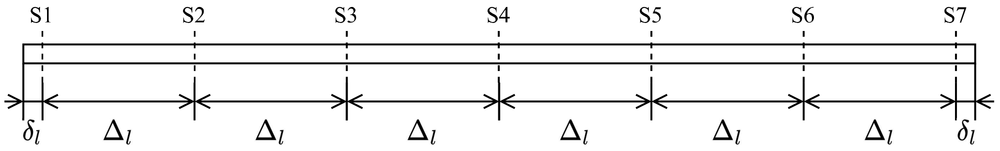

(a) Measurement sections

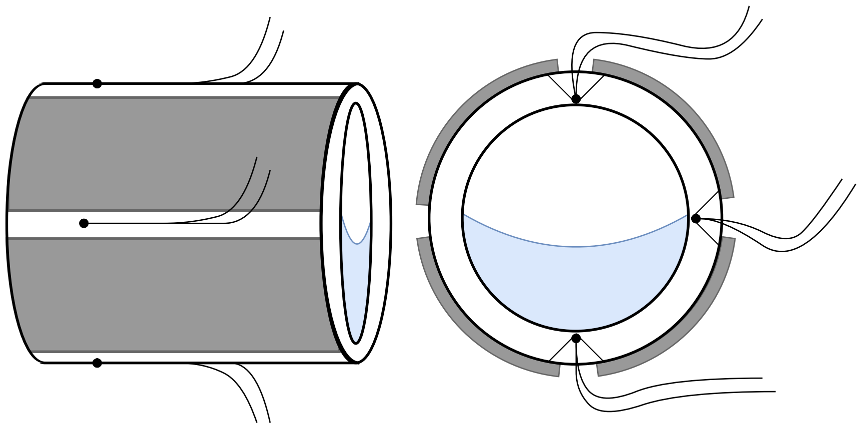

(b) Cross-section distribution

Source: Author.

A WARME/WTP-4010 pressure transmitter that ranges from 0-3 bar measures the absolute pressure at the test section inlet. While a Zürich/PSI.EX.H.DIF transmitter, with a range from 0-0.30 bar, measures the differential pressure on the test section. In addition, two T-type thermocouple probes are placed in direct contact with the fluid, one at the inlet and another at the outlet of the test section.

Figure 12 shows the viewing section in place. The viewing section developed by Cassol (2017) consists of a 0.1 m long borosilicate glass tube with a diameter equal to the test section. This tube is mounted into two pieces of stainless steel, which are connected to the hydraulic circuit through flanges. Two gaskets seal the glass tube and the stainless steel frame. Four threaded rods and nuts assemble all the pieces with the flanges. According to Cassol (2017), the maximum working pressure is 18 bar without thermal loads, which is higher than the working pressure (up to 3 bar).

Figure 13 illustrates the camera set-up to record the flow patterns. A high-speed camera PCO.1200hs records full-HD videos of the flow patterns at over 35,000 fps. A Nikon Carl Zeiss

Figure 12 – Viewing section.

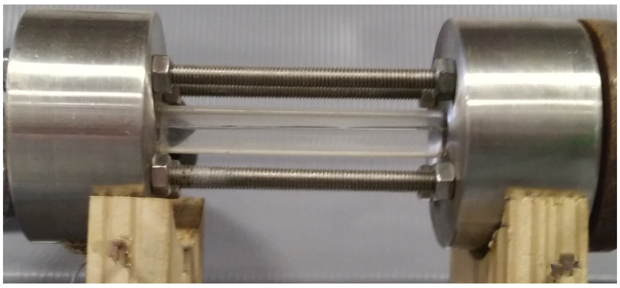

Source: Author.

lens is attached to the camera, and a high-intensity backlight is used to get high-contrast images. There is a light diffuser sheet between the backlights and the viewing section. Although the tube curvature distorts the images (lens effect), the patterns are easily identified.

Figure 13 – Camera set-up.

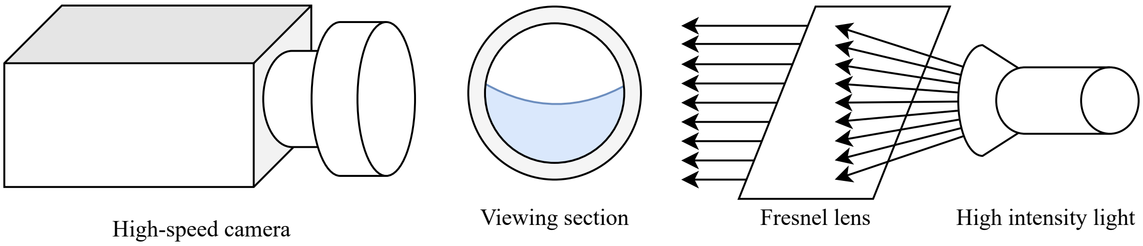

Source: Author.

The plate condenser configuration works in countercurrent flow for max heat transfer. A cooling bath, with water as the coolant, cools down the R141b until it reaches the subcooled liquid state. When the plate condenser can condense the fluid, the second condenser works as a temperature control for the fluid entering the storage tank. If the plate condenser cannot cool down the whole fluid, the second condenser ensures the fluid is in the subcooled liquid state.

The storage tank is a stainless steel vessel with one bottom outlet, which goes directly to the heat exchanger, and two inlets, one from the condenser and the other to fill the test rig. It also has a level indicator for liquid-level visualization. From the storage tank, the liquid flows to the preheater upstream of the pump. A cooling bath pushes water into the heat exchanger, which exchanges heat with the copper coil. The cooling bath allows controlling the water temperature and thus setting the fluid temperature that goes into the pump and thus to the preheater.

The Agilent 34972A data logger with two 34901A modules collect and store the data from the sensors. The modules have 20 channel multiplexers and two direct current channels each, which allows measuring up to 44 sensors. The data logger is connected to a computer through a USB cable. A free license software Agilent Benchlink Data Logger 3 manages data, provides real-time monitoring through graphics, and collects the data into a CSV file for further analysis.

3.1.3 Measuring techniques

Table 16 lists the measuring devices used to get data for the analysis. The Coriolis flowmeter measures the mass flow rate in kg h^{-1} and the density in kg m^{-3}. The current analog output gives a proportional signal for the mass flow rate ranging from 0 to 100 kg h^{-1}. The digital output (0-10 kHz) gives the fluid density in the range of 0-2900 kg m^{-3}. The pressure transmitters give an analog current signal (4-20 mA) proportional to 0-3 kPa (absolute) and 0-0.30 kPa (differential). The thermocouples produce a direct current voltage on the millivolt scale and were calibrated from 5 to 95 °C.

Table 16 – Measuring devices and their output signal and range.

Equipment	Brand/Model	Output signal	Range
Coriolis flowmeter	Siemens SITRANS F C MASS 2100 DI 3	4-20 mA 0-10 kHz	0-100 kg h^{-1} 0-2,900 kg m^{-3}
Differential pressure transmitter	Zürich/PSI.EX.H.DIF	4-20 mA	0-30 kPa
Absolute pressure transmitters	Warme/WTP-4010	4-20 mA	0-300 kPa
T-type thermocouple probe	Omega/⌀0.60 mm	Vdc	5-95 °C
E-type thermocouple wire	Omega/AWG-30 (⌀0.2546 mm)	Vdc	5-95 °C
Preheater shunt resistor	FL-2	0-75 mV	0-50 A
Test section shunt resistor	FL-2	0-75 mV	0-20 A
High speed camera	PCO/1200hs	10-bit	0-35,000 fps
Lens	Nikon/Carl Zeiss		
Light	Ovido		

Source: Author.

Figure 14 illustrates the thermocouple arrangement for measuring the temperatures at the test rig. The thermocouples signal are proportional to the difference in temperature between the measuring and the isothermal junction. The ice-measuring thermocouple gives the signal proportional to the temperature difference between the ice bath and the isothermal junction. As long as the isothermal junction is insulated, the measuring and the ice thermocouples signals are on the same reference. Then, the subtraction of the measuring thermocouples and the ice bath signals is proportional to the difference in temperature between them. Besides the test rig thermocouples, there are two in the ice bath as references and one measuring the room temperature.

Figure 14 – Thermocouple measurement schematics.

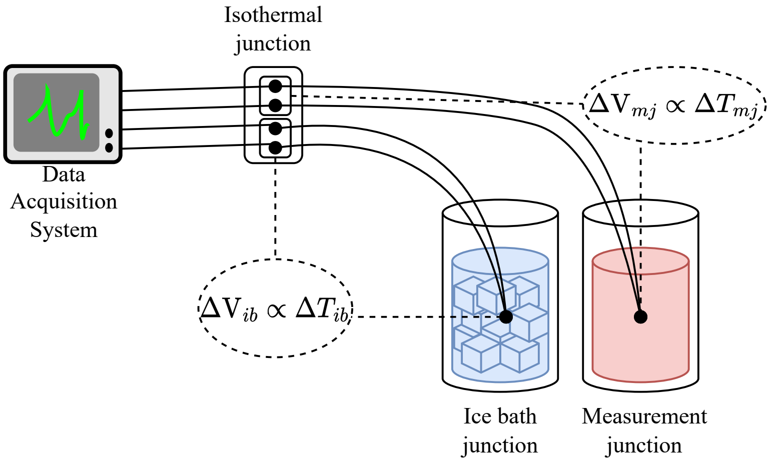

Source: Author.

Two shunt resistors, one for the preheater and one for the test section, are used to measure the current flowing through the resistances. Those shunts are calibrated to give 75 mV for the nominal value, 50 A to the preheater, and 20 A to the test section, with a precision of 0.5% of full scale. The voltage measurements at each resistance terminal, and the current measured through the shunt resistors, give the dissipated power at the preheater and the test section. Figure 15 illustrates the electrical circuit to measure the voltage drop in the resistance and in the shunt resistor.

Figure 15 – Eletrical circuit to measure the current and voltage drop in the preheater and in test section.

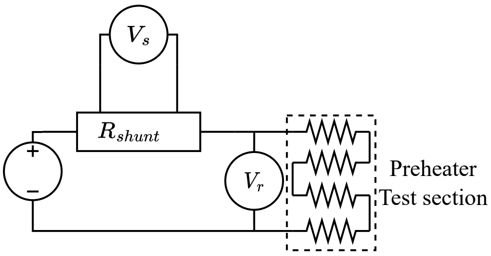

Source: Author.

3.1.4 Experimental features

The experimental features discuss the indirect measures from the sensors. First, it is presented power-related features such as heat rates and heat fluxes. Then, the temperature-related features (bulk and wall temperature) are discussed. The calculation of two-phase flow features such as subcooled level, mass velocity, and vapor quality are shown. Last, the local, sectional, and mean heat transfer coefficient and pressure drop gradient calculation are discussed.

- **Heat rate and heat flux**

The heat rates dissipated on the preheater and test section are calculated from the voltage drop in the resistances and the shunts. The product of the voltage times current gives the power dissipated at each section. The following equation gives the heat rate:

$$\dot{q} = \frac{V_r\, V_s}{R_s}, \tag{156}$$

where $\dot{q}$ is the heat rate dissipated through the resistances, V_r is the voltage drop in the resistance, V_s is the voltage drop in the shunt resistor, and R_s is the shunt resistance given by the ratio 75 mV/50 A for the preheater and 75 mV/20 A for the test section. The heat flux, q'', is given by the heat rate divided by the heated area, A_h, as follows:

$$q'' = \frac{\dot{q}}{A_h}, \tag{157}$$

where the heated area depends on the heating setup.

- **Bulk temperature**

For the single-phase experiments, since the heating is provided uniformly over the tube length, the bulk temperature at each measurement section is calculated by,

$$T_B(z) = T_{in} + \frac{\dot{q}_{ts}\Gamma}{\dot{m}c_p} z, \tag{158}$$

where $T_B(z)$ is the bulk temperature at z, T_{in} is the test section inlet temperature, $\dot{q}_{ts}$ is the heat rate on the test section, Γ is the heated perimeter, $\dot{m}$ is the mass flow rate, c_p is the fluid specific heat at constant pressure, and z is the tube length.

In the case of the two-phase flow, the bulk temperature along the test section is considered to be the saturation temperature at each cross-section. Since the pressure drops throughout the tube, the saturation temperature at each measuring section is given by the local pressure, considering that the two phases are in thermodynamic equilibrium. The local pressure is calculated from the inlet pressure, p_{ts} corrected by the pressure drop gradient, $\mathrm{d}p/\mathrm{d}z$, multiplied by the position z of each section, as described by:

$$p_{sat}\left(z\right) = p_{ts} - z\frac{\mathrm{d}p}{\mathrm{d}z}. \tag{159}$$

Since the differential pressure transmitter has not worked properly for single-phase and low vapor quality flows, the Friedel model and the Axelsson and Rouhani void fraction model were used to predict the pressure drop gradient over the test section. Those two models show the best agreement according to several researchers and thus were chosen for predicting the pressure drop (WOJTAN; URSENBACHER; THOME, 2005b). Then, the bulk temperature for the two-phase flow is given by:

$$T_B\left(z\right) = T_{sat}\left[p_{sat}\left(z\right)\right]. \tag{160}$$

- **Wall temperature**

Since the heating setup does not cover the entire tube circumference, a 1-D heat transfer modeling is not appropriate to infer the inner wall temperature. Then the thermocouple tips were placed into the tube wall close to the inner tube surface. To do so, a bench drilling machine with a 5 mm diameter drill bit drilled 0.6 mm through the tube wall (0.89 mm). A drilling template guaranteed the same depth for every measuring point.

Figure 16 shows three test cross-sections made on a sample tube. The wall thickness was measured with a caliper with 0.02 mm resolution, and the measurements are 0.28, 0.30, and 0.32 mm, respectively. A tin layer is brazed on top of the thermocouple tips allowing the heat to flow through the wall. The thermal resistance between the thermocouple tip and the tube inner wall, considering a thickness of 0.35 mm, is 7.15×10^{-4} K W^{-1}. For heat flux of 1,000 W m^{-2}, three times lower than the actual lower value used for this work, the temperature difference between the thermocouple tip and the inner wall is 0.012 K, which lower than the thermocouple calibration expanded uncertainty ($\approx$ 0.2 K). Therefore, the wall temperature was considered the same as the measured by the thermocouples.

Figure 16 – Three cross section samples for the thermocouple placement into the tube wall.

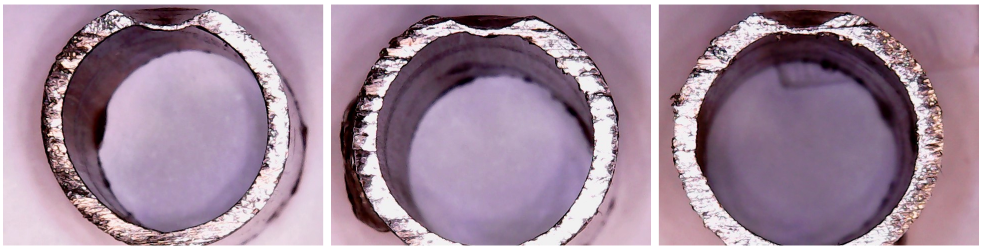

Source: Author.

- **Subcooled level**

The subcooled level is given by the difference between the saturation temperature given the pressure $T_{sat}\left(p_{in;ph}\right)$ and the temperature at the preheater inlet $T_{in;ph}$, given by:

$$\Delta T_{sub} = T_{sat}\left(p_{in;ph}\right) - T_{in;ph}. \tag{161}$$

- **Mass velocity**

The mass velocity is calculated by:

$$G = \frac{\dot{m}}{A_{cs}}, \tag{162}$$

where $\dot{m}$ is the mass flow rate, and A_{cs} is the cross section area given by:

$$A_{cs} = \pi \frac{{d_{in}}^2}{4}, \tag{163}$$

where d_{in} is the inner diameter of the tube.

- **Preheater inlet quality**

The preheater inlet quality is calculated as follows:

$$x_{ph} = \frac{h_{ph} - h_l}{h_{lv}}, \tag{164}$$

where h_l and h_{lv} are the liquid and the latent heat of vaporization for the saturation pressure at the preheater inlet, respectively, and h_{ph} is the enthalpy at the test section entrance, which is given by:

$$h_{ph} = f\left(T_{ph};p_{ph}\right), \tag{165}$$

where T_{ph} and p_{ph} are the temperature and pressure at the preheater inlet, respectively.

- **Test section inlet quality**

The test section inlet quality is given by:

$$x_{in} = \frac{h_{in} - h_l}{h_{lv}}, \tag{166}$$

where h_l and h_{lv} are the liquid and the latent heat of vaporization for the saturation pressure at the test section inlet, respectively, and h_{in} is the enthalpy at the test section entrance, which is given by:

$$h_{in} = h_{ph} + \frac{\dot{q}_{ph}}{\dot{m}}, \tag{167}$$

where h_{ph} is given by Equation 165, and $\dot{q}_{ph}$ is the heat rate at the preheater.

- **Test section outlet quality**

Similarly, the test section outlet quality is given by:

$$x_{out} = \frac{h_{out} - h_l}{h_{lv}}, \tag{168}$$

where h_{out} is the enthalpy at the test section outlet, given by:

$$h_{out} = h_{in} + \frac{\dot{q}_{ts}}{\dot{m}}, \tag{169}$$

where h_{in} is given by Equation 167, and $\dot{q}_{ts}$ is the power dissipated at the test section.

- **Local heat transfer coefficient**

The local heat transfer coefficient at each measuring point (top, side, and bottom) for each section is given by:

$$h_i\left(z\right) = \frac{q''_{ts}}{T_i\left(z\right) - T_B\left(z\right)}, \tag{170}$$

where q''_{TS} is the heat flux at the test section, $T_b(z)$ is the bulk temperature at the position z, and $T_i(z)$ is the wall temperature, for i being t, l, or b, meaning top, side, and bottom, respectively. This approach would suit uniform heating along the tube perimeter, which is not the case. Since the heat flux is applied on the outer surface and the temperature measurement is on the inner wall, the heat going to the fluid through the thermocouple position is not the same as the exterior wall. Therefore, the inner heat flux depends on the heat transfer intensity inside the tube. Then, a weighted value multiplying the heat flux accounts for the distortion in its value caused by the heating method. The Equation 170 can be rewritten as:

$$h_i(z) = \frac{w_i(z)\ q''_{ts}}{T_i(z) - T_B(z)}. \tag{171}$$

A steady state FEM analysis was carried out, using the Partial Differential Equation Toolbox from Matlab software (MATHWORKS, 2019), to comprehend the heat diffusion through the tube wall. The tube cross-section geometry was built within Matlab, and the material thermal conductivity set to 14.6 W m^{-1} K^{-1}, as it is a stainless steel (SS-AISI 316) tube. The geometry has four segments on the outer diameter for applying heat flux boundary conditions. The heated perimeter is the same size as the heating strips from the actual setup. The boundary condition inside the tube is set as convective heat transfer, which requires the heat transfer coefficient and the bulk temperature as inputs. The mesh is built from the geometry using the built-in functions from the package.

Figure 17 shows the radial heat flux for two conditions, one for low heat transfer coefficient [10 W m^{-2} K^{-1}], and one for high heat transfer coefficient [100 kW m^{-2} K^{-1}]. It is noticeable that the heat flux is lower and evenly distributed through the inner wall for the lower HTC case. On the other hand, the heat flux gets a clover shape for the high HTC. As expected, the portion of heat flux going through the thermocouple position is lower than the heat flux on the outer wall.

The weight value, $w_i(z)$, from Equation 171, can be estimated from the numerical analysis as the ratio between the heat flux at the thermocouple position (i.e., 90°, 0°, and 270°, for top, side, and bottom, respectively) and the heat flux applied as the boundary condition. The model gets only the bulk temperature, the heat flux, and the heat transfer coefficient as inputs. As the heat flux distribution on the inner tube wall depends on the heat transfer coefficient, the weights depend on it as well. Then, several analyses must be run from a range of HTC [50 to 5,000 W m^{-2} K^{-1}]. The wall temperature and weight matrices are collected in the form of:

$$\begin{bmatrix} w_{t,1} & w_{s,1} & w_{b,1} \\ \vdots & \vdots & \vdots \\ w_{t,n} & w_{s,n} & w_{b,n} \end{bmatrix} \rightarrow \begin{bmatrix} T_{t,1} & T_{s,1} & T_{b,1} \\ \vdots & \vdots & \vdots \\ T_{t,n} & T_{s,n} & T_{b,n} \end{bmatrix}, \tag{172}$$

where each row is the results for the n HTC from 50 to 5,000 W m^{-2} K^{-1}. For each solution, the Mean Absolute Error (MAE) between the experimental wall temperatures and the numerical

Figure 17 – Outer (solid line) and inner (dashed line) radial heat flux for uniform heating under (a) low HTC and (b) high HTC, and bottom only heating under (c) low HTC and (d) high HTC.

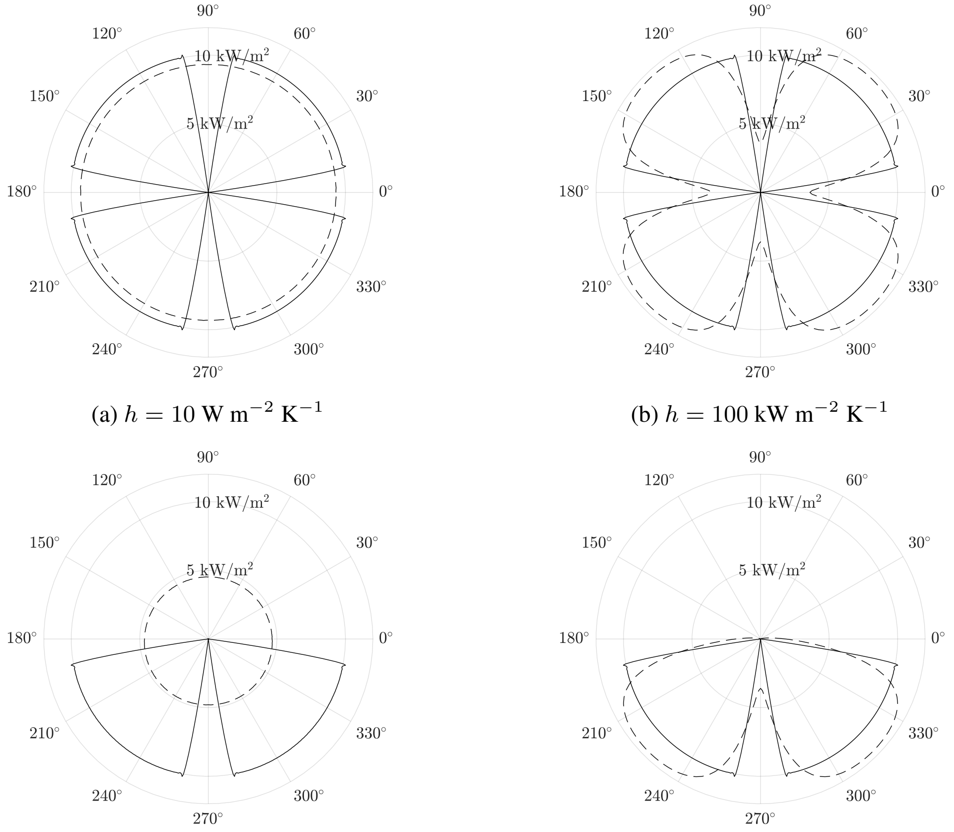

(a) $h = 10$ W m^{-2} K^{-1}

(b) $h = 100$ kW m^{-2} K^{-1}

(c) $h = 10$ W m^{-2} K^{-1}

(d) $h = 100$ kW m^{-2} K^{-1}

Source: Author.

modeling ones is calculated. The row that gives the least MAE returns the weights that better fit the heat flux distribution inside the tube wall.

- **Cross-section heat transfer coefficient**

The heat transfer coefficient for each section is given by the mean value from the bottom, side, and top ones, as follows:

$$h\left(z\right) = \frac{h_t\left(z\right) + 2h_s\left(z\right) + h_b\left(z\right)}{4}. \tag{173}$$

Since the heating is symmetric along the vertical axis the side HTC must be counted twice. For the non-uniform cases, bottom and top heating, only the side and bottom, and side and top, respectively, are considered for the mean.

- **Mean heat transfer coefficient**

The mean heat transfer coefficient throughout the test section is given by the numerical integration of the local heat transfer coefficient along the test section as follows:

$$h_m = \left[(h_1 + h_7) \left(\delta + \frac{\Delta l}{2} \right) + \Delta l \sum_{j=2}^{n=6} h_j \right] \Bigg/ L_{ts}, \tag{174}$$

where, δ is the length between the heating start point and the first section and the last section and the heating end point, and Δl is the length between measuring sections.

- **Pressure drop gradient**

The pressure drop gradient is calculated by dividing the pressure drop from the transmitter by the length between the sockets, as follows:

$$\frac{\mathrm{d}p}{\mathrm{d}z} = \frac{\Delta p}{L_{ts}}, \tag{175}$$

where Δp is the pressure drop over the tube length L_{ts}.

This approach considers the pressure drop to be linear along the test section. That is valid for medium values of quality but can induce some uncertainties when the pressure drop gradient is high, such as for low quality or dryout. Nonetheless, the results for the low quality presented high uncertainty anyway, and none dryout was observed through the tests.

As mentioned before, there were some cases where the pressure drop transmitter was not able to get proper measurements, such as for low vapor qualities and single-phase tests. The Friedel and Colebrook models were used to predict the pressure drop along the test section for these cases. This model was chosen because it consistently shows up as one of the best agreements for several works of horizontal two-phase flow (CIONCOLINI; THOME, 2012).

3.2 Tube surface characterization

Surface characterization is a standard procedure in boiling experiments. The active nucleation sites are the main parameter for boiling to occur or not. Usually, parameters such as arithmetic average height (Ra) and root mean square roughness (Rq) are required for heat transfer coefficient and pressure drop calculations. Even for smooth tubes, the characterization is pivotal for tube classification.

Figure 18 shows the samples and the roughness parameters testing. The experiment was performed at the UFSC LabMaT dependencies, using the Form Talysurf® i-Series equipment. The equipment returns several parameters of roughness, such as the root mean square roughness Rq, the maximum height of the profile Rt, the maximum height of peaks Rp, the maximum depth of valleys Rv, ten-point height Rz, and arithmetic average height Ra. Three samples of the tube cut in half, length-wise, were tested. Each sample got four rounds of 5.6 mm straight line measurements over its inner surface.

Figure 18 – Pictures of (a) tube samples and (b) surface characterization testing.

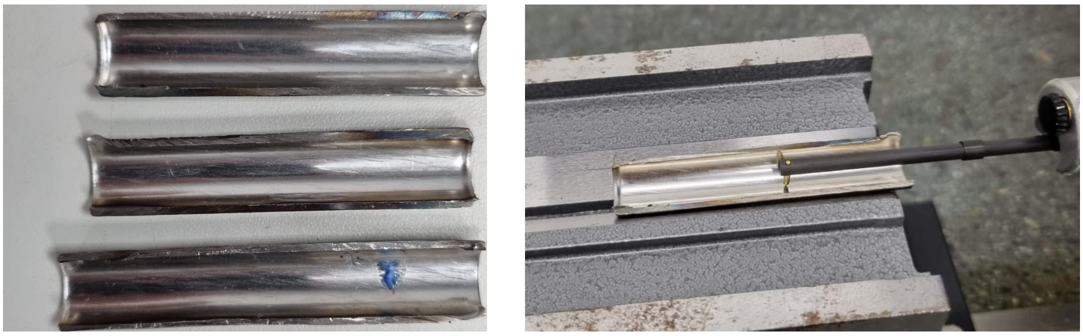

(a) Tube samples (b) Testing

Source: Author.

Table 17 shows the results from the experiment. The Ra and Rq mean values show that the tube can be considered a smooth tube (CENGEL; CIMBALA, 2015).

Table 17 – Results from surface characterization.

	rounds	Rq [µm]	Rt [µm]	Rp [µm]	Rv [µm]	Rz [µm]	Ra [µm]
Sample 1	1	0.3071	2.015	0.4797	0.9839	1.464	0.2268
	2	0.1941	2.624	0.5382	0.7180	1.256	0.1284
	3	0.2433	2.548	0.3220	0.7083	1.030	0.1612
	4	0.1620	2.312	0.4018	0.7059	1.108	0.1168
Sample 2	1	0.2017	2.416	0.6235	0.6600	1.284	0.1372
	2	0.1309	1.301	0.2590	0.5832	0.8422	0.09381
	3	0.2030	2.185	0.4944	0.6420	1.136	0.1355
	4	0.4092	8.997	0.7564	1.491	2.247	0.1811
Sample 3	1	0.2518	2.131	0.4414	0.7343	1.176	0.1775
	2	0.3091	3.423	0.3199	0.8603	1.180	0.1604
	3	0.2079	1.584	0.3682	0.7375	1.106	0.1460
	4	0.2597	3.281	0.3462	0.8044	1.151	0.1427
Mean		0.2400	2.901	0.4459	0.8024	1.248	0.1506
Uncertainty		0.1658	4.429	0.3141	0.5303	0.7653	0.07572

Source: Author.

3.3 Experimental procedure

The test rig was checked for leakage on low pressure using a vacuum pump and gauge pressure up to 200 kPa with an air compressor. Both water and R141b tests followed the same procedure, starting with filling the test rig. First, the vacuum pump sucked the air from the test rig continuously for one day. The fluid container was attached to the storage tank of the test rig through a globe valve. As the test rig pressure reached its minimum, the vacuum pump was switched off, the valve was opened, and the fluid entered the test rig. The cooling baths were set to a temperature close to the liquid saturation at the given pressure to remove the non-condensable gases dissolved in the fluid. After filling the circuit, the pump was turned on, and the fluid circulated for approximately three hours close to the saturation temperature before the experiment's batches.

The ice bath reference for the thermocouples was refilled at the beginning of each experiment round. After the fluid started circulating, the mass flow rate and the cooling bath temperatures were adjusted to the desired values. Once a steady state was attained, power settings for the preheater and test section were configured. Depending on the heat rate, each experimental batch was maintained for at least six minutes after reaching the steady state to yield no less than 72 data points at a 0.2 Hz acquisition frequency. The time was reduced to at least five minutes (60 data points) for higher power levels to avoid damage to the experimental apparatus. All the data were collected from the beginning to the end of the experiment.

For the two-phase flow, the experiment started as a single-phase flow. The power supply was turned off between experimental batches, and the mass velocity was increased to over 200 kg $\mathrm{m^{-2}s^{-1}}$ to remove the remaining bubbles trapped along the tube. As a safety precaution, the experiments for the mass velocity of 50 kg $\mathrm{m^{-2}s^{-1}}$, which required a lower heat rate, were tested first. Since the system pressure drop increased when the boiling flow started, the mass flow rate was set to a higher value than the target before applying power. The high-speed camera recorded an eight-second movie at 1,448.41 fps for each experimental point. From it, 3,600 frames were collected for flow pattern recognition and analysis.

As mentioned, the heat flux applied to the outer wall was the same regardless of the heating distribution, i.e., the heat rate for the bottom and top heating is half of the uniformly heated. Consequently, the quality gain between the uniform and non-uniform heating is different. The quality increase through the test section tube was set to a maximum of 6% and 3% for the uniform and non-uniform heating, respectively, to isolate the heating condition as the parameter influencing the flow boiling. On the other hand, the heat rate was kept constant at the preheater to ensure the same quality entering the test section, no matter the heating distribution. That approach allows comparing the uniform and non-uniform heating with the same heat flux but different heat rates applied to the outer wall with equivalent qualities on the test section. The differences between them are nearly indistinguishable from the point of view of the uncertainties in quality, ensuring the validity of the comparison.

3.4 Heat loss test

The following analysis accounts for the heat loss rate of the preheater and the test section to the ambient. The heat loss rate is an experimental parameter that allows for predicting the quality at the entrance and exit of the test section. The goal is to build a model that predicts the heat loss rate from the temperature difference between the environment and fluid. The following equation gives the heat loss of both the preheater and the test section:

$$\dot{q}_{loss} = (UA)_{loss} \left(\bar{T}_m - T_\infty\right), \tag{176}$$

where $\dot{q}_{loss}$ is the heat loss rate, $(UA)_{loss}$ is the overall heat loss coefficient, T_∞ is the ambient temperature, and $\bar{T}_m$ is the mean temperature of the fluid, given by the average value between the test section inlet and outlet temperatures, as follows:

$$\bar{T}_m = \frac{T_{in} + T_{out}}{2}. \tag{177}$$

Therefore, a set of experiments using distilled water, with the preheater and the test section insulated, were performed to quantify the heat loss rate at several temperature differences. From it, the overall heat loss coefficient can be determined, and the heat loss rate can be predicted.

For the experimental procedure, the mass flow rate of water was set to the lowest [50 kg m^{-2}s^{-1}] to get a measurable so as not to have a high experimental uncertainty temperature difference between the inlet and outlet of the preheater and the test section. Seven levels of inlet temperature were tested to build the curve $\dot{q}_{loss}$ versus ΔT. The procedure started at 95 °C and went down to 35 °C with intervals of 10 °C, which yields temperature differences $(\bar{T}_m - T_\infty)$ ranging from 10 to 65 °C. It was collected 60 data points (five minutes for an acquisition rate of 0.5 Hz) for each temperature after reaching the steady state. The criterion for the steady state was that the temperature did not change by two-tenths of a degree for 10 minutes straight. Each test was run three times to ensure repeatability.

The heat loss rate is calculated by measuring the sensible heat lost by the fluid while flowing through it. The sensible heat equation is:

$$\dot{q}_{loss} = \dot{m} c_p \left(T_{in} - T_{out}\right), \tag{178}$$

where $\dot{m}$ is the mass flow rate, c_p is the specific heat at constant pressure of the fluid, T_{in} is the temperature at the inlet, and T_{out} is the temperature at the outlet.

Figure 19 shows the heat loss for the preheater and the test section and their uncertainties. The overall heat loss coefficient is given by the slope of the curves. From Equation 176, the data were fitted to two first-order polynomial models. The model was built on the Scipy library using the function curvefit, which yielded $(UA)_{loss;ph}$ of 1.19 W m^{-2}K^{-1} for the preheater and $(UA)_{loss;ts}$ of 0.24 W m^{-2}K^{-1} for the test section.

The fitted curves are as follows,

$$\dot{q}_{loss;ph} = 1.19\ \Delta T_{ph}, \tag{179}$$

for the preheater, and,

$$\dot{q}_{loss;ts} = 0.24\ \Delta T_{ts}, \tag{180}$$

for the test section.

Figure 19 – Heat loss rate versus temperature difference between the ambient and the mean fluid temperature.

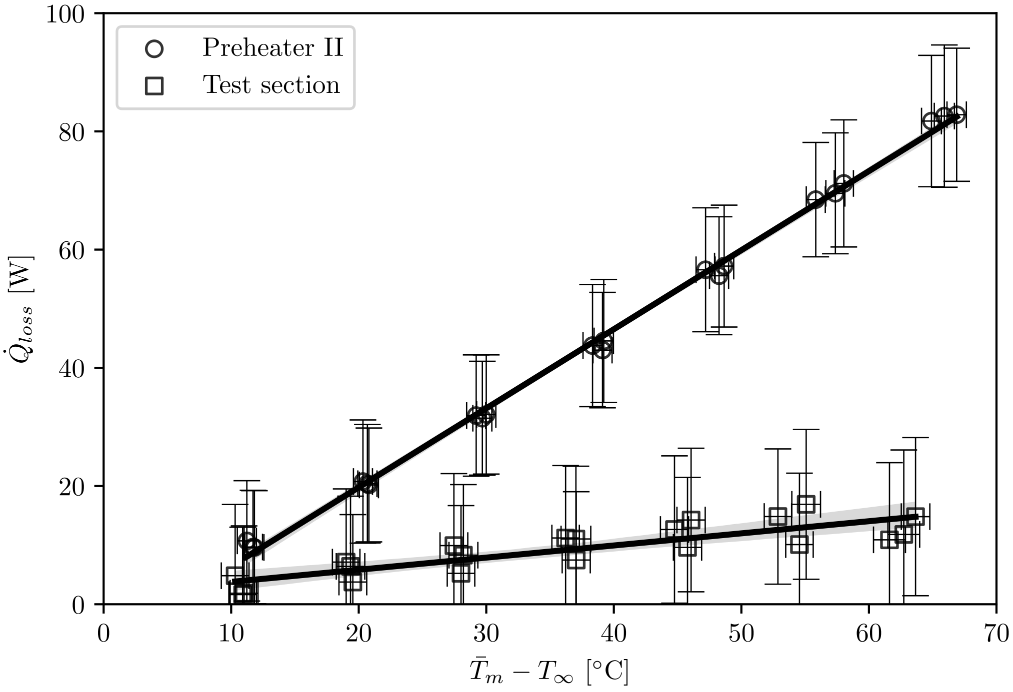

Source: Author.

Apart from the heat loss model, some tests with single-phase flow and heat input can give an idea of the thermal insulation efficiency. The heat power input is measured and compared with the sensible heat gained by the fluid through the preheater and test section. That measures the percentage of the heat lost to the environment.

Figure 20 shows the imposed versus absorbed heat rate for the preheater and test section. The maximum and minimum heat loss from the preheater was 5% and 1.9%, respectively, while for the test section, the maximum was 6.0% and the minimum was 1.5%. The heat loss was considered satisfactory and accounted for in the analysis.

3.5 Single-phase validation

Due to the lack of a generalized well-established correlation for the two-phase flow, it is common practice to validate the experimental setup for single-phase flow. That ensures the reliability of the data collected from the test rig. Thus, several test runs were performed, and the results were compared with the laminar and turbulent flow correlations. From Rohsenow *et al.* (1998), the following Gnielinski correlation is used to calculate the local Nusselt Number for Reynolds greater than 3,000:

$$\mathrm{Nu} = \frac{\left(\frac{f}{8}\right)(\mathrm{Re} - 1000)\,\mathrm{Pr}}{1 + 12.7\left(\frac{f}{8}\right)^{0.5}\left(\mathrm{Pr}^{2/3} - 1\right)} \quad \begin{cases} 3,000 \leq \mathrm{Re} \leq 5 \times 10^{6} \\ 0.5 \leq \mathrm{Pr} \leq 2,000 \end{cases}, \tag{181}$$

Figure 20 – Heat rate imposed versus ambsorbed by the preheater and test section.

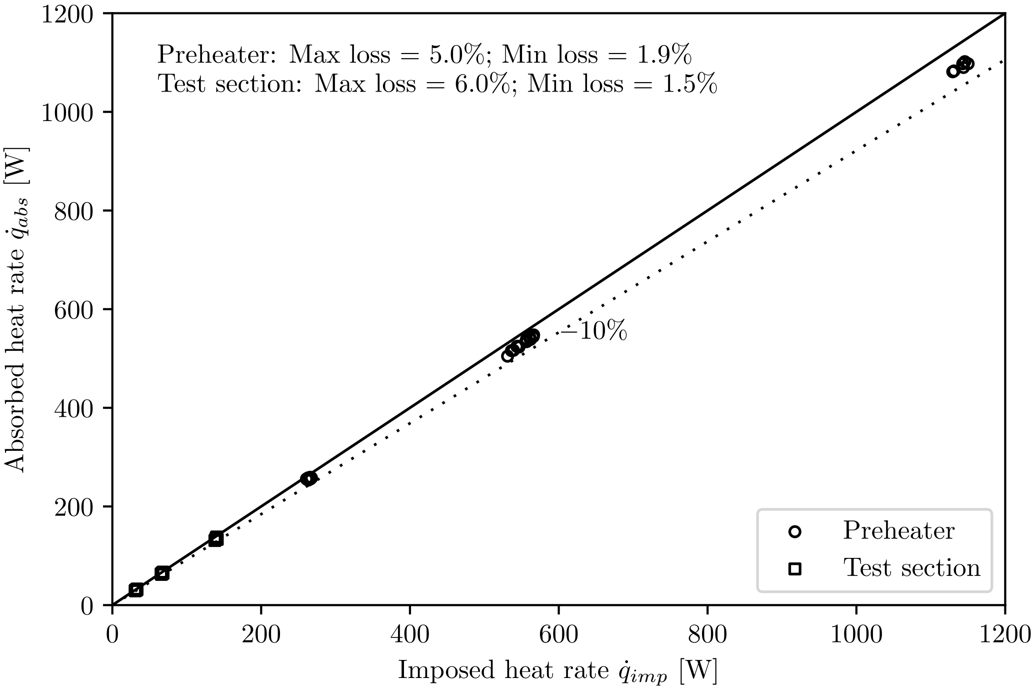

Source: Author.

where Re is the Reynolds number, Pr is the Prandtl number and f is the friction factor calculated by the Pethukov correlation:

$$f = (0.79 \ln \mathrm{Re} - 1.64)^{-2} \quad 3,000 \leq \mathrm{Re} \leq 5 \times 10^6. \tag{182}$$

The heat transfer coefficient is calculated by:

$$h = \mathrm{Nu}\frac{\kappa}{d_{in}}, \tag{183}$$

where κ is the thermal conductivity of the fluid for the bulk temperature. The bulk temperature at each section is calculated by Equation 158.

Since the entrance region for a tube with 10.92 mm of inner diameter is longer than the preheater plus the test section, the following correlation was used for laminar flow (Re < 2,300) (ROHSENOW *et al.*, 1998):

$$\mathrm{Nu} = \begin{cases} 1.953\,\mathrm{Gz}^{-1/3} - 1 & \text{for Gz} \leq 0.03 \\ 4.364 + 0.0722\,\mathrm{Gz}^{-1} & \text{for Gz} > 0.03 \end{cases}, \tag{184}$$

where Gz is the Graetz Number, given by:

$$\mathrm{Gz} = \frac{L_{ts}/d_{in}}{\mathrm{Re\,Pr}}. \tag{185}$$

Table 18 lists the single-phase experiment setup used to validate the test rig. Three levels of mass velocity, 50 to 295 kg $\mathrm{m}^{-2}\mathrm{s}^{-1}$ at inlet temperatures ranging from 5 to 25 °C, which

Table 18 – Experiments setup for test rig validation.

Experiment	Reynolds Number [-]	Heat flux q'' [kW m^{-2}]
1	665	2.9
2	1,212	7.7
3	2,320	12.6
4	2,856	16.9
5	2,298	12.5
6	2,840	16.8
7	2,974	14.4
8	3,163	14.5
9	3,317	14.5
10	4,123	14.6
11	4,648	14.7
12	4,752	14.7

Source: Author.

yields Reynolds numbers from 600 to 4,800, were tested. The heat flux ranged from 2.9 to 16.9 kW m^{-2}.

Figure 21 shows the comparison between the experimental and theoretical heat transfer coefficients. As can be seen, most of the points were within the 30% region (91.7%) and 66.7% within 15%. The only point out of that was the laminar flow with Reynolds Number of 1,211, which deviated 42.5%. given the data, the test rig validation was considered satisfactory.

Figure 21 – Predicted versus experimental HTC for single-phase flow validation.

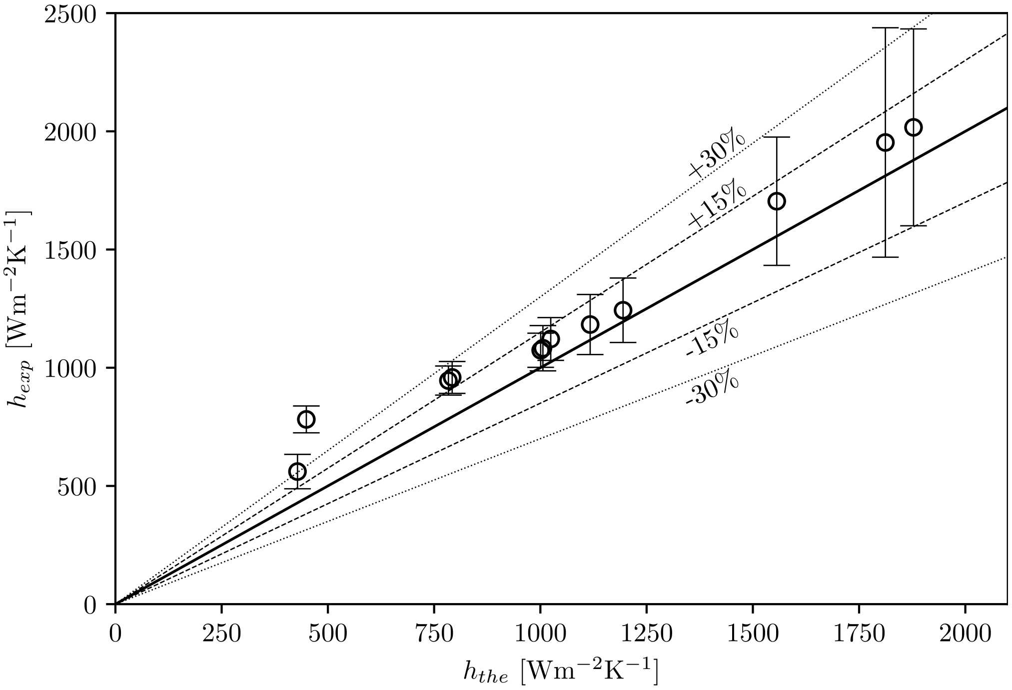

Source: Author.

3.6 Summary

The experimental apparatus and its components are described, along with the rationale behind the choices made for the test rig and experiments. The measurement techniques are discussed, and both the experimental variables and feature equations are presented. Given the heating non-uniformity, special attention is given to the calculation of the heat transfer coefficient and the heat flux distribution through the tube wall. The surface characterization has shown good agreement with smooth tube parameters. The experimental procedure for the tests is described, and the details of the data acquisition process are explained. The approach to calculating uncertainties is explained for both types A and B, as well as their combination with the calibration data from the sensors. The heat loss test is also described, including the coefficients used to account for it. Finally, the single-phase validation procedure is explained, and the results show satisfactory agreement with the correlations.

4 Results and discussion

This chapter presents results and discussions of single-phase and two-phase flow tests. First, the single-phase experimental parameters are highlighted. The ANOVA tests verify the effect of the non-uniform heating on the heat transfer coefficient, which is also compared with the Gnielinksi correlation. Then, the two-phase flow results are analyzed and discussed throughout each topic. Finally, a concise summary at the end compiles all the key features of the chapter.

4.1 Single-phase flow

Apart from the validation, several tests were performed to verify the effect of circumferential non-uniform heating on the heat transfer for the single-phase flow. Figure 22 illustrates the data points distribution for the inlet temperature, mass flow rate, heat flux, and heating condition. A total of 36 experimental points spread into three levels of heating conditions, and two levels of inlet temperature, mass flow rate, and heat flux were analyzed. This configuration yields four Reynolds numbers, with three data points for each Reynolds and heating condition level.

Figure 22 – Histogram of the single-phase data points for the inlet temperature, mass flow rate, heat flux, and heating condition.

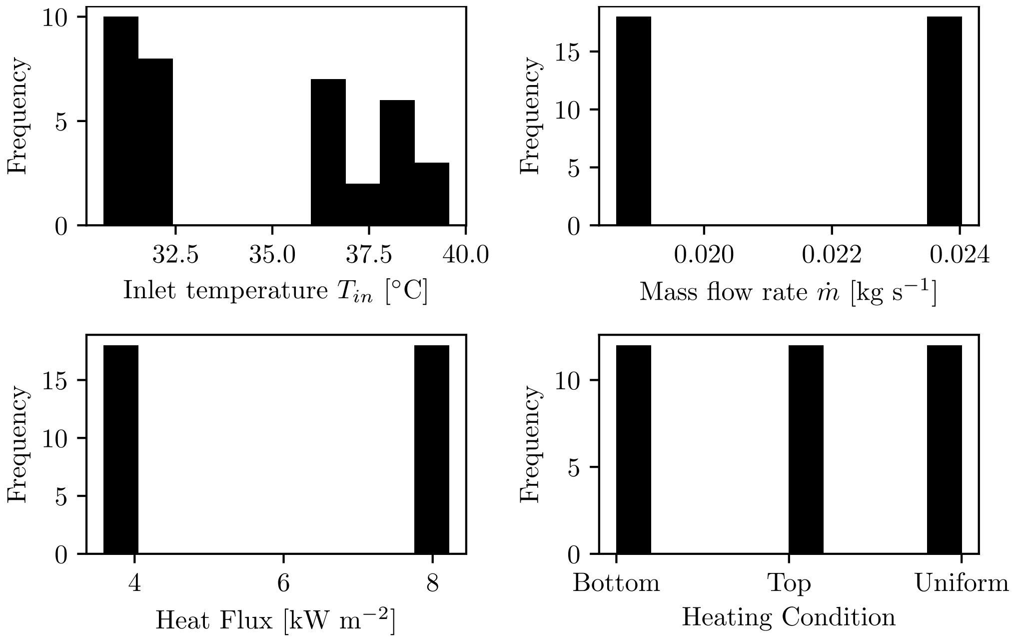

Source: Author.

Table 19 lists the relative uncertainties for the inlet temperature, mass flow rate, heat flux, and heat transfer coefficient for the single-phase flow experiments. The uncertainties were calculated following the procedures from Appendix C. The maximum uncertainty for the experimental heat transfer coefficient was 7.06% with a mean value of 3.52%. The uncertainties were considered satisfactory for experimental work with single-phase flow.

Table 19 – Relative uncertainties for the inlet temperature, mass flow rate, heat flux, and heat transfer coefficient for the single-phase flow experiments.

	T_{in}	$\dot{m}$	q''	h_{sp}
Mean	1.09%	0.27%	1.53%	3.52%
Min	0.78%	0.18%	1.17%	1.51%
Max	3.26%	0.45%	3.93%	7.06%

Source: Author.

The short length of the test section results in certain measurement sections situated within the thermal boundary layer development. Figure 23 illustrates the variation of the heat transfer coefficient along the tube length under different heating conditions. As expected, the HTC decreases with the tube length, indicating the development of the thermal boundary layer. The last two measurement sections appear to have fully developed or nearly fully developed thermal boundary layers. Therefore, only the average from those sections was used to evaluate the single-phase HTC and check for the effect of heat distribution on it. However, it's worth noting that the thermal boundary layer develops at a slower rate in the case of bottom heating compared to top and uniform heating. This difference may happen due to the larger volume of cold liquid surrounding the boundary layer in the bottom heating scenario. On the other hand, in the case of top heating, where the heated fluid remains concentrated at the top, the boundary layer is subject to fewer effects from the surrounding cold liquid.

Figure 23 – Single-phase heat transfer coefficient along the tube length for three heating conditions (uniform, bottom, and top).

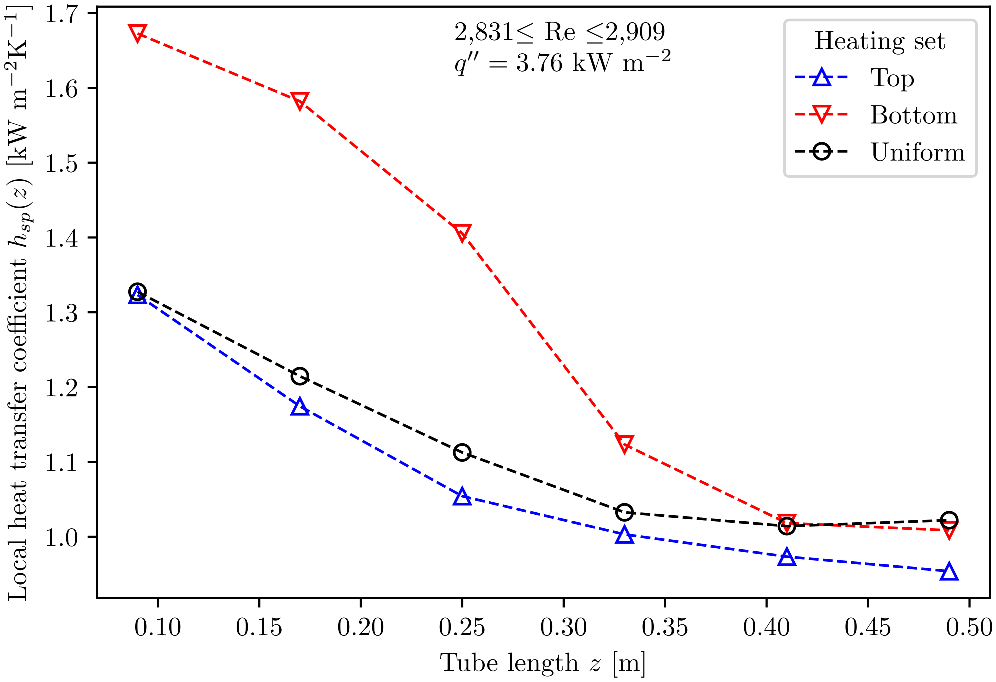

Source: Author.

According to Dirker, Meyer and Reid (2018), the secondary flow effect induced by buoyancy can be assessed using the Richardson number. When the Richardson number falls below 0.1, forced convection effects dominate the heat transfer; when it exceeds 1, buoyancy effects prevail; and when it ranges between 0.1 and 1, both factors should be considered. Based on the experimental data, the highest Richardson number observed was 0.005. Therefore, the heat transfer is primarily governed by forced convection, rendering the secondary flow effect negligible in terms of heat transfer.

Figure 24 shows the behavior of the Nusselt number against the Reynolds number for the single-phase experiments. The Nusselt number increased with the Reynolds number, though the heating condition does not seem to affect the Nusselt number. To statistically check the heating condition effects on the Nusselt number, a two-way ANOVA test was performed considering the four levels of the Reynolds number and three of the heating condition. Since the Reynolds Number is a continuous variable, binning was applied to convert it into a categorical feature with four levels.

Figure 24 – Single-phase Nusselt Number versus Reynolds Number for three heating conditions (uniform, bottom, and top).

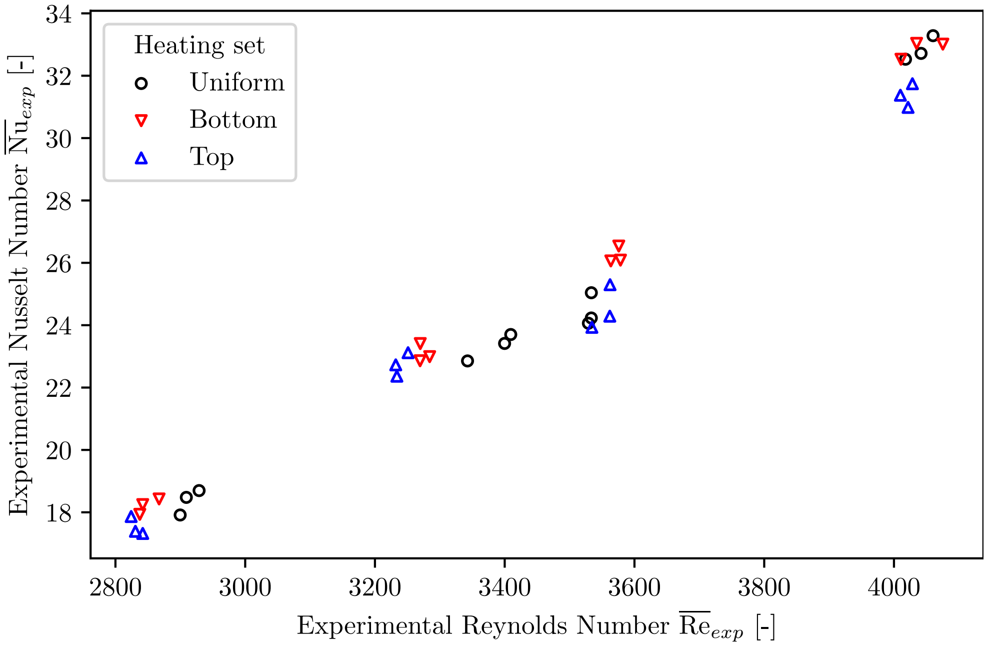

Source: Author.

Table 20 shows that considering all single-phase data points, the null hypothesis is accepted with a 95% confidence level, and the Reynolds number is the only source significantly influencing the Nusselt number. Given that the heat transfer coefficient for single-phase turbulent flow relies solely on the Reynolds number and the Prandtl number, it is reasonable that the heating condition would have no impact on the Nusselt number. The Prandtl and Reynolds numbers implicitly capture the effects of heat flux and heat rate on the Nusselt number.

Figure 25 compares the experimental and theoretical heat transfer coefficient for the

Table 20 – Two-way ANOVA test table for all single-phase data points.

Source	Sum of Squares	Degree of Freedom	F-Value	P-Value	H_0
Heating Condition	0.867	2	2.655	0.091	Accept
Reynolds Number	1026	3	2096	< 0.05	Reject
Interaction	1.250	6	1.276	0.30	Accept
Residual	3.919	24			

Source: Author.

Gnielinski correlation. The model presented a Mean Absolute Percentage Error (MAPE) of 7.29%, with 91.67% of the data within 15% error and 100% within 30%. The single-phase results were considered satisfactory, it also served as validation for the non-uniform heating cases, indicating that the test rig captures these effects as well.

Figure 25 – Comparison between the theoretical Nusselt number predicted by Gnielinski correlation and experimental Nusselt number for single-phase flow under three heating conditions (uniform, bottom, and top).

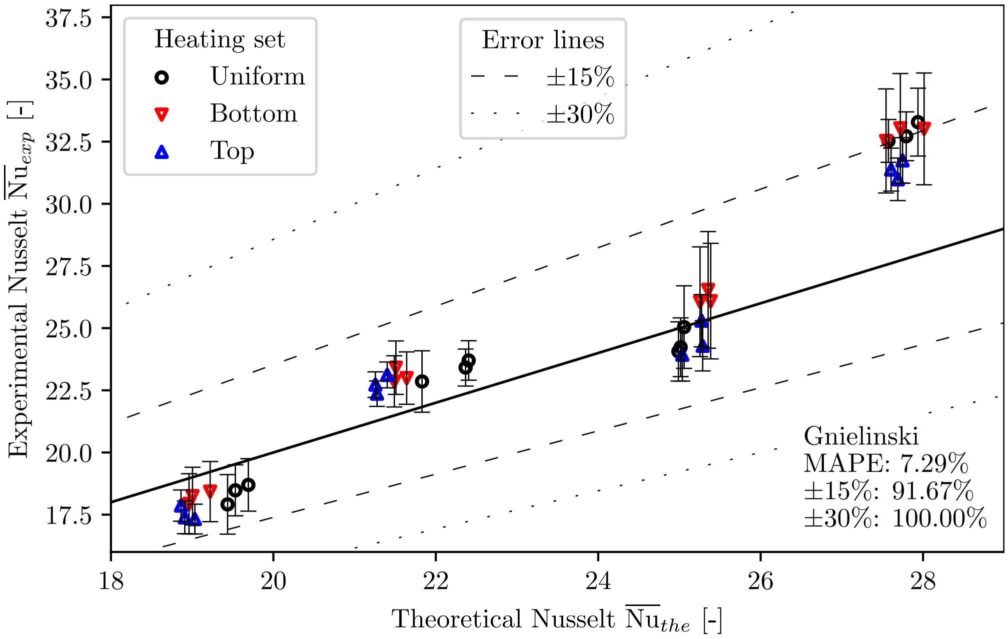

Source: Author.

4.2 Two-phase flow

All the two-phase flow analyses were done from the perspective of the non-uniform heating condition and covered the following subjects in order. First, the Onset of Nucleate Boiling (ONB) under non-uniform heat flux is discussed. Second, the flow pattern identification and its comparison with horizontal two-phase flow pattern maps are shown. Next, the heat transfer aspects and the dimensionless group analysis are presented, followed by the pressure drop and dryout observations. Last, an analysis of the temperature distribution throughout the tube wall is shown and explored.

Figure 26 illustrates the two-phase flow dataset histogram of the mass velocity, saturation temperature, heat flux, quality, flow pattern, and heating condition. A total of 186 data points were distributed into two mass velocities (50 and 150 kg $m^{-2}s^{-1}$), two groups of saturation pressure (110 and 130 kPa), two heat fluxes (3.4 and 11.0 kW m^{-2}), quality ranging from 0 to 95%, several flow patterns, and three heating conditions (uniform, bottom, and top). The combination of mass velocity, pressure, and heat flux was explained in the section 3.3.

Figure 26 – Two-phase flow dataset histogram of the following features: mass velocity, saturation temperature, heat flux, quality, flow pattern, and heating condition.

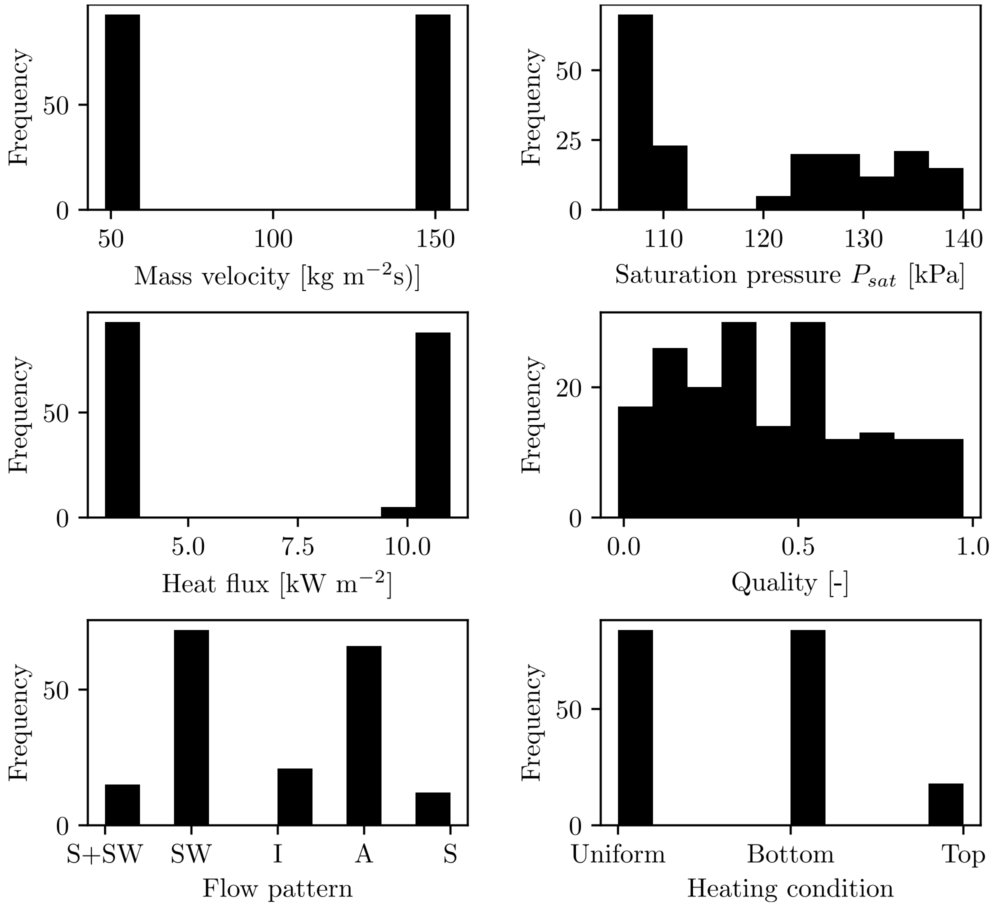

Source: Author.

Table 21 lists the quality uncertainty and the relative uncertainties for the saturation pressure, mass velocity, and heat flux for the two-phase flow experiments. For the experiments with low quality, i.e., close to saturated liquid, the relative uncertainty of the quality is high. Therefore, a decision was made to express its uncertainty in a non-relative manner.

4.2.1 Onset of nucleate boiling under non-uniform heat flux

The preheater was set to give enough power to get the inlet test section quality close to zero. Thus, with the heat input in the test section, the ONB would happen in it. ONB happens

Table 21 – Relative uncertainties for the saturation pressure, mass velocity, and heat flux, and quality uncertainty for the two-phase flow experiments.

	p_{sat}	G	q''	x
Mean	5.31%	0.67%	1.37%	0.57%
Min	4.47%	0.25%	0.98%	0.31%
Max	5.95%	2.45%	1.81%	1.12%

Source: Author.

when the wall superheat is enough to enable nucleation site activation, initiating the nucleate boiling regime. For heat flux applied to the tube, a sudden drop in wall temperature is expected when nucleate boiling starts. The temperature drop was checked for each measurement section to determine the position of the ONB and if it happened within the test section. Because of the nature of the experimental work, some ONB positions occurred before the test section, though some considerations are still worth mentioning.

Figure 27 shows the transient behavior of the seven cross-sections mean wall temperature, mean bulk temperature, and superheat temperature for uniform and bottom heating with $G \approx 50$ kg m^{-2}s^{-1}. As can be noted, all sections presented the temperature drop when nucleate boiling started, indicating that the ONB position is upstream of the test section. Since the heat rate is lower for the bottom heating, it took more time to start nucleate boiling. The uniform heating wall temperatures were higher than the wall superheat temperature, which indicates nucleate boiling might happen on the tube wall. For bottom heating, the wall temperatures are lower than the minimum wall superheat, and consequently, nucleate boiling might be suppressed in the test section.

Figure 28 shows the transient behavior of the seven cross-sections mean wall temperature, mean bulk temperature, and superheat temperature for uniform and bottom heating with $G \approx 150$ kg m^{-2}s^{-1}. Unlike the lower mass velocity, the first measurement section did not show a drop in wall temperature for uniform heating. That indicates the ONB position is between the first and second measurement sections. After flow boiling started, all wall temperature measurement sections were higher than the superheat temperature, indicating nucleate boiling may be happening in those sections. Despite some sections being higher than the wall superheat before flow boiling started, all wall temperatures presented values lower than the wall superheat for the bottom heating case.

A close look at the top, side, and bottom wall temperature can give insights into how non-uniform heating influences the wall temperature behavior during the transition from single-phase to two-phase flow. Figure 29 shows the transient behavior of top, side, and bottom wall temperature for the fourth cross-section (middle of the tube), heat flux, mass velocity, and saturation pressure for uniform (black lines) and bottom (gray lines) heating for $G \approx 50$ kg m^{-2}s^{-1}. The red lines indicate the minimum wall superheat for ONB with uniform (full line) and bottom (dashed line) heating. The valleys seen on the mass velocity before applying

Figure 27 – Transient behavior of mean wall temperature of each measurement section and superheat temperature for uniform and bottom heating with $G \approx 50$ kg m^{-2}s^{-1}.

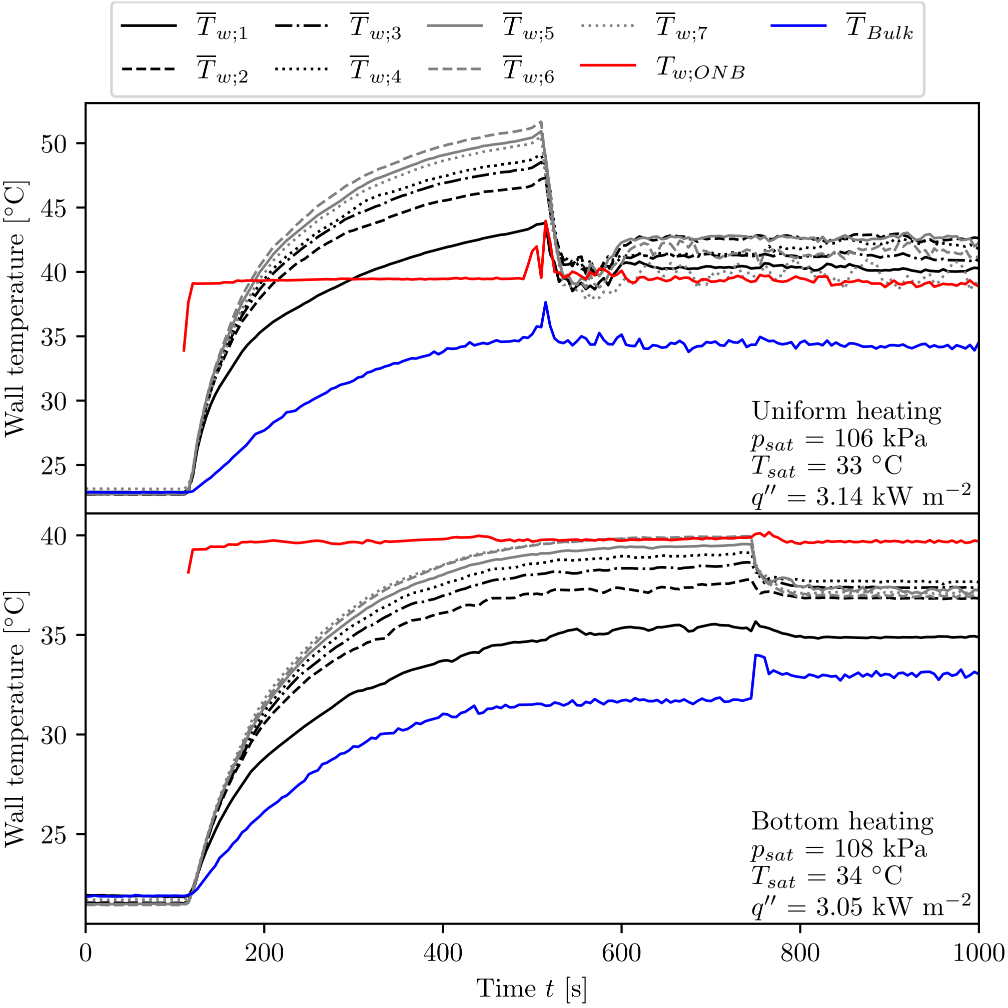

Source: Author.

heat ($t < 100$ s) for the bottom heating were due to the manual adjusting of it. The overall trend was similar for both heating conditions. The wall temperatures started to rise as the heat was provided to the tube and tended to reach a plateau. The flow was single-phase during this whole process. As soon as slugs appeared in the viewing section, the pressure increased, leading to a subsequent decrease in mass velocity. This effect was more significant for uniform heating. Since the mass velocity decreased, the pressure started dropping, and the mass velocity stabilized at a new steady point. This behavior is characteristic of Ledinegg instability, as was discussed in **??**

For uniform heating, all measurement sections presented a drop in temperature which suggests ONB position happened upstream of the test section. All wall temperatures are higher than the minimum superheated temperature needed for ONB to initiate, also indicating the ONB position may have happened upstream. Nevertheless, the top and side temperatures significantly dropped compared to the bottom position for the uniformly heated tube. For horizontal flow boiling, slugs tend to occupy the upper part of the tube, and the heat transfer with the thin liquid layer is higher for the top and side than for the bottom.

Figure 28 – Transient behavior of mean wall temperature of each measurement section and superheat temperature for uniform and bottom heating with $G \approx 150$ kg m^{-2}s^{-1}.

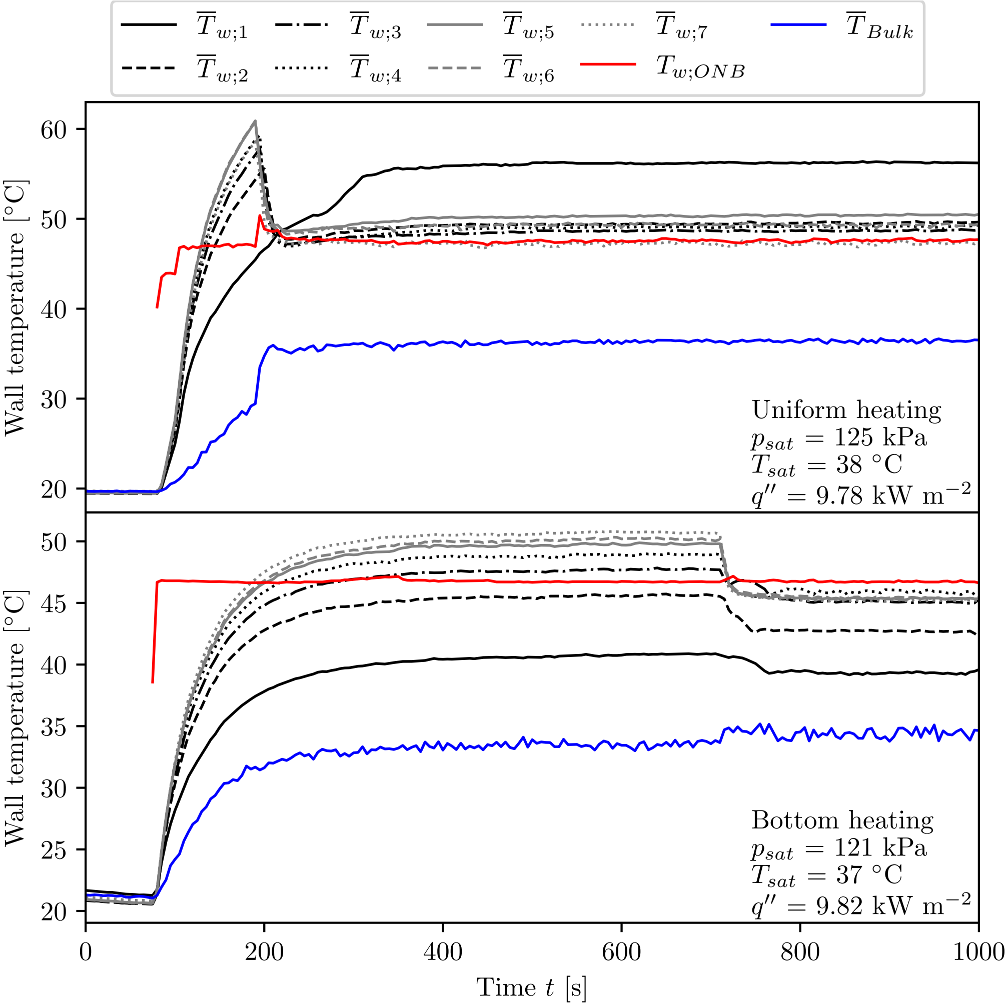

Source: Author.

For bottom heating, the ONB position happened within the test section. The temperature drop was seen from the third section onwards, although the wall temperature drop at the bottom was nonexistent at that position. However, the side and top wall temperatures presented the temperature drop seen for the ONB. This can indicate that nucleate boiling may have happened at the non-heated part of the tube, though the temperatures from the side and top are lower than the superheat temperature expected to initiate nucleate boiling. Since the upper wall was heated indirectly by diffusion, the wall temperatures at the top and side were lower than for the uniform heating. When nucleate boiling initiates, the increase in the HTC at the bottom changes the heat flux distribution inside the tube. Heat will flow through the easiest path, thus, increasing the heat flux on the bottom half. Even though the HTC increased, the heat flux change prevented the wall temperature from dropping. Since the ONB deflected the heat flux distribution to the bottom, the indirect diffusion heating of the side and top decreased, and as a consequence, the wall temperatures decreased as well.

Figure 30 shows the transient behavior of top, side, and bottom wall temperature for

Figure 29 – Transient behavior of top (T_t), side (T_s), and bottom (T_b) wall temperature for the fourth cross-section (middle of the tube), heat flux, mass velocity, and saturation pressure for uniform (black lines) and bottom (gray lines) heating for $G \approx 50\ \text{kg m}^{-2}\text{s}^{-1}$.

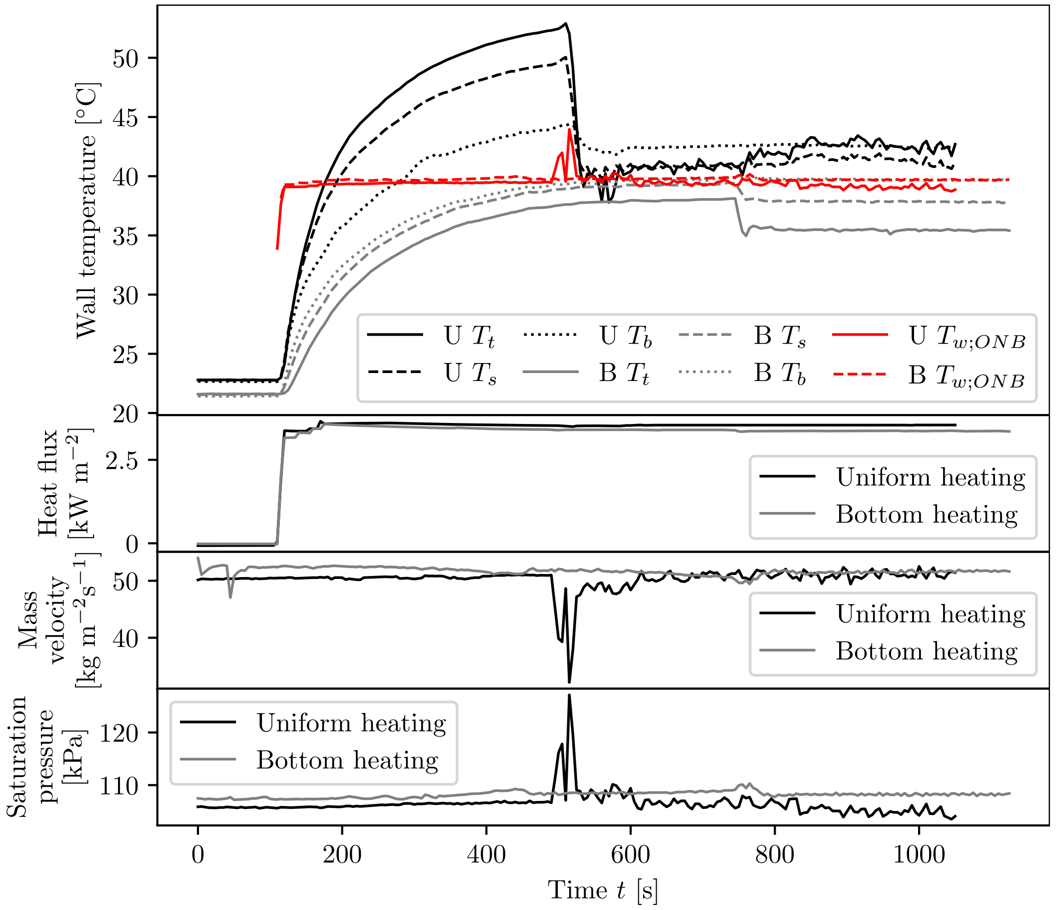

Source: Author.

the fourth cross-section (middle of the tube), heat flux, mass velocity, and saturation pressure for uniform (black lines) and bottom (gray lines) heating with $G \approx 150$ kg m^{-2}s^{-1}. The red lines indicate the minimum wall superheat needed for ONB with uniform (full line) and bottom (dashed line) heating. The peak observed for the bottom heating mass velocity before the heat was applied ($t < 100$ s) was due to the manual adjusting of it. A similar trend to the lower mass velocity was observed for the pressure and mass velocity behavior when ONB occurred, however, the temperature did not reach a plateau for the uniformly heated tube. This may happen because of the higher temperature rate due to the heat input when comparing the high and low mass velocities.

The ONB position happened after the first measurement section for the uniform heating. As for the low mass velocity, the temperatures dropped in different ratios for the top, side, and bottom. Before boiling started, the top wall temperature was the highest, but after ONB, it was lower than the side and bottom ones. For the bottom heating, the ONB position was also after the first section of measurement. For higher mass velocity, only the top temperature was lower than the superheat when nucleate boiling started, which might indicate nucleation only on the side

Figure 30 – Transient behavior of top (T_t), side (T_s), and bottom (T_b) wall temperature for the fourth cross-section (middle of the tube), heat flux, mass velocity, and saturation pressure for uniform (black lines) and bottom (gray lines) heating for $G \approx 150$ kg m^{-2}s^{-1}.

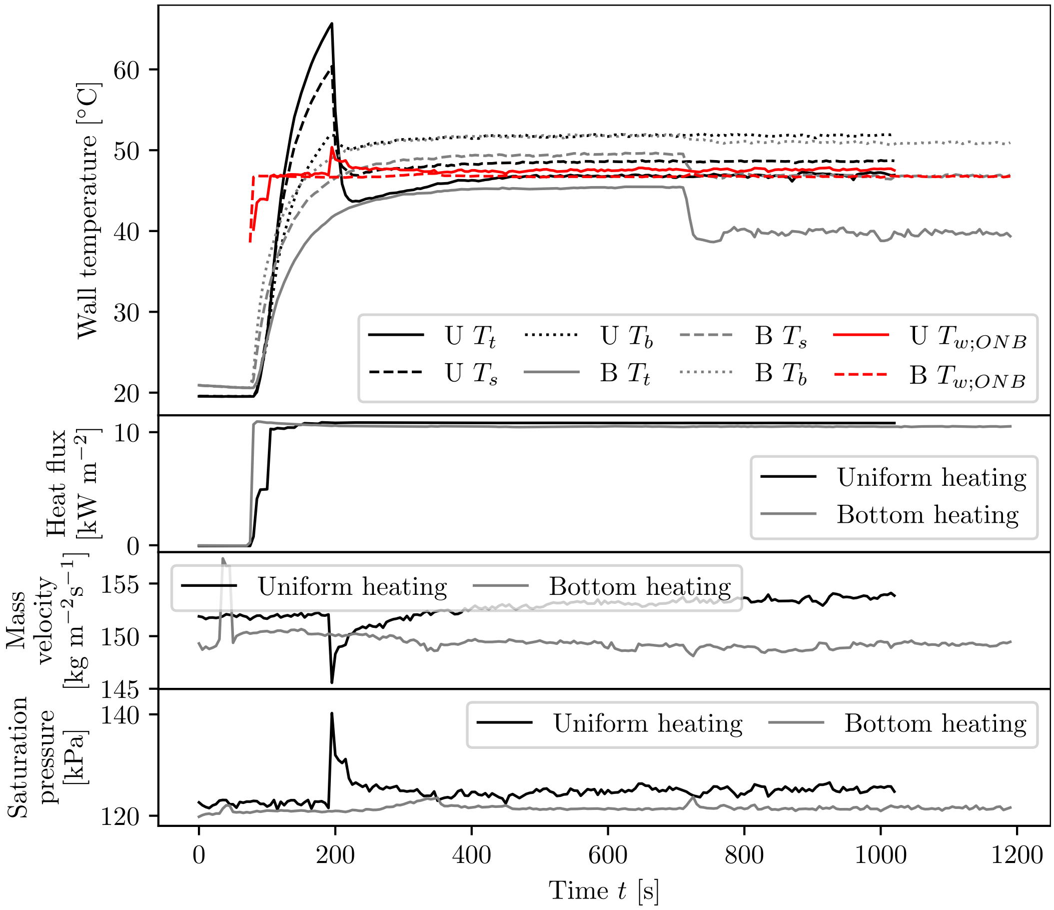

Source: Author.

and bottom of the tube. Although the same effect on the inner heat flux distribution happened, a slight temperature drop occurred for the bottom part of the tube.

4.2.2 Flow pattern identification

It is worth noting that the recordings were taken downstream of the test section, with the flow pattern at the viewing section considered the same as in the test section. Figure 31 illustrates all the flow patterns seen from the experiments and their labels. The labels for the flow regimes used for this work were the ones from Wojtan, Ursenbacher and Thome (2005a) since it is the only pattern-based model for HTC calculation used for comparison. For the low mass velocity and low quality, the slugs were long enough that waves traveled through the liquid-vapor interface. Therefore, this flow pattern was labeled as slug + stratified-wavy. None of the recordings captured the partial dryout, but when analyzing frame by frame, some droplets rewetted the upper part of the glass tube, which will be discussed later. Thus, some experimental points which were labeled as stratified-wavy might be partial dryout.

Figure 31 – Flow pattern pictures from the experimental work and how they were labeled.

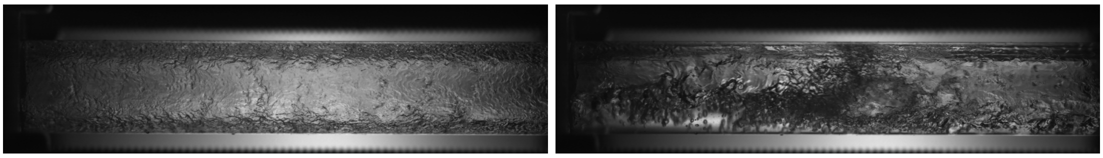

(a) Annular

(b) Intermittent

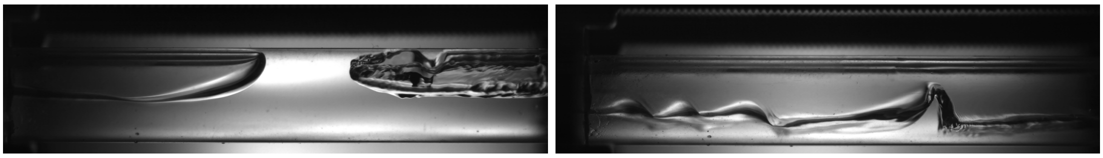

(c) Slug

(d) Stratified-Wavy

Source: Author.

Figure 32 illustrates a bar plot with the number of points for each flow pattern. More than 70% of the experiment was either annular flow or stratified-wavy. The slug, slug + stratified-wavy, and intermittent regimes represent around 25% of the data set and occurred only for low vapor quality. The prediction capability of Wojtan, Ursenbacher and Thome (2005b) pattern map was checked.

Figure 32 – Bar plot with the frequency of flow pattern for the two-phase flow experiments.

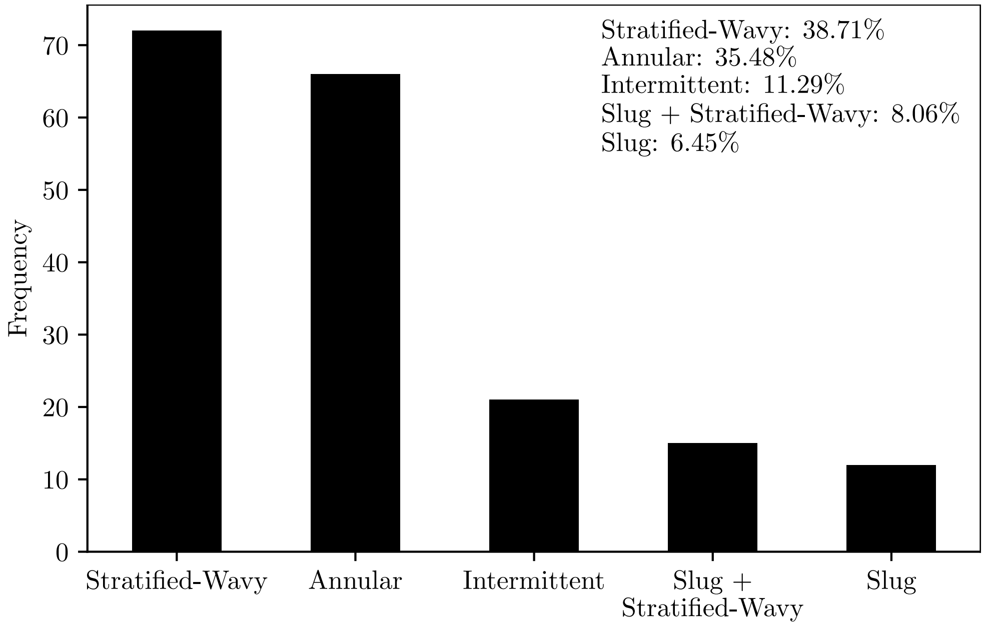

Source: Author.

Figure 33 shows the flow patterns identified from the recordings plotted on Wojtan's flow pattern map. It is important to mention that for the same quality and mass velocity, the flow pattern found in the viewing section was the same regardless of the heating condition. That's why no distinction was made for the heating methods in the figure. The map had an accuracy of 75.27%, mainly due to the annular and stratified wavy regimes. The value of the transition line between slug and slug + stratified-wavy is close to the mass velocity tested, and the data points near them may give the wrong idea of accuracy. Wang *et al.* (2019) noted that non-uniform heating induces instabilities, leading to an earlier transition from intermittent to annular flow. Unlike Wang *et al.* (2019), there were no noticeable differences between the flow patterns transition regarding the heating condition for this work. However, the transition from slug to intermittent occurred at a lower quality than Wojtan, Ursenbacher and Thome's map predicted, which Wang *et al.* (2019) also observed. Despite being depicted as sharp lines, the transition between regimes is blurry, and some uncertainty must be accounted for.

Figure 33 – Experimental flow pattern on the Wojtan flow pattern map for $p_{sat} = 140$ kPa, $d_{in} = 10.96$ mm, and $q'' = 11.0$ kW m^{-2}.

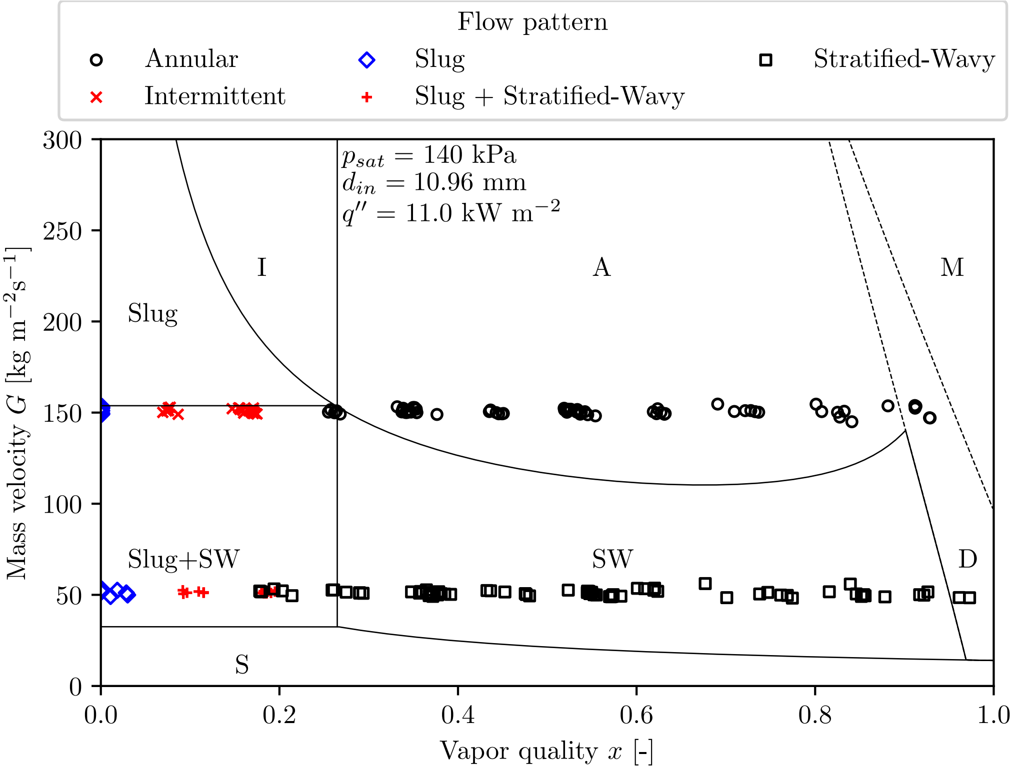

Source: Author.

According to Baptistella, Moreira and Ribatski (2023), the speed difference between small and large waves traveling through the liquid surface provokes a cycle of rewetting fronts. As soon as the larger waves pass, it thinner the liquid film, drying the tube wall. None of these behaviors was observed for the present work. In addition, dryout can also be inferred from the measurements. Partial dryout is usually observed as a sharp drop in HTC or a sudden rise in wall temperature. None of the experiments with $G = 150$ kg m^{-2}s^{-1} presented dryout characteristics, though the map predicted it for five data points (three for uniform heating and two for bottom heating). An ultrathin liquid film on the upper part of the tube was observed for the stratified-wavy regime with $G = 50$ kg m^{-2}s^{-1}. For high qualities, it was possible to see droplets of liquid rewetting the upper part of the viewing section tube, which could indicate dryout. Figure 34 shows the detail of a frame sequence of a droplet rewetting the upper surface of the viewing section tube.

Figure 34 – Frame sequence of a droplet rewetting the upper surface of the tube for $G = 50$ kg m^{-2}s^{-1} and quality over 90% with bottom heating.

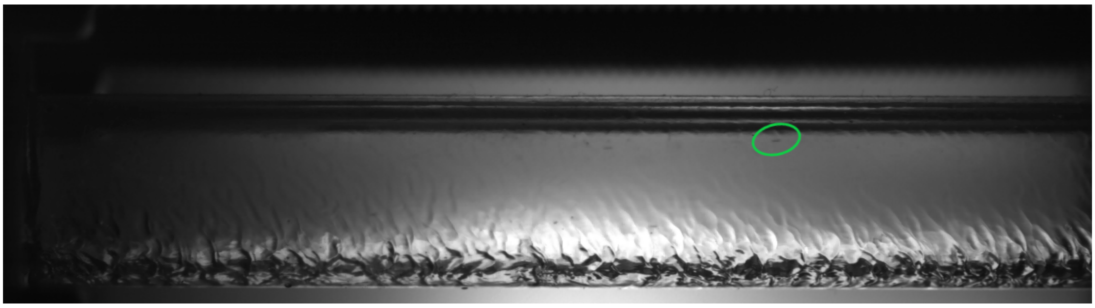

(a) $t = 0$ ms

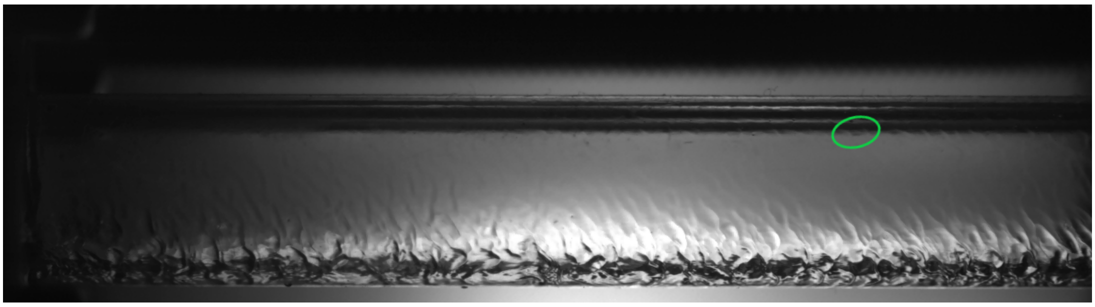

(b) $t = 0.7$ ms

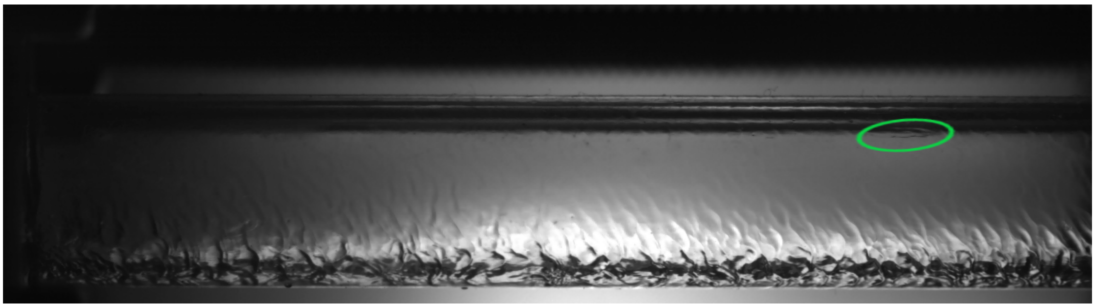

(c) $t = 1.4$ ms

Source: Author.

4.2.3 Pressure drop gradient

The pressure drop along the test section was small and the differential pressure transmitter could not capture any significant recordings for the lower mass velocity (50 kg m^{-2}s^{-1}). Therefore, only the results for $G = 150$ kg m^{-2}s^{-1} are presented in this section. In addition, the transmitter scale range was high for the pressure drop found in the test section. Thus, the uncertainties of the lower measurements were very high.

Figure 35 shows the pressure drop gradient against quality for three heating conditions and the 150 kg m^{-2}s^{-1} mass velocity. Overall, the pressure drop gradient increased as quality increased. Some data points within the $45 < x < 65$ range for the bottom heating exhibited deviations from the typical trend observed in the remaining data. Apart from those data points, the heating condition does not seem to influence the pressure drop gradient. A one-way ANOVA test can check the influence of the heating condition on the pressure drop gradient.

Figure 35 – Experimental pressure drop gradient versus quality for the three heating conditions (uniform, bottom, and top) and $G = 150$ kg m^{-2}s^{-1}, $T_{sat} = 39$ °C, $q'' = 10.5$ kW m^{-2}.

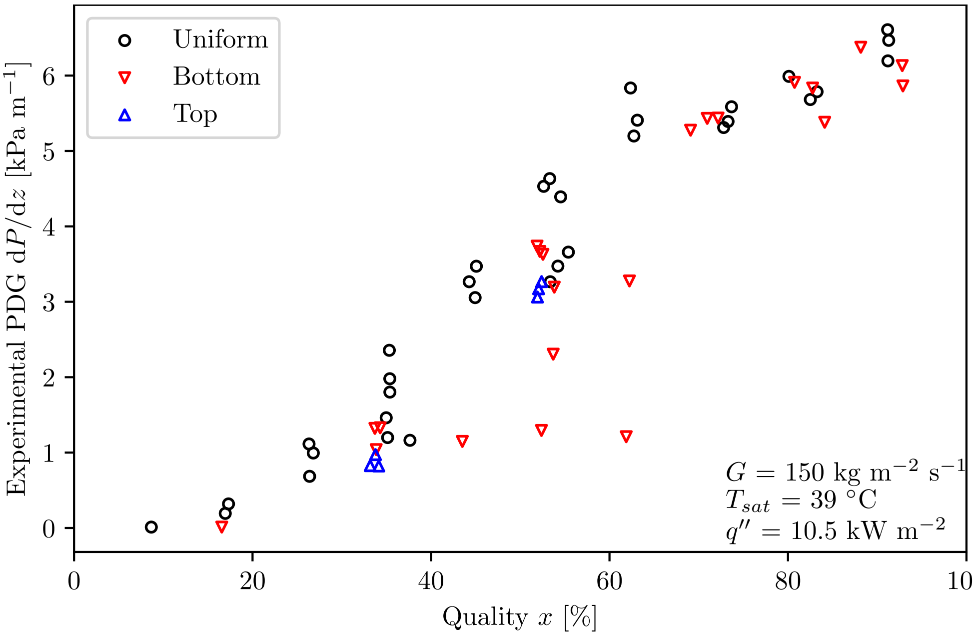

Source: Author.

Table 22 shows the one-way ANOVA test table to assess the influence of the heating condition on the pressure drop gradient. The null hypothesis is rejected with a 95% confidence level, which means the heating condition does not influence the pressure drop gradient for the experimental data of this work. As discussed, the flow pattern did not suffer any influence due to the heating distribution, and as the quality at the test section inlet and outlet are similar, the acceleration pressure drop must be as well. The only change, if it existed, should be on the friction pressure drop, though the mechanisms of such are unrelatable to the heat flux distribution. One can argue that for higher heat fluxes, nucleate boiling may disturb the boundary layer and consequently influence the friction pressure drop, but it goes beyond the scope of this research and will not be addressed. Dirker, Scheepers and Meyer (2022) stated that since the heat rate applied to the fluid volume was the same for all heat distribution, the increase of bulk temperature is constant, and so is the pressure reduction over the tube length. Despite variations in heat rate in non-uniform heating cases, the little difference in quality gain in the test section led to the same conclusion.

Table 22 – One-way ANOVA test table for all data points from two-phase flow pressure drop gradient.

Source	Sum of Squares	Degree of Freedom	F-Value	P-Value	H_0
Heating condition	12.70	2	1.52	0.227	Accept
Residual	242.1	58			

Source: Author.

Figure 36 shows the comparison between the experimental Pressure Drop Gradient (PDG) with the values predicted from the correlations presented at section 2.4. The statistics metrics (MPE, MAPE, and percentage of data within 30% error) considering all experimental data points are shown for each correlation. As the pressure drop gradient increases with the quality, the conclusions drawn for one can be extended to the other. Most of the correlations failed to capture the data trend. The homogeneous models of Cicchitti *et al.*, Dukler, Wicks III and Cleveland, and Beattie and Whalley showed similar behavior by underpredicting for low values of quality and underpredicting for the higher ones. Hardik and Prabhu's correlation by calculating the parameter C from the tube diameter had a slightly better performance than the Lockhart and Martinellis. Friedel, Müller-Steinhagen and Heck, and Nie *et al.* were accurate for low quality but underpredicted as it increased. Cioncolini, Thome and Lombardi presented the best results and could capture the data trend.

Table 23 lists the statistic metrics for each correlation. Cioncolini, Thome and Lombardi's correlation presented the best performance on predicting the pressure drop gradient (MAPE$=20.41\%$) and fitted most of the data within 30% (86.89%). The correlations based on the homogeneous models showed the highest MAPE values, though Cicchitti *et al.* (1959) fitted 50.82% of the data within 30%. Despite being built on a large dataset, Nie *et al.* (2023) fitted only 27.87% of the data within 30% and presented a MAPE of 42.15%. Müller-Steinhagen and Heck (1986) presented the lowest dispersion of the predicted values, though it failed to capture the data trend, which decreased its accuracy.

Table 23 – Summary of statistic metrics for correlations comparison with $G = 150$ kg m^{-2}s^{-1} of all data points, with the best values highlighted in bold.

Model	MPE [%]	MAPE [%]	σ_ϵ [%]	±30% [%]
Lockhart and Martinelli (1949)	-20.99	36.08	35.87	37.70
Cicchitti *et al.* (1959)	41.93	57.54	79.68	50.82
Dukler, Wicks III and Cleveland (1964b)	**-2.410**	49.21	67.25	29.51
Chisholm (1973)	-1.240	47.10	55.07	29.51
Friedel (1979)	-34.84	39.88	27.68	31.15
Beattie and Whalley (1982)	**3.970**	50.91	70.96	26.23
Müller-Steinhagen and Heck (1986)	-41.50	42.77	**21.91**	27.87
Cioncolini, Thome and Lombardi (2009)	**-4.490**	**20.41**	27.52	**86.89**
Hardik and Prabhu (2016)	-22.42	33.52	31.55	42.62
Nie *et al.* (2023)	-40.34	42.15	22.35	27.87

Source: Author.

Cioncolini, Thome and Lombardi's model, based on the momentum properties, showed the best agreement with the experimental data of this work. Only the higher mass velocities, where the flow pattern was predominantly annular, were analyzed. Their model is strongly based on annular flow, which may explain why it performed better for the data.

Figure 36 – Experimental pressure drop gradient versus the value predicted for each correlation with the lines of ±15% and ±30% error for $G = 150$ kg m^{-2}s^{-1}.

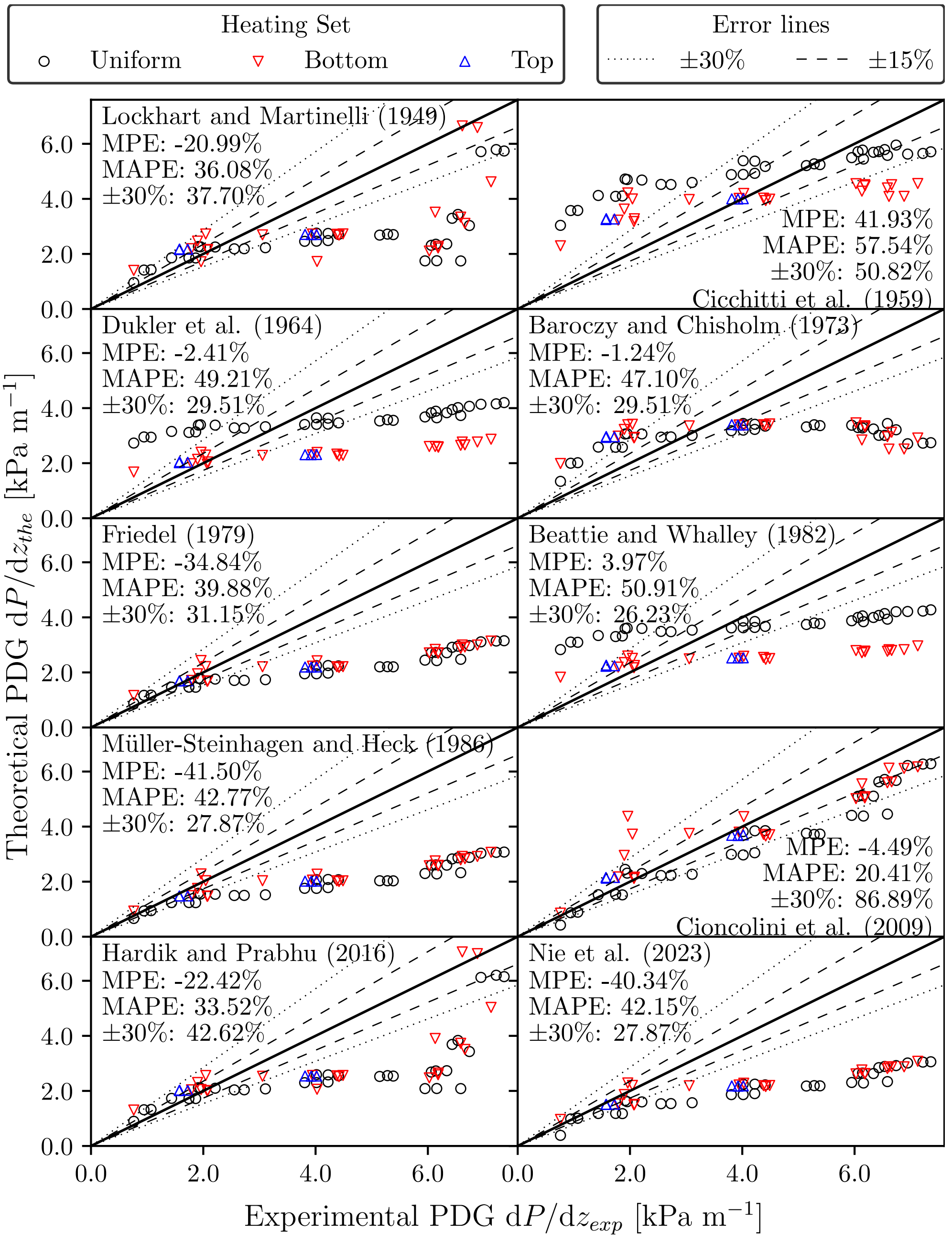

Source: Author.

4.2.4 Heat transfer coefficient

Given the limitation of the dataset in this study, which includes only one heat flux for each mass velocity, it is not possible to definitively determine the dominant heat transfer mechanism based solely on experimental data. However, upon evaluating superposition models such as those proposed by Liu and Winterton (1991), and Wattelet *et al.* (1993), it becomes apparent that convective boiling emerges as the primary heat transfer mechanism. Therefore, the results are discussed within this framework.

Figure 37 shows the heat transfer coefficient versus quality for the three sets of heating and two mass velocities. For $G = 50$ kg m^{-2}s^{-1}, the heat transfer coefficient increased with quality and decreased for values over 80%. Overall, the bottom heating showed higher HTC, which will be checked with ANOVA tests further in this work. Since the prevailing flow pattern is stratified wavy, the heat flux matches the wetted part of the tube. While for the uniform and top conditions, the heat also flows through the dry part. Although the HTC drop is not sharp, a dry out of the liquid film may be happening for high quality. For $G = 150$ kg m^{-2}s^{-1}, the HTC also increases with quality, though for values lower than 20%, the HTC for bottom heating was lower than for the uniform cases. When the quality was over 20%, the heating condition appeared to not influence the HTC, except when heating from the top. As for the low mass velocity case, this may happen due to the development of the flow patterns since from quality higher than 20%, the regime was annular. Typically, the top heating presented lower HTC than uniform and bottom heating for both mass velocities.

Figure 37 – Experimental heat transfer coefficient versus quality for the three heating conditions (uniform, bottom, and top): (a) $G = 50$ kg m^{-2}s^{-1}, $T_{sat} = 34$ °C, $q'' = 3.4$ kW m^{-2}; (b) $G = 150$ kg m^{-2}s^{-1}, $T_{sat} = 39$ °C, $q'' = 10.5$ kW m^{-2}.

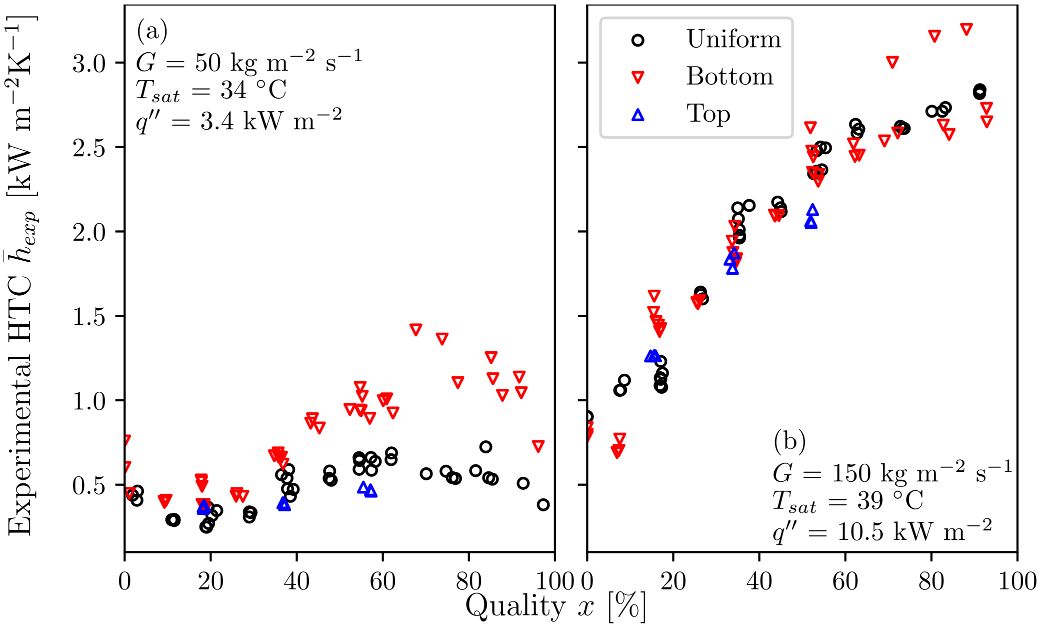

Source: Author.

Figure 38 illustrates the average value of HTC and quality, binned into 11 groups for each mass velocity. This approach allows a better understanding of how the HTC varies with quality. For $G = 50$ kg m^{-2}s^{-1}, the HTC drop is sharper for the bottom heating than for the uniformly heated. From quality lower than 40%, the HTC was systematically higher for the bottom heating case, and that difference increased for quality over 40%. The HTC for uniform heating reached a plateau from quality over 50% and started dropping from 70% and over. For the bottom heating, the HTC increased until quality reached approximately 70%, and it started dropping for higher values. The top heating seemed to follow the same trend as the bottom and uniform heating, although it presented lower values of HTC. For $G = 150$ kg m^{-2}s^{-1}, there was a sharp increase in HTC for the bottom heated from 10% to 20% of quality. The same was seen for the uniformly heated for quality from 20% to 30%. Overall, the bottom and uniform heating condition did not seem to influence the HTC for quality higher than 30%, which matches the transition from intermittent to annular flow. Despite being annular, the top heating presented lower HTC and seemed to reach a plateau earlier than the bottom and uniform heating.

Figure 38 – Average experimental heat transfer coefficient versus quality for the three heating conditions (uniform, bottom, and top): (a) $G = 50$ kg m^{-2}s^{-1}, $T_{sat} = 34$ °C, $q'' = 3.4$ kW m^{-2}; (b) $G = 150$ kg m^{-2}s^{-1}, $T_{sat} = 39$ °C, $q'' = 10.5$ kW m^{-2}.

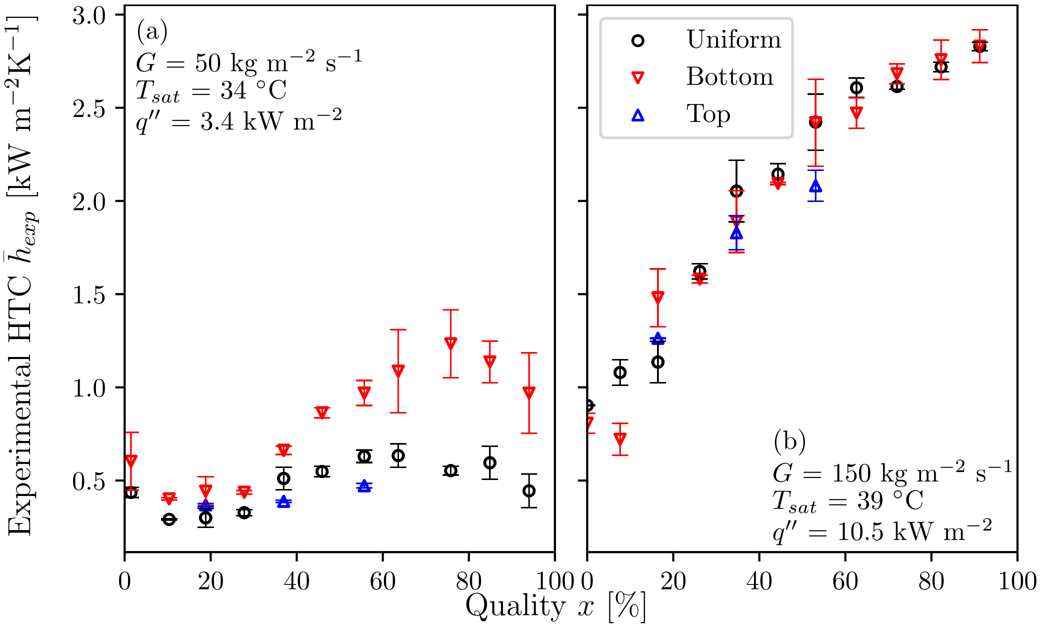

Source: Author.

An ANOVA analysis was conducted to assess the statistical significance of the heating condition's influence on the HTC. This analysis considered only the liquid Reynolds number, the heating condition, and their interaction as influencing factors. The Reynolds number had a cardinality of 23, while the heating condition presented a cardinality of three. The null hypothesis H_0 states that the given factor (Re$_l$, heating condition, and interaction) does not significantly influence the HTC. The null hypothesis is rejected when the p-value falls below 0.05 (at a 95% confidence level), indicating that the factor indeed influences the HTC.

Table 24 shows the two-way ANOVA table for all the data points. The ANOVA test rejected the null hypothesis for all factors, which means they do influence the HTC. However, as previously mentioned, the heating condition appears to have no significant impact on the HTC under annular flow conditions. Consequently, aiming to assess the significance of the factors, two ANOVA tests were conducted: one that included only the annular flow data points and another that excluded them.

Table 25 shows the two ANOVA tables analysis, one with only annular flow data points and the other without them. As can be noted, the ANOVA test accepts the null hypothesis for the heating condition and the interaction between the factors when accounting for only the

Table 24 – Two-way ANOVA test table for all data points from two-phase flow experiments.

Source	Sum of Squares [$\times 10^4$]	Degree of Freedom	F-Value	P-Value	H_0
Heating condition	1.315	2	37.21	< 0.05	Reject
Liquid Reynolds number	367.1	22	944.3	< 0.05	Reject
Interaction	7.613	44	9.793	< 0.05	Reject
Residual	2.368	134			

Source: Author.

annular flow data points. That corroborates the observation made from Figure 38, i.e., the heating condition does not influence the HTC when the flow is annular. The liquid Reynolds number still influences the HTC significantly (null hypothesis rejected), which is expected for convective flow boiling heat transfer. On the other hand, the second ANOVA test - without annular data points - rejects the null hypothesis for the three factors, i.e., the heating condition, liquid Reynolds number, and the interaction between them, significantly influence the HTC.

Table 25 – Two-way ANOVA test tables with and without annular data points from two-phase flow experiments.

Source (only Annular)	Sum of Squares [$\times 10^3$]	Degree of Freedom	F-Value	P-Value	H_0
Heating condition	1.013	2	1.677	0.198	Accept
Liquid Reynolds number	157.0	8	64.98	< 0.05	Reject
Interaction	9.765	16	2.021	0.053	Accept
Residual	13.90	46			
Source (without Annular)	**Sum of Squares [$\times 10^4$]**	**Degree of Freedom**	**F-Value**	**P-Value**	**H_0**
Heating condition	1.198	2	53.87	< 0.05	Reject
Liquid Reynolds number	13.12	13	90.78	< 0.05	Reject
Interaction	5.271	26	18.23	< 0.05	Reject
Residual	0.9784	88			

Source: Author.

Wang *et al.* (2019) and Dirker, Scheepers and Meyer (2022) applied higher heat fluxes for the non-uniform heating than for the uniform cases to keep the same heat transfer rate regardless of the region of the tube to which the heat was applied. Thus, independent of how the heat transfer occurs inside the tube, the heat flux density will be higher for the non-uniform cases than for the uniform. Wang *et al.*'s work, specifically, worked with higher heat fluxes, and by keeping the same heat rate, it goes from 11.2 (uniform heating) to 22.4 kW m^{-2} (bottom heating). According to Lillo *et al.* (2019) and Mastrullo, Mauro and Viscito (2019) nucleate boiling heat transfer mechanism is dominant for high heat fluxes (>20 kW m^{-2}) even at higher mass velocities (>300 kg $\mathrm{m}^{-2}\mathrm{s}^{-1}$). Wang *et al.* (2019) attributes the higher HTC from bottom heating to the higher density of heat on the bottom part of the tube, which favors nucleation sites to be active, enhancing the nucleate boiling HTC and, consequently, the HTC overall. Dirker, Scheepers and Meyer (2022) found that even for higher heat flux at the bottom part of the tube, the local HTC was equivalent to the uniformly heated, with a slight decrease at the very bottom. Since their research was limited to annular flow, the heat flux levels were low enough for the heat transfer to be dominated by convective boiling effects, even for bottom heating, where it showed higher heat flux at the heated region. Heat flux is a usual parameter for correlating nucleate boiling HTC; as heat flux increases, so does the HTC. However, for this work, the heat flux was kept constant for all heating conditions, i.e., the heat rate was lower for the non-uniform cases than for the uniform ones.

Figure 39 illustrates the inner heat flux distribution for six experimental points at quality around 0.55 for the two mass velocities and each heating condition at the same heat flux level applied on the outer surface of the tube. As can be seen, the heat flux is almost uniform for the uniformly heated case and concentrates in the lower and upper half of the tube for the bottom and top heating conditions, respectively, for both mass velocities. For $G = 150$ kg m^{-2}s^{-1}, the heat flux magnitude on the bottom and top heating are comparable to the uniform case. However, for $G = 50$ kg m^{-2}s^{-1}, the heat flux magnitude on the bottom and top heating are lower than the uniform case. Although the magnitude is lower, the scale of the heat fluxes are equivalent and thus should be the heat transfer mechanisms. Therefore, for this work, the increase in HTC for the bottom heating must come from another mechanism other than what Wang *et al.* (2019) suggested.

Figure 39 – Inner heat flux distribution in $\hat{r}$ direction for the three heating conditions (— uniform, — bottom, and — top) for $x \approx 0.55$ and mass velocities of (a) 50 kg m^{-2}s^{-1} and (b) 150 kg m^{-2}s^{-1}.

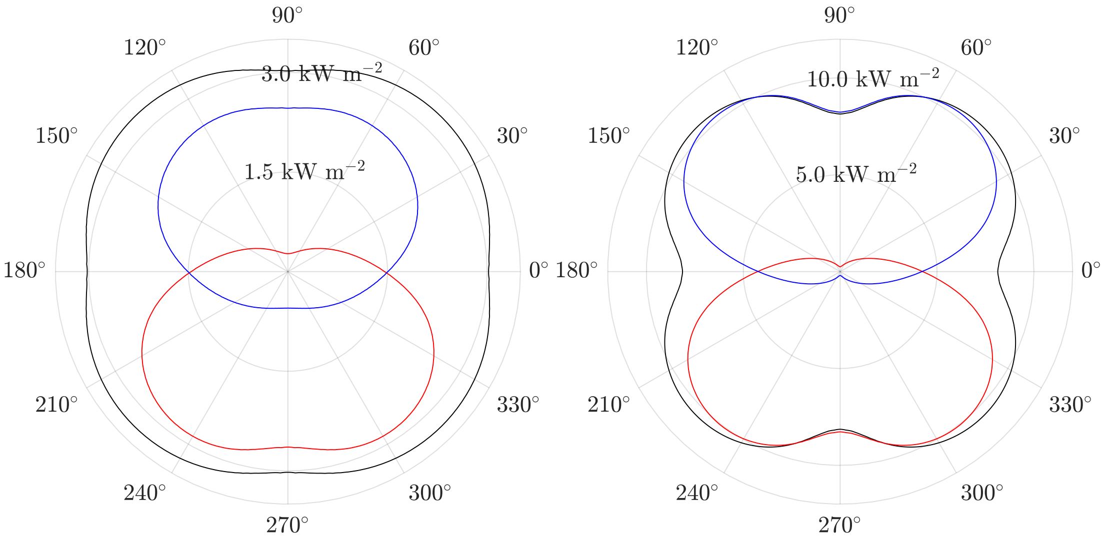

(a) $G \approx 50$ kg m^{-2}s^{-1} (b) $G \approx 150$ kg m^{-2}s^{-1}

Source: Author.

For uniform heating, the heat flows through the tube wall preferentially in one direction, radially from outside to inside, while for non-uniform cases, heat will also flow through the tube wall in the azimuthal direction. When the HTC is higher, heat preferentially flows in the radial direction; on the other hand, part of the heat will flow through the tube wall as the HTC decreases. That becomes evident from Figure 39a and Figure 39b, the heat fluxes spread less through the wall for the higher mass velocity, which presented higher HTC. As mentioned earlier, the flow pattern for the lower mass velocity is mainly stratified-wavy, and the liquid phase concentrates on the bottom half of the tube, matching the heat flux distribution for the bottom heating. Therefore, the gross heat is transferred through the wetted part of the tube, decreasing the superheat of the upper wall and increasing the local mean HTC. In contrast, the vapor phase accumulates on the upper half, matching the heat flux distribution for the top heating. Hence, heat transfer predominantly occurs within the dry part of the tube, which is less effective than with the wetted one. On top of that, it is evident that the nucleating boiling might deteriorate with the vapor accumulation and quick drying of the wall at the top of the tube. With a lower HTC, heat is more likely to flow through the tube wall for top heating. That is seen by the heat flux magnitude for top heating at 270° and for bottom heating at 90°, which is lower for the first one.

Thus, contrary to the Wang *et al.* (2019) work, it is believed that the HTC increased because of the matching between the heat flux distribution with wetted perimeter, i.e., due to the increase in forced convection. This observation aligns with the findings of the ANOVA test, which showed that in the case of annular flow, where the entire tube perimeter is wetted, the heating condition has no significant influence on the HTC. As a result, all heat transfer occurs through the liquid phase, no matter the heat flux distribution. In contrast, for the non-annular flow, there is always an accumulation of liquid on the lower half and vapor on the upper half, matching the heat flux distribution for the non-uniform heating conditions.

The comparison between the experimental and the predicted HTC, by the correlations presented at section 2.5, was divided into two groups, one for each mass velocity. The statistic metrics are presented for uniform heating and the entire dataset. This analysis provides an overview of how each correlation performs against the independent data of this work.

Figure 40 shows the comparison of the values predicted by the correlations and the experimental heat transfer coefficient for $G = 50$ kg m^{-2}s^{-1}. The MPE, MAPE, and percentage of data points within $\pm 30\%$ error interval, considering only uniform heating data points, are presented for each correlation. Since all correlations are built for uniform heating, they underestimated the bottom HTC and overestimated it for the top heating compared to the uniformly heated one. However, Fang, Wu and Yuan's correlation did not follow that trend and overestimated the HTC for the non-uniform heating cases compared to the uniform. Shah's, Kandlikar's, Liu and Winterton's, and Del Col's models presented similar trends, all of them overpredicted the HTC for uniform heating. Gungor and Winterton's, Wattelet *et al.*'s, Wojtan, Ursenbacher and Thome's and Wang *et al.*'s presented better agreement, but the data scattered over the 0% error line. Klimenko's and Cioncolini and Thome's correlations presented opposite behavior, while the first underpredict, the last overpredict the HTC heavily. It is unfair to evaluate Cioncolini and

Thome's HTC prediction for other flow patterns since the model is built for annular flow only. The correlation from Jabardo, Bandarra Filho and Lima presents better agreement than most with lower scattering. However, it showed a slight deviation from the match line, overpredicting the low values and underpredicting the higher ones. Fang, Wu and Yuan's correlation was accurate and had the lowest scattering for the uniform heating but overpredicted for the non-uniform cases. Except for Wang *et al.*, the models were built considering a uniformly heated pipe. Therefore, some deviation due to the heating condition is expected.

Figure 40 – Experimental heat transfer coefficient versus the value predicted for each correlation with the lines of ±15% and ±30% error for $G = 50$ kg m^{-2}s^{-1}.

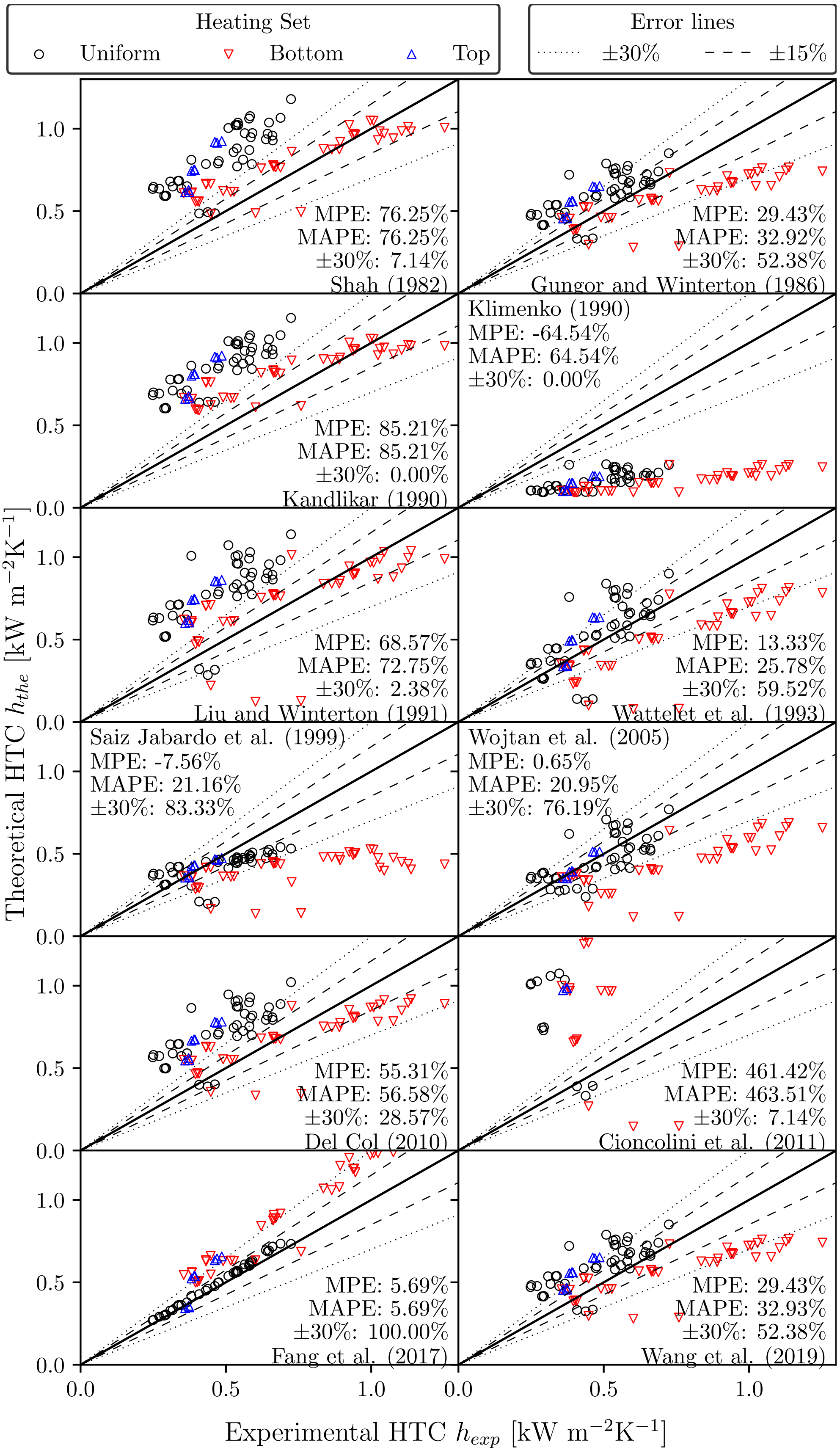

Source: Author.

Table 26 shows the MPE, the MAPE, the residuals standard deviation, and the percentage of data within $\pm 30\%$ error interval for each model considering only the uniform heating data points with $G = 50$ kg m^{-2}s^{-1}. The correlation of Fang, Wu and Yuan was the one that better fitted the data, with an MPE of 5.69% and MAPE of 5.69%. Their model also fitted all the data within the $\pm 30\%$ error interval and presented the lower dispersion ($\sigma_{\epsilon;u} = 1.92\%$). Jabardo, Bandarra Filho and Lima's and Wojtan, Ursenbacher and Thome's correlations had similar performance, they fitted 83.33% and 76.19% of the data into the $\pm 30\%$ error interval, respectively. Despite Klimenkos showing lower scattering, it failed to fit any data point within $\pm 30\%$. Kandlikar's also failed to fit any data point within $\pm 30\%$. In general, his model showed a systematic deviation from the experimental values. That might be attributed to the fluid-dependent parameter, which is undefined for R141b, and its accuracy might improve for a better-fitted value.

Table 26 – Summary of statistic metrics for correlations comparison with $G = 50$ kg m^{-2}s^{-1} of only the uniform heating condition data points, with the best values highlighted in bold.

Model	MPE$_u$ [%]	MAPE$_u$ [%]	$\sigma_{\epsilon;u}$ [%]	$\pm 30\%_u$ [%]
Shah (1982)	76.25	76.25	34.21	7.14
Gungor and Winterton (1986)	29.43	32.92	29.22	52.38
Kandlikar (1990)	85.21	85.21	36.83	0.00
Klimenko (1990)	-64.54	64.54	8.480	0.00
Liu and Winterton (1991)	68.57	72.75	43.50	2.380
Wattelet *et al.* (1993)	13.33	25.78	32.54	59.52
Jabardo, Bandarra Filho and Lima (1999)	-7.56	21.16	24.32	83.33
Wojtan, Ursenbacher and Thome (2005b)	0.65	20.95	25.00	76.19
Del Col (2010)	55.31	56.58	35.07	28.57
Cioncolini and Thome (2011)	461.4	463.5	646.7	7.14
Fang, Wu and Yuan (2017)	**5.69**	**5.69**	**1.92**	**100.0**
Wang *et al.* (2019)	29.43	32.93	29.23	52.38

Source: Author.

Table 27 shows the MPE, the MAPE, the residuals standard deviation, and the percentage of data between $\pm 30\%$ error interval for each correlation considering all the data points with $G = 50$ kg m^{-2}s^{-1}. All the correlations that overestimated the HTC improved the MAPE value, mainly because of the agreement with the bottom heating data points. The non-uniformly heated data points decreased the performance of the Fang *et al.*'s correlation. The average wall temperature for non-uniform heating is lower when compared to the uniformly heated, thus influencing their correlation prediction. Despite overestimating the HTC for non-uniform heating, Fang, Wu and Yuan's correlation still showed the lowest MAPE (20.24%) and fitted 70.97% of the points within $\pm 30\%$. Since Wang *et al.*'s correlation is only a modification of the suppression factor from Wang *et al.*'s correlation, their performance was very similar. Wattelet *et al.* and Wojtan, Ursenbacher and Thome were very similar as well, with MAPE of 27.70% and

27.07%, respectively. Since the model of Wojtan, Ursenbacher and Thome is pattern-based, the HTC calculation depends on the flow pattern map prediction, which can decrease its accuracy. Jabardo, Bandarra Filho and Lima (1999)'s correlation also had similar performance and fitted 59.14% of the data within $\pm 30\%$ with lower scattering ($\sigma_{\epsilon;u} = 27.94\%$) than most, though it has underpredicted the values for bottom heating condition heavily.

Table 27 – Summary of statistic metrics for correlations comparison with $G = 50$ kg m^{-2}s^{-1} of all data points, with the best values highlighted in bold.

Model	MPE [%]	MAPE [%]	σ_ϵ [%]	$\pm 30\%$ [%]
Shah (1982)	48.07	52.03	43.74	37.63
Gungor and Winterton (1986)	**8.24**	29.48	34.64	**60.22**
Kandlikar (1990)	55.91	59.39	47.13	32.26
Klimenko (1990)	-70.55	70.55	**9.38**	0.00
Liu and Winterton (1991)	41.19	51.59	49.27	35.48
Wattelet *et al.* (1993)	**-5.90**	**27.70**	34.27	58.06
Jabardo, Bandarra Filho and Lima (1999)	-21.83	28.72	27.94	**59.14**
Wojtan, Ursenbacher and Thome (2005b)	-16.67	**27.07**	28.51	54.84
Del Col (2010)	29.89	40.97	41.57	47.31
Cioncolini and Thome (2011)	336.7	341.8	486.6	3.23
Fang, Wu and Yuan (2017)	19.70	**20.24**	**19.45**	**70.97**
Wang *et al.* (2019)	**8.24**	29.48	34.64	**60.22**

Source: Author.

Figure 41 shows the comparison of the values predicted by the correlations and the experimental heat transfer coefficient for $G = 150$ kg m^{-2}s^{-1}. The MPE, MAPE, and percentage of data points within $\pm 30\%$ error interval, considering only uniform heating data points, are presented for each correlation. Less deviation on the HTC is expected from the heating condition since its effect seems smaller for high mass velocity compared to the lower one. All the correlations, but Klimenkos, showed good performance for higher mass velocity, with some deviation for lower and higher values of HTC. For higher mass velocity, the HTC continuously increases with quality, i.e., the trend for underpredicting low or high values of HTC is intrinsically related to the vapor quality. Shah's correlation and the ones derived from Gungor and Winterton's work - Liu and Winterton, Del Col, and Wang *et al.* - presented similar behavior. Wojtan, Ursenbacher and Thome's correlation incresed the overprediction for higher quality, while Jabardo, Bandarra Filho and Lima's underpredicted it. As for the lower mass velocity, Fang *et al.* captured the HTC trend for the uniformly heated data points, though it overpredicted the values for the non-uniform cases. It was expected a better performance from Cioncolini and Thomes since most of the data is for annular flow, though it systematically overpredicted the HTC.

Figure 41 – Experimental heat transfer coefficient versus the value predicted for each correlation with the lines of ±15% and ±30% error for $G = 150$ kg m^{-2}s^{-1}.

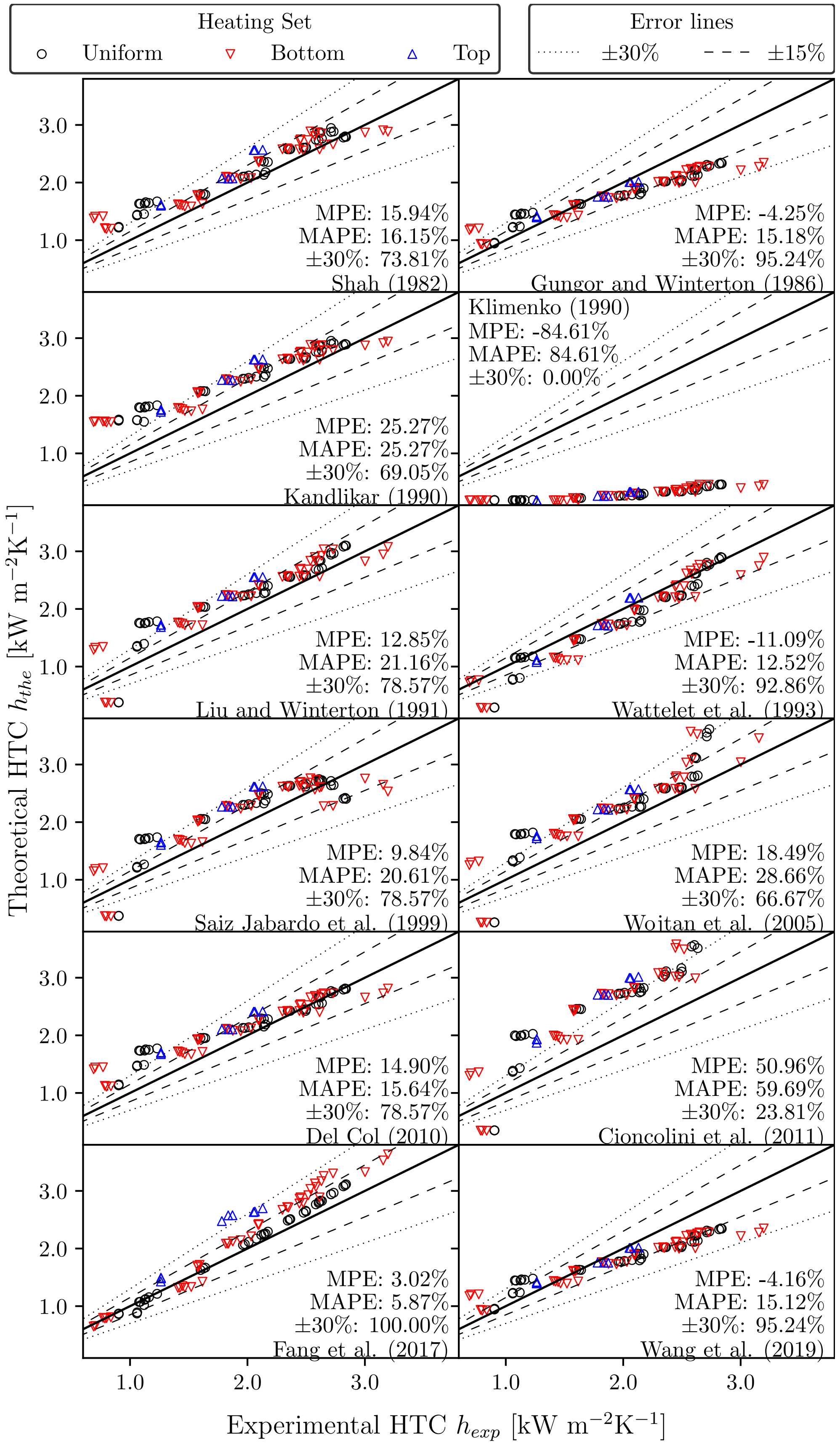

Source: Author.

Table 28 shows the MPE, the MAPE, the residuals standard deviation, and the percentage of data between ±30% error interval for each model considering only the uniform heating data points with $G = 150$ kg m^{-2}s^{-1}. As for the lower mass velocity, Fang, Wu and Yuan's model, with a MAPE of 5.87%, presented the best accuracy for the higher mass velocity. The model also fitted all data points within ±30% of error. Gungor and Winterton's and Wang *et al.*'s performances are also worth mentioning, both fitting more than 95% of the data within ±30% error and presented MAPE of 15.18% and 15.12%, respectively. Overall, many correlations presented MAPE lower than 30%, except Klimenko and Cioncolini and Thome, with the first failing to fit any point within ±30%.

Table 28 – Summary of statistic metrics for correlations comparison with $G = 150$ kg m^{-2}s^{-1} of only the uniform heating condition data points, with the best values highlighted in bold.

Model	MPE$_u$ [%]	MAPE$_u$ [%]	$\sigma_{\epsilon;u}$ [%]	±30%$_u$ [%]
Shah (1982)	15.94	16.15	16.10	73.81
Gungor and Winterton (1986)	-4.250	15.18	16.57	**95.24**
Kandlikar (1990)	25.27	25.27	23.65	69.05
Klimenko (1990)	-84.61	84.61	**2.11**	0.000
Liu and Winterton (1991)	12.85	21.16	26.20	78.57
Wattelet *et al.* (1993)	-11.09	12.52	18.00	92.86
Jabardo, Bandarra Filho and Lima (1999)	9.840	20.61	26.23	78.57
Wojtan, Ursenbacher and Thome (2005b)	18.49	28.66	31.71	66.67
Del Col (2010)	14.90	15.64	19.89	78.57
Cioncolini and Thome (2011)	50.96	59.69	52.53	23.81
Fang, Wu and Yuan (2017)	**3.02**	**5.87**	**6.26**	**100.0**
Wang *et al.* (2019)	-4.16	15.12	16.54	**95.24**

Source: Author.

Table 29 shows the MPE, the MAPE, the residuals standard deviation, and the percentage of data between ±30% error interval for each model considering all the data points and only uniform heating with $G = 150$ kg m^{-2}s^{-1}. As mentioned, the heating condition influence over the HTC is lower for the higher mass velocity, and the performances of the correlations were similar for all data points and only uniformly heated ones. When analyzing all data points, Fang, Wu and Yuan presented the lowest MAPE (10.88%) and fitted 96.77% of data points within ±30% error. Wattelet *et al.* also proved to be accurate with a 12.39% MAPE and fitting 92.47% within ±30% error. The correlations of Gungor and Winterton and Wang *et al.* also fitted a satisfactory amount of data within ±30% error (94.62%). Despite the lower scattering of the data ($\sigma_\epsilon = 2.95\%$), Klimenko presented the worst accuracy among the correlations, unable to fit any of the data points within 30% of error.

The correlations showed better agreement with higher mass velocity. Fang, Wu and Yuan had the best MAPE for both and predicted 100% of the datapoints within ±30% error band.

Table 29 – Summary of statistic metrics for correlations comparison with $G = 150$ kg m^{-2}s^{-1} of all data points, with the best values highlighted in bold.

Model	MPE [%]	MAPE [%]	σ_ϵ [%]	$\pm 30\%$ [%]
Shah (1982)	16.93	17.58	20.10	81.72
Gungor and Winterton (1986)	**-3.51**	14.59	18.67	**94.62**
Kandlikar (1990)	26.35	26.78	27.50	75.27
Klimenko (1990)	-84.53	84.53	**2.95**	0.00
Liu and Winterton (1991)	14.29	21.89	25.81	80.65
Wattelet *et al.* (1993)	-10.79	**12.39**	**16.95**	**92.47**
Jabardo, Bandarra Filho and Lima (1999)	11.03	21.06	25.04	81.72
Wojtan, Ursenbacher and Thome (2005b)	19.26	28.28	30.37	69.89
Del Col (2010)	15.79	17.18	22.41	80.65
Cioncolini and Thome (2011)	50.77	58.41	51.86	17.20
Fang, Wu and Yuan (2017)	8.04	**10.88**	**11.07**	**96.77**
Wang *et al.* (2019)	**-3.42**	14.52	18.64	**94.62**

Source: Author.

Many correlations presented MAPE lower than 30%, which is satisfactory for two-phase flow boiling. Despite overpredicting the HTC for the lower mass velocity, classical correlations had good performance for the higher one. The correlation of Wang *et al.* did not show relevant improvement on the Gungor and Winterton's prediction of the HTC for bottom heating. The approach of Fang, Wu and Yuan on the liquid viscosity at the wall temperature seems to capture some of the non-uniform heating effects on the HTC. However, in many practical cases, the wall temperature is unknown and is the objective of the heat transfer analysis.

4.2.5 Temperature distribution on tube wall

The circumferential wall temperature distribution might be a problem for very long tubes, such as the ones for CSP with DSG. As Serrano-Aguilera, Valenzuela and Parras (2014) showed, these temperature gradients can induce thermal stresses on the tube, causing bending and leading to failure. The standard deviation between the wall temperatures (T_t, T_s, and T_b) for each experimental point was used as a measure of the cross-section temperature distribution. Besides that, the variation of the top and bottom wall temperatures with quality was also discussed.

Figure 42 illustrates the wall temperature standard deviation variation with quality for both mass velocities and three heating conditions. In general, the standard deviation decreased with quality, though for the lower mass velocity and uniform heating, it started increasing from qualities higher than 60%. Although the standard deviation is not the circumferential temperature gradient, it does give an idea of its behavior, i.e., the higher the standard deviation, the greater the temperature gradient, and consequently, the thermal stress increases. The standard deviation for uniform heating and low mass velocity has three distinct regions. The first one for low quality (up to 20%) is characterized by the standard deviation raise, i.e., circumferential temperature gradient increase. For moderate quality, ranging from 20% to 60%, the temperature gradient decreases as quality increases. The last one for high quality, from 60% and higher, the standard deviation increased again. This behavior not only brings the thermal stresses circumferentially but also in the axial direction, which favors the bending of the tube.

Figure 42 – Wall temperature standard deviation for the cross-section of the tube against quality and two mass velocities.

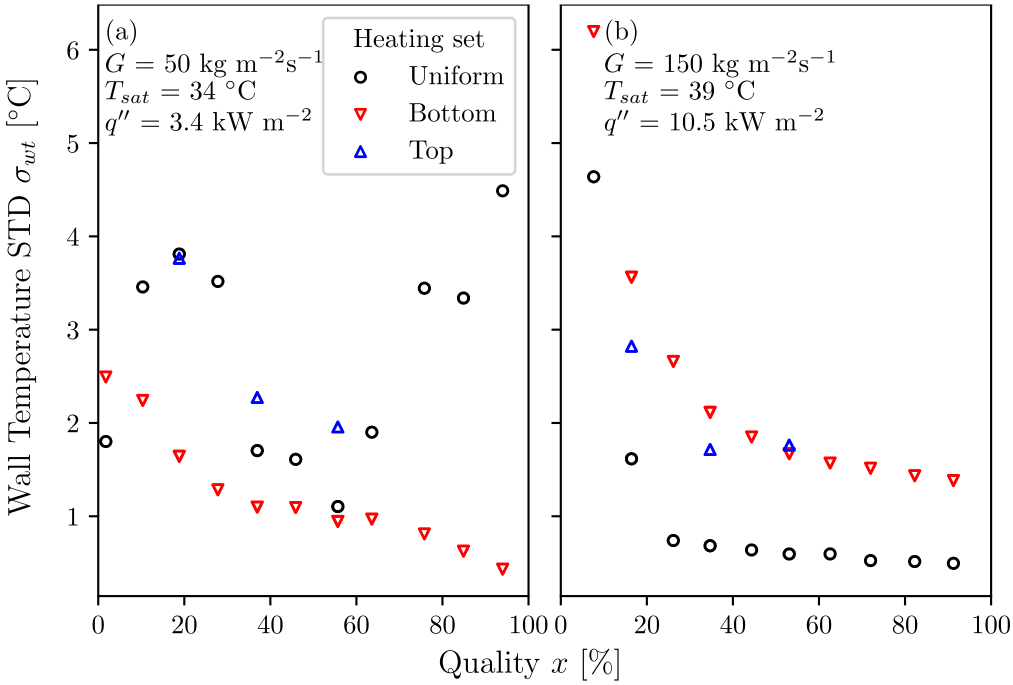

Source: Author.

The standard deviation for bottom heating and low mass velocity decreases with quality continuously. That means the circumferential temperature gradient is also decreasing, and consequently, the thermal stress on the tube wall. The top heating had a similar behavior as the other heating conditions for the range of quality tested. Unfortunately, there is no information for higher quality and top heating.

For higher mass velocity, the standard deviation decreases with quality reaching a plateau. The uniform heating presented a lower temperature gradient than the bottom heating, which indicates that the wall temperature is more homogeneous for the uniformly heated case than the bottom one. That may happen due to the flow pattern being annular and higher HTC. Since the heat flux is non-uniform, for the bottom and top heating, there will always be a temperature gradient on the tube wall, even for annular flow and higher HTC. It seems that the top heating reaches a plateau for lower quality than the bottom heating, but no conclusions were taken due to the lack of data points for higher qualities.

Although the wall temperature standard deviation can give insights into the circumferential temperature gradient, the top and bottom wall temperatures translate the heat transfer more directly. Figure 43 illustrates the top and bottom wall temperature variation with quality and the two mass velocities. As can be seen, for the low mass velocity and uniform heating, the top wall temperature drives the standard deviation. The bottom temperature decreases with quality, while the top one varies with the same trend as the standard deviation. The bottom and top wall temperatures are very similar for the lowest quality. Since the flow pattern is slug flow, the wall perimeter is wet, and the heat transfer occurs through the liquid phase. As quality increases, the slugs elongate, and most of the top wall transfers heat through the vapor phase. As it increases further, the flow pattern becomes stratified wavy, and the HTC increases, decreasing the top wall temperature. Since the bottom part is always wet, the heat transfer occurs only through the liquid phase, and as the HTC increases, the wall temperature decreases. From quality over 60%, the temperature difference between the top and bottom increases from ≈2 °C to ≈8 °C. That suggests that partial dryout might occur intermittently rather than conclusively.

Figure 43 – Top and bottom wall temperature against quality and two mass velocities.

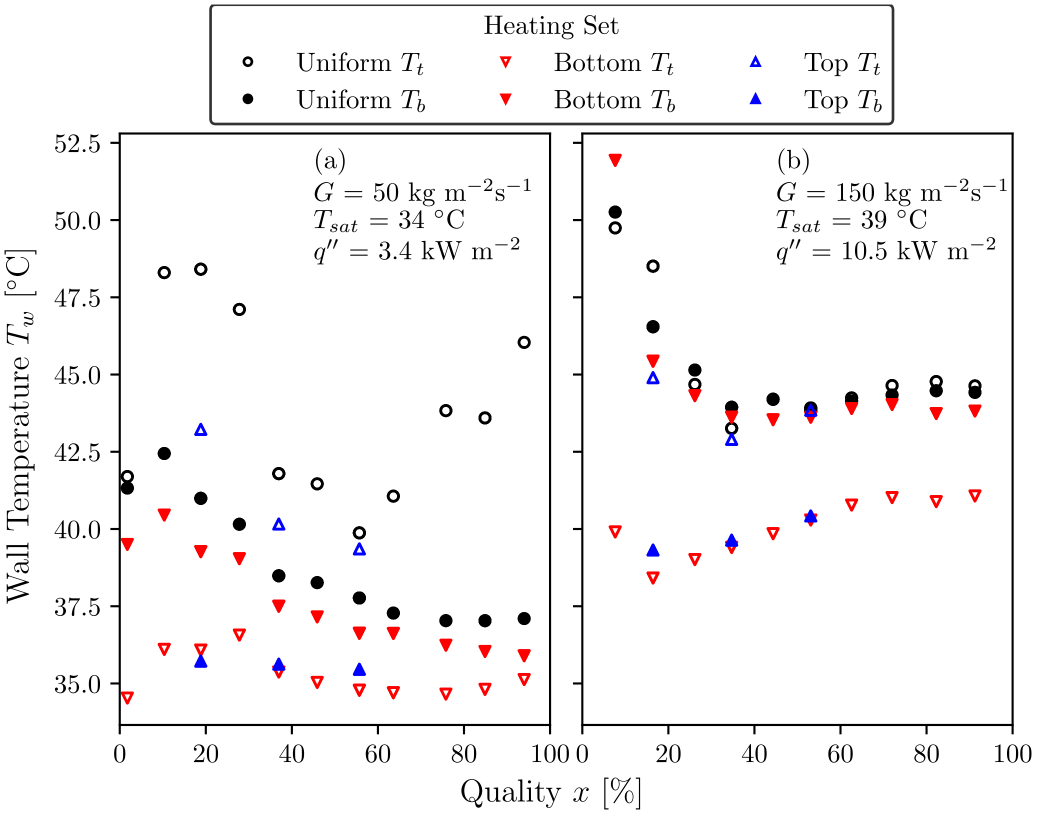

Source: Author.

For the bottom heating and lower mass velocity, as the quality increases, the top wall temperature remains constant, and the bottom one decreases. The top and bottom wall temperatures under the bottom and top heating conditions, respectively, approached T_{sat}. For higher quality and bottom heating, the top wall temperature is slightly increasing, which suggests the intermittently partial dryout seen for the uniformly heated case.

The wall temperatures showed similar behavior for all three heating conditions and higher mass velocity. Overall, the temperatures in the heated region were very close despite the heating conditions. The temperatures at the unheated part of the tube were close to the T_{sat}, suggesting most heat transfer occurs through the heated perimeter. As quality increases, the bottom and top temperature temperature differences decrease. The top and bottom wall temperatures were very close for the uniformly heated tube, which shows why the standard deviation was lower than the non-uniform cases.

Even though Dirker, Scheepers and Meyer (2022) applied the same heat rate for the non-uniform cases and studied only annular flow, they found similar results. The bottom heating showed a higher temperature gradient than the uniformly heated case. However, while for this work, the wall temperatures were lower for bottom heating conditions, Dirker, Scheepers and Meyer's were higher. Once more, this difference might be due to the higher heat rate for the bottom heating used by them.

As expected, the heating condition influences the circumferential wall temperature distribution, and depending on the flow pattern, it can decrease or increase the thermal stresses on the tubes compared to the uniformly heated case. For horizontal flow boiling, where gravity shapes the flow patterns (mainly stratified-wavy), the bottom heating leads to lower thermal stresses than the uniformly heated case. While for higher mass velocities and annular flow, the uniformly heated tube presented lower thermal stress.

4.2.6 Dimensionless group analysis

Maliska (1990) showed that the dimensionless numbers can be derived from scaling analysis. He shows that the Reynolds number for single-phase flow can be represented as the ratio of advection and diffusion of momentum in the flow direction. This approach considers the main transport mechanisms, which allows for a deeper understanding of the physical phenomena. Based on that, the two-phase flow Reynolds number can be built on the ratio of the vapor and liquid advection and diffusion as follows:

$$\frac{A_l^M + A_v^M}{D_l^M + D_v^M} \sim \frac{\rho_l u_l u_l + \rho_v u_v u_v}{\mu_l \dfrac{\partial u_l}{\partial r} + \mu_v \dfrac{\partial u_v}{\partial r}}, \tag{186}$$

where A_l^M and A_v^M are the advection of momentum by the liquid and vapor, respectively, and D_l^M and D_v^M are the diffusion of momentum by the liquid and vapor, respectively. The liquid and vapor velocities (u_l and u_v) can be scaled as the liquid and vapor surface velocities:

$$u_l \sim \frac{G\,(1-x)}{\rho_l\,(1-\alpha)} \text{ and } u_v \sim \frac{G\,x}{\rho_v\,\alpha}, \tag{187}$$

while $\partial u_l/\partial r$ and $\partial u_l/\partial r$ can be scaled as:

$$\frac{\partial u_l}{\partial r} \sim \frac{u_l}{d_{in}} \text{ and } \frac{\partial u_v}{\partial r} \sim \frac{u_v}{d_{in}}. \tag{188}$$

By combining Equation 187 and Equation 188 with Equation 186, and after some manipulation yields:

$$\mathrm{Re}_{2\phi} = \frac{G\, d_{in}}{\mu_l} \left[\frac{(1-x)}{(1-\alpha)} + \frac{x}{\alpha} S_f \right] \left(S_f + \frac{\mu_l}{\mu_v} \right)^{-1}, \tag{189}$$

where S_f is the slip factor, which can be written as:

$$S_f = \frac{\rho_l}{\rho_v} \frac{x}{(1-x)} \frac{(1-\alpha)}{\alpha}. \tag{190}$$

Considering that the momentum diffusion close to the tube wall is higher for the liquid phase than the vapor, the two-phase Reynolds number can also be written as the ratio of the liquid and vapor momentum advection and the liquid momentum diffusion only. Similar to what was done before, the two-phase Reynolds number can also be written as:

$$\mathrm{Re}_{2\phi} = \frac{G\, d_{in}}{\mu_l} \left[\frac{(1-x)}{(1-\alpha)} + \frac{x}{\alpha} S_f \right]. \tag{191}$$

To make it less confusing, the two-phase Reynolds number from Equation 186 will be called $\mathrm{Re}_{2\phi;2}$, and the one from Equation 191 $\mathrm{Re}_{2\phi;1}$. The 1 and 2 subscript refers to the liquid, and liquid and vapor momentum diffusion, respectively, considered in the analysis.

A comprehensive analysis of the dimensionless parameters from subsection 2.5.1 allows for assessing their relevance in predicting the two-phase Nusselt number. Therefore, the dimensionless parameters were calculated for each experimental point. The two-phase Nusselt number was calculated as follows:

$$\mathrm{Nu}_{tp} = h_{tp} \frac{d_i}{\kappa_l}. \tag{192}$$

The tube's inner diameter d_i was chosen as a characteristic length to make it independent of the flow pattern and the liquid thermal conductivity κ_l because most heat transfer occurs through the liquid phase. The dataset has 42 features, including 40 continuous variables (dimensionless parameters and the target Nu_{tp}) and two categorical variables (heating condition and flow pattern).

A mutual information analysis measures how much knowledge of a feature decreases the uncertainty of a target (Nu_{tp}). As presented in section C.7, it can capture any relationship between the feature and the target, even for categorical ones. The heating condition and flow pattern were encoded with Pandas package function “Series.factorize” for mutual information score calculation. As done by Lin *et al.* (2022), the dimensionless groups were categorized for a better understanding of the contribution of each mechanism or property relationship to the Nusselt number.

The forced convection set comprehends all the relations and variations of the Convection number, Froude number, Lockhart-Martinelli parameter, liquid Nusselt Number, Peclet number, Prandtl number, and Reynolds number. The nucleate boiling set includes the Boiling number, molecular weight, pressure parameter from Klimenko's work, and reduced pressure. All variations of the Bond number, Laplace constant from Klimenko's work, and Weber number were selected for the surface tension effects set. Finally, a set compiles the remaining features, such as the flow pattern, heating condition, and property ratios.

Figure 44 illustrates the Mutual Information scores (MI scores) for the forced convection set of dimensionless parameters. Both two-phase Reynolds numbers, derived from the ratio between the momentum advection and momentum diffusion of the liquid and vapor Equation 186 and Equation 191, presented the higher MI score, i.e., the lower uncertainty over the two-phase Nusselt number. Their value was even better than the ratio of the two-phase Nusselt number and the liquid Nusselt number, commonly used parameters to correlate the HTC. The liquid Reynolds number presented the best MI score of the standard variations of Reynolds numbers. The vapor and liquid Prandtl numbers showed similar values of MI score, much higher than the two-phase Prandtl number from Dorao, Drewes and Fernandino (2018) and Paul, Fernandino and Dorao (2021). As for the Prandtl numbers, the liquid and vapor Froude numbers had similar MI scores. Since, for this work, the two-phase Nusselt number is strongly dependent on the quality, the liquid and vapor versions of the dimensionless Reynolds and Froude number showed higher MI scores than the phase-only versions. Surprisingly, the Convection number and both versions of the Lockhart-Martinelli parameter showed the lowest MI score. Although mutual information can give an accurate idea of which features yield the lower uncertainty over a target, a lower value of the MI score does not indicate the feature does not influence it.

Figure 45 illustrates the MI scores for the nucleate boiling set of dimensionless parameters. The pressure parameter from Klimenko (1990) and the reduced pressure showed a similar MI score. Both are intrinsically linked to the bubble diameter and, consequently, to nucleate boiling heat transfer. The Boiling number presented a low MI score, though many correlations propose it to account for nucleate boiling effects. As expected, the molecular weight presented an MI score of zero. Knowing the molecular weight does not give any information about the target because only one fluid was tested in this work, and therefore, only one value for M.

Figure 46 illustrates the MI scores for the surface tension effect set of dimensionless parameters. As can be seen, the Bond number, Laplace constant, and the liquid and vapor Weber number presented similar MI scores. The Bond number accounts for the competition between the gravitational forces against the surface tension, while the Weber number is usually incorporated into the mini-channel models to contrast the inertial and capillarity terms. Once more the phase-only therms showed lower MI scores.

Figure 47 illustrates the MI scores for the property ratio and categorical features set. The Fang, Wu and Yuan (2017) liquid viscosity ratio showed the highest MI score overall. The authors did not provide a specific physical meaning of the ratio between the fluid liquid viscosities at the saturation and wall temperature other than it is a fluid parameter that changes with the wall temperature. The liquid and vapor property ratios and the Klimenko (1990) thermal conductivity ratio had similar MI scores. The Groeneveld factor to correct the fluid properties for homogeneous flow presented an equivalent MI score to the flow pattern. The heating condition

Figure 44 – Mutual information scores for the forced convection set of dimensionless parameters.

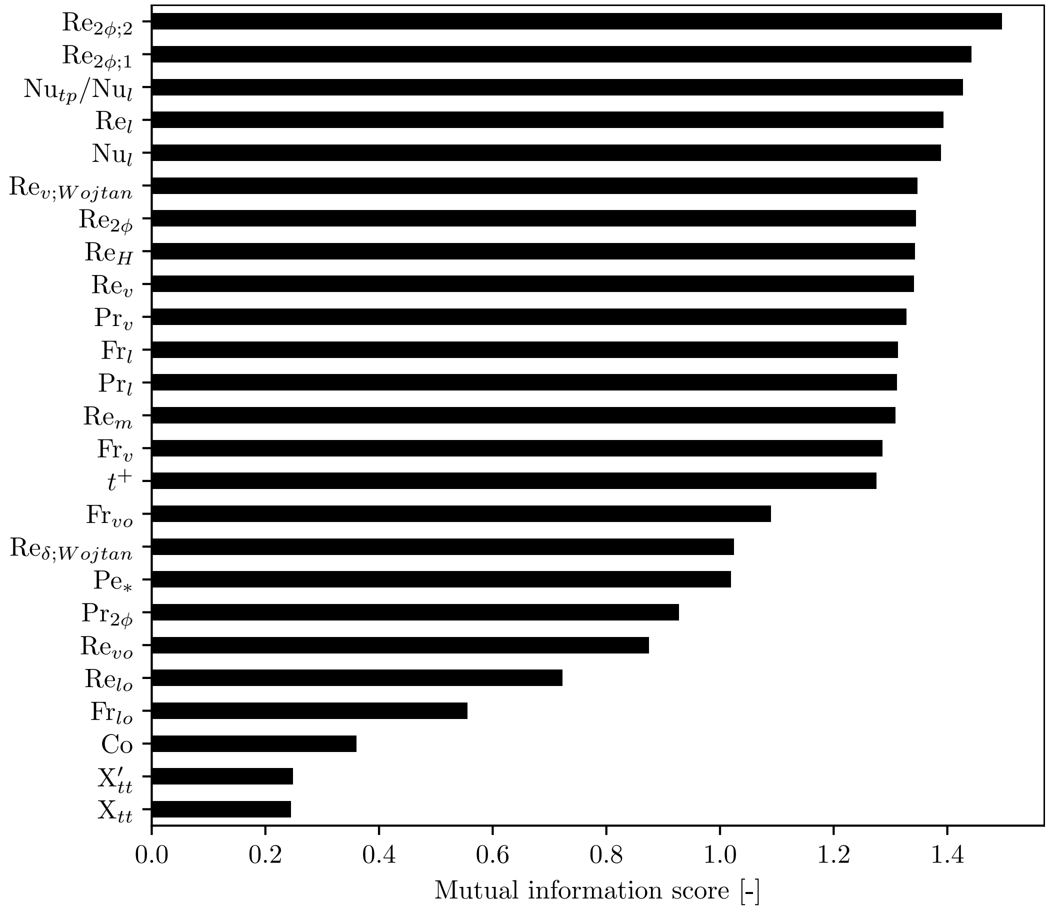

Source: Author.

Figure 45 – Mutual information scores for the nucleate boiling set of dimensionless parameters.

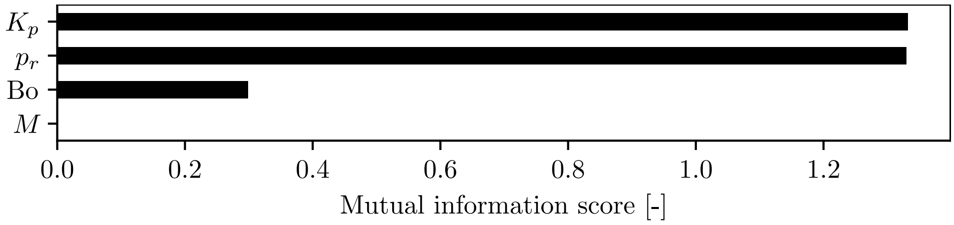

Source: Author.

showed a lower MI score, which might be expected since knowing how heat is provided to the fluid does not give an idea of the actual value of the HTC.

As stated before, mutual information can give insights into the best version of dimensionless parameters to better represent the two-phase Nusselt number. Overcomplicated parameters, such as the liquid film Reynolds number $\mathrm{Re}_{\delta;Wojtan}$ from Wojtan, Ursenbacher and Thome (2005a), proved less effective for representing the two-phase Nusselt number than the liquid form, per example. Some parameters that showed low MI scores are known to be relevant in predicting the HTC, such as the molecular weight and Boiling number. Both are present at Fang, Wu and Yuan's correlation, which proved robust to predict the HTC. According to Kim and Mudawar (2013) and Paul, Fernandino and Dorao (2021), for the heat flux level of this work,

Figure 46 – Mutual information scores for the surface tension effect set of dimensionless parameters.

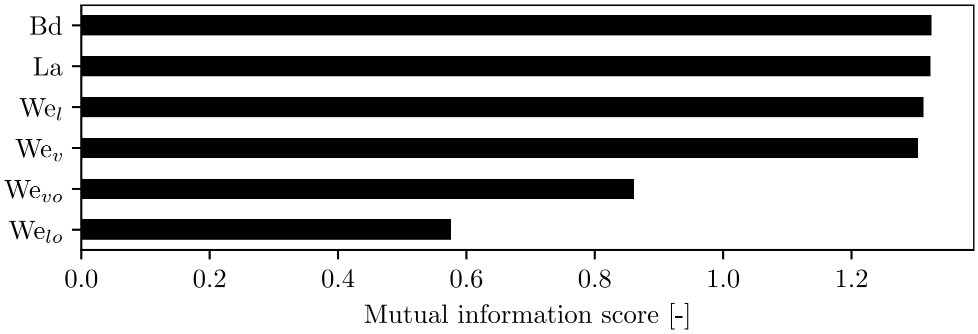

Source: Author.

Figure 47 – Mutual information scores for the property ratio and categorical features set.

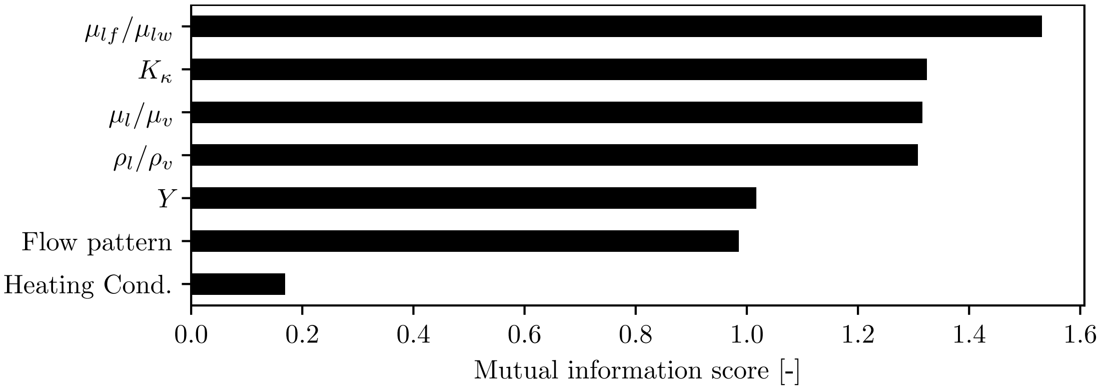

Source: Author.

the forced convection contribution to the heat transfer is higher than the nucleate boiling. That might justify the low MI score for the Boiling number. Even if a feature has a low MI score, its interaction with another feature can increase its relevance over the prediction of the HTC.

Other parameters, such as the Fang, Wu and Yuan (2017) liquid viscosity ratio, are shown to be precise in predicting the two-phase Nusselt number, but why is it? As the authors stated, for constant pressure, heat flux, and mass velocity, the wall temperature reflects the changes in HTC. Consequently, a liquid property at that temperature should represent it. After a deep investigation through the dataset, they came up with the viscosity ratio as it is. However, under constant heat flux conditions, does the wall temperature drive changes in heat transfer, or does heat transfer influence the wall temperature? From the definition of the HTC with constant heat flux, the temperature difference is inversely proportional to the HTC. By knowing the temperature and the heat flux, the HTC is over-defined, and there is no need for a correlation. It becomes clear that a parameter based on the wall temperature can capture any trend of the HTC, no matter the heat transfer phenomena. That is why Fang, Wu and Yuan (2017) states their correlation's accuracy might deteriorate when the wall temperature is unknown.

Unfortunately, the data set from this research is not large enough to attempt to build any correlation. Besides that, the range of most dimensionless groups limits themselves to one or two samples, such as molecular weight, reduced pressure, and so on. Nonetheless, the mutual information analysis showed that the two Reynolds numbers derived in this research can give lower uncertainties over the two-phase Nusselt number. In addition, they translate the ratio of momentum transport for the two-phase flow more intuitively than only the liquid or vapor Reynolds number.

5 Conclusions

Concentrating solar power with direct steam generation is an alternative to the cost reduction of solar power plants. The trapezoidal collector from linear Fresnel and parabolic troughs solar power plants features non-uniform heat flux on the tube walls. The heat distribution aspects of flow boiling, especially on long horizontal tubes, is a new boundary condition for an old problem, where even similar researchers showed different outcomes on the same subject. This doctoral thesis has successfully explored the effects of the heating condition on horizontal flow boiling. Through extensive research and analysis, it has contributed to the understanding of how non-uniform heating influences heat transfer, providing insights into the mechanisms and dimensionless parameters that translate the phenomena. The findings presented offer potential insights for better operating the concentrating solar power plants in order to minimize the thermal stresses on the collector's tubes. The main findings of this work are listed below:

- The nucleate boiling was harder to initiate when heating from the bottom than uniformly. As the wall is partially heated, the heat also flows circumferentially lowering the wall superheat.
- The wall temperature drop happens even for the upper half of the tube when heating from the bottom. When nucleate boiling starts, the heat transfer coefficient increases, and the heat flux distribution tends to accumulate on the bottom part, decreasing the temperature on the top of the tube.
- The heating condition appeared to have no significant influence on the development of the flow patterns. Although Wang *et al.* (2019) showed that the bottom heating anticipated the transition from intermittent to annular flow, no changes were perceived from the recordings of this work. Despite not showing evidence of dryout on the experimental data, some entrained droplets could be seen rewetting the upper half of the viewing section tube.
- As shown by Dirker, Scheepers and Meyer (2022) and confirmed by the ANOVA test, the heating distribution did not influence the pressure drop gradient. In fact, no influence should be expected since heat flux distribution is not related to the friction pressure drop mechanisms.
- The model proposed by Cioncolini, Thome and Lombardi (2009) based on the momentum properties showed the best performance by predicting the pressure drop gradient with a MAPE of 20.41%.
- ANOVA test showed that the heating condition influences the heat transfer coefficient when the pattern is not annular flow. Contrary to Wang *et al.* (2019), there was no evidence

of an increase in nucleate boiling due to bottom heating. The match between the liquid and vapor phases and the heat flux distribution inside the tube favors the heat transfer for the bottom heating and deteriorates for the top.

- Fang, Wu and Yuan's correlation presented the best performance in predicting the HTC with a MAPE of 5.69% and 5.87%, for the lower and high mas velocities, respectively, considering only the uniform heating data points. Their model also fitted 100% of the data points within 30% error. Apart from Fang, Wu and Yuan's, Jabardo, Bandarra Filho and Lima's and Wojtan, Ursenbacher and Thome's correlations presented the best accuracy with MAPEs of 21.16% and 20.95%, respectively, for the 50 kg $m^{-2}s^{-1}$ mass velocity. Many correlations presented MAPE lower than 20% for the higher mass velocity, but Wattelet *et al.*'s showed the best accuracy with a MAPE of 12.52%. For the lower mass velocity, where the heating condition influences the HTC considerably, the Wang *et al.*'s modifications to Gungor and Winterton's work to predict the bottom heating HTC did not show relevant improvement in the model accuracy.

- For lower mass velocity, the circumferential temperature distribution was more dispersed for the uniformly heated case than for the bottom heating. On the other hand, for higher mass velocity, the dispersion of the wall temperature was higher for the bottom heated case than for the uniform. The annular flow seems to evenly distribute the temperature around the tube wall, while for the stratified case, the upper wall temperature is higher due to the heat transfer with the vapor phase. For very long horizontal tubes heated from the bottom, it is preferable to operate at lower mass velocities. That decreases the thermal stresses on the tube wall, preventing bendings and failures, though it decreases the heat transfer efficiency. If uniformly heated, higher mass velocities will even the temperature distribution circumferentially and improve the heat transfer. In other words, for high heat transfer rates, it is better to have all the tube perimeter heated and high mass velocity.

- The two two-phase Reynolds numbers derived from the ratio of the liquid and vapor momentum advection and diffusion yielded the lowest uncertainty over the two-phase Nusselt number from a mutual information analysis.

- The liquid viscosity ratio introduced by Fang, Wu and Yuan (2017) proved accurate in predicting the two-phase Nusselt number, though as it depends on the tube wall temperature, its application to practical engineering is unlikely. Fang, Wu and Yuan's correlation takes the heat flux and wall temperature as inputs. As an over-defined problem, it is very accurate to predict data sets, but its applicability is questionable.

5.1 Recomendations for future works

The literature review showed that there are a lot of correlations for calculating the two-phase flow heat transfer coefficient and pressure drop gradient. New researchers emerge every day with new sets of experimental data. There is a trend among researchers to propose correlations to fit their experimental data, which floods the literature with correlations to do the same job. Efforts on theoretical research should be devoted to identifying the dimensionless groups that better represent the mechanisms of the flow boiling phenomena and how they relate to the two-phase Nusselt and pressure drop gradient. This work attempted to take a foot in that direction by evaluating the two-phase flow Reynolds number based on the momentum transport mechanisms. However, the lack of data to understand the relationship limits the conclusions. Theoretical works on the dimensionless groups that capture the mechanisms of flow boiling are still ongoing and will be presented after this thesis.

The test rig proved reliable in generating data for single-phase and two-phase flow. However, some improvements could be made by increasing the cooling power, differential pressure transmitter with a lower scale, proper calibration of the pressure transmitter, longer test section, more thermocouples attached to the tube wall, and uniformity on heat applied to the outer wall. That would allow for more robust and reliable results. Other mass velocities, reduced pressure, heat fluxes, and fluids should be tested to expand the database, allowing to check for the dimensionless groups that rule the heat transfer and pressure drop on horizontal flow boiling.

Bibliography

ABBAS, R.; MONTES, M.; ROVIRA, A.; MARTÍNEZ-VAL, J. Parabolic trough collector or linear fresnel collector? a comparison of optical features including thermal quality based on commercial solutions. *Solar Energy*, Elsevier, v. 124, p. 198–215, 2016. 27

AGUSTIARINI, N.; HOANG, H. N.; OH, J.-T.; KIM, J. K. Predictive modeling for the boiling heat transfer coefficient of r1234yf inside a multiport minichannel tube. *International Journal of Heat and Mass Transfer*, Elsevier, v. 211, p. 124188, 2023. 63

ALGUACIL, M.; PRIETO, C.; RODRÍGUEZ, A.; LOHR, J. Direct steam generation in parabolic trough collectors. *Energy Procedia*, Elsevier, v. 49, p. 21–29, 2014. 27

BAKER, O. Design of pipelines for the simultaneous flow of oil and gas. In: SOCIETY OF PETROLEUM ENGINEERS. *Fall Meeting of the Petroleum Branch of AIME*. [S.l.], 1953. 37

BAPTISTELLA, V. E. C.; MOREIRA, T. A.; RIBATSKI, G. Liquid-film thickness during flow boiling of pure hydrocarbons and their mixtures. *Experimental Thermal and Fluid Science*, Elsevier, v. 144, p. 110877, 2023. 100

BARBIERI, P.; JABARDO, J.; Bandarra Filho, E. Flow patterns in convective boiling of refrigerant r-134a in smooth tubes of several diameters. In: CITESEER. *Proceedings of the 5th European Thermal-Sciences Conference, Eindhoven, The Netherlands*. [S.l.], 2008. 12, 40, 41, 43

BAROCZY, C. *Correlation of liquid fraction in two-phase flow with application to liquid metals*. [S.l.]: Atomics International, 1963. 22, 47, 51

BASU, N.; WARRIER, G. R.; DHIR, V. K. Onset of nucleate boiling and active nucleation site density during subcooled flow boiling. *J. Heat Transfer*, v. 124, n. 4, p. 717–728, 2002. 34

BEATTIE, D. R.; WHALLEY, P. Simple two-phase frictional pressure drop calculation method. *Int. J. Multiphase Flow;(United Kingdom)*, v. 8, n. 1, 1982. 44, 45, 46, 103

BEDIAKO, E. G.; DANČOVÁ, P.; VÍT, T. Flow boiling heat transfer of r134a in a horizontal smooth tube: Experimental results, flow patterns, and assessment of correlations. *Energies*, MDPI, v. 15, n. 20, p. 7503, 2022. 54, 60

BERGER, M.; MOKHTAR, M.; ZAHLER, C.; AL-NAJAMI, M.; KRÜGER, D.; HENNECKE, K. Solar process steam for a pharmaceutical company in jordan. In: AIP PUBLISHING. *AIP Conference Proceedings*. [S.l.], 2016. v. 1734, n. 1, p. 100001. 27

BERGLES, A.; ROHSENOW, W. The determination of forced-convection surface-boiling heat transfer. *Journal of Heat Transfer*, ASME International, v. 86, n. 3, p. 365–372, 1964. 33, 34

BJORG, R. W.; HALL, G. R.; ROHSENOW, W. M. Correlation of forced convection boiling heat transfer data. *International Journal of Heat and Mass Transfer*, Elsevier, v. 25, n. 6, p. 753–757, 1982. 54

BUTTERWORTH, D. A comparison of some void-fraction relationships for co-current gas-liquid flow. *International Journal of Multiphase Flow*, Elsevier, v. 1, n. 6, p. 845–850, 1975. 51

CANIÈRE, H.; BAUWENS, B.; T'JOEN, C.; PAEPE, M. D. Mapping of horizontal refrigerant two-phase flow patterns based on clustering of capacitive sensor signals. *International Journal of Heat and Mass Transfer*, Elsevier, v. 53, n. 23-24, p. 5298–5307, 2010. 41

CASSOL, É. M. *Experimental analysis of convective heat transfer in two heating layouts*. 2017. Trabalho de Conclusão de Curso (graduação) - Universidade Federal de Santa Catarina, Centro Tecnológico, Graduação em Engenharia Mecânica, Florianópolis. 72

CELATA, G. R.; CUMO, M.; SETARO, T. Hysteresis phenomena in subcooled flow boiling of well-wetting fluids. *EXPERIMENTAL HEAT TRANSFER An International Journal*, Taylor & Francis, v. 5, n. 4, p. 253–275, 1992. 34, 36

CENGEL, Y. A.; CIMBALA, J. M. *Mecânica dos fluidos-3*. [S.l.]: Amgh Editora, 2015. 82

CHEN, D.; SHI, Y. Two-phase heat transfer and pressure drop of lng during saturated flow boiling in a horizontal tube. *Cryogenics*, Elsevier, v. 58, p. 45–54, 2013. 54

CHEN, D.; SHI, Y. Study on two-phase pressure drop of lng during flow boiling in a 8 mm horizontal smooth tube. *Experimental thermal and fluid science*, Elsevier, v. 57, p. 235–241, 2014. 43, 44, 48

CHEN, J. C. Correlation for boiling heat transfer to saturated fluids in convective flow. *Industrial & engineering chemistry process design and development*, ACS Publications, v. 5, n. 3, p. 322–329, 1966. 54, 64

CHENG, L.; RIBATSKI, G.; QUIBÉN, J. M.; THOME, J. R. New prediction methods for co2 evaporation inside tubes: Part i–a two-phase flow pattern map and a flow pattern based phenomenological model for two-phase flow frictional pressure drops. *International Journal of Heat and Mass Transfer*, Elsevier, v. 51, n. 1-2, p. 111–124, 2008. 39, 43

CHENG, L.; RIBATSKI, G.; THOME, J. R. Two-phase flow patterns and flow-pattern maps: fundamentals and applications. *Applied Mechanics Reviews*, American Society of Mechanical Engineers, v. 61, n. 5, p. 050802, 2008. 40

CHENG, L.; RIBATSKI, G.; WOJTAN, L.; THOME, J. R. New flow boiling heat transfer model and flow pattern map for carbon dioxide evaporating inside horizontal tubes. *International Journal of Heat and Mass Transfer*, Elsevier, v. 49, n. 21-22, p. 4082–4094, 2006. 39

CHISHOLM, D. Pressure gradients due to friction during the flow of evaporating two-phase mixtures in smooth tubes and channels. *International Journal of Heat and Mass Transfer*, Elsevier, v. 16, n. 2, p. 347–358, 1973. 15, 18, 44, 46, 47, 48, 103

CICCHITTI, A.; LOMBARDI, C.; SILVESTRI, M.; SOLDAINI, G.; ZAVATTARELLI, R. *Two-phase cooling experiments: pressure drop, heat transfer and burnout measurements*. [S.l.], 1959. 44, 45, 103

CIONCOLINI, A.; THOME, J. R. Algebraic turbulence modeling in adiabatic and evaporating annular two-phase flow. *International Journal of Heat and Fluid Flow*, Elsevier, v. 32, n. 4, p. 805–817, 2011. 21, 53, 54, 62, 65, 66, 109, 110, 112, 113, 115, 116

CIONCOLINI, A.; THOME, J. R. Void fraction prediction in annular two-phase flow. *International Journal of Multiphase Flow*, Elsevier, v. 43, p. 72–84, 2012. 52, 81

CIONCOLINI, A.; THOME, J. R. Pressure drop prediction in annular two-phase flow in macroscale tubes and channels. *International Journal of Multiphase Flow*, Elsevier, v. 89, p. 321–330, 2017. 44, 45, 49, 52

CIONCOLINI, A.; THOME, J. R.; LOMBARDI, C. Unified macro-to-microscale method to predict two-phase frictional pressure drops of annular flows. *International Journal of Multiphase Flow*, Elsevier, v. 35, n. 12, p. 1138–1148, 2009. 11, 49, 103, 125

COLLIER, J. G.; THOME, J. R. *Convective boiling and condensation*. [S.l.]: Clarendon Press, 1994. 47

COOPER, M. Heat flow rates in saturated nucleate pool boiling-a wide-ranging examination using reduced properties. In: *Advances in heat transfer*. [S.l.]: Elsevier, 1984. v. 16, p. 157–239. 56, 59, 61, 63

DÁRIO, E. R. *Ebulição convectiva do R-134a em microcanais paralelos e análise da distribuição do escoamento bifásico ar-água em um distribuidor acoplado a microcanais*. Tese (Doutorado) — Universidade Federal de Santa Catarina, 2013. 12, 35, 36

DAVIS, E. J.; ANDERSON, G. The incipience of nucleate boiling in forced convection flow. *AIChE Journal*, Wiley Online Library, v. 12, n. 4, p. 774–780, 1966. 33, 34

de Oliveira, J. D.; COPETTI, J. B.; PASSOS, J. C. Experimental investigation on flow boiling pressure drop of r-290 and r-600a in a horizontal small tube. *International Journal of refrigeration*, Elsevier, v. 84, p. 165–180, 2017. 43, 44, 45, 55

Del Col, D. Flow boiling of halogenated refrigerants at high saturation temperature in a horizontal smooth tube. *Experimental Thermal and Fluid Science*, Elsevier, v. 34, n. 2, p. 234–245, 2010. 53, 54, 56, 59, 62, 109, 112, 113, 115, 116

DELIL, A. Tutorial on quantification of differences between single-and two-component two-phase flow and heat transfer. In: AMERICAN INSTITUTE OF PHYSICS. *AIP Conference Proceedings*. [S.l.], 2003. v. 654, n. 1, p. 3–16. 63

DIRKER, J.; MEYER, J. P.; REID, W. Experimental investigation of circumferentially non-uniform heat flux on the heat transfer coefficient in a smooth horizontal tube with buoyancy driven secondary flow. *Experimental Thermal and Fluid Science*, Elsevier, v. 98, p. 480–496, 2018. 91

DIRKER, J.; SCHEEPERS, H.; MEYER, J. P. The effect of circumferentially non-uniform heat flux on flow boiling heat transfer in a horizontal tube. *International Journal of Heat and Mass Transfer*, Elsevier, v. 185, p. 122428, 2022. 10, 11, 12, 27, 28, 31, 32, 67, 102, 107, 108, 119, 125

DORAO, C. A.; DREWES, S.; FERNANDINO, M. Can the heat transfer coefficients for single-phase flow and for convective flow boiling be equivalent? *Applied Physics Letters*, AIP Publishing, v. 112, n. 6, 2018. 64, 121

DUKLER, A.; Wicks III, M.; CLEVELAND, R. Frictional pressure drop in two-phase flow: A. a comparison of existing correlations for pressure loss and holdup. *AIChE Journal*, Wiley Online Library, v. 10, n. 1, p. 38–43, 1964. 44

DUKLER, A. E.; Wicks III, M.; CLEVELAND, R. G. Frictional pressure drop in two-phase flow: B. an approach through similarity analysis. *AIChE Journal*, v. 10, n. 1, p. 44–51, 1964. 44, 45, 103

EATON, B. A.; KNOWLES, C. R.; SILBERBRG, I. *et al.* The prediction of flow patterns, liquid holdup and pressure losses occurring during continuous two-phase flow in horizontal pipelines. *Journal of Petroleum technology*, Society of Petroleum Engineers, v. 19, n. 06, p. 815–828, 1967. 37

FANG, X.; WU, Q.; YUAN, Y. A general correlation for saturated flow boiling heat transfer in channels of various sizes and flow directions. *International journal of heat and mass transfer*, Elsevier, v. 107, p. 972–981, 2017. 11, 53, 54, 60, 62, 67, 109, 110, 112, 113, 115, 116, 121, 122, 123, 126

FANG, X.; ZHUANG, F.; CHEN, C.; WU, Q.; CHEN, Y.; CHEN, Y.; HE, Y. Saturated flow boiling heat transfer: review and assessment of prediction methods. *Heat and Mass Transfer*, Springer, v. 55, p. 197–222, 2019. 54, 112, 113

FRIEDEL, L. Improved friction pressure drop correlations for horizontal and vertical two-phase pipe flow. In: *European Two-Phase Flow Group Meeting, Ispra, Italy, 1979*. [S.l.: s.n.], 1979. 18, 44, 47, 48, 51, 103

FROST, W.; DZAKOWIC, G. An extension of the method of predicting incipient boiling on commercialy finished surfaces, asme paper. 1967. 34

GARCÍA, F.; GARCÍA, J.; GARCÍA, R.; JOSEPH, D. Friction factor improved correlations for laminar and turbulent gas–liquid flow in horizontal pipelines. *International Journal of Multiphase Flow*, Elsevier, v. 33, n. 12, p. 1320–1336, 2007. 44, 45

GOVIER, G.; OMER, M. The horizontal pipeline flow of air-water mixtures. *The Canadian Journal of Chemical Engineering*, Wiley Online Library, v. 40, n. 3, p. 93–104, 1962. 37

GRAUSO, S.; MASTRULLO, R.; MAURO, A. W.; THOME, J.; VANOLI, G. P. Flow pattern map, heat transfer and pressure drops during evaporation of r-1234ze (e) and r134a in a horizontal, circular smooth tube: Experiments and assessment of predictive methods. *International journal of refrigeration*, Elsevier, v. 36, n. 2, p. 478–491, 2013. 54, 56, 58, 60

GROENEVELD, D. *Post-dryout heat transfer at reactor operating conditions*. [S.l.], 1973. 61

GUNGOR, K.; WINTERTON, R. S. Simplified general correlation for saturated flow boiling and comparisons of correlations with data. *Chemical engineering research & design*, v. 65, n. 2, p. 148–156, 1987. 54, 59

GUNGOR, K. E.; WINTERTON, R. A general correlation for flow boiling in tubes and annuli. *International Journal of Heat and Mass Transfer*, Elsevier, v. 29, n. 3, p. 351–358, 1986. 30, 52, 54, 56, 59, 62, 63, 64, 109, 112, 113, 115, 116, 126

HARDIK, B.; PRABHU, S. Boiling pressure drop and local heat transfer distribution of water in horizontal straight tubes at low pressure. *International Journal of Thermal Sciences*, Elsevier, v. 110, p. 65–82, 2016. 43, 44, 48, 50, 51, 54, 56, 58, 103

HEWITT, G. F.; ROBERTS, D. *Studies of two-phase flow patterns by simultaneous x-ray and flast photography*. [S.l.], 1969. 37

HINO, R.; UEDA, T. Studies on heat transfer and flow characteristics in subcooled flow boiling—part 1. boiling characteristics. *International journal of multiphase flow*, Elsevier, v. 11, n. 3, p. 269–281, 1985. 33, 34

HOOGENDOORN, C. Gas-liquid flow in horizontal pipes. *Chemical Engineering Science*, Elsevier, v. 9, n. 4, p. 205–217, 1959. 37

HSU, Y. Y. On the size range of active nucleation cavities on a heating surface. *J. Heat Transfer*, v. 84, p. 207–216, 1962. 33, 34

JABARDO, J. S.; Bandarra Filho, E. P.; LIMA, C. New correlation for convective boiling of pure halocarbon refrigerants flowing in horizontal tubes. *Braz. J. Mech. Sci*, v. 21, p. 245–258, 1999. 15, 53, 54, 56, 58, 60, 110, 112, 113, 115, 116, 126

Joint Committee for Guides in Metrology. Evaluation of measurement data—guide to the expression of uncertainty in measurement. *JCGM*, v. 100, n. 2008, p. 1–116, 2008. 146, 148

KANDLIKAR, S. G. A general correlation for saturated two-phase flow boiling heat transfer inside horizontal and vertical tubes. 1990. 15, 18, 52, 54, 56, 58, 60, 62, 64, 109, 112, 113, 115, 116

KATTAN, N.; THOME, J.; FAVRAT, D. Flow boiling in horizontal tubes: Part 1—development of a diabatic two-phase flow pattern map. *Journal of heat transfer*, American Society of Mechanical Engineers, v. 120, n. 1, p. 140–147, 1998. 12, 37, 38, 39, 40, 41, 43

KATTAN, N.; THOME, J. R.; FAVRAT, D. Flow boiling in horizontal tubes: part 3—development of a new heat transfer model based on flow pattern. *Journal of heat transfer*, American Society of Mechanical Engineers, v. 120, n. 1, p. 156–165, 1998. 52, 54, 60

KHARANGATE, C. R.; O'NEILL, L. E.; MUDAWAR, I. Effects of two-phase inlet quality, mass velocity, flow orientation, and heating perimeter on flow boiling in a rectangular channel: Part 1–two-phase flow and heat transfer results. *International journal of heat and mass transfer*, Elsevier, v. 103, p. 1261–1279, 2016. 27, 28, 31

KHARANGATE, C. R.; O'NEILL, L. E.; MUDAWAR, I. Effects of two-phase inlet quality, mass velocity, flow orientation, and heating perimeter on flow boiling in a rectangular channel: Part 2–chf experimental results and model. *International journal of heat and mass transfer*, Elsevier, v. 103, p. 1280–1296, 2016. 27, 28, 31

KHARANGATE, C. R.; O'NEILL, L. E.; MUDAWAR, I.; HASAN, M. M.; NAHRA, H. K.; BALASUBRAMANIAM, R.; HALL, N. R.; MACNER, A. M.; MACKEY, J. R. Flow boiling and critical heat flux in horizontal channel with one-sided and double-sided heating. *International Journal of Heat and Mass Transfer*, Elsevier, v. 90, p. 323–338, 2015. 27, 28, 31

KIM, S.-M.; MUDAWAR, I. Universal approach to predicting saturated flow boiling heat transfer in mini/micro-channels–part i. dryout incipience quality. *International Journal of Heat and Mass Transfer*, Elsevier, v. 64, p. 1226–1238, 2013. 122

KLIMENKO, V. A generalized correlation for two-phase forced flow heat transfer. *International Journal of heat and mass transfer*, Elsevier, v. 31, n. 3, p. 541–552, 1988. 54, 56

KLIMENKO, V. A generalized correlation for two-phase forced flow heat transfer—second assessment. *International journal of heat and mass transfer*, Elsevier, v. 33, n. 10, p. 2073–2088, 1990. 20, 52, 56, 57, 65, 66, 109, 112, 113, 115, 116, 120, 121

KRÜGER, D.; KRÜGER, J.; PANDIAN, Y.; O'CONNELL, B.; FELDHOFF, J. F.; KARTHIKEYAN, R.; HEMPEL, S.; MUNIASAMY, K.; HIRSCH, T.; EICKHOFF, M. *et al.* Experiences with direct steam generation at the kanchanaburi solar thermal power plant. In: *18th SolarPACES Conference, Marrakech, Morocco, Sept.* [S.l.: s.n.], 2012. p. 11–14. 27

KUBO, Y.; YAMADA, S.; MURAKAWA, H.; ASANO, H. Correlation between pressure loss and heat transfer coefficient in boiling flows in printed circuit heat exchangers with semicircular and circular mini-channels. *Applied Thermal Engineering*, Elsevier, v. 204, p. 117963, 2022. 63

LILLO, G.; MASTRULLO, R.; MAURO, A.; VISCITO, L. Flow boiling of r1233zd (e) in a horizontal tube: Experiments, assessment and correlation for asymmetric annular flow. *International Journal of Heat and Mass Transfer*, Elsevier, v. 129, p. 547–561, 2019. 54, 62, 107

LIMA, R. J. D. S.; THOME, J. R. Two-phase flow patterns in u-bends and their contiguous straight tubes for different orientations, tube and bend diameters. *International Journal of Refrigeration*, Elsevier, v. 35, n. 5, p. 1439–1454, 2012. 70

LIMA, R. J. da S.; THOME, J. R. Two-phase flow pressure drops in u-tubes: Towards more accurate measurement methods and prediction models. *International Journal of Refrigeration*, Elsevier, v. 36, n. 2, p. 492–503, 2013. 70

LIN, L.; GAO, L.; KEDZIERSKI, M. A.; HWANG, Y. A general model for flow boiling heat transfer in microfin tubes based on a new neural network architecture. *Energy and AI*, Elsevier, v. 8, p. 100151, 2022. 64, 120

LIU, Z.; WINTERTON, R. A general correlation for saturated and subcooled flow boiling in tubes and annuli, based on a nucleate pool boiling equation. *International journal of heat and mass transfer*, Elsevier, v. 34, n. 11, p. 2759–2766, 1991. 52, 54, 56, 59, 62, 104, 109, 112, 113, 115, 116

LIX, L. M.; KESELMAN, J. C.; KESELMAN, H. J. Consequences of assumption violations revisited: A quantitative review of alternatives to the one-way analysis of variance f test. *Review of educational research*, Sage Publications Sage CA: Thousand Oaks, CA, v. 66, n. 4, p. 579–619, 1996. 149

LOCKHART, W. R.; MARTINELLI, R. C. Proposed correlation of data for isothermal two-phase, two-component flow in pipes. *Chemical engineering progress*, v. 45, n. 1, p. 39–48, 1949. 18, 44, 46, 47, 48, 51, 103

MALISKA, C. R. On the physical significance of some dimensionless numbers used in heat transfer and fluid flow. *Federal University of Santa Catarina, Florianópolis, SC*, Citeseer, p. 137, 1990. 119

MANDHANE, J. M.; GREGORY, G. A.; AZIZ, K. A flow pattern map for gas—liquid flow in horizontal pipes. *International Journal of Multiphase Flow*, Elsevier, v. 1, n. 4, p. 537–553, 1974. 37

MARSH, W.; MUDAWAR, I. Predicting the onset of nucleate boiling in wavy free-falling turbulent liquid films. *International journal of heat and mass transfer*, Elsevier, v. 32, n. 2, p. 361–378, 1989. 33, 34, 36

MASTRULLO, R.; MAURO, A.; REVELLIN, R.; VISCITO, L. Flow boiling heat transfer and pressure drop of pure ethanol (99.8%) in a horizontal stainless steel tube at low reduced pressures. *Applied Thermal Engineering*, Elsevier, v. 145, p. 251–263, 2018. 44, 46, 48, 54, 59, 62

MASTRULLO, R.; MAURO, A.; VISCITO, L. Flow boiling of r452a: Heat transfer data, dry-out characteristics and a correlation. *Experimental Thermal and Fluid Science*, Elsevier, v. 105, p. 247–260, 2019. 107

MATHWORKS, I. T. *Partial Differential Equation Toolbox*. Natick, Massachusetts, United State, 2019. Disponível em: ⟨https://www.mathworks.com/help/pde/⟩. 79

MÜLLER-STEINHAGEN, H.; HECK, K. A simple friction pressure drop correlation for two-phase flow in pipes. *Chemical Engineering and Processing: Process Intensification*, Elsevier, v. 20, n. 6, p. 297–308, 1986. 18, 44, 45, 48, 51, 103

MUÑOZ-ANTÓN, J.; ABBAS, R.; MARTINEZ-VAL, J.; MONTES, M. Going further with fresnel receiver: new design window for direct steam generation. *Energy Procedia*, Elsevier, v. 49, p. 184–192, 2014. 27

NIE, F.; YAN, S.; WANG, H.; ZHAO, C.; ZHAO, Y.; GONG, M. A universal correlation for predicting two-phase frictional pressure drop in horizontal tubes based on machine learning. *International Journal of Multiphase Flow*, Elsevier, v. 160, p. 104377, 2023. 44, 48, 49, 51, 103

OKAFOR, I. F.; DIRKER, J.; MEYER, J. P. Influence of non-uniform heat flux distributions on the secondary flow, convective heat transfer and friction factors for a parabolic trough solar collector type absorber tube. *Renewable Energy*, Elsevier, v. 108, p. 287–302, 2017. 27, 28

ONG, C. L.; THOME, J. Macro-to-microchannel transition in two-phase flow: Part 1–two-phase flow patterns and film thickness measurements. *Experimental Thermal and Fluid Science*, Elsevier, v. 35, n. 1, p. 37–47, 2011. 41, 42

PAUL, S.; FERNANDINO, M.; DORAO, C. A. On the scaling of convective boiling heat transfer coefficient. *International Journal of Heat and Mass Transfer*, Elsevier, v. 164, p. 120589, 2021. 53, 54, 64, 65, 66, 121, 122

PICANÇO, M. A. S.; PASSOS, J. C.; Bandarra Filho, E. P. Heat transfer coefficient correlation for convective boiling inside plain and microfin tubes using genetic algorithms. *Heat transfer engineering*, Taylor & Francis, v. 30, n. 4, p. 316–323, 2009. 64

QI, S.; ZHANG, P.; WANG, R.; XU, L. Flow boiling of liquid nitrogen in micro-tubes: Part i–the onset of nucleate boiling, two-phase flow instability and two-phase flow pressure drop. *International journal of heat and mass transfer*, Elsevier, v. 50, n. 25-26, p. 4999–5016, 2007. 12, 34, 35

ROHSENOW, W. M.; HARTNETT, J. P.; CHO, Y. I. *et al. Handbook of heat transfer*. [S.l.]: Mcgraw-hill New York, 1998. v. 3. 85, 86

ROUHANI, S.; SOHAL, M. Two-phase flow patterns: A review of research results. *Progress in Nuclear Energy*, Elsevier, v. 11, n. 3, p. 219–259, 1983. 37

ROUHANI, S. Z.; AXELSSON, E. Calculation of void volume fraction in the subcooled and quality boiling regions. *International Journal of Heat and Mass Transfer*, Elsevier, v. 13, n. 2, p. 383–393, 1970. 51

SÁ, A. B. de; FILHO, V. C. P.; TADRIST, L.; PASSOS, J. C. Direct steam generation in linear solar concentration: Experimental and modeling investigation–a review. *Renewable and Sustainable Energy Reviews*, Elsevier, v. 90, p. 910–936, 2018. 27, 28

SATO, T.; MATSUMURA, H. On the conditions of incipient subcooled-boiling with forced convection. *JSME International Journal Series C Mechanical Systems, Machine Elements and Manufacturing*, The Japan Society of Mechanical Engineers, v. 7, n. 26, p. 392–398, 1964. 33, 34

SERRANO-AGUILERA, J.; VALENZUELA, L.; PARRAS, L. Thermal 3d model for direct solar steam generation under superheated conditions. *Applied Energy*, Elsevier, v. 132, p. 370–382, 2014. 27, 116

SHAH, M. M. A new correlation for heat transfer during boiling flow through pipes. *Ashrae Trans.*, v. 82, n. 2, p. 66–86, 1976. 54, 55

SHAH, M. M. Chart correlation for saturated boiling heat transfer: equations and further study. *ASHRAE Trans.;(United States)*, v. 88, n. CONF-820112-, 1982. 24, 52, 54, 55, 56, 109, 112, 113, 115, 116

SONG, J. H.; LEE, J.; CHANG, S. H.; JEONG, Y. H. Onset of nucleate boiling in narrow, rectangular channel for downward flow under low pressure. *Annals of Nuclear Energy*, Elsevier, v. 109, p. 498–506, 2017. 33, 35, 36

STEINER, D. Heat transfer to boiling saturated liquids. *VDI-Warmeatlas (VDI Heat Atlas)*, Verein Deutscher Ingenieure, de., VDI-Gessellschaft Verfahrenstechnik und ..., 1993. 37

STEINER, D.; KIND, M. Flow patterns in evaporator tubes. *VDI eV (Ed.), VDI Heat Atlas, VDI-buch, Online-Ausg., Springer-Verlag Berlin Heidelberg, Berlin, Heidelberg*, p. 796–800, 2010. 37, 38, 39, 43, 51

STEINER, D.; TABOREK, J. Flow boiling heat transfer in vertical tubes correlated by an asymptotic model. *Heat transfer engineering*, Taylor & Francis, v. 13, n. 2, p. 43–69, 1992. 34

TAITEL, Y.; DUKLER, A. E. A model for predicting flow regime transitions in horizontal and near horizontal gas-liquid flow. *AIChE journal*, Wiley Online Library, v. 22, n. 1, p. 47–55, 1976. 37, 38, 39, 40, 43

TANK, P.; HARDIK, B.; SRIDHARAN, A.; PRABHU, S. Pressure drop, local heat transfer coefficient, and critical heat flux of dnb type for flow boiling in a horizontal straight tube with r-123. *Heat and Mass Transfer*, Springer, v. 57, p. 223–250, 2021. 44, 46, 48

THOME, J. R.; El Hajal, J. Two-phase flow pattern map for evaporation in horizontal tubes: latest version. *Heat Transfer Engineering*, Taylor & Francis, v. 24, n. 6, p. 3–10, 2003. 39, 43

THOME, J. R.; HAJAL, J. E.; CAVALLINI, A. Condensation in horizontal tubes, part 2: new heat transfer model based on flow regimes. *International journal of heat and mass transfer*, Elsevier, v. 46, n. 18, p. 3365–3387, 2003. 61

WANG, D.; ZHAO, L.; NIE, X.; LU, Y.; DENG, S. Experimental study on flow boiling characteristics of r-245fa in circular tube under non-uniform heat flux. *International Journal of Heat and Mass Transfer*, Elsevier, v. 143, p. 118570, 2019. 10, 12, 27, 28, 30, 31, 32, 42, 53, 54, 56, 63, 67, 100, 107, 108, 109, 110, 112, 113, 115, 116, 125, 126

WATTELET, J.; CHATO, J.; SOUZA, A.; CHRISTOFFERSEN, B. Evaporative characteristics of r-134a, mp-39, and r-12 at low mass fluxes. *ASHRAE transactions*, 1993. 11, 53, 54, 55, 58, 59, 60, 65, 66, 104, 109, 112, 113, 115, 116, 126

WHITE, P.; HUNTINGTON, R. Horizontal co-current two-phase flow of fluids in pipe lines. *The Petroleum Engineer*, v. 27, n. 9, p. 40, 1955. 37

WOJTAN, L.; URSENBACHER, T.; THOME, J. R. Investigation of flow boiling in horizontal tubes: Part ii—development of a new heat transfer model for stratified-wavy, dryout and mist flow regimes. *International journal of heat and mass transfer*, Elsevier, v. 48, n. 14, p. 2970–2985, 2005. 52, 53, 54, 60, 61, 65, 66, 98, 109, 112, 113, 122, 126

WOJTAN, L.; URSENBACHER, T.; THOME, J. R. Investigation of flow boiling in horizontal tubes: Part i—a new diabatic two-phase flow pattern map. *International journal of heat and mass transfer*, Elsevier, v. 48, n. 14, p. 2955–2969, 2005. 10, 11, 12, 39, 40, 43, 54, 76, 99, 100, 112, 113, 115, 116

YANG, Z.-Q.; CHEN, G.-F.; ZHUANG, X.-R.; SONG, Q.-L.; DENG, Z.; SHEN, J.; GONG, M.-Q. A new flow pattern map for flow boiling of r1234ze (e) in a horizontal tube. *International Journal of Multiphase Flow*, Elsevier, v. 98, p. 24–35, 2018. 42

YANG, Z.-Q.; GONG, M.; CHEN, G.; LIN, Z.; HUANG, H.; FENG, H. A new diabatic two phase flow pattern transition model of r600a. *International Journal of Refrigeration*, Elsevier, v. 99, p. 138–144, 2019. 42, 43

YUAN, H.; TAN, S.; DU, W.; DING, S.; GUO, C. Heterogeneous bubble nucleation model on heated surface based on free energy analysis. *International Journal of Heat and Mass Transfer*, Elsevier, v. 122, p. 1198–1209, 2018. 36

YUAN, S.; CHENG, W.-L.; NIAN, Y.-L.; ZHONG, Q.; FAN, Y.-F.; HE, J. Evaluation of prediction methods for heat transfer coefficient of annular flow and a novel correlation. *Applied Thermal Engineering*, Elsevier, v. 114, p. 10–23, 2017. 54

ZARZA, E.; VALENZUELA, L.; LEÓN, J.; WEYERS, H.-D.; EICKHOFF, M.; ECK, M.; HENNECKE, K. The diss project: direct steam generation in parabolic trough systems. operation and maintenance experience and update on project status. *Journal of solar energy engineering*, American Society of Mechanical Engineers, v. 124, n. 2, p. 126–133, 2002. 27

ZARZA, E.; VALENZUELA, L.; LEON, J.; HENNECKE, K.; ECK, M.; WEYERS, H.-D.; EICKHOFF, M. Direct steam generation in parabolic troughs: Final results and conclusions of the diss project. *Energy*, Elsevier, v. 29, n. 5-6, p. 635–644, 2004. 27

ZHU, G.; WENDELIN, T.; WAGNER, M. J.; KUTSCHER, C. History, current state, and future of linear fresnel concentrating solar collectors. *Solar Energy*, Elsevier, v. 103, p. 639–652, 2014. 27, 28

ZHUANG, X.; GONG, M.; CHEN, G.; ZOU, X.; SHEN, J. Two-phase flow pattern map for r170 in a horizontal smooth tube. *International Journal of Heat and Mass Transfer*, Elsevier, v. 102, p. 1141–1149, 2016. 41, 42, 43

ZOU, X.; GONG, M.; CHEN, G.; SUN, Z.; ZHANG, Y.; WU, J. Experimental study on saturated flow boiling heat transfer of r170/r290 mixtures in a horizontal tube. *International Journal of Refrigeration*, Elsevier, v. 33, n. 2, p. 371–380, 2010. 52, 54, 59

ZOU, X.; GONG, M.; WU, J.; CHEN, G. Heat transfer correlations for flow boiling of hydrocarbon mixtures inside horizontal tubes. *Physics Procedia*, Elsevier, v. 67, p. 655–660, 2015. 54

ZÜRCHER, O.; FAVRAT, D.; THOME, J. Development of a diabatic two-phase flow pattern map for horizontal flow boiling. *International Journal of Heat and Mass Transfer*, Elsevier, v. 45, n. 2, p. 291–301, 2002. 38, 39, 43

ZÜRCHER, O.; THOME, J. R.; FAVRAT, D. An onset of nucleate boiling criterion for horizontal flow boiling. *International journal of thermal sciences*, Elsevier, v. 39, n. 9-11, p. 909–918, 2000. 34

APPENDIX A – Thermocouple calibration

This appendix details the fabrication and calibration procedure for the type E and T thermocouples utilized for temperature measurements on the test rig. Figure 48 presents the type E thermocouples' welded tips and their designated channel names. The Omega 30AWG (approximately $\phi 0.26$ mm) thermocouple wires were braided to facilitate welding and to ensure the tip's integrity. The exposed wire tip measures roughly 2 mm in length. The shielded probe type T thermocouples did not require welding and were ready to use.

Figure 48 – Omega 30AWG ($\approx \phi 0.26$ mm) thermocouple.

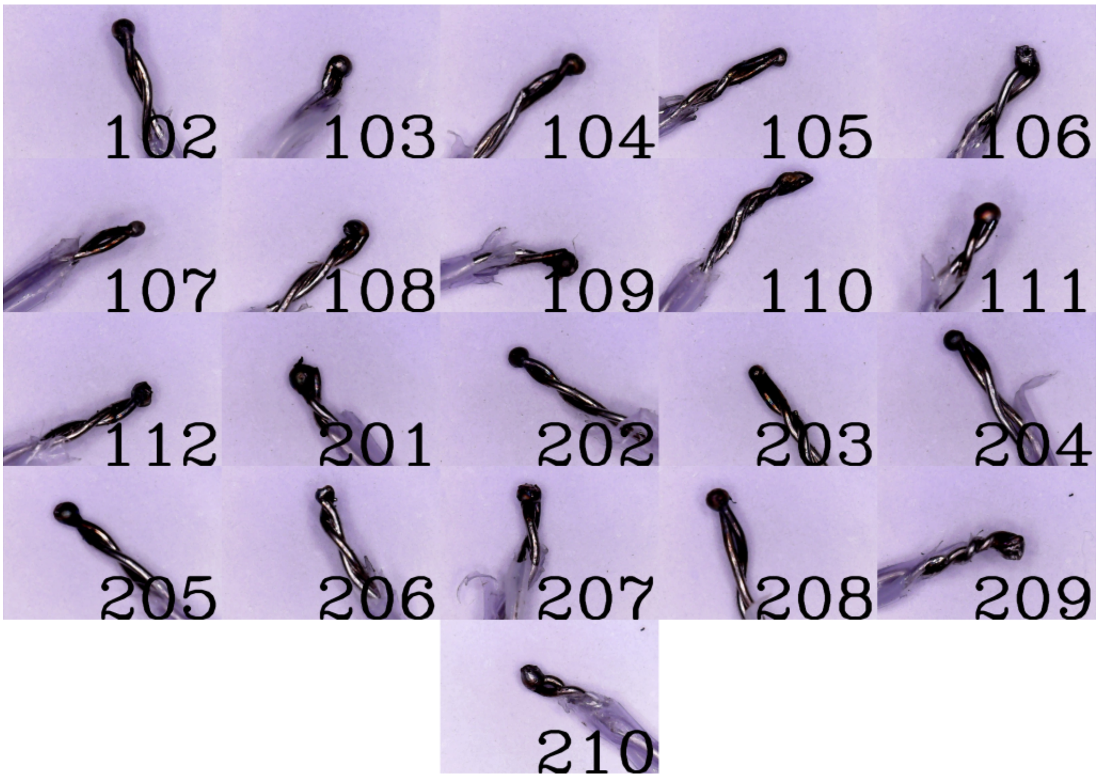

Source: Author.

The standard uncertainty of the type E thermocouple from Omega Instruments is 1.0 °C or 0.75%, whichever is the higher value. A calibration procedure can reduce the uncertainty level to tenths of a degree. A certified PT100 transducer provided the reference temperature for calibrating the thermocouples.

Figure 49 illustrates the schematics of the thermocouple calibration process. A cooling bath regulated the temperatures for each calibration point. All the thermocouple tips were positioned in proximity to the PT100 measurement tip. The assembly was placed within the cooling bath. The cooling bath pump circulated the water to ensure temperature uniformity. An Agilent 34972A datalogger recorded the data at a frequency of 0.2 Hz (every five seconds).

Figure 49 – Schematics of the calibration procedure.

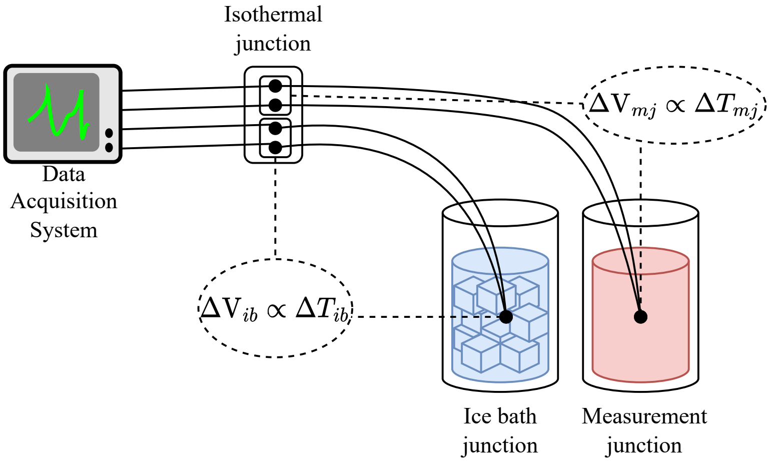

Source: Author.

Each calibration temperature level was maintained for six minutes straight after reaching the steady state to gather at least 60 data points. The thermocouples were calibrated within the range of 5 to 95 °C with increments of 10 °C. The tests were conducted six times, split into three ascending and three descending runs, to guarantee repeatability and robustness. The ice bath was renewed before starting each test.

Figure 50 illustrates the calibration measurements of the thermocouple on channel 109 against the reference temperature. The low measurement dispersion might give the impression that each temperature calibration level corresponds to just one data point, but in reality, each level consists of a cluster of 60 data points. A cubic function was fitted for each thermocouple using the Python Numpy package function “polyfit”. Table 30 lists the fitted coefficients for each thermocouple cubic function.

The reference temperature was corrected by the systematic error from the PT100 certification. The PT100 calibration uncertainty was also combined with the standard uncertainty of the thermocouple measurements. Both standard uncertainties from the PT100 and the thermocouple measurements were combined to the thermocouple calibration uncertainty. The following equation accounts for the thermocouple standard uncertainty for each temperature level:

$$u_{TC} = \sqrt{\left[\frac{\partial T}{\partial V}\left({\sigma_{TC}}^2 + {u_{daq;tc}}^2 + {\sigma_{ice}}^2 + {u_{daq;ice}}^2\right)\right]^2 + \left[{u_{cal;pt100}}^2 + \frac{\partial T}{\partial R}\left({\sigma_{pt100}}^2 + {u_{daq;pt100}}^2\right)\right]^2}, \tag{193}$$

where $\partial T/\partial V$ and $\partial T/\partial R$ are the sensibility function of the thermocouple and PT100, respectively, σ_{TC}, σ_{ice}, and σ_{pt100} are the standard deviation of the thermocouple, ice bath junction, and PT100 measurements, respectively, $u_{daq;tc}$, $u_{daq;ice}$, and $u_{daq;tc}$ are the uncertainty from the DAQ system of the thermocouple, ice bath junction, and PT100 measures, respectively, and

Figure 50 – Thermocouple signal from channel 109 versus reference temperature from PT100.

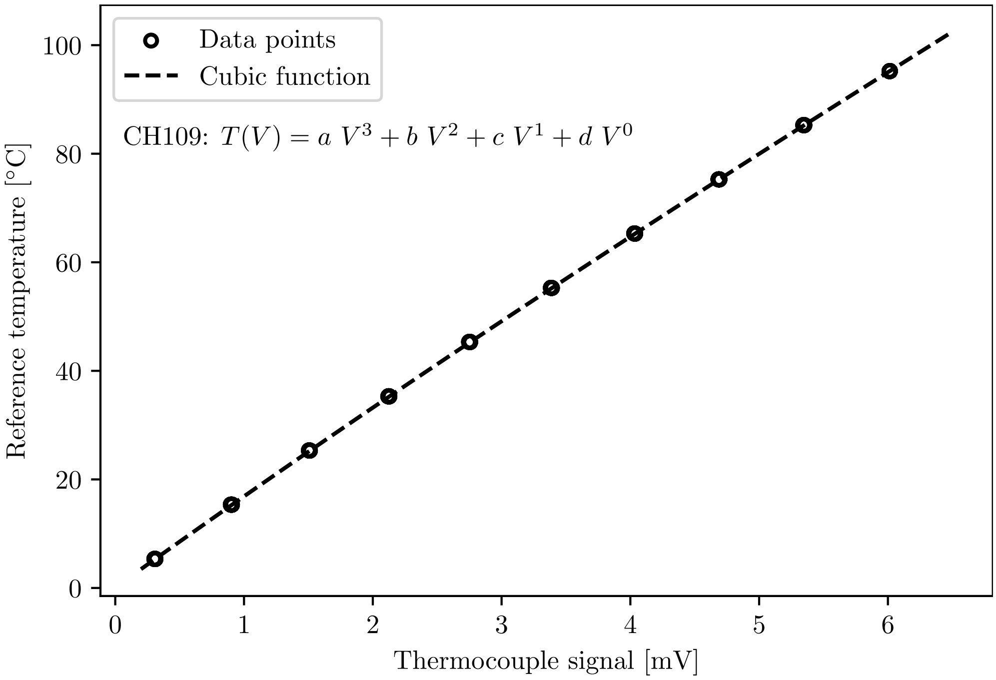

Source: Author.

$u_{cal;pt100}$ is the calibration standard uncertainty of the PT100. That yields a standard uncertainty for each calibration temperature. The highest value was considered the thermocouple calibration uncertainty to simplify the experimental uncertainty analysis.

Besides that, each standard uncertainty was combined with the systematic error from the cubic function as follows:

$$U_{TC} = \max\left[\epsilon_{tc} + u_{TC}; |\epsilon_{tc} - u_{TC}|\right]. \tag{194}$$

The maximum value among the temperature calibration levels was taken as the thermocouple calibration standard uncertainty. Table 31 lists the maximum standard uncertainty of all calibration temperature levels.

Table 30 – Cubic function coefficients for each thermocouple (type E: from CH102 to CH210, type T: from CH211 to CH213.

Channel	$a\,[\times 10^{-7}]$	$b\,[\times 10^{-5}]$	$c\,[\times 10^{-4}]$	$d\,[\times 10^{2}]$
CH102	1.055	-2.711	1.706	10.77
CH103	1.124	-2.730	1.706	11.12
CH104	1.114	-2.614	1.704	9.409
CH105	1.136	-2.599	1.703	5.212
CH106	0.846	-2.466	1.702	6.992
CH107	1.008	-2.619	1.706	4.903
CH108	1.092	-2.687	1.707	2.823
CH109	1.005	-2.683	1.707	6.474
CH110	0.899	-2.590	1.704	10.14
CH111	0.871	-2.579	1.704	8.571
CH112	0.842	-2.583	1.705	8.104
CH201	1.297	-2.853	1.708	11.98
CH202	0.766	-2.515	1.703	9.889
CH203	0.793	-2.470	1.701	15.78
CH204	0.739	-2.450	1.700	17.53
CH205	0.717	-2.434	1.701	10.08
CH206	0.754	-2.465	1.701	14.81
CH207	0.774	-2.493	1.702	12.10
CH208	0.725	-2.462	1.701	8.932
CH209	0.723	-2.469	1.702	13.81
CH210	0.726	-2.458	1.701	20.28
CH211	4.776	-8.195	2.585	29.61
CH212	4.226	-7.892	2.586	21.40
CH213	3.119	-7.132	2.570	25.06

Source: Author.

Table 31 – Calibration standard uncertainties for the thermocouples (type E: from CH102 to CH210, type T: from CH211 to CH213.

Channel	U_{TC} [°C]
CH102	0.092
CH103	0.089
CH104	0.132
CH105	0.130
CH106	0.111
CH107	0.094
CH108	0.088
CH109	0.084
CH110	0.081
CH111	0.083
CH112	0.082
CH201	0.097
CH202	0.081
CH203	0.083
CH204	0.084
CH205	0.082
CH206	0.080
CH207	0.078
CH208	0.080
CH209	0.079
CH210	0.080
CH211	0.133
CH212	0.164
CH213	0.223

Source: Author.

APPENDIX B – Pressure transmitter calibration

This appendix details the calibration procedure of the absolute pressure transmitters. The two Warme/WTP-4010 absolute pressure transmitters were calibrated to four pressure points (100, 150, 200, and 250 kPa). The 4-20 mA output signal of the transmitters is linearly proportional to 0-300 kPa, as follows:

$$P\left(I_A\right) = 187.5\, I_A - 0.75, \tag{195}$$

where I_A is the output signal in Amperes. A closed system with saturated water was used to calibrate them.

Figure 51 illustrates the calibration experimental apparatus. The thermosiphon is a copper pipe of 12.7 mm in diameter. The calibration procedure commences by positioning the transmitter into the upper socket and opening the valve. Thus, a vacuum pump is linked to the valve, removing all the air from the system over an hour. Subsequently, the valve is sealed, and the vacuum pump is replaced with a glass pipe filled with distilled water. The valve is opened again, and the atmospheric pressure pushes the water inside the thermosiphon. The valve is shut once the amount of water needed for saturation within the pipe has entered the system.

All the thermosiphon is insulated with a 25.4 mm thick Armaflex® insulation material. Heat is applied using a nickel-chrome resistance to the bottom of the thermosiphon, while a type E thermocouple measures the wall temperature at the upper adiabatic part of the tube. Since adiabatic, the wall temperature is the saturated vapor temperature inside the thermosiphon. Therefore, the saturation pressure can be inferred from the saturation temperature using the CoolProp Python library.

A UW1430-COEL temperature controller controlled the heat input to keep the desired wall temperature constant. As for the thermocouple calibration, an Agilent 34972A datalogger recorded the data at 0.2 Hz, i.e., every five seconds. The data was gathered for at least six minutes after reaching a steady state, yielding more than 60 data points for each calibration pressure point. Three runs of calibration for each pressure transmitter were done to ensure repeatability.

Figure 52 shows the reference pressure and the transmitter measurements. As the measured data closely matched the reference values, the approach involved assessing the errors for each calibration point. Basically, instead of building a correlation between the output signal and pressure, a correction for each calibration pressure will be used to correct the measured pressure values.

The uncertainty of each correction factor was calculated by combining the uncertainty

Figure 51 – Pressure transmitter calibration experimental apparatus.

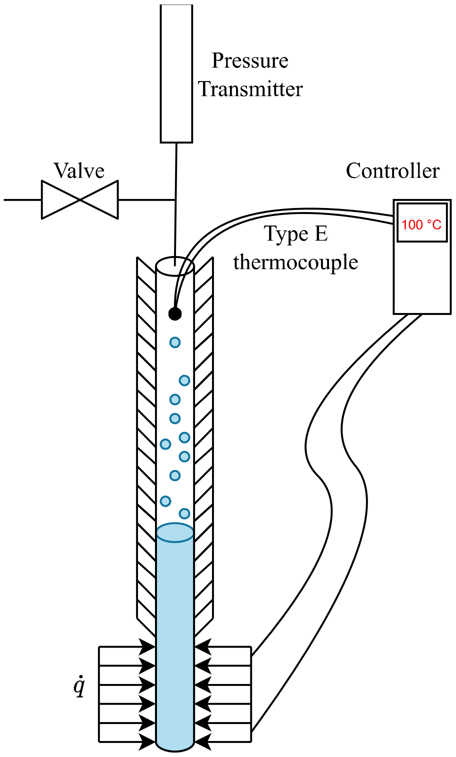

Source: Author.

of the DAQ system, thermocouple, and the standard deviation of both reference and transmitter measurements. Thus, the standard uncertainty of the correction factor can be calculated as follows:

$$u_c = \sqrt{\left(\frac{\partial p}{\partial I}\sqrt{{\sigma_{apt}}^2 + {u_{daq;apt}}^2}\right)^2 + \left\{\frac{\partial p_{sat}}{\partial T_{sat}}\left[{u_{TC}}^2 + \left(\frac{\partial T}{\partial V}\sqrt{{\sigma_{TC}}^2 + {u_{daq;TC}}^2}\right)^2\right]^{0.5}\right\}^2}, \tag{196}$$

where $\partial p/\partial I$, $\partial p_{sat}/\partial T_{sat}$, and $\partial T/\partial V$ are the sensibility functions of the absolute pressure transmitter, the saturation pressure and temperature, and the type E thermocouple, respectively, σ_{apt} and σ_{TC} are the standard deviation of the transmitter and thermocouple measurements, respectively, $u_{daq;apt}$ and $u_{daq;TC}$ are the DAQ system uncertainty for the transmitter and thermocouple measurements, respectively, and u_{TC} is the uncertainty of the thermocouple.

As done for the thermocouple calibration, the correction factor was incorporated by the standard uncertainty as follows:

$$u_{apt} = \max\left[\epsilon_{apt} + u_c; \left|\epsilon_{apt} - u_c\right|\right], \tag{197}$$

where ϵ_{apt} is the calibration error. To simplify the experimental uncertainty analysis, the maximum uncertainty was chosen as calibration uncertainty. Therefore, the standard calibration uncertainty is 3.125 and 3.460 kPa for each absolute pressure transmitter.

Figure 52 – Reference value and absolute pressure transmitter measurements for calibration.

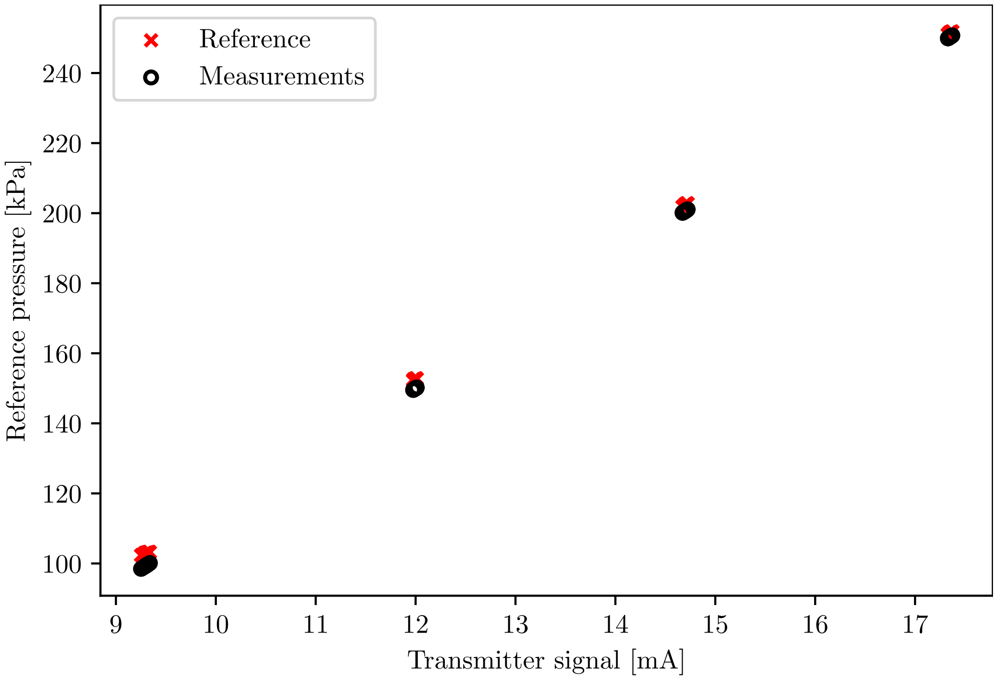

Source: Author.

APPENDIX C – Statistical analysis

The statistical analysis followed the procedures from Joint Committee for Guides in Metrology (2008). The guide specifies how to account for the experimental uncertainties types A and B. First, the uncertainty from the sensors' calibration and equipment, i.e., uncertainties type B, are discussed. Then, it shows how the uncertainties from random effects, i.e., uncertainties type A, are calculated. Last, the combined standard uncertainty and expanded uncertainty approach are presented.

C.1 Sensors calibration and type B uncertainties

The sensor calibration, such as thermocouples and absolute pressure transmitters, was performed at the Laboratory of Energy Conversion Engineering and Energy Technology (*Laboratórios de Engenharia de Processos de Conversão e Tecnologia de Energia*)/Boiling facilities. These calibration procedures are discussed in Appendix A and Appendix B, respectively. As a conservative measure, despite being calibrated in 2018, the Coriolis flowmeter accuracy was taken from its datasheet. The same approach was taken for the differential pressure transmitter accuracy and both shunt resistors.

The thermocouples were calibrated from 5 to 95 °C, with 10 °C intervals for the type E and 5 °C for the type T. A certified PT100 was used as a reference for the calibration. Six runs, three ascendant and three descendent, were taken to build each thermocouple a third-degree polynomial function. To make the analysis simple each thermocouple calibration uncertainty was calculated by combining the systematic error and the random effects as follows:

$$E_{c;tc} = \max\{e_s \pm u_c\}, \tag{198}$$

where e_s is the systematic error for each calibration point, and u_c is the combined uncertainty of the thermocouple variation, the ice reference variation, the PT100 variation, and the data acquisition system error. The u_c calculation is described in Appendix D. Thus, the maximum expanded calibration uncertainty of the thermocouples is 0.2012 °C. The coverage factor was considered as the t-student for 95% of confidence level and a degree of freedom of 59, which yields in $K_{tc} = 2.001$.

Unlike the thermocouples, the absolute pressure transmitter calibration was taken to check the error between the conversion function and the reference pressure. Three runs of calibration were taken for four points, 100, 150, 200, and 250 kPa. Similar to the thermocouples, the calibration error for the absolute pressure is given by:

$$E_{c;abt} = \max\{e_s \pm u_c\}, \tag{199}$$

where e_s is the systematic error for each calibration point, and u_c is the combined uncertainty of the pressure variation, the reference variation, and the data acquisition system error. The u_c calculation is described in Appendix D. The maximum expanded calibration uncertainty for the pressure transmitters is 4.441 kPa. Similarly to the thermocouple, the coverage factor is $K_{apt} = 2.001$.

From the Coriolis flowmeter datasheet, the measuring accuracy is 0.1%, and the repeatability error is 0.05% for mass flow measurements. For density measurements, the standard measuring accuracy is 5 kg m^{-3}, and the repeatability error is 0.2 kg m^{-3}. The differential pressure transmitter datasheet gives 0.25% of the full scale, which yields a precision of 75 Pa. Both shunt resistors have an accuracy of 0.5% of the full scale, which yields 0.10 A and 0.25 A for the 20 A and 50 A resistors, respectively. Table 32 lists the calibration uncertainties and errors from the sensors.

Table 32 – Type B uncertainty from sensors calibration and errors.

Measurand	Calibration uncertainty	Coverage factor
Temperature	0.2012 °C	2.001
Pressure	4.441 kPa	2.001
Mass flow rate	0.1% acc. 0.05% rep.	
Density	5 kg m^{-3} acc. 0.2 kg m^{-3} rep.	
Differential Pressure	75 Pa	
Shunt 20 A	0.10 A	
Shunt 50 A	0.25 A	

Source: Author.

The error associated to the data acquisition system was also considered into the type B uncertainty. Table 33 lists the accuracy of readings and range of measurements from the 34970A/34972A accuracy specification chart.

Table 33 – Accuracy of readings and range for the 34972A data logger.

Measurand	Range	Reading acc. [%]	Range acc. [%]
DC Voltage	100.0 mV	0.0050	0.0040
DC Voltage	10.0 V	0.0035	0.0005
AC Voltage	100.0 mV	0.06	0.04
AC Voltage	100.0 V	0.06	0.04
DC Current	10.0 mA	0.050	0.020
Frequency	40 Hz-300 kHz	0.01	

Source: Author.

C.2 Type A uncertainties

As discussed in section 3.3, a set of 60 data points, from five minutes straight of experimenting, were collected for each experimental point. That way, all 60 observations are under the same condition of measurement. According to Joint Committee for Guides in Metrology (2008), the experimental standard deviation of the mean is the standard uncertainty, although, as the measurands are variable, the sample standard deviation was chosen as the standard uncertainty. Then, the experimental standard uncertainty for an arbitrary variable x is given by:

$$u^2(x_j) = s^2(x_j) = \frac{1}{n-1}\sum_{j=1}^{n}(x_j - \bar{x})^2\,. \tag{200}$$

Since all the data were collected as electrical signals, apart from the dissipating resistances voltage drop, all the uncertainties type A must be converted into physical units such as [A], [°C], [kPa] and [kg m^{-3}]. This procedure is described in the next subsection.

C.3 Combined standard uncertainties

The uncertainty for a generic feature y which is calculated from multivariables $f(x_1, x_2, ..., x_N)$ is given as follows:

$$u_c{}^2(y) = \sum_{i=1}^{N}\left[\frac{\partial f}{\partial x_i}u(x_i)\right]^2, \tag{201}$$

where $\partial f/\partial x_i$ is the partial derivative of the conversion function $y = f(x_1, x_2, ..., x_N)$. First, the type A uncertainties from the electrical signals are converted into physical units. Then, the type B and A uncertainties are combined, so that the experimental standard uncertainty of each sensor is known. The standard uncertainties of the experimental features were calculated following the same procedure. The equations of each combined uncertainty are described in Appendix D.

C.4 Expanded uncertainties

The Joint Committee for Guides in Metrology (2008) suggests calculating the expanded uncertainty from the effective degrees of freedom. However, to keep the analysis simple, the coverage factor for the expanded uncertainty was calculated as the t-score for a confidence level of 95% and degrees of freedom of 59 from the 60 observations. The following equation shows the expanded uncertainty calculation:

$$U = t_{0.975;59}u_c, \tag{202}$$

where $t_{0.975;59}$ is 2.001.

C.5 Statistic metrics for evaluating models

The Mean Absolute Percentage Error (MAPE) and the Mean Percentage Error (MPE) are the main parameters used to evaluate the performance of correlations. The first returns the mean absolute deviation for each experimental point, while the second accounts for the mean relative deviation. The MAPE is given by:

$$MAPE = \frac{100}{n}\sum_{i=1}^{n}\left|\frac{y_{the} - y_{exp}}{y_{exp}}\right|, \tag{203}$$

where n is the number of points, y_{the} is the predicted value, and y_{exp} is the real value or the experimental value. The MPE is given as:

$$MPE = \frac{100}{n}\sum_{i=1}^{n}\frac{y_{the} - y_{exp}}{y_{exp}}. \tag{204}$$

While MAPE returns only positive numbers, MPE can assume negative values. Therefore, MPE gives an idea if the model is over or underpredicting the target.

Another way of evaluating the models is through the standard deviation of the residuals ($\epsilon = y_{the} - y_{exp}$). That gives information about how the predicted values are scattered over the mean of the residuals. A widely used metric for assessing model performance is the count of data points falling within a $\pm 30\%$ error band. Usually, more than 80% of points are considered satisfactory.

C.6 ANOVA test

The Analysis of Variance ANOVA is a commonly used statistical tool for comparing means of two or more factors or conditions (independent variables) over a target (dependent variable), especially for categorical features, such as the type of heating. It is based on a test of hypothesis, where the null hypothesis usually states the factor has no significance over the target. The requisites for ANOVA applications are the normal distribution of each group sample and homogeneity of variance, i.e., common variance between the groups. Some researchers say the ANOVA test is robust enough to give insights even for nonnormal distribution if the deviation is moderate (LIX; KESELMAN; KESELMAN, 1996).

The Kolmogorov-Smirnov test is a frequently used test for checking the normality of a sample, while the Levene test can be used for determining the homogeneity of variance. Both tests are available as functions in the Scipy Python package written as "scipy.stats.kstest" and "scipy.stats.levene", respectively. The kstest function takes the sample as input and returns the p-value for significance analysis. The Levene function receives the n samples as input and, as kstest, returns the p-value for significance analysis. Usually, a 95% confidence level is enough to ensure the normality of the sample and homogeneity of variance.

The ANOVA can be applied to a single factor, even when there are additional influencing features at play. For example, it is well known the Reynolds number and the Prandtl number influence the HTC, but what about the heating condition? An ANOVA test only for the heating condition factor can be performed to measure if it significantly influences the HTC. The mathematics of the ANOVA, Kolmogorov-Smirnov, and Levene tests can be easily found in any statistics book.

C.7 Mutual information

Mutual information is a statistical measure that summarizes how much two variables share information, i.e., how much a feature (independent variable, e.g., Reynolds number) can reduce uncertainty about a target (dependent variable, e.g., HTC). In other words, a mutual information score close to zero implies that knowing the value of a feature provides little insight into the target variable. On the other hand, a higher mutual information score indicates a reduced level of uncertainty regarding the target value. This measure is frequently used in machine learning projects for feature selection to decrease the problem dimensionality. Despite being very similar to correlation analysis, mutual information can capture any relationship between variables. It also accounts for categorical features such as heating conditions and flow patterns.

To calculate the mutual information score, continuous independent variables must be binned into groups, and the probability of each bin occurring must be accounted for. The mutual information score is given by:

$$I\left(X,Y\right)=\sum_{x}\sum_{y}p\left(x,y\right)\log\left[\frac{p\left(x,y\right)}{p\left(x\right)p\left(y\right)}\right], \tag{205}$$

where, $I\left(X,Y\right)$ is the mutual information score, X is the independent variable, Y is the dependent variable, $p(x,y)$ is the joint probability of X being x and Y being y, $p(x)$ is the probability of X being x, and $p(y)$ is the probability of Y being y. A function from the scikit-learn package for Python, written as “sklearn.feature_selection.mutual_info_regression”, returns the mutual information score given a feature and a target.

As shown in subsection 2.5.1, there are many ways of writing the same dimensionless parameters. Mutual information not only provides insights into the dominant dimensionless numbers that are more suitable for HTC correlations but also suggests the most effective way to represent them to capture the effects they describe.

APPENDIX D – Uncertainties

This appendix details the experimental uncertainty analysis and shows the equations for its calculation. First, the experimental uncertainty of the direct measurements is presented. Then, the experimental features' uncertainty is described. Last, a table with the maximum uncertainty of each parameter is shown.

D.1 Direct measurement sparameters

For the direct measurement parameters, the standard uncertainties were calculated by combining the calibration uncertainty (when applicable), the standard deviation of the measurements, and the DAQ uncertainty. The mean and standard deviation were calculated from 60 data points for every experimental point. All data were considered normally distributed, and the uncertainty from data sheets and DAQ system rectangular distribution.

D.1.1 Temperatures

The temperature standard uncertainties are given by:

$$u_T = \left\{ {u_C}^2 + \left[\frac{\partial T}{\partial V} \left({\sigma_{V;T}}^2 + {\sigma_{V;ice}}^2 + {u_{daq;mV}}^2 \right)^{0.5} \right]^2 \right\}^{0.5}, \tag{206}$$

where u_C is the calibration uncertainty, $\partial T / \partial V$ is the sensibility factor, $\sigma_{V;T}$ is the thermocouple measurement standard deviation, $\sigma_{V;ice}$ is the ice bath thermocouple standard deviation, and $u_{daq;mV}$ is the DAQ uncertainty for measurements in mV.

D.1.2 Pressure

The pressure standard uncertainties are given by:

$$u_p = \left\{ {u_C}^2 + \left[\frac{\partial p}{\partial I} \left({\sigma_{A;p}}^2 + {u_{daq;mA}}^2 \right)^{0.5} \right]^2 \right\}^{0.5}, \tag{207}$$

where u_C is the calibration uncertainty, $\partial p / \partial I$ is the sensibility factor, $\sigma_{A;p}$ is the transmitter measurement standard deviation, and $u_{daq;mA}$ is the DAQ uncertainty for measurements in mA.

D.1.3 Mass flow rate

The mass flow rate standard uncertainty is given by:

$$u_{\dot{m}} = \left\{ {u_{coriolis}}^2 + \left[\frac{\partial \dot{m}}{\partial I} \left({\sigma_{A;\dot{m}}}^2 + {u_{daq;mA}}^2 \right)^{0.5} \right]^2 \right\}^{0.5}, \tag{208}$$

where $u_{coriolis}$ is the coriolis data sheet uncertainty, $\partial \dot{m}/\partial I$ is the sensibility factor, $\sigma_{A;\dot{m}}$ is the transmitter measurement standard deviation, and $u_{daq;mA}$ is the DAQ uncertainty for measurements in mA.

D.1.4 Voltage and current

The voltage standard uncertainties are given by:

$$u_V = \left({\sigma_V}^2 + {u_{daq;V}}^2\right)^{0.5}, \tag{209}$$

where σ_V is the transmitter measurement standard deviation, and $u_{daq;V}$ is the DAQ uncertainty for measurements in V.

The current standard uncertainties are given by:

$$u_I = \left\{\left[\frac{\partial I}{\partial V}\left({u_{shunt}}^2 + {\sigma_V}^2 + {u_{daq;V}}^2\right)^{0.5}\right]^2\right\}^{0.5}, \tag{210}$$

where u_{shunt} is the shunt data sheet uncertainty, $\partial I/\partial V$ is the sensibility factor, σ_V is the transmitter measurement standard deviation, and $u_{daq;V}$ is the DAQ uncertainty for measurements in V.

D.2 Experimental features uncertainty

The experimental features uncertainties are calculated by combining the uncertainties from the direct measurements and the given sensibility factor for each variable. The sensibility factors are derived from the equations presented at subsection 3.1.4.

D.2.1 Heat rates

The heat rates uncertainties are given by:

$$u_{\dot{q}} = \left[\left(\frac{\partial \dot{q}}{\partial V}u_V\right)^2 + \left(\frac{\partial \dot{q}}{\partial I}u_I\right)^2\right]^{0.5}, \tag{211}$$

where u_V is the uncertainty of the voltage, u_I is the uncertainty of the current, and the sensibility factors are given by:

$$\frac{\partial \dot{q}}{\partial V} = \overline{I} \text{ and } \frac{\partial \dot{q}}{\partial I} = \overline{V}, \tag{212}$$

where $\overline{I}$ and $\overline{V}$ are the mean measured current and voltage, respectively. Then, the uncertainty is given as:

$$u_{\dot{q}} = \left[\left(\overline{I}\, u_V\right)^2 + \left(\overline{V}\, u_I\right)^2\right]^{0.5}. \tag{213}$$

D.2.2 Heat fluxes

The heat fluxes uncertainties are given by:

$$u_{q''} = \sqrt{\left(\frac{\partial q''}{\partial \dot{q}} u_{\dot{q}}\right)^2}, \tag{214}$$

where the sensibility factor is given by:

$$\frac{\partial q''}{\partial \dot{q}} = \frac{1}{A_h}, \tag{215}$$

where A_h is the heated area. Then, the uncertainty is given as:

$$u_{q''} = \sqrt{\left(\frac{u_{\dot{q}}}{A_h}\right)^2}. \tag{216}$$

D.2.3 Single phase bulk temperature

The single-phase bulk temperatures uncertainties are given by:

$$u_{T_B} = \sqrt{{u_{T_{in}}}^2 + \left(\frac{\partial T_B}{\partial \dot{q}} u_{\dot{q}}\right)^2 + \left(\frac{\partial T_B}{\partial \dot{m}} u_{\dot{m}}\right)^2}, \tag{217}$$

where the sensibility factors are given by:

$$\frac{\partial T_B}{\partial \dot{q}} = \frac{\Gamma z}{\bar{\dot{m}} c_p} \text{ and } \frac{\partial T_B}{\partial \dot{m}} = -\frac{\bar{\dot{q}} \Gamma z}{\bar{\dot{m}}^2 c_p}. \tag{218}$$

Then, the uncertainty is given as:

$$u_{T_B} = \sqrt{{u_{T_{in}}}^2 + \left(\frac{\Gamma z}{\bar{\dot{m}} c_p} u_{\dot{q}}\right)^2 + \left(-\frac{\bar{\dot{q}} \Gamma z}{\bar{\dot{m}}^2 c_p} u_{\dot{m}}\right)^2}. \tag{219}$$

D.2.4 Two phase bulk temperature

The two-phase bulk temperatures uncertainties are given by:

$$u_{T_B} = \sqrt{\left[\frac{\partial T_{sat}}{\partial p} \left({u_{p_{in}}}^2 + \frac{\partial p}{\partial \Delta p} {u_{\Delta p}}^2\right)^{0.5}\right]^2}, \tag{220}$$

where the sensibility factors are given by:

$$\frac{\partial T_{sat}}{\partial p} = \left.\frac{\partial T_{sat}}{\partial p}\right|_{x=0} \text{ and } \frac{\partial p}{\partial \Delta p} = \frac{1}{z}. \tag{221}$$

Then, the uncertainty is given as:

$$u_{T_B} = \sqrt{\left\{\left.\frac{\partial T_{sat}}{\partial p}\right|_{x=0} \left[{u_{p_{in}}}^2 + \left(\frac{u_{\Delta p}}{z}\right)^2\right]^{0.5}\right\}^2}. \tag{222}$$

D.2.5 Mass velocity

The mass velocity uncertainty is given by:

$$u_G = \sqrt{\left(\frac{\partial G}{\partial \dot{m}} u_{\dot{m}}\right)^2}, \tag{223}$$

where the sensibility factor is given by:

$$\frac{\partial G}{\partial \dot{m}} = \frac{1}{A_{cs}}. \tag{224}$$

Then, the uncertainty is given as:

$$u_G = \sqrt{\left(\frac{u_{\dot{m}}}{A_{cs}}\right)^2}. \tag{225}$$

D.2.6 Test section inlet quality

The test section inlet quality uncertainty is given by:

$$u_{x_{in}} = \sqrt{\left(\frac{\partial x_{in}}{\partial h_l}\frac{\partial h_l}{\partial p_{in}} u_{p_{in}}\right)^2 + \left(\frac{\partial x_{in}}{\partial h_{lv}}\frac{\partial h_{lv}}{\partial p_{in}} u_{p_{in}}\right)^2 + \left(\frac{\partial x_{in}}{\partial h_{in}} u_{h_{in}}\right)^2}, \tag{226}$$

where the sensibility factors are given by:

$$\frac{\partial x_{in}}{\partial h_l} = -\frac{1}{h_{lv}}, \frac{\partial h_l}{\partial p_{in}} = \left.\frac{\partial h_l}{\partial p_{in}}\right|_{T=cte}, \frac{\partial x_{in}}{\partial h_{lv}} = -\frac{(h_{in} - h_l)}{{h_{lv}}^2}, \text{ and } \frac{\partial h_{lv}}{\partial p_{in}} = \left.\frac{\partial h_{lv}}{\partial p_{in}}\right|_{T=cte}. \tag{227}$$

The $u_{h_{in}}$ is given by:

$$u_{h_{in}} = \left[\left(\frac{\partial h_{in}}{\partial h_{in;ph}} u_{h_{in;ph}}\right)^2 + \left(\frac{\partial h_{in}}{\partial \dot{q}_{ph}} u_{\dot{q}_{ph}}\right)^2 + \left(\frac{\partial h_{in}}{\partial \dot{m}} u_{\dot{m}}\right)^2\right]^{0.5}, \tag{228}$$

where the sensibility factors are:

$$\frac{\partial h_{in}}{\partial \dot{q}_{ph}} = \frac{1}{\dot{m}} \text{ and } \frac{\partial h_{in}}{\partial \dot{m}} = -\frac{\dot{q}_{ph}}{\dot{m}^2}. \tag{229}$$

The $u_{h_{in;ph}}$ and its sensibility factors are calculated as follows:

$$u_{h_{in;ph}} = \left[\left(\frac{\partial h_{in;ph}}{\partial p_{in;ph}} u_{p_{in;ph}}\right)^2 + \left(\frac{\partial h_{in;ph}}{\partial T_{in;ph}} u_{T_{in;ph}}\right)^2\right]^{0.5}, \tag{230}$$

where the sensibility factors are given as:

$$\frac{\partial h_{in;ph}}{\partial p_{in;ph}} = \left.\frac{\partial h_{in;ph}}{\partial p_{in;ph}}\right|_{T=cte} \text{ and } \frac{\partial h_{in;ph}}{\partial T_{in;ph}} = \left.\frac{\partial h_{in;ph}}{\partial T_{in;ph}}\right|_{p=cte}. \tag{231}$$

D.2.7 Test section outlet quality

The test section outlet quality uncertainty is given by:

$$u_{x_{out}} = \sqrt{\left(\frac{\partial x_{out}}{\partial h_l}\frac{\partial h_l}{\partial p_{ts}}u_{p_{ts}}\right)^2 + \left(\frac{\partial x_{out}}{\partial h_{lv}}\frac{\partial h_{lv}}{\partial p_{ts}}u_{p_{ts}}\right)^2 + \left(\frac{\partial x_{out}}{\partial h_{ts}}u_{h_{out}}\right)^2}, \tag{232}$$

where the sensibility factors are given by:

$$\frac{\partial x_{out}}{\partial h_l} = -\frac{1}{h_{lv}}, \frac{\partial h_l}{\partial p_{ts}} = \left.\frac{\partial h_l}{\partial p_{ts}}\right|_{T=cte}, \frac{\partial x_{out}}{\partial h_{lv}} = -\frac{(h_{out}-h_l)}{{h_{lv}}^2}, \text{ and } \frac{\partial h_{lv}}{\partial p_{ts}} = \left.\frac{\partial h_{lv}}{\partial p_{ts}}\right|_{T=cte}. \tag{233}$$

The $u_{h_{out}}$ is given by:

$$u_{h_{out}} = \left[\left(\frac{\partial h_{out}}{\partial h_{in}}u_{h_{in}}\right)^2 + \left(\frac{\partial h_{out}}{\partial \dot{q}_{ts}}u_{\dot{q}_{ts}}\right)^2 + \left(\frac{\partial h_{out}}{\partial \dot{m}}u_{\dot{m}}\right)^2\right]^{0.5}, \tag{234}$$

where the sensibility factors are:

$$\frac{\partial h_{out}}{\partial \dot{q}_{ts}} = \frac{1}{\dot{m}} \text{ and } \frac{\partial h_{out}}{\partial \dot{m}} = -\frac{\dot{q}_{ts}}{\dot{m}^2}. \tag{235}$$

The $u_{h_{in}}$ is calculated from Equation 228 and its sensibility factor is given by:

$$\frac{\partial h_{out}}{\partial h_{in}} = 1. \tag{236}$$

D.2.8 Local heat transfer coefficient

The local heat transfer coefficient uncertainties are given as:

$$u_h = \sqrt{\left(\frac{\partial h}{\partial h_t}u_{h_t}\right)^2 + \left(\frac{\partial h}{\partial h_l}u_{h_l}\right)^2 + \left(\frac{\partial h}{\partial h_b}u_{h_b}\right)^2} \tag{237}$$

where the sensibility factors are:

$$\frac{\partial h}{\partial h_t} = \frac{1}{4}, \frac{\partial h}{\partial h_l} = \frac{1}{2}, \text{ and } \frac{\partial h}{\partial h_b} = \frac{1}{4}. \tag{238}$$

The u_t is given by:

$$u_{h_t} = \left[\left(\frac{\partial h_t}{\partial q''_{ts}}u_{q''_{ts}}\right)^2 + \left(\frac{\partial h_t}{\partial T_t}u_{T_t}\right)^2 + \left(\frac{\partial h_t}{\partial T_B}u_{T_B}\right)^2\right]^{0.5} \tag{239}$$

where the sensibility factors are given by:

$$\frac{\partial h_t}{\partial q''_{ts}} = \frac{w_t}{T_t - T_B}, \frac{\partial h_t}{\partial T_t} = -\frac{w_t q''_{ts}}{(T_t - T_B)^2}, \text{ and } \frac{\partial h_t}{\partial T_B} = \frac{w_t q''_{ts}}{(T_t - T_B)^2} \tag{240}$$

The u_{h_l} is given by:

$$u_{h_l} = \left[\left(\frac{\partial h_l}{\partial q''_{ts}}u_{q''_{ts}}\right)^2 + \left(\frac{\partial h_l}{\partial T_l}u_{T_t}\right)^2 + \left(\frac{\partial h_l}{\partial T_B}u_{T_B}\right)^2\right]^{0.5} \tag{241}$$

where the sensibility factors are given by:

$$\frac{\partial h_l}{\partial q''_{ts}} = \frac{w_l}{T_l - T_B}, \frac{\partial h_l}{\partial T_l} = -\frac{w_l q''_{ts}}{(T_l - T_B)^2}, \text{ and } \frac{\partial h_l}{\partial T_B} = \frac{w_l q''_{ts}}{(T_l - T_B)^2} \tag{242}$$

The u_{h_b} is given by:

$$u_{h_b} = \left[\left(\frac{\partial h_b}{\partial q''_{ts}} u_{q''_{ts}} \right)^2 + \left(\frac{\partial h_b}{\partial T_b} u_{T_b} \right)^2 + \left(\frac{\partial h_b}{\partial T_B} u_{T_B} \right)^2 \right]^{0.5} \tag{243}$$

where the sensibility factors are given by:

$$\frac{\partial h_b}{\partial q''_{ts}} = \frac{w_b}{T_b - T_B}, \frac{\partial h_b}{\partial T_b} = -\frac{w_b q''_{ts}}{(T_b - T_B)^2}, \text{ and } \frac{\partial h_b}{\partial T_B} = \frac{w_b q''_{ts}}{(T_b - T_B)^2} \tag{244}$$

D.2.9 Test section mean heat transfer coefficient

The test section mean heat transfer coefficient is given by:

$$u_{h_m} = \sqrt{\sum_{i=1}^{7} \left(\frac{\partial h_m}{\partial h_i} u_{h_i} \right)^2}, \tag{245}$$

where the sensibility factors are:

$$\frac{\partial h_m}{\partial h_i} = \begin{cases} (\delta_l + \Delta_l/2)/L_{ts} & \text{for } i = 1,\ 7 \\ \Delta_l/L_{ts} & \text{for } 2 \leq i \leq 6 \end{cases}. \tag{246}$$

The u_{h_i} are calculated by Equation 237 for each measurement cross-section.

D.2.10 Pressure drop gradient

The test section pressure drop gradient is given by:

$$u_{\mathrm{d}p/\mathrm{d}z} = \sqrt{\left(\frac{\partial \mathrm{d}p/\mathrm{d}z}{\partial \Delta p} u_{\Delta p} \right)^2}, \tag{247}$$

where the sensibility factors are:

$$\frac{\partial \mathrm{d}p/\mathrm{d}z}{\partial \Delta p} = \frac{1}{L_{ts}} \tag{248}$$

The $u_{\mathrm{d}p/\mathrm{d}z}$ becomes:

$$u_{\mathrm{d}p/\mathrm{d}z} = \sqrt{\left(\frac{u_{\Delta p}}{L_{ts}} \right)^2}. \tag{249}$$

D.3 Uncertainty values table for all data

Table 34 lists the maximum, minimum, and the 90% percentile of the relative uncertainties for the indirect experimental data.

Table 35 lists the maximum, minimum, and the 90% percentile of the relative uncertainties for the indirect experimental data.

Table 34 – Maximum, minimum, and 90% percentile of uncertainties for all direct experimental points.

	Parameters	min	max	90%
CH102	$T_{t;1}$ [°C]	0.206	0.533	0.387
CH103	$T_{l;1}$ [°C]	0.201	0.443	0.311
CH104	$T_{b;1}$ [°C]	0.280	0.328	0.289
CH105	$T_{t;2}$ [°C]	0.276	0.560	0.411
CH106	$T_{l;2}$ [°C]	0.242	0.438	0.320
CH107	$T_{b;2}$ [°C]	0.209	0.266	0.221
CH108	$T_{t;3}$ [°C]	0.199	0.508	0.320
CH109	$T_{l;3}$ [°C]	0.191	0.406	0.269
CH110	$T_{b;3}$ [°C]	0.187	0.236	0.201
CH111	$T_{t;4}$ [°C]	0.191	0.576	0.325
CH112	$T_{l;4}$ [°C]	0.189	0.420	0.267
CH201	$T_{b;4}$ [°C]	0.215	0.268	0.230
CH202	$T_{t;5}$ [°C]	0.187	0.529	0.301
CH203	$T_{l;5}$ [°C]	0.190	0.398	0.254
CH204	$T_{b;5}$ [°C]	0.192	0.245	0.211
CH205	$T_{t;6}$ [°C]	0.190	0.450	0.306
CH206	$T_{l;6}$ [°C]	0.186	0.342	0.253
CH207	$T_{b;6}$ [°C]	0.181	0.262	0.203
CH208	$T_{t;7}$ [°C]	0.186	0.410	0.278
CH209	$T_{l;7}$ [°C]	0.184	0.345	0.244
CH210	$T_{b;7}$ [°C]	0.186	0.281	0.203
CH212	$T_{in;ph}$ [°C]	0.263	0.273	0.263
CH211	$T_{in;ts}$ [°C]	0.254	0.462	0.359
CH213	$T_{out;ts}$ [°C]	0.469	0.591	0.520
CH215	T_{∞} [°C]	0.577	0.577	0.577
CH121	$P_{in;ph}$ [kPa]	6.921	7.134	7.026
CH122	P_{in} [kPa]	6.248	6.418	6.330
CH221	$\dot{m}$ [g s^{-1}]	0.034	0.112	0.076
CH115	V_{ph} [V]	0.289	0.290	0.289
CH116	I_{ph} [A]	0.053	0.208	0.143
CH113	V_{ts} [V]	0.116	0.121	0.116
CH114	I_{ts} [A]	0.001	0.009	0.002

Source: Author.

Table 35 – Maximum, minimum, and 90$\%$ percentile of relative uncertainties for all indirect experimental points.

	Parameters	min	max	90$\%$
Ph heat rate	$\dot{q}_{ph}$	1.276	11.680	5.300
Ph heat flux	q''_{ph}	1.190	10.894	4.944
Ts heat rate	$\dot{q}_{ts}$	1.050	1.936	1.884
Ts heat flux	q''_{ts}	0.979	1.806	1.758
Bulk temp. 1	$T_{B;1}$	3.289	5.138	5.024
Bulk temp. 2	$T_{B;2}$	3.294	5.139	5.025
Bulk temp. 3	$T_{B;3}$	3.298	5.140	5.026
Bulk temp. 4	$T_{B;4}$	3.303	5.141	5.027
Bulk temp. 5	$T_{B;5}$	3.307	5.142	5.028
Bulk temp. 6	$T_{B;6}$	3.312	5.144	5.028
Bulk temp. 7	$T_{B;7}$	3.316	5.145	5.029
Sat. Temperature	T_{sat}	3.412	5.612	5.491
Mass velocity	G	0.251	2.446	1.590
Inlet quality	x_{in}	2.028	635.716	9.377
Outlet quality	x_{out}	2.131	93.214	10.058
HTC 1	h_1	3.487	102.072	28.852
HTC 2	h_2	3.617	42.540	21.116
HTC 3	h_3	3.539	38.309	21.921
HTC 4	h_4	3.258	40.283	21.868
HTC 5	h_5	3.461	43.397	22.301
HTC 6	h_6	3.781	51.305	30.143
HTC 7	h_7	4.403	36.876	26.769
Mean HTC	$\overline{h}_{tp}$	3.991	86.661	22.408

Source: Author.